# NON-GAUSSIAN DENSITY FIELDS AND THEIR SIGNATURES IN REDSHIFT SURVEYS

Alison Janet Stirling

Presented for the degree of Doctor of Philosophy at
The University of Edinburgh
1998

This thesis is solely my own composition, except where specifically indicated in the text.

Alison Stirling,
September 1998.

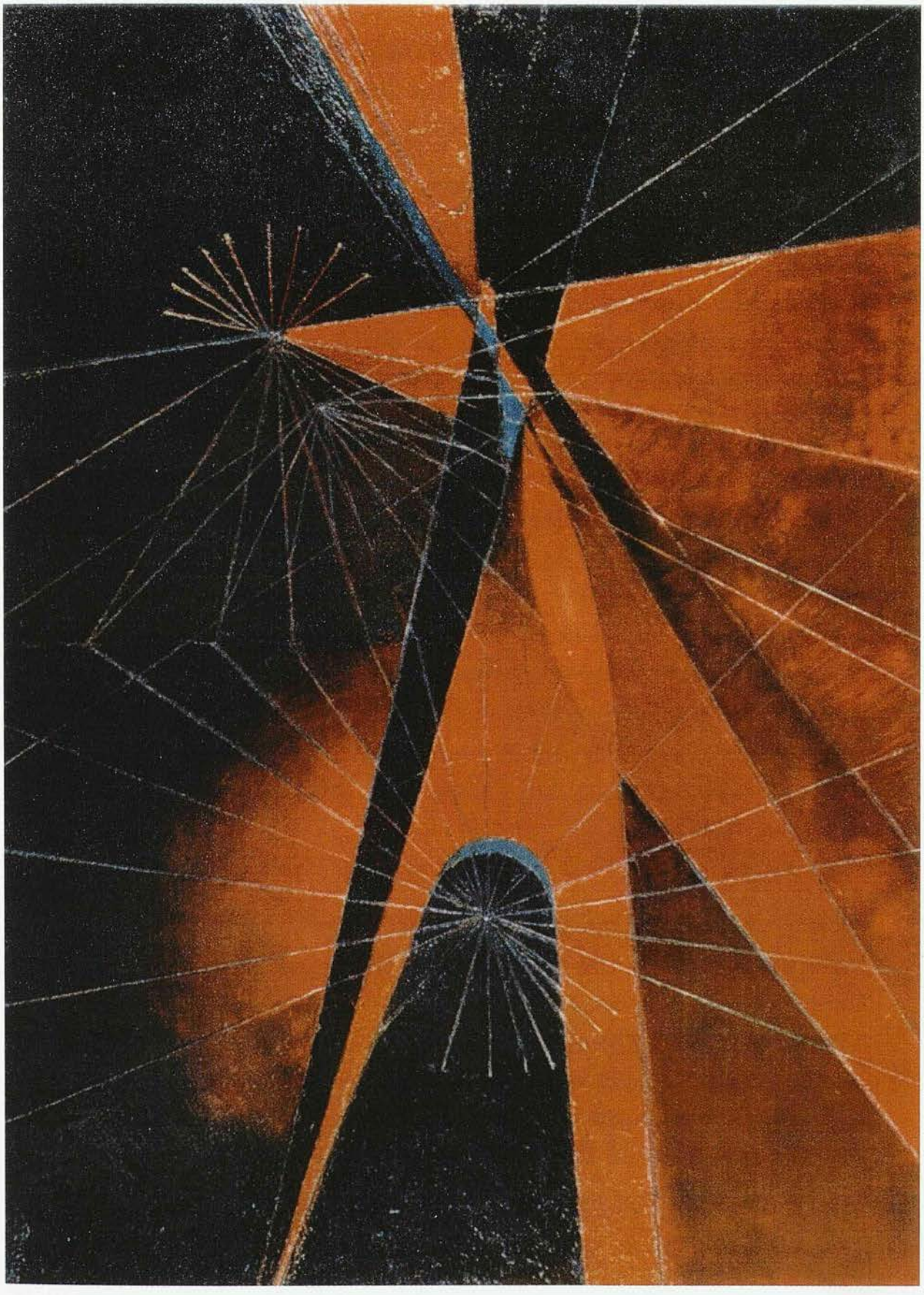

'Naissance de l'Univers', Antoine Pevsner, 1933

# Acknowledgements

My experience of doing a phD suggests that it requires a mixture of dedication, inspiration, luck, support, and a level of determination that approaches bloody mindedness to finish. I am indebted to the following people for their role in this game.

I have to thank my supervisor John Peacock for always making time for me, giving me ideas when stuck, in the last stages of writing up giving the encouragement needed to get to the end, and for sending an email that resulted in an excellent trip to Japan. Other people in the department whose interest in my work and ideas were much appreciated are Alan Heavens, who kindly read this manuscript, and Andy Taylor for many an interesting discussion. Thanks also to Bob Mann for providing the biasing code which is used in chapter 3.

The students in the ROE have been great fun to be with, and I feel I must thank several of them, so at the risk of sounding like a wedding speech here goes: I start with my fellow classmates with whom I shared the rigours of kamikazes, a catalogue of talks and poster sessions, and general comradeship: thanks to Richard Brockie for his enthusiasm and general goodnaturedness, Nick for providing support with the contrary, and Paulina for dragging me to aerobics. Thanks also to Harry for an interesting foursome dinner, Jonny for an uneatably hot curry, Steve for fellow comeradeship, Doddsy for general good humouredness in the face of much abuse, Mike for conversations about life, Bill for cosmological companionship, a honeymoon in Leiden, and many an early rendez-vous outside court 1, Henry for his earnestness and encouragement, and Jo for teaching me how to make oboe reeds and lending me her squash racquet for several months.

In my last couple of years I had the fortune to share offices with some really great people whose friendships became invaluable – first of these is Peet, whose thoughtfulness and interest in cosmology combined to be a great source of interesting discussions. I shall remember him for an alarmingly accelerated view of Cameron Toll, and for his tangential sense of humour, which while sometimes only understood by himself, was immense fun. He is greatly missed. From R8 to the occupants of the Remote Observing room – the group who six handedly kept me (more or less) sane while writing up – with their sense of humour, many a BLT hour spent discussing important issues of the day, and with

their supportive and jovial spirit, they were truly a great bunch of people to be with – individually thanks to 'trajectorially challenged' Simon for keeping us in good spirits with a seemingly endless source of pranks, Richard for combining good naturedness, sighs of futility with an unweildingly panoramic vocabulary and Elese for her real sense of delight in the world, and a much appreciated friendship that has ranged from making me cups of tea, providing encouragement, sympathy, and many a revitalising walk around Blackford Hill.

Further afield I am indebted to James both for his respect, and his disrespect (and for finding a copy of the cover painting), Zam for Saturday excursions, his faith in me and much valued friendship, Matthew for his sense of excitement about the world, and for being the model phD student, Martin for long evenings in restaurants scribbling formulae on serviettes, and Bondy for introducing me to Nanci, being a good companion on Lake District bound trains, and for indulging my penchant for French films[1].

Back in Edinburgh, I thank Andrew for his constant friendship, peace, plenty of resetting walks, and in the final few days of writing up feeding me (rognons free) sandwiches, prof reding, and sitting up with me while this ream was printing out – love and many thanks.

Finally I'd like to thank my family – my brother Iain for his companionship and sense of humour, and my parents for their continued interest, generous financial assistance, and unconditional support.

[1](A propos: The people at l'Observatoire Midi-Pyrénées in Toulouse are thanked for their generous hospitality and providing a very agreable transition from student to post-doc life.)

# Contents

# ABSTRACT

The wealth of structure observed from galactic to super-cluster scales is believed to have formed through the gravitational collapse of tiny inhomogeneities that existed in the matter field in the early universe. The origin of these inhomogeneities, however, is still a matter of debate, and there are a number of theories that set out to explain their initiation. A possible distinguishing factor between these theories is the nature of the distribution of the primordial density fluctuations.

This thesis is concerned with the measurement of the statistics of density fluctuations from redshift surveys with a view to placing constraints on the distribution of fluctuations in the primordial density field. The first approach considered is the effect of different statistical distributions on the evolution of the power spectrum into the highly non-linear regime. This has been explored by running N-body simulations with different non-Gaussian initial conditions, and comparing the locus of evolution from the linear to the non-linear power spectrum with that derived for initially Gaussian fields. The evolution of power for a field with $\chi^2$ initial conditions is used to form a test for the viability of an isocurvature $\chi^2$ model which has been proposed in the literature. Higher order moments of evolved simulations of this model under various biasing schemes are then compared with existing measurements of higher order moments from the APM galaxy survey.

Having investigated the evolution of the power spectrum of initially non-Gaussian fields, a natural progression is to consider higher order Fourier statistics as a test for non-Gaussian fields. A four-point Fourier based test is developed in which correlations between the amplitude squared of the density modes (power modes) are compared with

the Gaussian prediction, which is a function of the selection function only. The test has been applied to the combined QDOT and 1.2 Jy redshift surveys, and the results have enabled quantitative limits to be placed on a particular class of non-Gaussian models. The projected increase in sensitivity of the test for forthcoming surveys has also been calculated.

The power correlations test is to some degree affected by redshift distortions, and extensions to the test are developed to take into account their effect for spherical redshift surveys. The emphasis is then shifted, and the correlations between Fourier modes are used as a new method for measuring the redshift distortion parameter, $\beta$. This approach does not rely on the distant observer approximation, and extensions have been made to deal with the mildly non-linear regime, in which the randomised velocities of galaxies in clusters damp the linear redshift distortions, and form the so called 'fingers of god'. The method is applied to an ensemble of simulations to test its reliability, including some mock QDOT+1.2 Jy and PSCz surveys. Finally, the test is applied to the real QDOT+1.2 Jy survey, and an estimate found for the redshift distortion parameter, $\beta$.

# Chapter 1

# INTRODUCTION

Human beings have a long record of fascination about their own existence. This has been evident from the first simple cave drawings, through a varied history of mythology, and latterly with the tremendous developments in physics that have enabled quantitative predictions to be made about our environment. While our mythological history sheds light on many ages and cultures, most would agree that it is to the physical world that one has to look to explain how these creative beings come to find themselves occasionally pondering their own existence.

Cosmology is the attempt to understand through science the origin, evolution, and behaviour of the Universe as a whole. It has a long and remarkable history, and while we have come a long way since the Copernican debate about the centre of rotation of our solar system, current discrepancies coupled with experience of the past suggests that we too have a long way to go.

The first part of this chapter contains a brief review of modern physical cosmology, including some of the unresolved issues in cosmology, as well as some of the theories that have arisen to address these issues. The second part of the chapter introduces much of the mathematical formalism required for the work in the rest of this thesis. This includes some of the mathematical techniques used in the field of large scale structure.

The Cosmological Principle asserts that any fundamental observer placed anywhere in the Universe will find it to be isotropic in all its measurable quantities. This assumption

further implies that the Universe must be homogeneous, since this is the only means by which two randomly placed observers may both observe spherical symmetry. While philosophical and perhaps even pragmatic in origin, the cosmological principle is supported on large scales with a wealth of evidence. This ranges from observations of the microwave background, which has been found to be uniform to one part in $10^5$ over scales hundreds of times larger than the horizon scale at the epoch of recombination (Górski *et al.* 1996), to galaxy counts, which also appear to be independent of orientation, for example in the Las Campanas survey (Shectman *et al.* 1996), and the QDOT 1-in-6 all sky redshift survey (Saunders *et al.* 1991). These observations confirm our isotropic picture of the Universe, but redshift surveys have also enabled us to measure the local density field in three dimensions. On scales above $\sim 100\,h^{-1}\,\mathrm{Mpc}$, the mean square deviation from the average density is found to be of order a few percent (*e.g.* Tadros *et al.* 1998), providing evidence for homogeneity in the local Universe.

The importance of the cosmological principle and its supporting evidence is that it gives us license to extrapolate (with suitable care) our observations of the local Universe to the Universe as a whole – and thus to test models for the evolution and nature of the whole Universe.

## 1.1 Dynamics of the Universe

Cosmology owes its beginnings as a mathematical science to Newton. Newton not only established a framework for mechanics, with his famous three laws of motion, but he also came up with **The law of universal gravitation**, which was first formulated in 1665. This describes the force exerted on a mass $M_1$ due to another mass, $M_2$ when they are separated by a distance $r$:

$$\mathbf{F} = \frac{GM_1M_2\mathbf{r}}{r^3}. \tag{1.1}$$

Implicit in Newton's 'universal' law of gravitation is the equivalence of gravitational and inertial masses – resistance to motion described by the constant of proportionality between force and acceleration in Newton's second law, $\mathbf{F} = m\mathbf{a}$, turns out to be the same property that affects the magnitude of the gravitational pull.

This 'weak equivalence principle' was built on by Einstein, who further asserted that the physics in inertial frames is equivalent to (or indistinguishable from) freely falling frames. This is known as the **strong equivalence principle**, and formed the basis for General Relativity.

### 1.1.1 The Robertson-Walker metric and the Friedmann equations

In General Relativity, the basic idea is to use the equivalence of inertial and free fall frames to transform gravity into a property of spacetime itself – thus building on Mach's ideas of motion being defined by the overall distribution of matter. The general relativistic formalism is in tensor notation to enable the curvature of space to be incorporated easily.

The interval between two events for curved space is given by:

$$\mathrm{d}s^2 = g_{\mu\nu}\mathrm{d}x^\mu \mathrm{d}x^\nu \tag{1.2}$$

where indices $\mu$ and $\nu$ run from 0 to 3, $x^0 = ct$ is the time coordinate and $x^1, x^2, x^3$ are spatial coordinates. $g_{\mu\nu}$ is the metric tensor which describes the geometry of spacetime. In flat, Minkowski spacetime, it is simply given by: diag$[1, -1, -1, -1]$. The Einstein equations relate properties of the curvature of space-time to the energy-momentum tensor, $T_{\mu\nu}$,

$$G_{\mu\nu} \equiv R_{\mu\nu} - \frac{1}{2}Rg_{\mu\nu} - \Lambda g_{\mu\nu} = \frac{8\pi G}{c^4}T_{\mu\nu}, \tag{1.3}$$

where $R_{\mu\nu}$ is the Ricci tensor, providing information about spatial curvature, $R \equiv g^{\mu\nu}R_{\mu\nu}$ is the Ricci or curvature scalar, and $\Lambda$ is known as the cosmological constant. The contravariant form of the Einstein tensor, $G^{\mu\nu}$ has the property that its covariant divergence is zero, thus retaining conservation of energy (see *e.g.* Møller, 1972).

In an isotropic and homogeneous universe, the metric, $g_{\mu\nu}$ can be described by the Robertson-Walker metric, which in polar spatial coordinates $(r, \theta, \phi)$ is (see *e.g.* Longair 1984 for a derivation):

$$\mathrm{d}s^2 = (c\,\mathrm{d}t)^2 - a\,(t)^2\left[\frac{\mathrm{d}r^2}{1 - Kr^2} + r^2\left(\mathrm{d}\theta^2 + \sin^2\theta\mathrm{d}\phi^2\right)\right], \tag{1.4}$$

where $r$ is the comoving angular diameter distance, and $a(t)$ is the scale factor. $K$ is a free parameter which allows three different spatial curvatures in the model. These are:

*i.* $K = 0$. This describes Euclidean 'flat' space.

*ii.* $K > 0$. Here the space is curved, and is described by the surface of a 3-sphere (a higher-dimensional equivalent of (say) the surface of an orange, which is a 2-sphere). The angles of a triangle in this space add up to more than 180°.

*iii.* $K < 0$. This space is hyperbolic, and is more akin to our notion of a saddle-like surface. Angles of a triangle in this world would sum to less than 180°.

With equation 1.4 as the metric, the Einstein equations are given by the Friedmann cosmological equations:

$$\dot{a}^2 = \frac{8\pi G}{3}\rho a^2 - Kc^2 + \left[\frac{\Lambda c^2 a^2}{3}\right] \tag{1.5}$$

$$\ddot{a} = -\frac{4}{3}\pi G\left(\rho + \frac{3p}{c^2}\right)a + \left[\frac{\Lambda c^2 a}{3}\right]. \tag{1.6}$$

Equation 1.5 comes from the spatial part of the metric, and equation 1.6 from the time component. These two equations are not independent, and equation 1.6 can be derived from equation 1.5 if one can relate the evolution of density to the pressure, which we shall now do.

If the Universe can be treated as an ideal fluid, then the first law of thermodynamics can be expected to apply:

$$\mathrm{d}U = -p\mathrm{d}V + \mathrm{d}Q, \tag{1.7}$$

where $U$ represents the fluid's internal energy; $Q$ heat energy; $p$ pressure; and $V$ volume. If the Universe is homogeneous, then the net transfer of energy from any one region to another will be expected to be zero, and so statistically there is no heat transfer. The expansion can therefore be treated as adiabatic, with $\mathrm{d}Q = 0$. This gives:

$$\mathrm{d}\left(\rho a^3 c^2\right) = -p\,\mathrm{d}a^3, \tag{1.8}$$

where the left hand side is the internal 'rest mass' energy of the fluid, and the right hand side signifies the work done as a result of the expansion. Given an equation of state, we

can now predict how the density will vary with scale factor, and thus use the Friedmann equations to determine the dynamics of the Universe.

We consider two scenarios:

*i.* **Dust models.** Here the Universe is dominated by non-relativistic matter, and the pressure contribution is much smaller than the inertial mass energy density, so $p \simeq 0$, giving $\mathrm{d}\left(\rho a^3 c^2\right) = 0$, and so:

$$\rho_g\left(a\right) \propto \rho_g\left(a_0\right) a^{-3}. \tag{1.9}$$

*ii.* **Radiation-dominated models.** In the early Universe the photon energy dominates over the matter energy, and in this case pressure cannot be neglected. The total energy density $\epsilon$ of radiation is given by:

$$\epsilon = \sum_{\nu} h\nu N\left(h\nu\right), \tag{1.10}$$

where

$$\epsilon = \rho_r c^2, \tag{1.11}$$

and $N\left(h\nu\right)$ is the number density of photons of frequency $\nu$. Since the number of photons is conserved, the number density goes as $N\left(h\nu\right) \propto N_0\left(h\nu\right)/a^3$ as the Universe expands. In addition each photon suffers a redshift, resulting in a frequency shift of $\nu = \nu_0/a$. So

$$\epsilon = \frac{\epsilon_0}{a^4}, \tag{1.12}$$

giving

$$\rho_r\left(a\right) \propto \rho_r\left(a_0\right) a^{-4}. \tag{1.13}$$

Substituting $\rho_r$ into equation 1.8 gives the equation of state for radiation: $p_r = \frac{1}{3}\rho_r c^2$.

### 1.1.2 Redshifts and the Hubble parameter

The redshift is defined as:

$$z \equiv \frac{\lambda_o - \lambda_e}{\lambda_e}, \tag{1.14}$$

where $\lambda_o$ is the observed wavelength of light from (say) a galaxy, and $\lambda_e$ is the wavelength at which the light was emitted. In practice it is determined by matching the galaxy

spectrum with atomic transitions for which the rest frame wavelength $\lambda_e$ is known. This effect was initially ascribed to the **Doppler shift.**

Consider a body moving with velocity $v_x$ relative to an observer. If it emits light with wave crests separated in time by $\Delta t$ (in its own rest frame) then the observer will measure the separation in time between wave crests as $\Delta t'$, where $\Delta t'$ is given by the usual Lorentz transformation:

$$\Delta t' = \frac{\Delta t - (-\mathbf{v}) \cdot \mathbf{\Delta x}/c^2}{\sqrt{1 - v^2/c^2}}. \tag{1.15}$$

So if $\Delta t' = \lambda_o/c$, and $\Delta t = \lambda_e/c$, then

$$\lambda_o = \lambda_e \frac{1 + (v/c)\cos\theta}{\sqrt{1 - v^2/c^2}}, \tag{1.16}$$

$$1 + z = \frac{1 + (v/c)\cos\theta}{\sqrt{1 - v^2/c^2}}. \tag{1.17}$$

The dominant contribution to $z$ comes from the radial part of the motion, $v_r = v\cos\theta$, and in the limit $v_{\rm transverse} \ll v_{\rm radial}$,

$$1 + z \simeq \left[\frac{1 + v_r/c}{1 - v_r/c}\right]^{\frac{1}{2}}, \tag{1.18}$$

where $v_r$ is the proper velocity of the object.

In 1929 Hubble discovered that the redshift of a galaxy was highly correlated with its distance. This has been formulated into 'Hubble's Law', which states that the recession velocity of an object is proportional to its proper distance, $d_{\rm pr}$:

$$v_r = H d_{\rm pr}\,, \tag{1.19}$$

where $H$ is the **Hubble constant.** Present estimates for its value place it between:

$$40 \text{ km s}^{-1} \text{ Mpc}^{-1} \leq H_0 \leq 90 \text{ km s}^{-1} \text{ Mpc}^{-1} \tag{1.20}$$

(see *e.g.* Freedman *et al.* 1998, Rowan-Robinson 1988 for a review). This discovery initiated the idea of an expanding Universe, with galaxy separations increasing with time. If we consider a light ray emitted at time $t_e$ with a subsequent wave crest emitted at $t_e + \delta t_e$, and observed at $t_o$ and $t_o + \delta t_o$, then we can relate the redshift to the expansion

of the scale factor. Integrating up the Robertson-Walker metric (see equation 1.4) for a null geodesic ($ds^2 = 0$) we have:

$$\int_{t_1}^{t_2} \frac{c}{a(t)} dt = \int_0^r \frac{dr}{\sqrt{1 - Kr^2}} \equiv f(r). \tag{1.21}$$

So for light pulses sent between two places separated by constant comoving distance,

$$\int_{t_e}^{t_o} \frac{c}{a(t)} dt = \int_{t_e+\delta t_e}^{t_o+\delta t_o} \frac{c}{a(t)} dt \tag{1.22}$$

which on rearrangement yields:

$$\frac{\delta t_e}{a(t_e)} \simeq \frac{\delta t_o}{a(t_o)}, \tag{1.23}$$

and since we can set $\delta t_o / \delta t_e = \lambda_o / \lambda_e = 1 + z$ then the redshift can be given as

$$1 + z = \frac{a(t_o)}{a(t_e)}. \tag{1.24}$$

This is thought to be the main contribution to cosmological redshifts.

We can derive the Hubble parameter in terms of the scale factor, $a$ by considering how the proper distance, $d_{\rm pr}$ is expected to change with time. Integrating up the spatial part of the Robertson-Walker metric, we have:

$$d_{\rm pr} = \int_0^r \frac{a(t)\, dr'}{\sqrt{1 - Kr'^2}} \equiv a(t) f(r). \tag{1.25}$$

Now if the object we are looking at has a recessional velocity, $v_r$, then $v_r = \dot{d}_{\rm pr} = \dot{a}(t) f(r)$, and so

$$H(t) = \frac{\dot{a}(t)}{a(t)}. \tag{1.26}$$

In the absence of knowledge of $H_0$, distances are generally quoted as a function of $h \equiv H_0/(100\,{\rm km\,s^{-1}Mpc^{-1}})$. Typical cosmological units of scale are then $h^{-1}\,{\rm Mpc}$.

Another contribution to the redshift which becomes increasingly important at very large distances is the **gravitational redshift**. Light undergoes a change in wavelength if it arrives at a place of differing gravitational potential from its origin. This gives a contribution to the redshift of:

$$z = \frac{\Delta\phi}{c^2}. \tag{1.27}$$

This is simply an extension of conservation of energy to photons in gravitational fields. While for small distances, the gravitational contribution to the redshift is small, for

a homogeneous universe, the contribution grows as the square of the distance. The potential between two points can be thought of as the potential arising from collapsing all the matter in a sphere of radius the point-separation down to a point. $\Delta\phi$ is then:

$$\Delta\phi = \frac{4\pi G\rho r^3}{3r}, \tag{1.28}$$

(*e.g.* Bondi 1947). If $r \simeq c/H$, then $\Delta\phi/c^2 \sim 4\pi G\rho/3H^2 \sim \Omega/2$. So on scales of order the horizon (see section 1.1.6), the gravitational contribution to the redshift is of order $0.1 - 1$, which is still a relatively small contribution.

### 1.1.3 The density parameter, $\Omega$, and the deceleration parameter, $q$.

Until now we have left spatial curvature as a free parameter in the Robertson-Walker metric. It is time now to consider what governs this parameter. From equation 1.5 in the absence of a cosmological constant, we have

$$\dot{a}^2 = \frac{8\pi G\rho_0}{3a^{n-2}} - Kc^2, \tag{1.29}$$

where $n = 3$ for matter dominated models, and $n = 4$ for radiation dominated models. As $a$ increases, the rate of expansion decreases, and for $K > 0$ (closed models) the expansion eventually stops, and eventually the Universe starts to contract. For $K < 0$ the expansion rate remains finite, slowly tending to $|K|^{1/2}c$, and for $K = 0$ the rate of expansion tends asymptotically to zero. In this case, the Universe is said to have critical density, $\rho_c$, where

$$\rho_c = \left(\frac{\dot{a}}{a}\right)^2 \frac{3}{8\pi G} = \frac{3H^2}{8\pi G}. \tag{1.30}$$

The dynamics therefore depend on the value of density relative to $\rho_c$, and this leads to the definition of the density parameter, $\Omega$:

$$\Omega \equiv \frac{\rho}{\rho_c}. \tag{1.31}$$

Spatially closed models require $\Omega > 1$, and open models $\Omega < 1$. Current estimates of the density parameter lie in the range (see *e.g.* Trimble 1987, Carr 1994)

$$0.2 < \Omega_0 < 1\ , \tag{1.32}$$

although its value is in some dispute, as we shall see later. We can also define a deceleration parameter, $q$, which describes the rate of deceleration in the Universe. It is defined to be:

$$q(t) = -\frac{\ddot{a}(t)\, a(t)}{\dot{a}^2}. \tag{1.33}$$

In general, using equation 1.6

$$q_0 = \frac{\Omega_0}{2} - \frac{1}{3}\frac{\Lambda c^2}{H_0^2} = \frac{\Omega_0}{2} - \Omega_\Lambda \tag{1.34}$$

(where $\Omega_\Lambda \equiv \Lambda c^2/[3H_0^2]$). Attempts to measure $q_0$ have mainly come from the use of supernovae as standard candles (*e.g.* Kim *et al.* 1997, Riess *et al.* 1998, Perlmutter *et al.* 1998). The latest estimates are (Riess *et al.* 1998):

$$-1.75 \lesssim q_0 \lesssim 0 \tag{1.35}$$

at the 99.5% to 99.9% confidence level, suggesting that the Universe is undergoing accelerated expansion. This limit also favours the existence of a cosmological constant, whose value is $\Omega_\Lambda > 0.1$ if we use the current lower limit for $\Omega_0$ in equation 1.32.

### 1.1.4 The cosmological constant, $\Lambda$

This constant was originally added into Einstein's equations to create a static universe. It is now treated as a vacuum energy which provides a source of negative pressure. While somewhat counterintuitive, the negative pressure can be derived by considering a syringe of the vacuum, and remembering that the vacuum has constant energy density, $\epsilon_v$. If we move the plunger out by an amount $\mathrm{d}V$, then the energy change $\mathrm{d}U = \epsilon_v \mathrm{d}V = -p\mathrm{d}V$, thus giving $p = -\epsilon_v$. In the absence of any matter, *i.e.* $\rho = 0, p = 0, K = 0$, and non zero cosmological constant, the scale factor goes as:

$$a(t) \propto \exp\left[\left(\frac{\Lambda}{3}\right)^{1/2} ct\right], \tag{1.36}$$

so the vacuum energy drives an exponential expansion. This is known as the de Sitter model (1917), and it has proved of interest to inflationary models (see section 1.3.3). Another model worthy of note is the Einstein-de Sitter model, in which $p = 0, \Lambda = 0$ and $\Omega = 1$. Here the scale factor follows a power law expansion:

$$\begin{aligned} a(t) &\propto t^{2/3}, \text{ and} \\ H(t) &= \frac{2}{3t}, \text{ with } q_0 = \frac{1}{2}. \end{aligned} \tag{1.37}$$

### 1.1.5 Evolution of the density parameter

The density at any epoch can be broken up into its component contributions:

$$\rho_{\rm tot} = \rho_r a^{-4} + \rho_m a^{-3} + \rho_v, \tag{1.38}$$

where subscripts $r$, $m$, and $v$ stand for radiation, matter, and vacuum respectively. We can determine how the density evolves by substituting equation 1.38 into equation 1.5, and noting that $Kc^2 = a^2H^2(\Omega - 1) =$ constant. With a little rearrangement, and remembering $\rho_c = 3H^2/8\pi G$ we get:

$$\Omega(a) - 1 = \frac{\Omega_0 - 1}{[\Omega_{r0}\, a^{-2} + \Omega_{m0}\, a^{-1} + \Omega_{v0}\, a^2 - \Omega_0 + 1]}. \tag{1.39}$$

Clearly as $a \to 0$, the right hand side of this equation $\to 0$, implying that the density parameter tends towards 1 at early epochs. In the presence of a non-zero cosmological constant, as $a \to \infty$, the left hand side also tends to zero, implying that universes with non-zero $\Lambda$ also tend towards $\Omega = 1$ at late times.

### 1.1.6 The particle horizon

If the age of the Universe is finite, as the Friedmann models (with no $\Lambda$) coupled with the observed expansion of the Universe suggest, then light can only have travelled a finite distance within the Universe. Particles separated by less than this distance are said to be causally connected, and information (for example gravitational waves) has had time to propagate between the two particles. The limiting distance for which this is true is called the particle horizon. At separations greater than this horizon, no information transfer can have occurred. The particle horizon, $R_H$ is given by:

$$R_H(t) = a(t) \int_0^t \frac{c\mathrm{d}t'}{a(t')} \tag{1.40}$$

(which comes from integrating up $\mathrm{d}l = c\,\mathrm{d}t/a$, and converting to a proper distance). If $a(t)$ is a power law, $a \propto t^x$, then the integral diverges for $x \geq 1$. In this case $R_H \to \infty$, and one can expect all particles in the Universe to have been in causal contact.

## 1.2 Standard model physics of the early Universe

The dust and radiation models of the Universe suggest that the energy density increased inversely with scale factor, and so at early times the energy density was much greater than it is now. The standard model hypothesises that the physics of today also applied in the early Universe (at corresponding energy scales), and this allows us to use our experience of stellar processes, and high energy physics experiments to make inferences about equivalent energy scales of the early Universe. Of course, progressing even further back in time, one soon reaches energy scales far greater than those of which we have experience, and on these scales we can only speculate about what might have occurred.

Outlined below is a brief account of the important eras in the early Universe.

1. **The Planck Era** $T_{\rm P} \simeq 10^{19}$ GeV

This represents the time interval during which the cosmological horizon is of order the de Broglie wavelength of one particle. Quantum gravitational effects on this timescale are expected to be important, and in the absence of a working theory of quantum gravity we can say little about this era.

2. **Grand Unified Era** (GUT) $T_{\rm P} > T > T_{\rm GUT} \simeq 10^{15}$ GeV

In this temperature range it is speculated that interactions are described by a grand unified theory, in which electroweak, strong and presumably gravitational interactions are unified. In particular, quarks and leptons would have been governed by the same unified field, possibly allowing changes in the baryon number. This would be of great importance in explaining the observed baryon – anti-baryon asymmetry.

3. **Phase Transitions** $T < T_{\rm GUT}$

As the Universe expanded and cooled, its thermal energy dropped below the energy scales of a number of different physical processes, so changing the physics that occurred in the fluid.

The first of these changes was a series of phase transitions occurring from spontaneous symmetry breaking processes in the GUT field. These are thought to have given rise

to the fields we now observe. This era has also been suggested to give rise both to topological defects, and an inflationary era. These are described in section 1.3 below.

*i.* $T = T_{\rm EW} \simeq 300$ GeV. The first symmetry to go (after gravitation) was between that unifying the strong and electroweak fields. This is possibly when the baryon – anti-baryon asymmetry was initiated.

*ii.* $T > T_{\rm QH} \simeq 200 - 300$ MeV. In this phase transition leptons acquired masses and the intermediate vector bosons gave rise to the massive bosons: $W^+, W^-$ and $Z_0$ as well as photons. When the temperature reached $T_{\rm QH}$, strong interactions between the quarks led to their confinement within hadrons.

4. **Particle Annihilation**

Next came the annihilation of particle – anti-particle pairs, which occurred when the thermal energy of the Universe dropped to below the mass energy of the particle pairs. The heavier particles were therefore the first to go:

*i.* At a temperature of $T_{\rm H} \simeq 130$ MeV $\simeq 10^{12}$ K the hadron era ended, and saw the annihilation of charged mesons (*e.g.* pions: $\pi^+, \pi^-$). Neutral mesons (*e.g.* $\pi^0$) decayed into photons.

*ii.* At lower temperatures ($T_e \simeq 0.5$ MeV $\simeq 10^9$ K) the $\tau$, and $\mu$ type lepton pairs annihilated, followed by the electron pairs ($e^+, e^-$). They too left a background of photons. The $e^+, e^-$ annihilation marked the end of the lepton era.

5. **Decoupling**

At around $T \simeq 10^{10}$ K, the characteristic time scale for neutrino collisions with the other particles became much larger than the time scale for expansion, and so the neutrinos lost thermal equilibrium with the rest of matter. Once the neutrinos had decoupled they evolved independently of the rest of the fluid. The photons were the next species to decouple, but this happened somewhat later on (see below).

6. **Nucleosynthesis** $t \simeq 300$ seconds.

When the fluid reached $T \simeq 10^9$ K, it was composed mostly of protons, neutrons,

positrons, electrons and photons. At these temperatures the protons and neutrons fused to form the first of the light elements. This is described briefly in section 1.2.1

7. **Matter-radiation Equality** $z = 23,500\Omega h^2$

Since the contributions to the energy density from radiation and matter have different scale factor dependencies ($\epsilon_r \propto a^{-4}$, and $\epsilon_m \propto a^{-3}$), as the scale factor increased, there was a shift in the ratio of contributions from radiation and matter. Matter-radiation equality marked the cross over between radiation and matter dominated eras. The equation of state moved to a matter dominated variety, and the expansion of the Universe slowed. This was the first time when fluctuations in the matter field survived photon interactions without being erased, and so in the case of cold dark matter, they would have begun to grow.

8. **Recombination** $z \simeq 1500$

Until this stage the thermal energy was much greater than Coulomb interactions, and the fluid behaved like a plasma. Thermal equilibrium was maintained by photons Thomson scattering off free electrons, but finally the thermal energy dropped below the ionisation potential of the positively charged ions, and the electrons combined to form neutral atoms. In the absence of free electrons, photons were no longer scattered, and the optical depth increased enormously. They could now travel unperturbed across vast stretches of the Universe, and these are the photons we believe are now being detected as the microwave background. A few properties of the microwave background are explored in section 1.2.2.

### 1.2.1 Nucleosynthesis

While the stellar models for nucleosynthesis accurately predict the abundance of the heavier elements (from helium up), stars do not possess high enough temperatures in which to make deuterium and the observed abundance of helium (Reeves *et al.* 1973), and so it is to the increasing temperatures of the early Universe that we turn to for their origin. The primordial origin of the light elements was first proposed by Gamow (1948), and Alpher & Herman (1949), and the beauty of this model is that it predicts the ratio

of light element abundances ($^7$Li, $^4$He, $^3$He, D, and H), and these are found to agree with observations. Primordial light element production is thought to have started with the following equilibrium nuclear reactions:

$$p + e^- \rightleftharpoons n + \nu_e \tag{1.41}$$

$$n + e^+ \rightleftharpoons p + \overline{\nu}_e \tag{1.42}$$

$$n \rightleftharpoons p + e^- + \overline{\nu}_e. \tag{1.43}$$

As the temperature dropped, the thermal equilibrium of these weak interactions was lost, and the proportion of protons to neutrons became fixed. At still lower temperatures the photon energy became low enough for deuterium to be formed in significant quantities without being destroyed by photo-dissociation processes:

$$p + n \rightarrow d + \gamma. \tag{1.44}$$

The subsequent nuclear reactions required two body deuterium interactions which resulted in a delay, or 'bottleneck' while the deuterium density became large enough to allow the next stages of the process which ultimately gave rise to helium. Tritium was formed first:

$$\begin{aligned} d + d &\rightarrow {}^3\mathrm{He} + n \rightarrow {}^3\mathrm{H} + p \\ d + d &\rightarrow {}^3\mathrm{H} + p. \end{aligned} \tag{1.45}$$

The tritium and deuterium are then thought to have reacted to form $^4$He:

$${}^3\mathrm{H} + d \rightarrow {}^4\mathrm{He} + n. \tag{1.46}$$

The initial density of nucleons determines the amount of deuterium produced, and the higher the density of deuterium, the greater the production of helium. The rate of this reaction increases with $\Omega h^2$ and since the temperature at which helium ceases to be produced is only weakly dependent on density, the remaining abundance of deuterium after it freezes out (when $t_{\mathrm{reaction}} > H^{-1}$) remains roughly constant. This results in highly baryonic universes tending to have low relative deuterium abundances (D/H). In the lifetime of a galaxy deuterium tends to get destroyed, mostly being converted into $^3$He. A measure of the present abundance of deuterium therefore provides a lower limit to the amount that could have emerged from the big bang. An upper limit can also be

estimated by measuring the observed abundance of $d + {}^3\mathrm{He}$, and assuming that all (or a model dependent fraction) of the ${}^3\mathrm{He}$ was formed from deuterium. From the deuterium abundance and models of the rate of formation of deuterium one can estimate the baryon density of the Universe. This is currently calculated to lie in the range (Walker *et al.* 1991):

$$0.010 \lesssim \Omega_B h^2 \lesssim 0.015\,. \tag{1.47}$$

This estimate for the baryon content is significantly lower than estimates of the total mass density from cluster and galactic dynamics, which place $\Omega_{\mathrm{Total}}$ somewhere in the range $0.2 \lesssim \Omega_{\mathrm{Total}} \lesssim 1$ (see equation 1.32). If both these estimates are to be believed, then a large fraction of the mass contribution must come from non-baryonic matter. This is not the only discrepancy to be found in the field of estimating the matter content of the Universe, as we shall see in section 1.4.

### 1.2.2 The microwave background

The discovery of the microwave background in 1965 by Penzias and Wilson has proved of tremendous importance to cosmology. Not only did it provide extremely convincing evidence in support of the hot big bang model, but it gave new scope for the determination of cosmological parameters, and the testing of cosmological theories. The photon background is measured to have a present temperature of

$$T_{\mathrm{CMB}} = 2.726 \pm 0.010\,\mathrm{K}, \tag{1.48}$$

(Mather *et al.* 1994), and this is found to be uniform to one part in $10^5$ on scales of 10 degrees across all regions of the sky (Banday *et al.* 1997). It is also measured to have a black-body spectrum to an accuracy of one part in $10^4$ (Mather *et al.* 1994), *i.e.* it has the form:

$$I_\nu = \frac{2h\nu^3}{c^2\left(e^{h\nu/kT} - 1\right)}, \tag{1.49}$$

where $I_\nu$ is the intensity of radiation at a frequency $\nu$. There are several points worthy of note about this. The first is that its black body nature suggests that the photons have come from a region where matter and radiation were in strict thermodynamic

equilibrium. The lack of distortion of the spectrum also suggests that it has passed through 'empty' space since it left the thermodynamic equilibrium[1].

The preservation of a black body form also requires that the photon temperature decreases at the same rate as the frequency during the Universe's expansion. We know from the definition of redshift that the frequency of light decreases as $(1+z)^{-1}$ with redshift. From Stephan's law for a black-body, the energy density is related to the temperature by:

$$\epsilon = \sigma_r T^4. \tag{1.50}$$

As we saw from equation 1.13, the radiation energy density decreases as the fourth power of $(1+z)$, and so $T \propto (1+z)^{-1}$. The fact that the temperature to frequency ratio does indeed remain constant as predicted, and that the temperature today is measured to be so small provides strong support for an expanding model in which proper volumes in the Universe change as the third power of the scale factor.

There are two redshifts associated with the cosmic microwave background (CMB). The first, recombination, is calculated from requiring that the thermal energy at the time of recombination was of order the ionisation potential of a hydrogen atom (13.6eV) – in fact at this energy, photons released when the electrons combine with the protons would have sufficient energy to ionise surrounding atoms, so recombination actually occurs at a lower temperature in a two stage process (so that the individual energy of each photon is less than the ionisation potential). The 'epoch' of recombination is then defined to occur when the fractional ionisation of the protons was $\simeq 0.5$, this is thought to be around $z_{\rm rec} \simeq 1500$ (*e.g.* Coles & Lucchin 1995). The second redshift is that marking the surface of last scattering (from which time the observed microwave photons originated). This is taken to be when the optical depth decreased to about 1, and occurred at a redshift of $z_{\rm ls} \simeq 1080$ (*e.g.* Silk 1986) with little dependence on parameters $\Omega, \Omega_b, h$ & $\Lambda$.

We shall now calculate the angular size of the particle horizon at the epoch of last scattering, as it tells us something interesting. We have from equation 1.40 that the

[1] Clearly there are exceptions to this – for example where the photons have passed through protoclusters, and have been reheated as seen with the Sunyaev Zel'dovich effect.

proper length of the particle horizon at a time $t_{\rm ls}$ is given by:

$$\begin{aligned} R_H(t_{\rm ls}) &= a(t_{\rm ls}) \int_0^{t_{\rm ls}} \frac{c\mathrm{d}t'}{a(t')} \\ &= b\,c\,a(t_{\rm ls}) \int_0^{t_{\rm ls}} t'^{-1/2}\mathrm{d}t' \\ &= 2\,b\,c\,a(t_{\rm ls})\,t_{\rm ls}^{1/2}, \end{aligned} \tag{1.51}$$

where we have made the simplifying assumption that the Universe is radiation dominated from $t = 0$ until recombination (so $a = b\,t^{1/2}$), where $b$ is just a constant of proportionality. The angle an object of comoving size $r_1$ subtends at a comoving distance $r_2$ is:

$$\theta = \frac{r_1}{f(r_2)} = \frac{r_1}{r_2}, \tag{1.52}$$

where $f(r_2)$ depends on the spatial curvature ($= \sin(kr)$ for $k = +1, \sinh(kr)$ for $k = -1$, and $r$ for $k = 0$), and we have assumed that we are in a Euclidean universe. The comoving distance to the surface of last scattering is given simply by:

$$r_{\rm com} = \int_{t_{\rm ls}}^{t_{\rm now}} \frac{c\mathrm{d}t'}{a(t')}. \tag{1.53}$$

This can be solved using $a \propto t^{2/3}$ (for an Einstein-de Sitter universe), since we are now matter dominated. So bearing in mind that the comoving horizon is given by $R_H/a\,(t_{\rm ls})$, that $t_{\rm now} \gg t_{\rm ls}$, and that $a \propto (1+z)^{-1}$ irrespective of the equation of state, we get:

$$\theta = \frac{2}{3}\,(1+z_{\rm ls})^{-1/2}\,. \tag{1.54}$$

So for $z_{\rm ls} = 1000$, the horizon subtends an angle of about 1°. The existence, therefore of fluctuations on a scale of 10° might well seem surprising.

## 1.3 Fluctuations and their initiation

In fact the existence of fluctuations on any scale is not predicted by the standard model, which describes a completely homogeneous universe. Clearly, given the wealth of structure observed today, we can reasonably conclude that there must have been matter fluctuations early on, and that these may either have been present as an initial condition in the early Universe, or another physical mechanism might have caused their initiation. This section describes the possible types of fluctuations and addresses two theories which are not part of the standard model, but which predict the existence of matter fluctuations in the early Universe.

### 1.3.1 Types of fluctuation

Fluctuations can occur in either the matter distribution only, or both the matter and the radiation distribution. The precise nature of the fluctuations is still a matter of debate, and there are three main models.

**Adiabatic perturbations.** Here the fluctuations in the radiation density are 4/3 times those in the matter distribution at all times. This close relationship between the photon and baryon fluctuations is as a result of the tight coupling approximation, in which Thomson scattering keeps the photons following the baryon perturbations closely even on small scales. The perturbations are adiabatic because the entropy per baryon remains constant (owing to the entropy contribution coming from the photons, whose number density tracks the baryons).

**Isothermal perturbations.** In this scenario there are no fluctuations in the radiation distribution, and so the photon temperature is constant.

**Isocurvature perturbations.** As the name suggests these perturbations initially have zero curvature because overdensities in the matter distribution are exactly cancelled by underdensities in the photon fluctuations, resulting in a homogeneous energy density. At early times on large scales, isocurvature perturbations resemble isothermal perturbations, since the isocurvature radiation fluctuations tend to zero as $t \to 0$. As time progresses, and the Universe moves towards matter domination, the fluctuations in the radiation (on scales greater than the Jeans' length) grow to compensate for the decrease in energy density of the radiation part of the fluid. Conversely the matter fluctuations get smaller, and at late times tend to zero.

On scales smaller than the Jeans' length, the radiation pressure acts to homogenise the radiation field, and in doing so, the photons also drag matter with them from the high photon density regions to the low photon density regions. Since the low photon density regions correspond to high baryon density regions, this acts to increase the amplitude of matter fluctuations.

### 1.3.2 Topological Defects

Phase transitions have been proposed as a possible physical process that would give rise to matter fluctuations in the early Universe. As we have seen earlier, these arise naturally from the standard model, for example when free quarks become confined to hadrons. In general phase transitions occur when the minimum free energy, $F$ $(= E - TS)$ of a system changes, and the system assumes the new minimum energy configuration. This change in minimum free energy generally results in a change in the level of order of the system, for example the phase change that occurs when water freezes results in the water molecules moving from random locations to a crystalline structure.

In the case of the early Universe, it is speculated that there could have been phase changes in unknown scalar fields, which resulted in the fields adopting new energy configurations. Topological defects are thought to arise when the system has more than one minimum energy configuration – while some parts of the Universe will move to one minimum energy configuration, other causally unconnected regions may assume a different configuration, and at the boundaries of these regions, (since the field has to remain continuous), there has to be a region of space that is trapped in a non-minimum energy configuration. These interfaces are known as topological defects, and have the property that space is warped around them. This spatial 'twisting' is equivalent to having a gravitational field around the defect, and so they act as seeds for matter fluctuations.

There are a number of possible defects, each arising from a different dimensionality of the scalar field. These include magnetic monopoles, cosmic strings, domain walls, and textures. The existence of domain walls and magnetic monopoles can be ruled out as a source for matter fluctuations, since their energy density is far too high to be compatible (to within several orders of magnitude) with our estimates of $\Omega$. Textures and strings, however remain potentially feasible. These are predicted to give scale invariant potential fluctuations [*i.e.* $\Delta^2_\phi \propto k^0$, and $\Delta^2(k) \propto k^4$, see equation 1.101 for a definition of $\Delta^2(k)$], and the resulting matter distribution would be expected to contain large scale correlations (owing to the defects' extensive influences on surrounding matter), and thus would give rise to an initially non-Gaussian matter distribution.

### 1.3.3 Inflation

Inflation has been motivated by a number of problems[2] with the standard model, only one of which is the problem of the existence of matter fluctuations. It was first proposed by Guth in 1981.

*i.* **The flatness problem.** As we noted earlier from equation 1.39, except in the case where $\Omega = 1$, the Universe evolves away from the spatially flat solution. The fact that we measure $\Omega$ to be of order 1 now implies that $\Omega$ was extremely close to 1 in the early Universe. The options available to explain this are either some fine tuning of initial conditions, or a physical mechanism that gives rise to this 'tuning' naturally.

*ii.* **The horizon problem.** In the discussion of the CMB (subsection 1.2.2), we calculated that the horizon size of the microwave background at the epoch of recombination is presently observed to be $\sim 1°$, but fluctuations are observed to exist on scales as large as 10°. The level of these fluctuations is also consistent over all directions of the sky, which could be deemed as odd given that regions separated by more than a couple of degrees are expected never to have been in causal contact. Again in the absence of new physics, the problem is only resolved by imposing a further set of initial conditions in the early Universe.

*iii.* **The magnetic monopole problem.** If strong and electroweak forces were unified at one stage, then the symmetry breaking process surrounding their subsequent 'disunification' is expected to generate magnetic monopoles as a result of the phase transition. In this case an explanation as to why the density of magnetic monopoles is so low that we don't detect them is required (for example in our measurement of $\Omega$) .

*iv.* **The cosmological constant problem.** This is another fine tuning argument based on the present upper limit for the cosmological constant. If we use the relation $q_0 = \Omega_0/2 - \Omega_\Lambda$, and the current constraints for $q_0$, and $\Omega_0$, the contribution to the vacuum energy is limited by: $\Omega_\Lambda \lesssim 2$. This yields a limit for the cosmological constant

[2](unfortunately for defect advocates, it is also motivated by problems with the topological defect predictions)

of

$$|\Lambda| \lesssim 10^{-52} m^{-2} \; ; \; i.e. \tag{1.55}$$

$$\frac{\rho_\Lambda}{\rho_{\text{Planck}}} \lesssim 10^{-123} \tag{1.56}$$

which is extremely small, and hard to justify from 'natural' constants.

The general idea behind inflation is that the Universe underwent a period of exponential growth early on. This expansion led to an increase in the scale factor by about fifty orders of magnitude. The rapid expansion forced regions that were once in causal contact outside the standard model prediction for their particle horizon, and so explains the uniformity, and fluctuations observed on so called super-horizon scales in the microwave background. Another consequence of such an expansion is the prediction that $\Omega$ must be equal to 1 now – unlike the standard model, inflation predicts that universes of any initial density get driven towards unity through the massive expansion of the scale factor. Matter fluctuations also arise naturally from the amplification in scale of local quantum fluctuations in the gravitational potential. In the simplest inflation models, because the fluctuations come from quantum uncertainties, they have a random phase, and so would be expected to be Gaussian distributed. The problem of the absence of a large population of monopoles is also neatly sidestepped – as their density is diluted to less than one per horizon volume. The major predictions from inflation are:

*i.* $K = 0 \Rightarrow \Omega = 1$, (for $\Lambda = 0$)

*ii.* Gaussian matter fluctuations arising from random quantum fluctuations in the matter potential (some inflationary models predict non-Gaussian fluctuations, see below).

*iii.* Scale invariant (Harrison-Zel'dovich) fluctuations (Harrison, 1970; Zel'dovich, 1970). The mean square amplitude of potential fluctuations on different scales is predicted to be constant. In Fourier space, this gives $|\phi_k|^2 k^3 = \text{const.}$, and from the comoving Poisson equation: $\nabla^2 \phi = 4\pi G \overline{\rho} \delta$ (see section 1.6), we get $k^2 \phi_k \propto \delta_k$. The power spectrum for matter fluctuations, $P(k) \sim |\delta_k|^2$ is therefore $\propto k$.

There are however problems with the most basic model, for instance getting the Universe to stop inflating before the energy density in each 'horizon' volume becomes too small, and that our current estimates of $\Omega$ do not favour a flat universe. The first two predictions

can be side stepped with more elaborate models of inflation, generally requiring two epochs of exponential expansion, leading both to possible low density universes and non-Gaussian fluctuations (*e.g.* Yi & Vishniac, 1993) (see below). These 'refined' models appear somewhat contrived, and the predictive power of inflation is lost by these tunable models (*e.g.* Barrow & Liddle, 1997).

## 1.4 Dark Matter

### 1.4.1 Evidence for Dark Matter

In 1933 Zwicky found that the mass of the Coma cluster inferred from motions of galaxies in the cluster did not agree with the mass that would be inferred from simply measuring the total luminosity of the galaxies and multiplying by the mass-to-light ratio for galaxies. The same discrepancy between the dynamical mass and the luminous mass has been found for spiral galaxy rotation curves which indicate the existence of matter way past the visible extent of the galaxy. These measurements are generally expressed as a mass to light ratio in solar units – for example galaxy mass to light ratios are found to be of order $10 M_\odot/L_\odot$, whereas rich cluster mass to light ratios lie in the range $100 - 300 M_\odot/L_\odot$ (Trimble 1987, Carr 1994). Some of the discrepancy between cluster and galaxy mass to light ratios can be accounted for by the existence of hot X-ray emitting intracluster gas which lies between the galaxies, and this can account for as much as 30% of the cluster mass. There is still, however potentially a discrepancy between the galaxy $M/L$ ratios and those found for clusters, suggesting that perhaps there is more matter present than is observed at the measured wavelengths. From cluster dynamical arguments, the density of the Universe is found to be $\Omega \simeq 0.2$. However, if the nucleosynthesis constraints on the baryon content are to be believed, $\Omega_B \simeq 0.02$, further suggesting that 90% of matter must be non-baryonic. There are two main proposals for the nature of this dark matter. These are:

**Hot Dark Matter.** (HDM) These particles are supposed to have an extremely high velocity dispersion, and candidates for the particles include massive neutrinos. Their effect is to wipe out fluctuations on small scales, so structures would be expected to be

far more extended than we actually observe. This has been ruled out as the dominant contribution to the matter content on account of observations of far more power on small scales than is predicted by HDM (White, Frenk & Davis 1983).

**Cold Dark Matter.** (CDM) These are non-relativistic particles such as axions which do not form part of the particle physics standard model. In the standard CDM scenario, $\Omega = 1$. This model has proved to be very successful, and it is commonly adopted as a standard cosmological model against which to test observations. In recent years, however, it has had trouble predicting enough power (structure) on large scales compared with observations (see subsection 1.8.2).

Alternative scenarios have been suggested in which the matter is either warm, or a mixture of hot and cold dark matter (*e.g.* Taylor & Rowan-Robinson 1992). A problem with the latter is the requirement of approximately equal contributions from both sources, which may require some fine tuning.

### 1.4.2 Biased galaxy formation

If the Universe has a high percentage of dark matter, then using luminous galaxies to trace the matter content is not necessarily reliable, especially given the existence of inter-galactic gas in clusters. This uncertainty between the positions of galaxies relative to the underlying matter distribution is termed as bias, and is generally defined as a parameter, $b$ relating the galaxy correlation function to the mass correlation function (see equation 1.90 for a definition of the correlation function),

$$b = \sqrt{\frac{\xi_{\rm galaxies}}{\xi_{\rm mass}}}. \tag{1.57}$$

If bias is a purely local function, $b$ can be shown to be a monotonic function of scale (Coles 1993). On large scales, then, we expect the discrepancy to tend towards a linear relationship between the underlying dark matter, and the galactic matter. In Fourier space the bias, $b'$, can be defined in terms of the power spectrum (see equation 1.95):

$$P^{\rm g}(k) = b'^2 P^{\rm tot}(k). \tag{1.58}$$

$b$ and $b'$ are only equivalent if $\delta_{\rm galaxies} = b\delta_{\rm mass}$ on all scales. The way in which galaxies are biased relative to the underlying matter, and the mechanisms giving rise to bias are

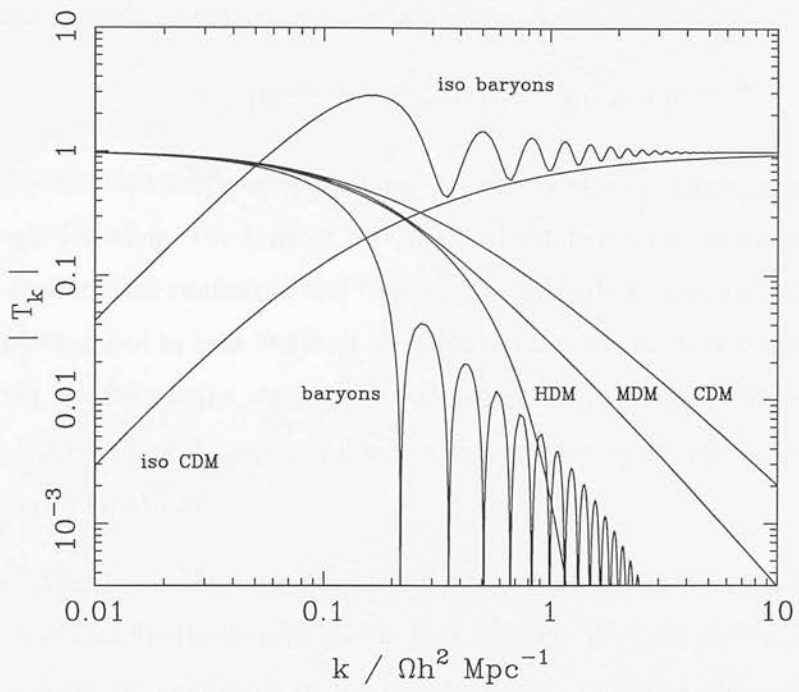


Figure 1.1: Transfer functions for a number of different types of primordial fluctuation – baryons, pure CDM, pure HDM, and MDM (30% HDM, 70% CDM). The baryonic transfer function does not scale exactly with $\Omega h^2$, and here $\Omega = 1$, $h = 0.5$. This plot is reproduced from Peacock (1998).

themselves unknown, although possible physical processes are discussed in Dekel & Rees (1987). It is common therefore to employ different functional forms for the bias, with characteristics that cover the feasible alternatives of bias. Some of these functional forms are discussed in Chapter 3.

## 1.5 Transfer functions

So far we have considered fluctuations in the early Universe without considering their present observable properties. A number of processes occur in the early Universe that act to distort the primordial spectrum of fluctuations, and these are considered here.

The transfer function, $T(k)$ itself relates the primordial power spectrum to the one after

matter radiation equality and recombination:

$$P(k)^{\text{after recomb}} = D(t)^2 T(k)^2 P(k)^{\text{primordial}}. \tag{1.59}$$

This is a convenient way of confining the effects of early Universe physical processes to a single function. The form of $T(k)$ generally depends on the nature and proportion of the dark matter content of the Universe, as this affects the level of photon coupling to the matter, and in turn the level of damping that occurs. It is calculated numerically by solving the Boltzmann equation for the particular cosmology. We can gain some insight about the form of the transfer function by considering the various processes that distort density fluctuations.

**The Mészáros effect.** In the radiation dominated era, the expansion of the Universe is so fast that fluctuations inside the horizon grow only very slowly. Fluctuations outside the horizon are unaffected by the expansion rate, and so continue to grow. This results in a tilt in the power spectrum – large scale fluctuations have a boosted amplitude relative to the small scale fluctuations. This effect ceases at the epoch of matter radiation equality, when the expansion slows down, and fluctuations inside and outside the horizon grow at the same rate. In the cold dark matter case, the Mészáros effect (1974) is dominant, yielding a break in the resulting power spectrum on the horizon scale at matter radiation equality. On scales larger than the break scale, the spectrum remains Harrison-Zel'dovich, whereas smaller scales have a shallower spectrum, tending to a spectral index of $n = -3$.

**Baryonic oscillations.** In purely baryonic universes the photons are more strongly coupled to the baryons, and so matter is supported by radiation pressure. As fluctuations grow, so too does the radiation pressure, and oscillations are established in the fluid. The photons only decouple from the fluid on recombination, and so the oscillatory nature of the baryon transfer function is due to the phase of the oscillation of each fluctuation mode at the epoch of recombination (see figure 1.1).

**Silk Damping.** Another effect that can be important is Silk damping (Silk 1967) – this is where photons diffuse from gravitational potential wells, dragging matter with them, and so damping the fluctuation amplitude.

**Free Streaming.** Damping also occurs if there are relativistic particles present in the fluid, and they erase structures on scales of their free streaming length. As the Universe expands, these particles slow down and cease to move relativistically. This causes their free streaming length to drop, giving rise to a feature in the power spectrum on a scale corresponding to the horizon size at the epoch at which the particles cease to move relativistically. On scales smaller than this, fluctuations are highly damped.

## 1.6 Growth of structure

This section probes the dynamics of fluctuations in the Universe, approximating matter to be an ideal fluid, and considering only the Newtonian limit. An ideal fluid is described by three principal equations:

**The continuity equation.** This is just mass conservation *i.e.* the rate of change in density in a given region is given by the net rate at which matter flows into the region,

$$\frac{\partial \rho}{\partial t} = -\nabla \cdot \rho \mathbf{v}. \tag{1.60}$$

**The Euler equation.** This is an expression for conservation of momentum in a fluid. The left hand side is the convective velocity derivative *i.e.* the rate of change of the fluid velocity as one moves with the bulk flow, and the right hand side is the force acting on the fluid ($\phi$ denotes gravitational potential):

$$\frac{\partial \mathbf{v}}{\partial t} + (\mathbf{v} \cdot \nabla)\,\mathbf{v} = -\frac{1}{\rho}\nabla p - \nabla \phi. \tag{1.61}$$

**The Poisson equation.** This is essentially conservation of energy – relating the gravitational potential to the mass density (in the Newtonian approximation),

$$\nabla^2 \phi = 4\pi G \rho. \tag{1.62}$$

From these relations we can derive how an overdensity is expected to evolve with time in the limit of small density perturbations. The velocities and spatial derivatives above are in proper coordinates, so the first step is to transform them into comoving coordinates, thus bringing the scale factor in explicitly whose dynamics we can deduce from the

Friedmann equations. Converting to comoving coordinates, we have $\mathbf{r} = a\mathbf{x}$, where $\mathbf{r}$ is the proper distance, and $\mathbf{x}$ is the comoving distance, and $\mathbf{v} = (\dot{a}/a)\,\mathbf{r} + \mathbf{u}$, where $\mathbf{v}$ is the proper velocity and $\mathbf{u}$ is the peculiar velocity (*i.e.* the velocity in excess of the expansion).

Changing variables from proper to comoving coordinates gives $\nabla_p \rightarrow \nabla_c/a$. Also, in proper coordinates, $\rho = \rho(\mathbf{r}, t)$, whereas in comoving coordinates $\rho = \rho(\mathbf{r}/a, t)$, so that

$$\left[\frac{\partial \rho\left(\mathbf{r}/a\left(t\right), t\right)}{\partial t}\right]_p = \left[\frac{\partial \rho\left(\mathbf{x}, t\right)}{\partial t}\right]_c - \frac{\dot{a}}{a}\mathbf{x} \cdot \nabla_c \rho\left(\mathbf{x}, t\right), \tag{1.63}$$

where $[\,]_c$ denotes a partial derivative where $\mathbf{x}$ is held constant, and $[\,]_p$ where $a\mathbf{x}$ is held constant. So the mass conservation equation (eqn 1.60) in comoving coordinates becomes:

$$\frac{\partial \rho}{\partial t} + \frac{3\dot{a}}{a}\rho + \frac{1}{a}\nabla_c \cdot (\rho \mathbf{u}) = 0. \tag{1.64}$$

Applying the same procedure to the Euler equation (eqn 1.61), gives

$$\ddot{a}\mathbf{x} + \frac{\partial \mathbf{u}}{\partial t} + \frac{1}{a}(\mathbf{u} \cdot \nabla_c)\,\mathbf{u} + \frac{\dot{a}}{a}\mathbf{u} = -\frac{1}{\rho a}\nabla_c p - \frac{1}{a}\nabla_c\left(\Phi - \frac{1}{2}a\ddot{a}x^2\right), \tag{1.65}$$

where we have made the substitution

$$\phi = \Phi - \frac{1}{2}a\ddot{a}x^2. \tag{1.66}$$

Cancelling terms in equation 1.65 and defining the density contrast, $\delta$ as

$$\delta = \frac{\rho\left(t\right)}{\overline{\rho}\left(t\right)} - 1, \tag{1.67}$$

and remembering that $\overline{\rho} \propto a\left(t\right)^{-3}$ in the matter-dominated era gives:

$$\frac{\partial \mathbf{u}}{\partial t} + \frac{1}{a}(\mathbf{u} \cdot \nabla)\,\mathbf{u} + \frac{\dot{a}}{a}\mathbf{u} = -\frac{1}{\rho a}\nabla p - \frac{1}{a}\nabla\Phi \tag{1.68}$$

and

$$\frac{\partial \delta}{\partial t} + \frac{1}{a}\nabla \cdot (1+\delta)\,\mathbf{u} = 0. \tag{1.69}$$

We can go two stages further, and combine the last two relations (equations 1.69 and 1.68) by multiplying equation 1.68 by $\rho$, and equation 1.69 by $\mathbf{u}$, adding the two together, and then taking the divergence of this equation to give our final relation:

$$\frac{\partial^2 \delta}{\partial t^2} + 2\frac{\dot{a}}{a}\frac{\partial \delta}{\partial t} = \frac{\nabla^2 p}{\overline{\rho} a^2} + \frac{1}{a^2}\nabla \cdot [(1+\delta)\,\nabla\Phi] + \frac{1}{a^2}\frac{\partial^2}{\partial x^\alpha \partial x^\beta}\left[(1+\delta)\,u^\alpha u^\beta\right]. \tag{1.70}$$

This describes the complete dynamics of fluctuations in the fluid. Owing to its non-linear nature, complete solutions are left to numerical modelling (see Chapter 2).

### The linear regime

It is, however possible to examine how the fluctuations grow in the linear regime, which we shall now do. In the linear regime we stipulate that $|\delta| \ll 1$, and that the amplitude of the velocities in the fluid, along with the rate of fluctuation evolution are all $\ll 1$. Given that the fluid velocities and evolution are dependent entirely on the amplitude of $\delta$, this seems a reasonable approximation to make, and it turns out to compare well with numerical solutions to the problem.

So in the linear regime for a matter dominated universe in which the pressure contribution is negligible compared with the energy density, equation 1.70 reduces to:

$$\frac{\partial^2 \delta}{\partial t^2} + 2\frac{\dot{a}}{a}\frac{\partial \delta}{\partial t} = \frac{1}{a^2}\nabla^2 \Phi. \tag{1.71}$$

Now

$$\nabla^2 \Phi = \nabla^2 \phi + a\ddot{a}\nabla^2 \mathbf{x} \cdot \mathbf{x}/2 = 4\pi G\rho a^2 + 3a\ddot{a}, \tag{1.72}$$

and from the second Friedmann equation (equation 1.6), $\ddot{a} = -4\pi G\overline{\rho}a/3$, so

$$\nabla^2 \Phi = 4\pi G a^2 \left(\rho - \overline{\rho}\right). \tag{1.73}$$

So we end up with

$$\frac{\partial^2 \delta}{\partial t^2} + 2\frac{\dot{a}}{a}\frac{\partial \delta}{\partial t} = 4\pi G\overline{\rho}\delta, \tag{1.74}$$

and from equation 1.69 the linearised version becomes:

$$\frac{\partial \delta}{\partial t} + \frac{1}{a}\nabla \cdot \mathbf{u} = 0. \tag{1.75}$$

These can be solved to give the time evolution for the overdensity. For instance in an Einstein de Sitter universe ($\Omega = 1, \Lambda = 0$) in the matter dominated era ($\overline{\rho} \propto a^{-3}$, and $a \propto t^{2/3}$), substituting the time dependencies into equation 1.74, and looking for a solution of the form $\delta(\mathbf{x}, t) = \sum_i D_i(t) A_i(\mathbf{x})$ yields two time dependent solutions: $\delta = A(\mathbf{x}) t^{2/3} + B(\mathbf{x}) t^{-1}$, where the first term is referred to (for obvious reasons) as the growing mode, and the second as the decaying mode. The important thing to note here is that the equation of state influences the rate at which a mode grows, which gives rise to the Mészáros effect as discussed in section 1.5.

One other useful bit of manipulation is to investigate the relationship between overdensities and the fluid velocities (equation 1.75). If we substitute the growing mode solution $\delta = A(\mathbf{x})\, D(t)$ into equation 1.75, and rearrange a little we get:

$$\frac{\dot{D}}{D}\frac{a}{\dot{a}}\frac{\dot{a}}{a}\delta = -\frac{1}{a}\boldsymbol{\nabla}\cdot\mathbf{u} = fH\delta, \tag{1.76}$$

where $f = (\dot{D}a)/(D\dot{a}) \equiv \mathrm{d}\ln D/\mathrm{d}\ln a$. We have substituted for $f$ because it turns out that while the general time dependence of $D$ is not straightforward to calculate, the combination $f$ can be calculated numerically, and is a function that is dependent only (or mostly) on the density parameter, $\Omega$. $f$ is generally approximated by (Peebles, 1980):

$$f(\Omega) = \Omega^{0.6}. \tag{1.77}$$

This is of great use in our quest to determine the density of the Universe, as it provides a simple relation between the dynamics of 'overdensities' and the fluctuation amplitude. This relation is used in Chapter 2 to generate initial velocity fields for a set of particles, and in Chapter 5 to try to measure $f(\Omega)$. Unfortunately this relation is complicated by the effects of biased galaxy formation, and for a linear bias parameter $b$ (see subsection 1.4.2), $f(\Omega) \rightarrow \Omega^{0.6}/b$. This is known as the redshift distortion parameter, and is usually denoted as $\beta$. It is discussed at length in Chapter 5.

It is also worth noting here that equations 1.74 and 1.75 are easily solved in Fourier space, since derivatives of a function are replaced by multiples of the wave-vector, $\mathbf{k}$:

$$\mathcal{F}.T.\{\boldsymbol{\nabla} f\} = -i\mathbf{k}\tilde{F}(k). \tag{1.78}$$

For example, the transform of equation 1.75 is:

$$f(\Omega)\, H\delta_{\mathbf{k}} - \frac{i}{a}\mathbf{k}\cdot\mathbf{u}_{\mathbf{k}} = 0. \tag{1.79}$$

In Fourier space, equations 1.74 and 1.75 therefore reduce to a set of uncoupled equations, each describing a single Fourier density mode – *i.e.* in linear theory, the Fourier modes evolve independently of one another, which is of great use in analysing matter evolution as we shall see subsequent chapters.

### 1.6.1 Probing the non-linear regime

#### Perturbation Theory

We have just seen how equation 1.70 can be simplified in the limit of very small amplitude fluctuations. This subsection shows how the linearisation method can be used for larger amplitude fluctuations (as $\delta$ approaches unity) using second (or higher) order perturbation theory. This method can give some insight into what is occurring at the 'onset' of the non-linear regime, (although the method can result in divergent integrals, which are generally side stepped by cutting off the power spectrum contribution below a certain scale). The basic idea is to expand the overdensity, $\delta$ about its mean value:

$$\delta = \delta_{(1)} + \delta_{(2)} + \delta_{(3)} + \ldots, \tag{1.80}$$

where $|\delta_{(1)}| \ll 1$, and $\delta_{(n)} \simeq O\left({\delta_{(1)}}^n\right)$. This is substituted into equation 1.70, and terms of order $n+1$ and higher are dropped. So for instance in second order perturbation theory, terms of order ${\delta_{(1)}}^3$ are deemed negligible. Terms to first order in $\delta_{(1)}$ drop out, since this is the first order solution to equation 1.70, and in the second order case one gets left with (for negligible pressure):

$$\frac{\partial^2 \delta_{(2)}}{\partial t^2} + 2\frac{\dot{a}}{a}\frac{\partial \delta_{(2)}}{\partial t} = 4\pi G\overline{\rho}\left[\delta_{(2)} + {\delta_{(1)}}^2\right] + \frac{1}{a^2}\nabla\delta_{(1)} \cdot \nabla\Phi + \frac{1}{a^2}\frac{\partial^2}{\partial x^\alpha \partial x^\beta} u^\alpha u^\beta. \tag{1.81}$$

This can then be solved by substituting in the solution for the potential $\phi = -G\overline{\rho}a^2 f(\mathbf{x})$, where $f(\mathbf{x}) = \int \mathrm{d}^3x' \delta(\mathbf{x}') / |\mathbf{x} - \mathbf{x}'|$, and using the linearised continuity equation 1.75 to get solve for $u^\alpha$. This is best solved in Fourier space, because one can get rid of the spatial derivatives (see equation 1.78).

#### The Zel'dovich Approximation

Another method for probing the onset of non-linear behaviour is to use a Lagrangian approach. In this approach we deal with particle displacements rather than density fluctuations, and the Zel'dovich approximation (Zel'dovich 1970) is simply a linearisation procedure on the particle displacements. In Lagrangian theory particles are specified by their displacements, $\boldsymbol{\xi}(\mathbf{q}, t)$ which relates to the particle's comoving Eulerian coordinate,

x, by:

$$\mathbf{x}(t, \mathbf{q}) = \mathbf{q} - \boldsymbol{\xi}(\mathbf{q}, t), \tag{1.82}$$

where $\mathbf{q}$ is the particle's initial position. In the Zel'dovich approximation, the displacement is given by:

$$\boldsymbol{\xi}(\mathbf{q}) = D(t)\, \boldsymbol{\xi}_L(\mathbf{q}). \tag{1.83}$$

Where $D(t)$ is the linear growth factor from the growing mode (derived above for the Einstein-de Sitter case), and $\boldsymbol{\xi}_L(\mathbf{q})$ is the linear displacement field. This approximates that particles maintain their initial trajectories with their displacements growing according to the linear theory time factor, $D(t)$. This turns out to be a better approximation than taking the densities to linear order, and can be understood in terms of the continuity equation 1.76 – in Fourier space the particle velocity on a given scale is a factor of $1/k$ times the particle overdensity. For power spectra with indices $n > -3$, the velocity 'power spectrum' $\Delta_u^2 \propto k^3 \langle |u_k|^2 \rangle$ is shallower than the matter power spectrum. It therefore reaches non-linear behaviour at later times than the matter power spectrum, and so there is a period of time during which the velocity field is still linear on a given scale, while the overdensities on this scale have begun to become non-linear (*i.e.* $\Delta^2(k) \simeq 1$).

The Zel'dovich approximation breaks down around the time when particle trajectories cross over. First caustics of very high particle density form, and then instead of being slowed down by the large over-density, they pass straight through it.

## 1.7 Mathematical tools

### 1.7.1 Fourier relations

As we saw in section 1.6, the dynamical equations for density evolution are more easily solved in Fourier space. Owing to the requirement of homogeneity on large scales, the $\delta_k$ modes of the Universe are statistically independent, making errors generally much easier to evaluate in Fourier space than in real space. These advantages coupled with the ability to probe fluctuations of a particular scale without contamination from smaller (possibly highly non-linear scales), make Fourier analysis an attractive means for studying the

density field. This subsection sets up the formalism that will be used in the rest of the thesis.

The three dimensional Fourier transform of a function $f(\mathbf{x})$ is defined to be:

$$\tilde{f}(\mathbf{k}) = \int f(\mathbf{x})\, e^{i\mathbf{k}\cdot\mathbf{x}} \mathrm{d}^3\mathbf{x}, \tag{1.84}$$

and the inverse relation is

$$f(\mathbf{x}) = \frac{1}{(2\pi)^3} \int \tilde{f}(\mathbf{k}) e^{-i\mathbf{k}\cdot\mathbf{x}} \mathrm{d}^3\mathbf{k}. \tag{1.85}$$

A useful property of Fourier transforms is the convolution theorem which relates the convolution of two functions to the Fourier transform of their product:

$$\begin{aligned} \tilde{f}(\mathbf{k}) \star \tilde{g}(\mathbf{k}) &\equiv \frac{1}{(2\pi)^3} \int \tilde{f}(\mathbf{k}-\mathbf{k}')\, \tilde{g}(\mathbf{k}')\, \mathrm{d}^3\mathbf{k}' \\ &= \int f(\mathbf{x}) g(\mathbf{x}) e^{i\mathbf{k}\cdot\mathbf{x}} \mathrm{d}^3\mathbf{x}. \end{aligned} \tag{1.86}$$

The convolution theorem is useful when dealing with non-uniform galaxy samples of the density field. Galaxy surveys with a selection function allow one to probe only the product of the selection function with the underlying density field, and this becomes a convolution in Fourier space.

The analogous discrete relations are useful since these are used in the Fast Fourier transform – enabling transforms of data to be performed much faster. These are (*e.g.* Arfken 1985):

$$\tilde{f}(\mathbf{k}_{pqr}) = \sum_{i,j,k=0}^{2N-1} f(\mathbf{x}_{ijk})\, e^{i\mathbf{k}_{pqr}\cdot\mathbf{x}_{ijk}}\,, \tag{1.87}$$

and

$$f(\mathbf{x}_{ijk}) = \frac{1}{(2N)^3} \sum_{p,q,r=0}^{2N-1} \tilde{f}(\mathbf{k}_{pqr}) e^{-i\mathbf{k}_{pqr}\cdot\mathbf{x}_{ijk}} \tag{1.88}$$

where $\mathbf{x}_{ijk} \equiv (x_i, y_j, z_k)$ and $\mathbf{k}_{pqr} \equiv \left(k_p^x, k_q^y, k_r^z\right)$ .

### 1.7.2 Statistics of the density field

In a Gaussian distributed density field, the only free parameters are the mean of the distribution ($\overline{\rho}$), and the variance ($\sigma^2$), which can vary with scale. The mean is generally

factored out of the problem by defining a dimensionless overdensity, $\delta$, which is given by:

$$\delta \equiv \frac{\rho - \overline{\rho}}{\overline{\rho}}. \tag{1.89}$$

The variance can be expressed either as a **correlation function**, or as a **power spectrum** both of which are described below.

### The correlation function (and a digression about ergodicity)

The correlation function is a measure of the level of clustering in a field, and is given by:

$$\xi(\Delta \mathbf{x}) = \langle \delta(\mathbf{x} + \Delta \mathbf{x})\, \delta(\mathbf{x}) \rangle, \tag{1.90}$$

where angle brackets denote the average taken over an ensemble of universes. In the absence of such data sets, we resort to an application of ergodic theory, which states that for ergodic fields, the ensemble average is equivalent to the spatial average (the average taken over many regions of space) provided the number of independent patches of space is large. An ergodic field is required to have finite expectation values for all moments of the field, *i.e.*

$$\mathcal{E}\left\{ |X^i(t)| \right\} < \infty. \tag{1.91}$$

Also, the integral of $\mathbf{X}$ over the surface of a sphere, $\sigma$, of radius $T$ must be finite for any $T$:

$$\exists \int_{\sigma(T)} \mathbf{X}(t)\, \mathrm{d}t; \quad 0 < T < \infty. \tag{1.92}$$

This basically requires that there must exist a finite separation R for which correlations between points of this separation tend to zero. For a Gaussian distributed density field this applies so long as:

$$0 < P_r\left[X(\mathbf{x}_i) \,|X(\mathbf{x}_j)\right] < 1 \;\; ; \; \mathbf{x}_i \neq \mathbf{x}_j, \tag{1.93}$$

where $P_r\left[X(\mathbf{x}_i) \,|X(\mathbf{x}_j)\right]$ is the probability of finding a value $X(\mathbf{x}_i)$, at $\mathbf{x}_i$, given that a value $X(\mathbf{x}_j)$ has been found at position $\mathbf{x}_j$, (*e.g.* Adler 1981).

In an isotropic and homogeneous field, $\xi$ is independent of direction and position. As applied to galaxy clustering, $\xi$ can be thought of as describing the excess probability that

a galaxy will have a neighbour at a separation $\mathbf{\Delta x}$ compared with a random (Poisson) distribution of galaxies:

$$\delta P_r = \overline{n}^2 \left[1 + \xi\left(\Delta x\right)\right] \delta V_1 \delta V_2, \tag{1.94}$$

where $\delta V_1$, and $\delta V_2$ are volume elements containing the two galaxies separated by $\Delta x$, and $\overline{n}$ is the mean density (in this case of galaxies).

### The power spectrum

In Fourier space, the clustering can be described by the power spectrum, $P\left(k\right)$, which is the Fourier transform of the correlation function:

$$P\left(k\right) = \frac{1}{V} \int_V \xi\left(r\right) e^{i\mathbf{k}\cdot\mathbf{r}} \mathrm{d}^3 r, \tag{1.95}$$

where $V$ is the volume of the space sampled. This factor is needed for finite samples of the density field, where

$$\int_V e^{i(\mathbf{k}_1 - \mathbf{k}_2)\cdot\mathbf{r}} \mathrm{d}^3 r = V \delta^{\kappa}_{\mathbf{k}_1,\mathbf{k}_2}, \tag{1.96}$$

and $\delta^{\kappa}_{\mathbf{k}_1,\mathbf{k}_2}$ is the Kronecker delta function, which takes values zero for $\mathbf{k}_1 \neq \mathbf{k}_2$, and 1 for $\mathbf{k}_1 = \mathbf{k}_2$. In the limit of infinite density fields, the factor, $V\delta^{\kappa}_{\mathbf{k}_1\mathbf{k}_2}$ is replaced with the usual $\left(2\pi\right)^3 \delta^D\left(\mathbf{k}_1 - \mathbf{k}_2\right)$. We can also calculate the power spectrum in terms of the Fourier modes of the density field. In Fourier space, the density modes are defined as:

$$\delta_{\mathbf{k}} = \frac{1}{V} \int_V \delta\left(\mathbf{x}\right) e^{i\mathbf{k}\cdot\mathbf{x}} \mathrm{d}^3 x, \tag{1.97}$$

now, looking at the correlations between these modes, we have:

$$\begin{aligned} \left\langle \delta_{\mathbf{k}_1} \delta_{\mathbf{k}_2} \right\rangle &= \frac{1}{V^2} \int_V \left\langle \delta\left(\mathbf{x}'\right) \delta\left(\mathbf{x}''\right) \right\rangle e^{i\mathbf{k}_1\cdot\mathbf{x}' + i\mathbf{k}_2\cdot\mathbf{x}''} \mathrm{d}^3 x' \mathrm{d}^3 x'' \\ &= \frac{1}{V^2} \int_V \xi\left(\Delta x\right) e^{i\mathbf{k}_2\cdot\Delta\mathbf{x}} \mathrm{d}^3 \Delta x \int_V e^{i(\mathbf{k}_1 + \mathbf{k}_2)\cdot\mathbf{x}'} \mathrm{d}^3 x'. \end{aligned} \tag{1.98}$$

The second line has come from invoking isotropy and homogeneity in the density field, so that the correlation between overdensities is a function only of their separation, and not their actual positions. In the limit of infinite density fields, we can write this as

$$\left\langle \delta_{\mathbf{k}_1} \delta_{\mathbf{k}_2} \right\rangle = \frac{\left(2\pi\right)^3}{V} P\left(k\right) \delta^D\left(\mathbf{k}_1 + \mathbf{k}_2\right), \tag{1.99}$$

where in the infinite case, $V$ is generally set to one. For a finite sample of the density field we have

$$\begin{aligned} \langle \delta_{\mathbf{k}_1} \delta_{\mathbf{k}_2} \rangle &= P(k_1)\, \delta^{\kappa}_{\mathbf{k}_1,-\mathbf{k}_2}, \ i.e. \\ \left\langle |\delta_{\mathbf{k}_1}|^2 \right\rangle &= P(k_1). \end{aligned} \tag{1.100}$$

In dimensionless form, the power spectrum can be expressed as $\Delta^2(k)$ where

$$\Delta^2(k) \equiv \frac{Vk^3}{2\pi^2} P(k). \tag{1.101}$$

$\Delta^2(k)$ can be thought of as the contribution per unit logarithmic interval to the variance in $\delta$, since:

$$\int_{-\infty}^{\infty} \Delta^2(k)\, \mathrm{d}\ln k = \frac{V}{(2\pi)^3} \int_0^{\infty} P(k)\, \mathrm{d}^3 k = \langle \delta^2(\mathbf{x}) \rangle, \tag{1.102}$$

where $\langle \delta^2(\mathbf{x}) \rangle$ and $P(k)$ are related through Parseval's theorem. This definition of the power spectrum $[\Delta^2(k)]$ has the advantage of being independent of Fourier convention.

### 1.7.3 Definition of a Gaussian random field

The statistics of primordial fluctuations in the density field are predicted to be Gaussian in most inflationary scenarios. Since much of this thesis is devoted to analysing the statistics of density fluctuations, it is worth specifying exactly what is meant by a Gaussian random field. We shall start by defining a Gaussian distribution. A random variable, $X$, is said to have a Gaussian distribution if it has finite mean, $\mu = \mathcal{E}\{X\}$, (where $\mathcal{E}$ denotes the expectation value) and non-zero, finite variance, $\sigma^2 = \mathcal{E}\{|X-\mu|^2\}$, and if it has a one point probability distribution given by:

$$P_r(X : x \to x + \mathrm{d}x) = \frac{1}{(2\pi\sigma^2)^{\frac{1}{2}}} \exp\left[-\frac{(x-\mu)^2}{2\sigma^2}\right] \mathrm{d}x. \tag{1.103}$$

A Gaussian random field is defined to be a set of random variables whose combined distributions are all multivariate Gaussian. And a multivariate Gaussian (of dimension $n$) is a set of random variables, ($\mathbf{X} = \{X_1, \ldots, X_n\}$) for which any linear combination of these variables is itself Gaussian distributed. So a multivariate Gaussian has a probability distribution given by:

$$P_r(X_1, \ldots, X_n) = \frac{1}{(2\pi)^{n/2} |\mathbf{C}|^{1/2}} \exp\left[-\frac{1}{2} (\mathbf{X}-\boldsymbol{\mu})^T \mathbf{C}^{-1} (\mathbf{X}-\boldsymbol{\mu})\right], \tag{1.104}$$

where $\mathbf{C}$ is the covariance matrix, and is given by $C_{ij} = \mathcal{E}\{(X_i - \mu_i)(X_j - \mu_j)\}$.

For a Gaussian random density field, (as a direct consequence of the above statements) the Fourier modes are described by a two dimensional Gaussian random variable on the Argand plane, in which real and imaginary parts are independent, and so the phases are random. The amplitude squared of the Fourier modes is given by an exponential distribution *i.e.*

$$P_r\left(|\delta_k|^2\right) = \frac{1}{P(k)} \exp\left[-|\delta_k|^2/P(k)\right]. \tag{1.105}$$

### 1.7.4 Moment description of probability distributions

As we shall see later, quantitative assessments of distributions often involve looking at the moments of the distribution, the first few of which generally characterise the distribution. For a random variable, X, the $n^{th}$ order moment is defined about some arbitrary point $\overline{X}$ to be:

$$\mu'_n = \mathcal{E}\left\{\left(X - \overline{X}\right)^n\right\}. \tag{1.106}$$

If $\overline{X}$ is the mean, $\mu$, then the moments are conventionally written without a prime. For the Gaussian case, all $\mu_n$ can be described in terms of $\mu$ and $\sigma$, with odd moments being zero. The first deviations from a Gaussian distribution can be described by the skewness $\equiv \mu_3^2/\mu_2^{3/2}$, which measures the deviation from a symmetrical form, and the kurtosis $\equiv \mu_4/\mu_2^2$, which gives an indication of the degree of peaking of the distribution. A Gaussian distribution has zero skewness, and a kurtosis of 3.

The moments of a distribution $f_1(x)$ (where $x$ has been standardised to be $(X - \mu)/\sigma$) can be obtained from the moment generating function, $m_x(t)$ which is defined as:

$$m_x(t) \equiv \mathcal{E}\{e^{tx}\}. \tag{1.107}$$

We can also express this as:

$$m_x(t) = \int_x f_1(x)\, e^{tx} \mathrm{d}x. \tag{1.108}$$

The exponential can be expanded to give:

$$\begin{aligned} m_x(t) &= \mathcal{E}\{1 + tx + \frac{1}{2!}(tx)^2 \ldots\} \\ &= \sum_n \frac{1}{n!} \mu'_n t^n \ . \end{aligned} \tag{1.109}$$

We can now obtain the $n^{th}$ moment $\mu_n{}'$ simply by differentiating $m_x(t)$ with respect to $t$, $n$ times, and evaluating this at $t = 0$. Thus we can say:

$$\mu'_n = \frac{\mathrm{d}^n m_x(t)}{\mathrm{d}t^n}|_{t=0} \tag{1.110}$$

and we can find $m_x(it) \equiv \phi_x(t)$ simply by Fourier transforming the probability distribution function, $f_1(x)$. $\phi_x$ is called the characteristic function.

### 1.7.5 The Central Limit Theorem

The central limit theorem is of tremendous use in the field of statistics. It states that for a set of independent random variables, $X_1, \ldots, X_n$, each with the same distribution and for which both a mean and a variance exist, then $Z_n \equiv \left(\overline{X}_n - \mu\right)/\sigma$ (where $\overline{X}_n = \sum_i X_i/n$) has a distribution that approaches a standard normal distribution as $n \to \infty$. The statistics of Gaussian fields are much simpler to work with than most other random fields because they are entirely specified by their first two moments, so to be able to approximate the sum of many variables from an unknown distribution with a Gaussian proves to be very useful.

The beauty of this theorem comes from the fact that, other than requiring the existence of a mean and a variance, it states nothing about the form of the original density function from which $X_i$ are drawn. For the case of a completely general distribution, the proof requires some advanced mathematical techniques, and considerable quantities of paper. However in the case where the distribution has a moment generating function, the proof is quite straightforward, as we shall see below. (See *e.g.* Feller 1966).

Recalling from subsection 1.7.4, the moment generating function of a distribution $W$, where $W = (W' - \mu)/\sigma$ is defined as:

$$m_W(t) = \mathcal{E}\{e^{tW}\} = \mathcal{E}\{1 + tW + \frac{1}{2}(tW)^2 + \ldots\}. \tag{1.111}$$

If $W'$ comes from a normal distribution, then all the odd expectation values vanish, and we are left with:

$$m_W(t) = 1 + \frac{1}{2!}t^2\frac{\mu_2}{\sigma^2} + \frac{1}{4!}t^4\frac{\mu_4}{\sigma^4} + \ldots . \tag{1.112}$$

Now since $\mu_{2n} = \sigma^{2n}(2n)!/(n!\,2^n)$, this reduces to:

$$m_W(t) = \sum_n \frac{1}{(n-1)!}\left[\frac{t^2}{2}\right]^{n-1} = \exp\left[\frac{1}{2}t^2\right]. \tag{1.113}$$

Let us now find the moment generating function for the distribution $Z_n$ defined above. This can be written as:

$$\begin{aligned} m_{Z_n}(t) &= \mathcal{E}\left\{\exp\left[t\frac{\left(\overline{X}_n - \mu\right)}{\sigma/\sqrt{n}}\right]\right\} = \mathcal{E}\left\{\exp\left[\frac{t}{n}\frac{\sum(X_i-\mu)}{\sigma/\sqrt{n}}\right]\right\} \\ &= \mathcal{E}\left\{\prod_i \exp\left[\frac{t}{n}\frac{(X_i-\mu)}{\sigma/\sqrt{n}}\right]\right\} = \prod_i \mathcal{E}\left\{\exp\left[\frac{t}{n}\frac{(X_i-\mu)}{\sigma/\sqrt{n}}\right]\right\}, \end{aligned} \tag{1.114}$$

where the last line uses the independence of $X_i \ldots X_n$. Note that it is this step that distinguishes between the predictions made concerning the density distribution for inflation and topological defects – in inflation, $X_i$ are independent, where as in topological defects, they are not. Let us now define $Y_i = (X_i - \mu)/\sigma$ for future simplicity of notation. We then have

$$\begin{aligned} \prod_i \mathcal{E}\left\{\exp\left[\frac{t}{\sqrt{n}}\frac{(X_i-\mu)}{\sigma}\right]\right\} &= \prod_i \mathcal{E}\left\{\exp\left[\frac{t}{\sqrt{n}}Y_i\right]\right\} \\ &= \prod_{i=1}^{n} m_{Y_i}\left(\frac{t}{\sqrt{n}}\right) = \left[m_Y\left(\frac{t}{\sqrt{n}}\right)\right]^n \end{aligned} \tag{1.115}$$

where we have called $m_{Y_i}$, $m_Y$ since $Y_i$ all come from the same distribution, and thus have the same moment generating function. Using equation 1.112, $m_Y\left(\frac{t}{\sqrt{n}}\right)$ can be written as:

$$m_Y\left(\frac{t}{\sqrt{n}}\right) = 1 + \frac{t}{\sqrt{n}}\frac{\mu_1}{\sigma} + \frac{1}{2!}\left(\frac{t}{\sqrt{n}}\right)^2\frac{\mu_2}{\sigma^2} + \frac{1}{3!}\left(\frac{t}{\sqrt{n}}\right)^3\frac{\mu_3}{\sigma^3}\ldots. \tag{1.116}$$

$\mu_1 = 0$, and $\mu_2 = \sigma^2$ by virtue of the standardisation, so:

$$m_Y\left(\frac{t}{\sqrt{n}}\right) = 1 + \frac{1}{n}\left[\frac{1}{2}t^2 + \frac{1}{3!}\frac{t^3\mu_3}{\sqrt{n}\sigma^3} + \ldots\right]. \tag{1.117}$$

If we let the bracketed part $= U(n)$ then

$$m_{Z_n}(t) = \left[1 + \frac{U(n)}{n}\right]^n \tag{1.118}$$

For large n, $U(n) \to \frac{1}{2}t^2$, and

$$m_{Z_n}(t) \to \exp\left[\frac{t^2}{2}\right] \quad \text{as} \quad n \to \infty, \tag{1.119}$$

which is the moment generating function for a normal distribution, as we have shown above.

### Fields that are exempt from the central limit theorem

There are some random fields that do not alter their form on taking linear combinations of random variables from the field. The Gaussian field (unsurprisingly given the central limit theorem) is one example, but in general they have the property that the $n$-product of their characteristic function (c.f.), $\phi_x(t)$, [where $\phi_x \equiv m_x(it)$], yields a characteristic function of the same form as the individual variable's c.f., *i.e.*

$$\phi_{x_1}(t) \ldots \phi_{x_n}(t) = \phi_x(nt). \tag{1.120}$$

This requirement is satisfied by the class of functions,

$$\phi_x(t) = \exp\left[-\alpha t^\beta\right]. \tag{1.121}$$

If $\beta = 2$, the field is Gaussian, and for $\beta = 1$ we have a Cauchy field. Since the sum of many random variables from these fields has the same distribution as the original field, this class of fields does not tend towards a Gaussian distribution in the limit of large sums (with the trivial exception of the $\beta = 2$ field).

### Implications of the central limit theorem

Since this thesis deals largely with the detection of non-Gaussian fields, the central limit theorem is of considerable consequence to the subsequent chapters. In general the extent of the effect depends both on the field, and the statistic used to measure the non-Gaussianity. Statistics that involve averaging over portions of the field on scales larger than the typical correlation scale of the field are likely to erase the most information about non-Gaussian fields.

## 1.8 Motivations non-Gaussian fields.

A large part of this thesis explores the possibility of non-Gaussian fields with a view to constraining models that initiate fluctuations, so it is worth considering here what types of non-Gaussian field have been proposed as an alternative to the random phase Gaussian hypothesis. The proposed non-Gaussian fields can be divided into three classes

– those that arise from topological defect models, those that can be constructed from inflationary scenarios, and lastly those that are motivated empirically from large scale structure observations.

### 1.8.1 Theoretical motivations

**Topological Defects.** This class is arguably the least contrived, since fluctuations from 'topological seeds' generate quite naturally a spatial coherence in the density field which acts to correlate the phases of the Fourier modes. These phase correlations remain significant because the number of seeds per horizon is initially of order one, and so there are limited randomising effects from other density seeds. The exact nature of the non-Gaussian distribution, however is model dependent and generally requires numerical simulations to calculate. The two potentially viable topological defect models are global textures and cosmic strings.

The global texture model has been promoted as an interesting alternative for adiabatic inflationary structure formation by Cen *et al.* (1991). This has been analysed by Gaztañaga & Mähönen, (1996, and references therein) who analyse the density distribution of the global texture model, and predict that the hierarchical skewness, $S_3$, (where $S_J \equiv \bar{\xi}_J/\bar{\xi}_2^{J-1}$, see Chapter 2) on scales of $30\,h^{-1}\,\mathrm{Mpc}$ would be expected to be $S_3 \simeq 5 \pm 1$, which is three times larger than the expected Gaussian skewness. For the kurtosis on the same scale, they predict $S_4 \simeq 40 \pm 10$ – ten times larger than the Gaussian prediction.

The cosmic string model has recently been investigated by Avelino, Shellard & Wu (1998). The nature of this non-Gaussian distribution is to give increased skewness and kurtosis, with the effect becoming significant ($\langle(\delta/\sigma)^3\rangle \sim 1$, and $\langle(\delta/\sigma)^4\rangle \sim 1$) on scales $\lesssim 1.5\,(\Omega h^2)^{-1}$ – corresponding to scales of $20\,h^{-1}\,\mathrm{Mpc}$ for $\Omega = 0.3, h = 0.5$. It is debatable whether such an effect could be distinguished from gravitational evolution on these scales, although for open or $\Lambda$ universes with $\Gamma = \Omega h \lesssim 0.2$ these scales would be expected to be linear or mildly non-linear.

**Inflationary tuning.** The standard model of inflation predicts Gaussian density fluc-

tuations (*e.g.* Guth & Pi 1982, Bardeen *et al.* 1983) arising from the amplification in scale of quantum fluctuations in the potential field. However, it is possible to generate non-Gaussian fields for instance by invoking double inflation (two periods of inflation), or chaotic inflation (where the scalar field is initially inhomogeneous, and inflation is initiated at a number of points in the Universe rather than at every point in space). Yi & Vishniac (1993) find that the resulting distribution, however, is strongly model dependent, but conclude that adiabatic fluctuations would only look non-Gaussian on super horizon scales because of CMB constraints on the level of anisotropy in the density field.

The non-Gaussian distributions that do arise, again appear to have increased skewness or kurtosis (or both) *e.g.* Allen, Grinstein & Wise (1987), who consider quantum fluctuations in an axion field which give rise to non-Gaussian isocurvature mass density fluctuations. They conclude that such fluctuations would have a high Fourier kurtosis.

### 1.8.2 Observationally motivated non-Gaussian models

The final class of non-Gaussian models has been motivated from current observations of large scale structure. Over the years Peebles has been a strong advocate of such models, and we consider two of them here.

The first was put forward as a suggestion to resolve arguments over whether structure formation was hierarchical (small structures forming first, and aggregating into larger structures), or fragmentary (large structures forming first, and breaking up into smaller ones). The arguments in favour of the fragmentary scenario are that correlations in the density field are found to exist over a wide range of scales, but the hierarchical picture looked more likely on the grounds that we are moving towards the Virgo cluster rather than away from it, as might have been expected in a fragmentary scenario. Peebles (1983) postulated instead a non-Gaussian field which is the product of two Gaussian fields, ($\delta$ and $\eta$) where the resultant is given by:

$$\delta' = \delta\,(1+\eta)\,. \tag{1.122}$$

This could give the large scale correlations, while still allowing hierarchical structure

growth. This 'modulated field' model is considered in Chapters 3 & 4.

Recent advances in observational cosmology have enabled some constraints to be placed on the standard CDM model. The first of these is the compilation of several redshift surveys which probe scales of up to $\sim 100\,h^{-1}\,\mathrm{Mpc}$ (*e.g.* IRAS-QDOT, Saunders *et al.* 1991; IRAS-1.2Jy, Fisher *et al.* 1993; APM-Stromlo, Loveday *et al.* 1996b; PSCz, Saunders *et al.* 1998). These have resulted in measurements of the power spectrum and the redshift distortion parameter, $\beta$. The shape of the power spectrum is now commonly found to be inconsistent with a standard CDM model with constant or monotonic bias (*e.g.* Peacock 1997, Canavezes *et al.* 1998). This model either under-predicts the large scale power, or over-predicts the small scale power depending on how it is normalised.

Another potential problem for the standard CDM model is the discovery of large over-densities of Lyman-$\alpha$ break galaxies at redshifts of $\sim 3$ (Steidel *et al.* 1998), and the inference of the existence of collapsed objects at very high redshifts ($z \simeq 6$), deduced from the discovery of old star forming galaxies at redshifts of $z \simeq 1.5$ (*e.g.* Dunlop *et al.* 1996). The density field appears to be more highly evolved at high redshift than can be accounted for by CDM models unless these galaxies are highly biased relative to the mass field (with $b \simeq 6$).

Low density CDM models, can be made to fit the data better, but still require a high level of biasing at high redshift (*e.g.* Peacock *et al.* 1998). It is possible, however, that Lyman-$\alpha$ galaxies are indeed highly biased relative to the mass density field, and recent simulations of galaxy assembly have found this to be plausible (*e.g.* Governato *et al.* 1998).

While the above problems with standard CDM can be fixed by using combinations of low density, mixed dark matter universes, a primordially non-Gaussian field could also provide the required early collapse of objects. With this in mind, Peebles (1997, 1998) has put forward an inflationary non-Gaussian isocurvature model, which involves three scalar fields. The resulting density field is the square of a Gaussian process (*i.e.* it has a $\chi^2$ distribution with one degree of freedom) which is thought to enable the density field to be highly evolved on small scales at early epochs, since for initially skew positive models, the power spectrum evolves into the non-linear regime faster than for Gaussian

models. The evolution of such non-Gaussian power spectra, along with the viability of such a $\chi^2$ model are considered in Chapter 3.

## 1.9 Thesis layout

Work in the field of non-Gaussian models has taken a number of directions – we have already considered some of the theoretical work that has motivated invoking primordial non-Gaussian fields in section 1.8.1, and have seen that there is also observational scope for such models. Much consideration has also been given to how non-Gaussian fields evolve under gravity. This has been tackled mathematically using perturbation approaches to investigate the mildly non-linear regime (*e.g.* Fry & Scherrer 1994; Chodorowski & Bouchet 1996; Gaztañaga & Fosalba 1997) as well as empirically, using N-body simulations to generate and evolve different non-Gaussian models (*e.g.* Moscardini *et al.* 1991; Weinberg & Cole 1992; Coles *et al.* 1993; Gaztañaga & Mähönen 1996).

Chapters 2 and 3 build on this work by comparing the highly non-linear evolution of the power spectrum with the predictions of Peacock & Dodds (1996) for Gaussian initial conditions. Chapter 2 is principally a description of some of the standard techniques used in the field, both to set up N-body simulation initial conditions, and then to measure the power spectrum and higher order moments from such simulations. It goes on to describe the Peacock and Dodds fitting formula (1994,1996) to map between linear and non-linear power spectra, and briefly explores an extension to this mapping to deal with cases where the power spectrum is not just a power law.

The first part of Chapter 3 looks at how the power spectrum of non-Gaussian density fields evolves into the highly non-linear regime, comparing it with the fitting formula derived for initially Gaussian fields. Since much of the empirical work has preceded the theoretical work, Chapter 3 also examines some of the theoretical findings in the light of the results from Chapter 3, and other authors' results. The second part of Chapter 3 explores the viability of a non-Gaussian isocurvature model (Peebles 1997, 1998a, 1998b) which has been promoted recently in the literature.

Perhaps the most important work on non-Gaussian fields has been to develop statistics

to analyse the observed density field, and to test the hypothesis that the density field was primordially Gaussian. Here the work has mainly been in real space, looking at the higher order moments of the density field from redshift surveys (*e.g.* Saunders *et al.* 1991; Gaztañaga 1992; Nusser *et al.* 1995), and using topology to estimate the genus of the density field (for instance Coles *et al.* 1993, Gott *et al.* 1987, Moore *et al.* 1992; Park *et al.* 1992; Vogeley *et al.* 1994). Much of the work on higher order moments has concentrated on measuring statistics of the density field in the quasi-linear regime, and comparing the observed non-Gaussian characteristics with what would be expected for the gravitational evolution of initially Gaussian fluctuations. In the above analyses the density field has been found to be consistent with a distribution that was initially Gaussian. However, in all this work, it is necessary to smooth the galaxy distribution with some filter, averaging the effect of different regions of space. The central limit theorem then suggests that there is the danger that the appearance of Gaussian statistics will always be produced, whatever the underlying distribution.

In the light of this problem, Chapter 4 develops a Fourier based four point test for non-Gaussian fields, which is sensitive to phase correlations, and as such it is thought to be less susceptible to the effects of the central limit theorem (Fan & Bardeen 1995). It also has the advantage of being able to probe large scales without contamination from smaller scales. This four point test is applied to the QDOT+1.2Jy redshift survey, and limits are placed on a particular class of non-Gaussian models. Future improvements to the sensitivity of the results with forthcoming surveys are then considered.

Chapter 5 provides an extension to the power correlations test to take into account the effect of redshift distortions, and the test is modified to measure the redshift distortion parameter $\beta$ from spherical surveys. This new method does not require the distant observer approximation, allowing large angle surveys to be analysed. The method is applied to a number of simulations, and then to the QDOT+1.2 Jy redshift survey to find an estimate for $\beta$.

The thesis closes with a summary of the main results from the preceding chapters, and a short discussion of the prospects for future work in the field.

# Chapter 2

# N-BODY SIMULATIONS AND THE EVOLUTION OF POWER

This chapter is mainly a technical precursor to the work in Chapter 3 which concentrates on the evolution of non-Gaussian fields into the non-linear regime. It contains a general discussion of N-body simulations, with a description of how to set up initial conditions for such simulations. This is followed with details about the measurement of statistics such as the skewness, kurtosis, and the power spectrum from simulations.

The second part of the chapter describes the use of a fitting formula to relate the non-linear power spectrum to the linear power spectrum (Peacock & Dodds 1994, 1996), and extensions to this idea are offered to account for non-monotonic power spectra.

## 2.1 N-body Simulations

### 2.1.1 Introduction

The primordial fluctuations set up in the density field are thought to evolve under gravitational instability to create the clustering observed today, so a comparison of the effect of different non-Gaussian initial conditions on clustering at the present epoch therefore requires studying the gravitational evolution of the initial conditions. This evolution

is described by a set of non-linear fluid equations which originate from conservation of matter, energy, and momentum. They can be combined into a single equation, which describes the dynamics of the fluctuations (see Chapter 1, section 1.6 for a derivation):

$$\frac{\partial^2\delta}{\partial t^2} + 2\frac{\dot{a}}{a}\frac{\partial\delta}{\partial t} = \frac{\nabla^2 p}{\rho_b\, a^2} + \frac{1}{a^2}\boldsymbol{\nabla}\cdot(1+\delta)\,\boldsymbol{\nabla}\Phi + \frac{1}{a^2}\frac{\partial^2}{\partial x^\alpha \partial x^\beta}[(1+\delta)\,u^\alpha u^\beta]. \tag{2.1}$$

The non-linear behaviour of this equation makes a complete analytical treatment of the density fluctuations' evolution impossible, and while approximations using linear and second order perturbation theory for $|\delta| \ll 1$ can be obtained (see Chapter 1, subsection 1.6.1), tracking $\delta$ well into the non-linear regime requires a numerical approach. Since the purpose of the work in the following chapter is to examine the effect of initial conditions on clustering at the present epoch, where $|\delta| \gg 1$ on scales $< 20\,h^{-1}$ Mpc, the simplest approach is to solve the equation numerically using an N-body simulation.

### 2.1.2 Equations of motion

In N-body simulations discrete particles are used to represent a continuous matter distribution where, in the evolved simulation, each particle represents a Poisson sampling of the underlying distribution. The simulation is evolved by calculating the gravitational force exerted on each particle from all the other particles, changing their velocities, and displacements over some small time step accordingly, and then re-evaluating the gravitational field. This process is repeated until the desired level of clustering is reached.

In order to get clustering into the non-linear regime and owing to restrictions on the number of particles that can be used (due to computer memory restrictions), the simulation represents a volume much smaller than the horizon size. On these scales, Newtonian gravity and dynamics can be used to describe the equations of motion for the system. We start with the comoving Euler equation, which is Newton's second law for a fluid (see Chapter 1, equation 1.65),

$$\ddot{a}\mathbf{x} + \frac{\partial\mathbf{u}}{\partial t} + \frac{1}{a}(\mathbf{u}\cdot\nabla_c)\,\mathbf{u} + \frac{\dot{a}}{a}\mathbf{u} = -\frac{1}{\rho a}\nabla_c p - \frac{1}{a}\nabla_c\phi, \tag{2.2}$$

where $p$ is the pressure, $\rho$ density, and $_c$ denotes the use of comoving coordinates. Here, $\mathbf{x} = \mathbf{r}/a$ is the comoving position vector, and $\mathbf{u} = a\dot{\mathbf{x}}$. We now want to rewrite $\mathbf{u}$ in

terms of time derivatives of $\mathbf{x}$ only, so defining $\mathbf{w} \equiv \dot{\mathbf{x}} = \mathbf{u}/a$, and substituting $\mathbf{w}$ into the above equation (eqn 2.2), we have:

$$\ddot{a}\mathbf{x} + \dot{a}\mathbf{w} + a\frac{\partial \mathbf{w}}{\partial t} + a\left(\mathbf{w}\cdot\nabla_c\right)\mathbf{w} + \dot{a}\mathbf{w} = -\frac{1}{\rho a}\nabla_c p - \frac{1}{a}\nabla_c\phi. \tag{2.3}$$

For N-body simulations, which start off in the matter dominated era, the pressure term on the right hand side of equation 2.3 can be taken to be negligible. So we are left with:

$$\ddot{a}\mathbf{x} + a\frac{D\mathbf{w}}{Dt} + 2\dot{a}\mathbf{w} = -\frac{1}{a}\nabla_c\phi, \tag{2.4}$$

where $D/Dt \equiv \partial/\partial t + \mathbf{w}\cdot\nabla_\mathbf{c}$ is the convective derivative describing the rate of change of a fluid element's velocity as one moves with the fluid. In the absence of peculiar velocities and peculiar accelerations, (*i.e.* $\mathbf{w}, \dot{\mathbf{w}} = 0$), the unperturbed relation 2.4 becomes:

$$\ddot{a}\mathbf{x} = -\frac{1}{a}\nabla_c\phi_0, \tag{2.5}$$

and subtracting the unperturbed equation (eqn 2.5) from equation 2.4 gives our final relation:

$$a\frac{D\mathbf{w}}{Dt} + 2\dot{a}\mathbf{w} = -\frac{1}{a}\nabla_c\delta\phi, \tag{2.6}$$

where $\delta\phi \equiv \phi - \phi_0$. This is the comoving equation of motion used for N-body simulations. Note that even in the absence of 'external forces', the comoving velocity is slowed by the expansion of the universe, which is manifest as a drag term on the left hand side of equation 2.6.

It now remains to convert equation 2.6 into a computational method. For a fuller description of the methods outlined here, consult Hockney & Eastwood's book 'Computer simulation using particles', (1988).

### 2.1.3 Solving for w – The leapfrog algorithm

Once the force has been calculated, each particle's displacement, $\delta\mathbf{x}$, and velocity is adjusted accordingly. This requires solution of the differential equation 2.6, which involves converting the differential equation into a finite difference equation. For a sufficiently small time step, $\mathbf{w}$ can be written as:

$$\mathbf{w}_n = \frac{\dot{\mathbf{x}}_{n+\frac{1}{2}} + \dot{\mathbf{x}}_{n-\frac{1}{2}}}{2}, \tag{2.7}$$

and $D\mathbf{w}/Dt$ as:

$$\dot{\mathbf{w}}_n = \frac{\dot{\mathbf{x}}_{n+\frac{1}{2}} - \dot{\mathbf{x}}_{n-\frac{1}{2}}}{\delta t}. \tag{2.8}$$

This turns equation 2.6 into:

$$\frac{\dot{\mathbf{x}}_{n+\frac{1}{2}} - \dot{\mathbf{x}}_{n-\frac{1}{2}}}{\delta t} + 2\left(\frac{\dot{a}}{a}\right)\frac{\dot{\mathbf{x}}_{n+\frac{1}{2}} + \dot{\mathbf{x}}_{n-\frac{1}{2}}}{2} = -\frac{1}{a^2}\nabla_c \delta\phi. \tag{2.9}$$

This can be solved for $\dot{\mathbf{x}}_{n+\frac{1}{2}}$, and the new particle positions are:

$$\mathbf{x}_{n+1} = \mathbf{x}_n + \dot{\mathbf{x}}_{n+\frac{1}{2}}\delta t. \tag{2.10}$$

The use of time steps before and after the $n^{th}$ time step to calculate a property at the $n^{th}$ time value is known as the leapfrog algorithm, and is used to reduce truncation errors arising from representing continuous variables with discrete values. We can see this if we substitute equation 2.10 into equation 2.9 and get:

$$\frac{\mathbf{x}_{n+1} - 2\mathbf{x}_n + \mathbf{x}_{n-1}}{\delta t^2} + \left(\frac{\dot{a}}{a}\right)\frac{\mathbf{x}_{n+1} - \mathbf{x}_{n-1}}{\delta t} = -\frac{1}{a^2}\nabla_c \delta\phi. \tag{2.11}$$

Now if we Taylor expand $\mathbf{x}_{n+1}$ and $\mathbf{x}_{n-1}$ about $\mathbf{x}_n$ we get

$$\begin{aligned}
\mathbf{x}_{n+1} &= \mathbf{x}_n + \delta t\mathbf{x}'_n + \frac{\delta t^2}{2!}\mathbf{x}''_n + \frac{\delta t^3}{3!}\mathbf{x}'''_n + \frac{\delta t^4}{4!}\mathbf{x}''''_n \\
\mathbf{x}_{n-1} &= \mathbf{x}_n - \delta t\mathbf{x}'_n + \frac{\delta t^2}{2!}\mathbf{x}''_n - \frac{\delta t^3}{3!}\mathbf{x}'''_n + \frac{\delta t^4}{4!}\mathbf{x}''''_n.
\end{aligned} \tag{2.12}$$

Substituting equations 2.12 into 2.11 and subtracting off equation 2.6 gives a residual error in the force of order $\delta t^2$ – a second order error.

### 2.1.4 Solving for $\nabla\phi$

We now turn to the problem of calculating the forces, $\nabla\phi$. The simplest method is to sum all the gravitational forces acting on each particle in turn:

$$\nabla_c \phi_j = \sum_{i=1}^{N} Gm\frac{(\mathbf{x}_j - \mathbf{x}_i)}{|\mathbf{x}_j - \mathbf{x}_i|^3}. \tag{2.13}$$

This is computationally expensive, as the c.p.u. time required goes as $N(N-1)$. Another approach is to solve Poisson's equation:

$$\nabla^2\phi = 4\pi G\delta, \tag{2.14}$$

which is easily solved in Fourier space, and has the advantage that it can be carried out quickly ($\sim N \log N$) owing to the Fast Fourier Transform (FFT) (Cooley & Tukey 1965). In Fourier space, equation 2.14 becomes:

$$-k^2\phi_k = 4\pi G\delta_k, \tag{2.15}$$

so

$$\nabla\phi = \mathcal{F}.\mathcal{T}.\left[\frac{i\mathbf{k}\delta_k}{k^2}\right]. \tag{2.16}$$

If an FFT is used, then the simulation box is treated as having triply periodic boundary conditions, which allows the density field to be described by a finite set of Fourier modes. This is useful for setting up the initial conditions as we shall see later. In order to carry out the FFT, the density field needs to be averaged onto a grid, and this can be achieved in a number of ways – the simplest being to assign each particle to its nearest grid point (NGP). More sophisticated (and thus more computationally expensive) methods involve interpolating between nearest mesh points to various orders. First order, linear interpolation ensures continuity in the density and is called the Cloud in Cell scheme (CIC). The second order interpolation (Triangular Shaped Cloud) gives continuity of the first derivative, and is generally used as a reasonable compromise between accuracy and c.p.u. time.

### 2.1.5 Types of N-body code

#### Particle Mesh codes

The simplest N-body algorithm computes inter-particle forces by solving Poisson's equation on a grid. It is called the particle mesh (PM) code, and it can be broken into the following operations:

(1) Assign particles to mesh

(2) Solve Poisson's equation on mesh using an FFT

(3) Find the force on each particle by finding the potential derivatives. This can be done either by finding the difference in potential between grid positions in real space, or by Fourier transforming the potential field, multiplying by $-i\mathbf{k}$, and transforming back.

(4) Interpolate the mesh forces to the particle positions

(5) Adjust each particle's velocity and displacement – this is most accurately done by using the leapfrog algorithm.

(6) Re-evaluate the potential, and iterate steps (2)-(6).

Since forces are calculated on a mesh, this algorithm has limited resolution of order the mesh size.

### Particle$^3$ Mesh codes

A refinement of the PM code that increases the force resolution is to perform a direct sum of forces for particles at small separations. This is used in the particle-particle, particle-mesh ($P^3M$) technique of Eastwood and Hockney (1974), which retains the mesh calculation for larger separations. This code tends to slow down as the level of clustering increases, and the short range direct sum comes to dominate the force calculation.

### $AP^3M$ codes

The computational cost of increasing the force resolution can be reduced by refining the $P^3M$ algorithm one stage further. This is done by replacing the direct sum for the densest regions of the simulation in the $P^3M$ code with a refined PM calculation in which dense regions are identified, assigned to a finer mesh and treated independently of the rest of the simulation. In this case the boundary conditions for the refined PM operations are not periodic – instead, a mesh twice the volume of the chosen high density region is chosen, and regions outside the mesh or containing no particles within the mesh are treated as having zero over density (this is known as zero padding). This code is known as the Adaptive $P^3M$ code, owing to Hugh Couchman (1991), and can be 10-20 times faster than the conventional $P^3M$ code for highly clustered states.

### Tree codes

Another adaptive method is the Tree Code (Barnes & Hut 1986). This is non-periodic, and does not rely on Fourier techniques for calculating the forces. The main idea here, is to treat groups of distant particles subtending an angle less than a specified angle, $\theta$ (which sets the accuracy of the simulation) as one massive particle positioned at the centroid of the group of particles. To achieve this, the simulation box is recursively divided into sub-boxes until each particle sits in a box of its own. The forces on each particle are then calculated by choosing the largest sub-box that subtends an angle less than $\theta$, and calculating the sum of forces between the $i$ th particle, and the centroids of the sub-boxes that contain all the other particles. While this code compares well in terms of speed with the AP$^3$M code, it has a high memory requirement to store all the combinations of sub-boxes.

## 2.1.6 Simulation accuracy

The simulations used for the work in Chapter 3 use the AP$^3$M code provided by Hugh Couchman, and adapted by Peacock and Dodds for use in open and $\Lambda$ universe models.

In order for the simulations to reflect actual gravitational growth of clustering, the evolved power on the scale of the box has been kept lower than $\Delta^2(k) < 0.02$ so that modes on the scale of the box are still growing linearly. This is because when the growth starts to become non-linear, the Fourier modes cease to evolve independently, and information between modes is mixed. If the modes on the scale of the box are allowed to become non-linear, they will have no larger scale modes with which to mix, and thus their evolution will no longer reflect that of a universe which has an infinite number of modes, and approaches homogeneity on large scales. Also, since there are very few large scale modes of order the size of the box, estimates of the power spectrum on these scales are subject to larger errors, so when tracking the power spectrum into the non-linear regime, it is best to have the interesting non-linear power modes well sampled, and thus keep them on scales much smaller than the box size.

The accuracy of the simulation procedure can be checked by measuring the total energy



EX BIBL UNIV. GRONINGEN

of the system during the run. In comoving coordinates, conservation of energy can be written as (Layzer 1963, Irvine 1961):

$$\frac{\mathrm{d}}{\mathrm{d}t}\left(a^4 T\right) + a\frac{\mathrm{d}W}{\mathrm{d}t} = 0, \tag{2.17}$$

where $T$ is the kinetic energy:

$$T = \sum_i \frac{1}{2} m_i a u_i^2, \tag{2.18}$$

and $W$ is the potential energy:

$$W = \sum_i m_i \phi\left(\mathbf{x}_i\right). \tag{2.19}$$

Using discrete time-steps, the Layzer-Irvine equation, (eqn 2.17) can be written as follows:

$$\frac{a_{n+1}^4 T_{n+1} - a_n^4 T_n}{\delta t} + \frac{a_{n+1} W_{n+1} - a_n W_n}{\delta t} - W_{n+1}\dot{a}_{n+1} = 0. \tag{2.20}$$

If one sums equation 2.20 for $n+1 = m, m-1, \ldots, 0$, then most of the terms cancel, leaving:

$$a_m^4 T_m + a_m W_m - \sum_{n=1}^{m} \delta t W_n \dot{a}_n = a_0^4 T_0 + a_0 W_0 \equiv C. \tag{2.21}$$

The left hand side of equation 2.21 can be computed during the run, and its constancy checked. This has been carried out for the $\Omega = 1$ AP$^3$M simulations used here, and for 200 time-steps, $\Delta C/W_m$ is of order 0.05.

### 2.1.7 Initial Conditions

The initial positions of the particles in an N-body simulation need to give the correct linear power spectrum for the simulation, and reflect the one point statistical properties of the density field. The method for obtaining these initial positions is originally due to Efstathiou *et al.* (1985), and for most of the non-Gaussian simulations considered here is extended in much the same way as implemented in Coles & Barrow (1987). We start by generating a realisation of a Gaussian field (from which non-Gaussian fields can be obtained by performing non-linear operations on the density field). Since the N-body box is taken to be periodic, the density field can be completely described by a finite number of Fourier modes. Each of these will have random phase, and an amplitude squared that is exponentially distributed about the true power spectrum. Because of the finite

number of modes, the measured power spectrum in the simulation is only an estimator of the true mean power spectrum. Once the Fourier modes are assigned for each grid position in Fourier space, the velocity field can be determined by using the linearised continuity equation (see Chapter 1, equation 1.79). In Fourier space this becomes:

$$\mathbf{w_k} = i\, H\, f(\Omega)\, \frac{\delta_\mathbf{k}\, \mathbf{k}}{k^2}. \tag{2.22}$$

Now particles can be brought onto the scene, and each one is assigned a grid point so as to give a uniform distribution of particles. Using the Zel'dovich approximation (discussed in Chapter 1) which describes the position, $\mathbf{x}$, of a particle in terms of its displacement, $\boldsymbol{\xi}$, from its initial position, $\mathbf{q}$:

$$\mathbf{x}(t) = \mathbf{q} - D(t)\boldsymbol{\xi}(\mathbf{q}), \tag{2.23}$$

and for small displacements, $\boldsymbol{\xi} \propto \mathbf{w}$. The velocity field can therefore be obtained by moving particles a distance proportional to the velocity field measured at that grid point.

The next consideration is how to specify $\delta_k$. If the fluctuations are to come from a Gaussian distribution with a specified power spectrum, then we need $\langle|\delta_k|^2\rangle = P(k)$. For a Gaussian distribution, the real and imaginary parts of $\delta_k$ must also come from a Gaussian distribution, with a random phase relating the $\mathcal{R}e$, and $\mathcal{I}m$ parts. The non-Gaussian cases considered in the next chapter mainly involve non-linear operations on a Gaussian field, in which case the Gaussian fluctuations, $\delta_k$ are generated, converted back to real space, and $\delta^{\mathrm{NG}} = F\left(\delta^G\right)$, where $F$ is some non-linear function of the density field (this process is described in more detail in Chapter 3).

The steps can be summarised as follows:

(1) Generate Fourier modes with amplitude squared given by an exponential distribution with mean power, $P(k)$, and random phases:

$$\begin{aligned} \mathcal{R}e\,[\delta_\mathbf{k}] &= [P(k) * \log_e(\mathrm{rand}_1)]^{\frac{1}{2}} \cos(2\pi \mathrm{rand}_2) \\ \mathcal{I}m\,[\delta_\mathbf{k}] &= [P(k) * \log_e(\mathrm{rand}_1)]^{\frac{1}{2}} \sin(2\pi \mathrm{rand}_2), \end{aligned} \tag{2.24}$$

where rand is a random variable coming from a uniform distribution between 0 and 1.

Then for non-Gaussian fields involving a non-linear operation on the Gaussian field:

Fourier transform back to get real space densities

Apply non-linear transformation to density field

Transform back to get Fourier modes

(2) Assign velocities according to

$$w_k^i \propto \frac{k^i}{k^2}\delta_k \tag{2.25}$$

(3) Fourier transform back to get real space velocities

(4) Put $N^3$ particles on a grid

(5) Move each particle a distance proportional to its velocity.

The way in which the particles are placed in the box before they are perturbed can affect the initial power spectrum that the simulation is given. For instance if they are placed precisely onto a grid then the simulation will have a spike in the power spectrum on the scale of the grid. In theory, a random assignment of positions within the box would best reflect the true matter distribution, but for the number of particles used in these simulations and the initial amplitude of power spectrum, the shot noise due to the random placements would dominate the initial power spectrum. Compromises include placing each particle randomly within allocated cells of the box, and a sub-random 'glass' distribution which has no regular structure, but the particles are arranged so as to give maximal average inter-particle separation (*e.g.* Baugh *et al.* 1995). Each method, however, gives a contribution to the measured power spectrum for a finite number of particles. To evaluate this contribution, a reference set of initial conditions with zero input power is used to determine the power arising from gridding the particles, and this is subtracted from the linear power estimate. For the simulations used in this work, randomly placed particles within their allocated boxes worked well for the $n = 0$, and $n = -1$ spectra, but for shallower spectra such as $n = -1.5$, placement on a grid was required in order to beat down the power contribution on scales greater than the grid size.

## 2.2 Counts in Cells

We now turn to the issue of analysing the statistics of evolved simulations, and a useful tool for this is the counts in cells technique. Here we describe how to calculate moments of the simulated density field, and define some statistics that will be used in Chapter 3. The counts in cells technique is described in detail in *e.g.* Peebles (1980, §36), Gaztañaga (1994) and Baugh, Gaztañaga & Efstathiou (1995; BGE95).

Since the density field in both redshift surveys and N-body simulations is represented by a discrete set of points, in order to define the density at a point, it is useful to be able to smooth the discrete density field with a window function. The smoothed density field, $\delta_W(\mathbf{x})$ is given by

$$\delta_W(\mathbf{x}) = \frac{1}{V_W} \int \mathrm{d}\mathbf{x}' \delta(\mathbf{x}') W(\mathbf{x} - \mathbf{x}'), \tag{2.26}$$

where $W$ is a window function with volume $V_W$. For a spherical top hat window function of radius $R$,

$$\delta_W(\mathbf{x}) = \frac{N(\mathbf{x}, R) - \overline{N}}{\overline{N}}, \tag{2.27}$$

where $N(\mathbf{x}, R)$ is the number of particles in a spherical volume of radius $R$, centred on $\mathbf{x}$, and $\overline{N}$ is the expected number count in a volume $V_W = 4\pi R^3/3$ for a uniform distribution.

The moments of the mass distribution are given by:

$$m_J(R) = \left\langle \left[ N(\mathbf{x}, R) - \overline{N}(R) \right]^J \right\rangle \simeq \frac{1}{M} \sum_{i=1}^{M} \left[ N(\mathbf{x}_i, R) - \overline{N}(R) \right]^J, \tag{2.28}$$

where the ensemble average has been replaced by a sum over different spatial positions, $\mathbf{x}_i$. The first few reduced moments, $\mu_J$ are:

$$\mu_2 = m_2 \tag{2.29}$$

$$\mu_3 = m_3 \tag{2.30}$$

$$\mu_4 = m_4 - 3m_2^2. \tag{2.31}$$

We can now introduce $\overline{\xi}_J$ which is the volume averaged J-point correlation function. It is a measure of the moments of the density field, and in the continuous limit (*i.e.* in the

absence of shot noise) is defined to be:

$$\overline{\xi}_J \equiv \left\langle \delta_W^J \right\rangle_c . \tag{2.32}$$

The subscript $c$ denotes that this is a connected moment, which is basically the excess moment once the Gaussian contribution from lower order moments has been subtracted. This can be written as:

$$\left\langle \delta_W^J \right\rangle_c = \begin{cases} \left\langle \delta_W^J \right\rangle & \text{for odd J} \\ \left\langle \delta_W^J \right\rangle - \prod_{i=1}^{J/2} (2i-1) \left\langle \delta_W^2 \right\rangle^{J/2} & \text{for even J.} \end{cases} \tag{2.33}$$

$\overline{\xi}_J$ is related to the J-point correlation function by:

$$\overline{\xi}_J = \frac{1}{V_W^J} \int \mathrm{d}\mathbf{r}_1 \ldots \mathrm{d}\mathbf{r}_J W(\mathbf{r}_1) \ldots W(\mathbf{r}_J) \, \xi_J(\mathbf{r}_1, \ldots, \mathbf{r}_J) , \tag{2.34}$$

where $\xi_J(\mathbf{r}_1, \ldots, \mathbf{r}_J) \equiv \langle \delta(\mathbf{r}_1) \ldots \delta(\mathbf{r}_J) \rangle_c$. In the absence of shot noise, $\overline{\xi}_J$ can be written in terms of the reduced moments, $\mu_J$:

$$\overline{\xi}_J(R) = \mu_J(R) / \overline{N}^J . \tag{2.35}$$

Here $R$ is the scale over which the density field has been averaged.

We can now define the **hierarchical moments**, $S_J$:

$$S_J \equiv \frac{\overline{\xi}_J}{\overline{\xi}_2^{J-1}} . \tag{2.36}$$

Another definition for the higher order moments is the **dimensionless moment**, $D_J$:

$$D_J \equiv \frac{\overline{\xi}_J}{\overline{\xi}_2^{J/2}} . \tag{2.37}$$

$S_J$ turn out to be useful when considering weakly evolved density fields, as we shall see later.

So far we have considered $\overline{\xi}_J$ in the continuous limit, but since in practice, moments are measured from the distribution of particles, we now need to consider the effect of shot noise. This noise arises from the assumption that galaxies or particles are drawn at random from an underlying continuous field, but in any realisation, the density field at each point can only have 'one or zero status' – either there is a galaxy at position $\mathbf{x}$, or there is not – so if at $\mathbf{x}$ the probability, $p$ of having a particle is less than one, then

for an ensemble of realisations, while the mean number of particles at position $\mathbf{x}$ will be equal to $p$, this mean will have non-zero standard deviation given also by $p$.

In order to account for shot noise, it is convenient to use the approach adopted by Peebles, (1980) in which the cell of volume $V$ is divided into infinitesimal subvolumes, $\delta V_l$ with occupation number, $n_l = 0$ or 1, so that $\langle n_l^J \rangle = \langle n_l \rangle$. Using this notation, the number of particles in a volume $V$, $N(V)$, is given by:

$$N(V) = \sum_l n_l, \tag{2.38}$$

so $\langle N(V)^2 \rangle$ becomes:

$$\begin{aligned}
\langle N(V)^2 \rangle &= \left\langle \sum_l n_l \sum_m n_m \right\rangle \\
&= \sum_l \langle n_l^2 \rangle + \sum_{l \neq m} \langle n_l n_m \rangle \\
&= \sum_l \langle n_l \rangle + \sum_{l \neq m} \overline{N}(V)^2 \frac{\delta V_l \, \delta V_m}{V^2} \left[1 + \xi_{lm}\right] \\
&= \overline{N}(V) + \overline{N}(V)^2 \left[1 + \frac{1}{V^2} \int \xi_{lm} \, dV_m \, dV_l\right] \\
&= \overline{N}(V) + \overline{N}(V)^2 \left[1 + \overline{\xi}_2\right],
\end{aligned} \tag{2.39}$$

and

$$\left\langle \left[N(V) - \overline{N}(V)\right]^2 \right\rangle = \overline{N}(V) + \overline{N}(V)^2 \, \overline{\xi}_2. \tag{2.40}$$

If the particles come from a Poisson distribution, then $\overline{\xi}_2$ is zero, giving a shot noise contribution to the second moment, $m_2$ of $\overline{N}$. An estimate of $\overline{\xi}_2$ is therefore given by:

$$\overline{\xi}_2(R) = \left(m_2 - \overline{N}\right) / \overline{N}^2. \tag{2.41}$$

A similar analysis can be performed to obtain shot noise corrections for the higher order correlations, giving for $\overline{\xi}_3$ and $\overline{\xi}_4$:

$$\overline{\xi}_3(R) = \left(m_3 - 3m_2 + 2\overline{N}\right) / \overline{N}^3 \tag{2.42}$$

$$\overline{\xi}_4(R) = \left(m_4 - 3m_2^2 - 6m_3 + 11m_2 - 6\overline{N}\right) / \overline{N}^4. \tag{2.43}$$

### 2.2.1 Second order perturbation predictions

For power law spectra, an approximation for the higher order moments of a gravitationally evolved matter distribution can be obtained by solving the fluid equation 2.1 to

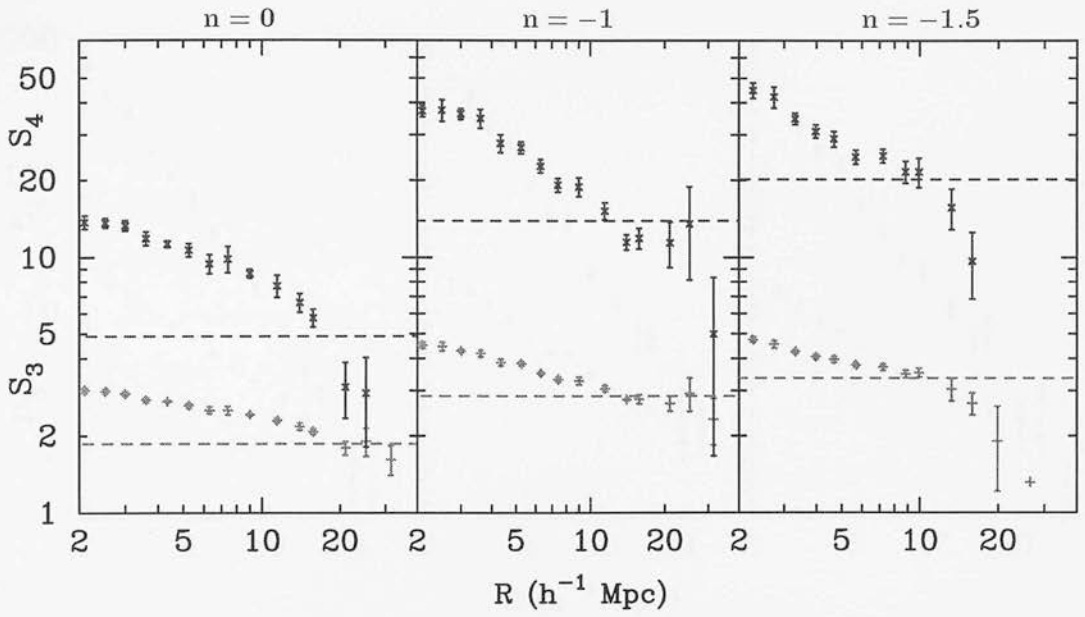


Figure 2.1: Moments of evolved Gaussian fields. Lower points denote hierarchical skewness, $S_3$, and upper points, hierarchical kurtosis, $S_4$. Dashed lines indicate the second order perturbation predictions for a field smoothed with a spherical top-hat. The left panel has a linear power spectrum spectral index of $n = 0.0$; centre panel $n = -1.0$; right $n = -1.5$.

second order in $\delta$. For mild gravitational evolution and smoothing with a spherical top hat, the hierarchical skewness and kurtosis are given by:

$$S_3 = \frac{34}{7} - (n+3) \tag{2.44}$$

$$S_4 = \frac{60712}{1323} - \frac{62}{3}(n+3) + \frac{7}{3}(n+3)^2, \tag{2.45}$$

(*e.g.* Juskiewicz *et al.* 1993, Bernardeau *et al.* 1995, Bernardeau 1994). Figure 2.1 shows the higher order moment results for simulations with spectral indices $n = 0$, $n = -1$, and $n = -1.5$, with the perturbation theory lines plotted. The equivalent dimensionless results are plotted in figure 2.2.

From figure 2.1, the perturbation theory predictions are clearly only valid for scales greater than $10\,h^{-1}$ Mpc for the $n = -1$, and $n = -1.5$ models, and for scales greater than about $20\,h^{-1}$ Mpc for the $n = 0$ model. On smaller scales, a scale dependence develops. This has been explored by Colombi *et al.* (1997) who have found that one can greatly improve the perturbation theory predictions if one uses an effective spectral index, $n_{\rm eff}$, instead of the linear spectral index. $n_{\rm eff}$ is determined by measuring $S_3$, and

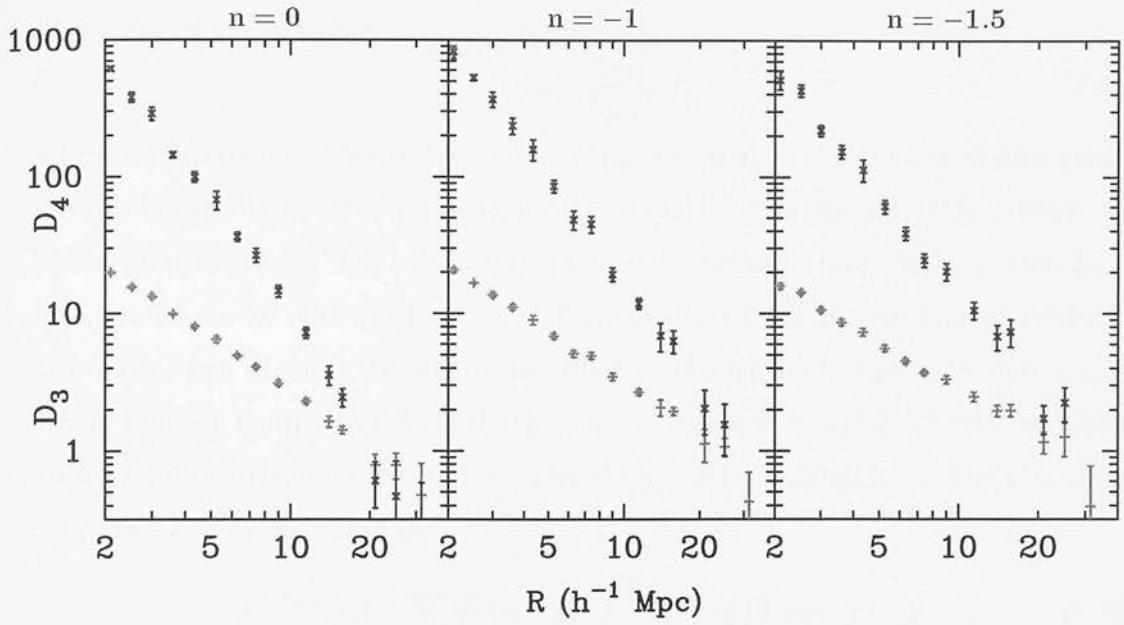


Figure 2.2: Moments of evolved Gaussian fields. Lower points are for dimensionless skewness, ($D_3 \equiv \langle\delta^3\rangle/\sigma^3$), upper points are dimensionless kurtosis ($D_4 \equiv \langle\delta^4\rangle/\sigma^4$). Left panel has a linear power spectrum spectral index of $n = 0.0$, centre panel $n = -1.0$, right $n = -1.5$.

assuming that relation 2.44 is exact if $n$ is replaced by $n_{\rm eff}$. *i.e.*

$$n_{\rm eff} \equiv \frac{34}{7} - 3 - S_3^{\rm measured}. \tag{2.46}$$

$n_{\rm eff}$ can then be used instead of $n$ to determine the higher order moments (*e.g.* $S_4$, and $S_5$) to good accuracy.

## 2.3 Measuring the power spectrum

The power spectrum has been calculated for the work in this section using a method based on that described in Peacock & Nicholson (1991), with the refinements included in Peacock & Dodds (1996; PD96). The particles are binned onto a grid and fast Fourier transformed. The fast Fourier transform, or FFT relates directly to a direct Fourier transform of the binned particles if the box is taken to be periodic. The periodicity of the box means that the density distribution can be represented by a Fourier series, in which a finite set of Fourier modes can completely describe the density distribution.

These modes are given by:

$$k_i = \frac{2\pi i}{L_{\rm box}}, \tag{2.47}$$

where the maximum value of $k_i^{\rm max} = \pi {\rm n_g}/L_{\rm box}$ where $\rm n_g$ is the number of grid points used to bin the data. $k_i^{\rm max}$ probes scales the size of the grid spacing. This is known as the Nyquist frequency. The largest scale that can be probed is given by $k_{\rm box} = 2\pi/L_{\rm box}$. The Fourier modes obtained from an FFT are different from the true Fourier modes in two ways, both of which are due to the effect of binning up the particles onto a grid before they are Fourier transformed. These are discussed in Baugh & Efstathiou, (1994, BE94), and in PD96, but we shall consider them in a little detail here. The binning of a function can be expressed as:

$$\delta^{\rm binned}\left({\rm x}_i\right) = \sum_i \delta^{\rm D}\left({\rm x} - {\rm x}_i\right) \int_{-\infty}^{\infty} \delta^{\rm true}\left({\rm y}\right) T\left({\rm x} - {\rm y}\right) d^3{\rm y}, \tag{2.48}$$

where $T$ is a top hat of width $b$, and ${\rm x}_i = b\,{\rm Int}\left({\rm x}/b\right)$. This is a convolution of the true modes with a top hat, multiplied by a three dimensional comb of delta functions. In the limit of small $k$, equation 2.48 in Fourier space becomes:

$$\delta^{\rm binned}\left({\rm k}\right) \simeq \delta^{\rm true}\left({\rm k}\right) \frac{\sin\left(bk_x/2\right)}{bk_x/2} \frac{\sin\left(bk_y/2\right)}{bk_y/2} \frac{\sin\left(bk_z/2\right)}{bk_z/2}. \tag{2.49}$$

To second order in $b$ the binned power spectrum can thus be approximated as:

$$P^{\rm binned}\left(k\right) \simeq P^{\rm true}\left(k\right) \left(1 - \frac{b^2k^2}{12}\right). \tag{2.50}$$

The discreteness of the bin centres represented here by the comb of delta functions leads to an aliasing effect between the power modes for small scales, resulting in a reduction of the measured power. An analytic expression for the effect this has on power law power spectra is given in BE94, which shows that for power laws with spectral indices between 0 and $-2$, the effect increases with $k$-number to $k_g$ ratio, where $k_g$ is the wavenumber on the scale of the smallest grid division. The maximum ratio considered here is about 0.1:1, for which the measured power spectrum is expected to be lower than observed power by a factor of around 4%.

When using the Fast Fourier Transform, the smallest scales one can probe are determined by the number of cells in the Fourier mesh. If the number of mesh cells is L, then the smallest scale that can be probed using Fast Fourier techniques is the Nyquist frequency,

$k_{\rm Ny} = \pi/b$ where $b$ is the width of the smallest grid cell. So, to probe scales smaller than $k_{\rm Ny}$, the number of grid cells on the mesh needs to be increased. For three dimensional FFTs, increasing the resolution of the mesh quickly runs into computer time and memory limitations. A neat way to obtain modes for the smaller scales without encountering computer memory problems was proposed by Jenkins *et al.* (1998). The trick is to fold the box into a smaller sub-box, making use of $\exp(\mathrm{ik}\cdot\mathrm{r} + \mathrm{i}2\pi) = \exp(\mathrm{ik}\cdot\mathrm{r})$. Particles are translated according to $R' \rightarrow R - 2\pi n/\mathrm{k_{box}}$ where $n$ is an integer. Now, since the $k$-modes in an FFT are given by $mk_{\rm box}$ (see equation 2.47), then:

$$\begin{aligned} \exp[i\mathbf{k}\cdot\mathbf{R}'] &= \exp\left[i\mathbf{k}\cdot\mathbf{R} - \frac{2\pi i n}{k_{\rm box}} m k_{\rm box}\right] \\ &= \exp[i\mathbf{k}\cdot\mathbf{R}]. \end{aligned} \tag{2.51}$$

This allows the simulation volume to be compressed into a smaller box which, when Fourier transformed will give the same result as the Fourier transform of the larger box (although with a smaller number of modes). This allows much smaller scales to be probed without meeting the computer memory limits, and without bringing down the power estimate significantly as a result of aliasing.

The Fourier density modes, $\delta_{\mathbf{k}_i}$, are given by:

$$\delta_{\mathbf{k}_i} = \frac{1}{N}\sum_{j=1}^{N} e^{i\mathbf{k}_i\cdot\mathbf{x}_j}, \tag{2.52}$$

where $\mathbf{x}_j$ is the $j$-th particle's position, and $N$ is the total number of particles. The normalisation in equation 2.52 differs from the standard normalisation of the FFT, which generally divides the sum of exponentials by the square root of the total number of bins used to grid up the data. In the limit of infinite numbers of particles, the power spectrum can be written as:

$$P'(k) = \frac{1}{m}\sum_{i=1}^{m} |\delta_{\mathbf{k}_i}|^2, \tag{2.53}$$

where $m$ is the number of $\mathbf{k}$ modes in reciprocal space with amplitude k.

As we saw in section 2.2, for a finite number of particles representing a continuous distribution, shot noise contributes to the error in one's estimate of the variance, or in this case the power spectrum. This contribution can be calculated by substituting

equation 2.52 into equation 2.53, giving:

$$P'(k) = \frac{1}{m}\sum_{i=1}^{m}\frac{1}{N^2}\sum_{l,j} e^{i\mathbf{k}_i\cdot\mathbf{x}_j}e^{-i\mathbf{k}_1\cdot\mathbf{x}_l}. \tag{2.54}$$

Clearly, when $\mathbf{x}_l = \mathbf{x}_j$, irrespective of the distribution of particles, there is a contribution to the power. In the absence of clustering, then the power spectrum is purely shot noise, which is given by:

$$P^{\text{shot}}(k) = \frac{1}{m}\sum_{i=1}^{m}\frac{1}{N} = \frac{1}{N}. \tag{2.55}$$

It is worth noting here that initial conditions which are set up by limiting each grid cell to have one particle have substantially less noise than the Poisson shot noise prediction. For later time outputs, the Poisson shot noise model becomes a reasonable estimate of the noise, since the particles have by then moved sufficiently far from their initial grid positions to erase the structure of the grid. The particle position can then be treated as being influenced by a random Poisson process (and of course the clustering pattern of the simulation). Including the effects of binning and shot noise, the power spectrum is estimated to be:

$$P(k) = \frac{P'(k) - \frac{1}{N}}{1 - \frac{b^2k^2}{12}}. \tag{2.56}$$

For the work in this and the following chapter, we shall use the dimensionless form of the power spectrum (see also Chapter 1):

$$\Delta^2(k) \equiv \frac{d\sigma^2}{d\ln k} = V\frac{P(k)\,k^3}{2\pi^2}, \tag{2.57}$$

where $\sigma^2(k)$ is given by:

$$\sigma^2(k) = \int_0^k 4\pi V k^2 P(k)\,\mathrm{d}k. \tag{2.58}$$

## 2.4 Non-linear to linear power mapping

In this section, we look at a fitting formula that predicts the non-linear power spectrum given an input linear power spectrum. The idea that non-linear clustering is a unique function of the linear clustering amplitude was originally conceived by Hamilton *et al.* (1991; HKLM). In HKLM the authors interpolate between the growth of density fluctuations in the linear regime where $\Delta^2_{\text{NL}} \propto a^2$, and the clustering in the highly non-linear

regime, where clustering has become stable, giving $\Delta^2_{\rm NL} \propto a^3$. (The stable clustering scaling comes from considering the non-linear correlation function as a measure of the ratio of the excess density of galaxies compared with the background density. Since the proper size of the clusters does not evolve in the stable clustering regime, the excess density is constant. The background density decreases as $a^{-3}$ due to the expansion, so the non-linear correlation function and power spectrum evolve as $a^3$.) HKLM postulate that the clustering in the transitional region between linear growth and stable clustering is a function only of the linear clustering on a specified larger scale, where the mapping between the non-linear and linear scales ($r_{\rm L} \rightarrow r_{\rm NL}$) is dependent on the volume averaged non-linear correlation function:

$$r_{\rm L} = [1 + \overline{\xi}_{\rm NL}\,(r_{\rm NL})]^{1/3} r_{\rm NL}, \tag{2.59}$$

and the mapping itself is determined empirically from N-body simulations. This method gives a locus from which, for initially power law models, the volume averaged non-linear correlation function can be described by a fitting formula which is dependent only on the amplitude of the linear correlation function.

This formalism has subsequently been adapted to predict non-linear power spectra, and refined to take into account the effect of different power law slopes of the linear power spectrum, (Peacock & Dodds 1994, 1996 (PD94, PD96); Jain, Mo, & White 1995). PD96's fitting formula also takes open and $\Lambda$ models into account.

Here, we outline the formalism described in PD96. The general idea is that the non-linear power spectrum, $\Delta^2_{\rm NL}$ on a particular scale, $\rm k_{NL}$ can be described as a mapping from the linear power spectrum $\Delta^2_{\rm L}$ on a larger scale $\rm k_L$ which is set by a second mapping. The mapping between the non-linear and linear power spectra can be written as:

$$\Delta^2_{\rm NL}\,(k_{\rm NL}) = f_{\rm NL}\left[\Delta^2_{\rm L}\,(k_{\rm L})\right], \tag{2.60}$$

where the non-linear scale is related to the linear scale by:

$$k_{\rm NL} = \left[1 + \Delta^2_{\rm NL}\,(k_{\rm NL})\right]^{\frac{1}{3}} k_{\rm L}. \tag{2.61}$$

The mapping between scales is to account for the decrease in size of over-dense clumps as they collapse, and it is essentially the $k$-space analogue of the real space mapping in

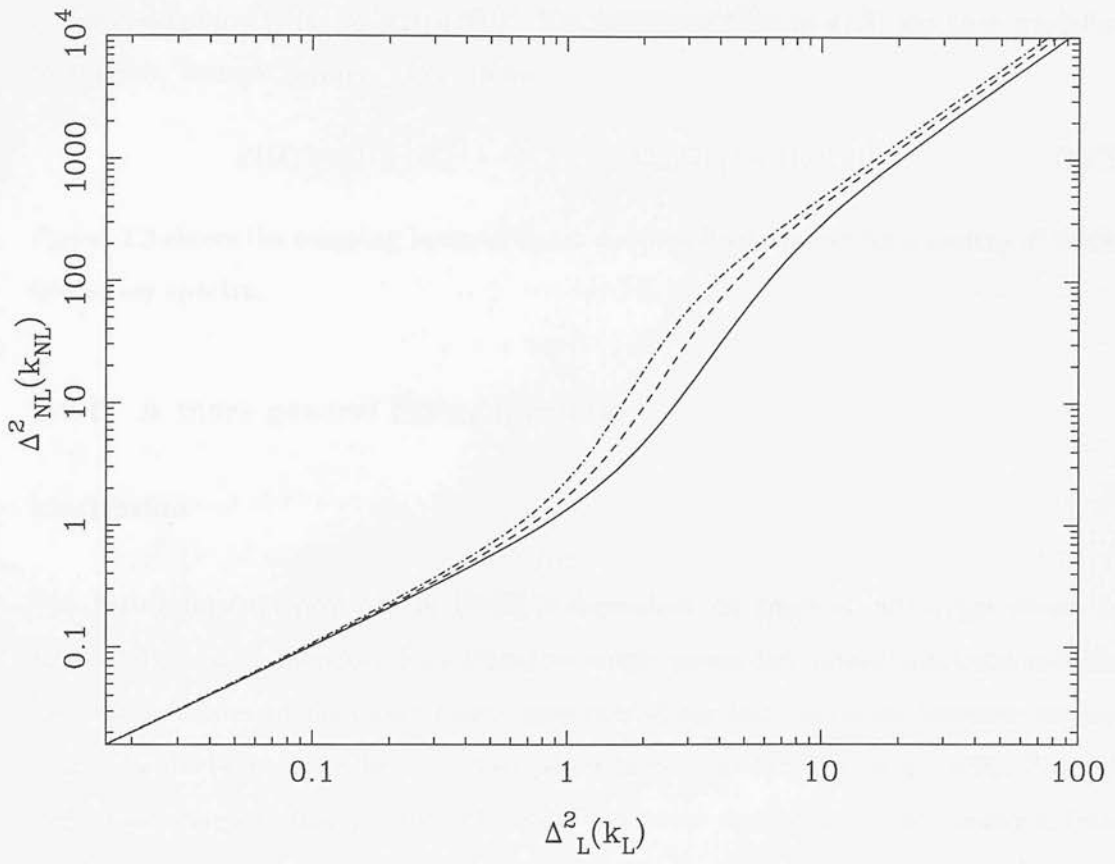


Figure 2.3: The non-linear power as a function of linear power for a variety of spectral indices, taken from the fitting formula in equation 2.62 using $\Omega_m = 1$, $\Omega_v = 0$. Spectral indices are: $n = 0$ solid; $n = -1$ dashed; $n = -1.5$ dot-dashed.

equation 2.59. The fitting formula between linear and non-linear power, $f_{\rm NL}$ is deduced empirically from N-body simulations – initial conditions with power law linear power spectra of a variety of spectral indices are evolved into the highly non-linear regime, and the locus that describes the mapping between the linear and non-linear power is fitted for. In PD96, this locus is given by:

$$f_{\rm NL}\left(x\right) = x\left[\frac{1 + B\beta x + \left[Ax\right]^{\alpha\beta}}{1 + \left(\left[Ax\right]^{\alpha} g^3\left(\Omega\right) / \left[Vx^{1/2}\right]\right)^{\beta}}\right]^{1/\beta}, \tag{2.62}$$

where $x \equiv \Delta^2_{\rm L}\left(k_{\rm L}\right)$, and the non-linear power spectrum on a scale $k_{\rm NL}$ is given by $f_{\rm NL}\left(x\right)$. $A, B, \alpha, \beta$, and $V$ are parameters that depend on the spectral index of the linear power spectrum, $n$. They all take the functional form $y\left(1 + n/3\right)^z$, where $y$, and $z$ are constants specific to each of the parameters $A, B, \alpha$, and $\beta$. $g\left(\Omega\right)$ is a density dependent growth factor which describes the suppression of the linear growth of the

power spectrum: $\Delta_{\rm L}^2(k) \propto [a(t)\, g(\Omega)]^2$. The functional form of $g(\Omega)$ has been modelled by Carroll, Press & Turner (1992) to be:

$$g(\Omega) = \frac{5}{2}\Omega_{\rm m}\left[\Omega_{\rm m}^{4/7} - \Omega_{\rm v} + (1+\Omega_{\rm m}/2)\,(1+\Omega_{\rm v}/70)\right]^{-1}. \qquad (2.63)$$

Figure 2.3 shows the mapping between linear and non-linear power for a variety of power law power spectra.

### 2.4.1 A more general fitting formula

#### Motivation

The fitting formula provided in PD96 is dependent on spectral index, (as shown in figure 2.3), and is therefore best suited to single power law power spectrum models. Current estimates of the linear power spectrum of our local universe, however suggest that it could be a break between two power laws (*e.g.* Maddox *et al.* 1996, Peacock 1997, Gaztañaga & Baugh 1998). In order to obtain the linear power spectrum from non-linear data using the PD96 formalism, an iterative process is required in which one guesses a tangential effective spectral index for the linear power spectrum at $k = k_{\rm L}/2$, and uses this to obtain a first estimate for the linear power spectrum. One can find out how well this linear spectrum has been estimated by winding the process forward to find the non-linear power expected from the linear spectrum estimate. The tangential spectral index guess can then be refined, and the process iterated to find a stable result. The stability of the linear power prediction also relies on the local spectral index not approaching $n = -3$, for which the PD96 mapping blows up. Ideally one would like to have a fitting formula which is independent of spectral index, so that the linearisation process is independent of the linear power spectral shape, and so that models with rapidly varying spectral indices, or non-monotonic spectra can be considered.

In the next section a refined method is presented which is substantially less dependent on the spectral index of the linear power spectrum, and so allows easier determination of linear power spectra from their non-linear counterparts. It is found to be very successful for mapping between smoothly varying power spectra, with no iteration or assumption

about the form of the spectral index required. It has also been applied to power spectra containing features, for which in detail it performs less well.

### Method

This new method was motivated by the observation that for shallower linear power spectra (*i.e.* with a more negative spectral index), the amplitude of the non-linear power is greater for a given amplitude of the linear power spectrum. This can be seen by looking at figure 2.3, where for a given linear power value on the x-axis, the non-linear power is greater, the more negative the spectral index. This led to the idea that perhaps the amplitude of the non-linear power spectrum on a particular scale is influenced by the power on a range of scales larger than the one in question. In particular that it is the integrated power on larger scales that determines the amplitude of the non-linear power on a given scale.

This idea can be formalised by hypothesising that the integrated non-linear power up to a wavenumber $k_{\rm NL}$ is a function purely of the integrated linear power up to $k_{\rm L}$, where $k_{\rm L}$ is a known function of $k_{\rm NL}$, *i.e.*

$$\int^{k_{\rm NL}} \Delta^2_{\rm NL}(k)\,\frac{{\rm d}k}{k} = f\left[\int^{k_{\rm L}} \Delta^2_{\rm L}(k)\,\frac{{\rm d}k}{k}\right]. \tag{2.64}$$

The relationship between linear and non-linear wavenumbers, $k_{\rm L}$, and $k_{\rm NL}$ can take a variety of forms, so long as it reflects the trend that clustering moves to smaller scales in the non-linear regime, and that the more clustering there is on a given linear scale, the smaller the non-linear scale to which the clustering is mapped. The choice of $k_{\rm NL}(k_{\rm L})$ relationship does however affect the functional form of the relationship between the integrated non-linear power, and the integrated linear power, and it also changes the level of spectral index dependence in the mapping. A convenient possible option for relating the linear scales to the non-linear scales is, by analogy with the PD96 method:

$$k_{\rm NL} = \left[1 + \Delta^2_{\rm NL}(k_{\rm NL})\right]^{\frac{1}{3}} k_{\rm L}. \tag{2.65}$$

The above relationship (equation 2.65) is useful for obtaining the linear power from the non-linear power spectrum, but inconvenient if one wants to find the non-linear from the linear power. This is because in order to determine the non-linear power, one

needs to differentiate its integrated form, and to do this one needs to know $k_{\rm NL}$ for each $\int \Delta^2_{\rm NL} {\rm d}k/k$. If $k_{\rm NL}$ is itself dependent on $\Delta^2_{\rm NL}$, then one is left needing to solve an integral equation for the non-linear power. A better option for this process is:

$$k_{\rm L} = \left[1 + \Delta^2_{\rm L}\left(k_{\rm L}\right)\right]^{-\frac{1}{3}} k_{\rm NL}. \tag{2.66}$$

Another option for the linear to non-linear $k$-relation is to use:

$$k_{\rm L} = \left[1 + \int \Delta^2_{\rm L}\left(k\right) \frac{{\rm d}k}{k}\right]^{-\frac{1}{3}} k_{\rm NL}, \tag{2.67}$$

or

$$k_{\rm L} = \left[1 + \int \Delta^2_{\rm NL}\left(k\right) \frac{{\rm d}k}{k}\right]^{-\frac{1}{3}} k_{\rm NL}. \tag{2.68}$$

While relations 2.68 and 2.67 produce a larger spectral dependence than using equation 2.66 or 2.65, they will prove useful when we come to consider non-monotonic power spectra later on. The locus for each of these $k$-relations is shown in figure 2.4.

The top panels in figure 2.4 show that the integrated power loci using relations 2.65 and 2.66 are only very weakly dependent on spectral index. Compare this with figure 2.3, which has a larger spectral index dependence. These curves can be well described by a parametric form given by:

$$f\left(x\right) = x\left[\frac{1 + bex + \left(ax\right)^{de}}{1 + g^3\left(\Omega\right)\left[\left(ax\right)^d / \left(c\sqrt{x}\right)\right]^e}\right]^{\frac{1}{e}} \tag{2.69}$$

where parameters $a, b, c, d, \& \ e$ take the form:

$$a = x_i\left(1 + y_i n\right). \tag{2.70}$$

These parameters are summarised in table 2.1.

The procedure for using these loci to obtain the non-linear power from the linear power is as follows:

(1) Find the integral of the linear power as a function of $k$. *i.e.*

$$\int_0^{k_j} \Delta^2_{\rm L}\left(k\right) \frac{{\rm d}k}{k} \simeq \sum_{i=1}^{i=j} \Delta^2_{\rm L}\left(k_i\right) \frac{\Delta k_i}{k_i} \tag{2.71}$$

(2) Choose which $k$ mapping to use. For monotonic power spectra going from linear to non-linear the best relation to use is equation 2.66

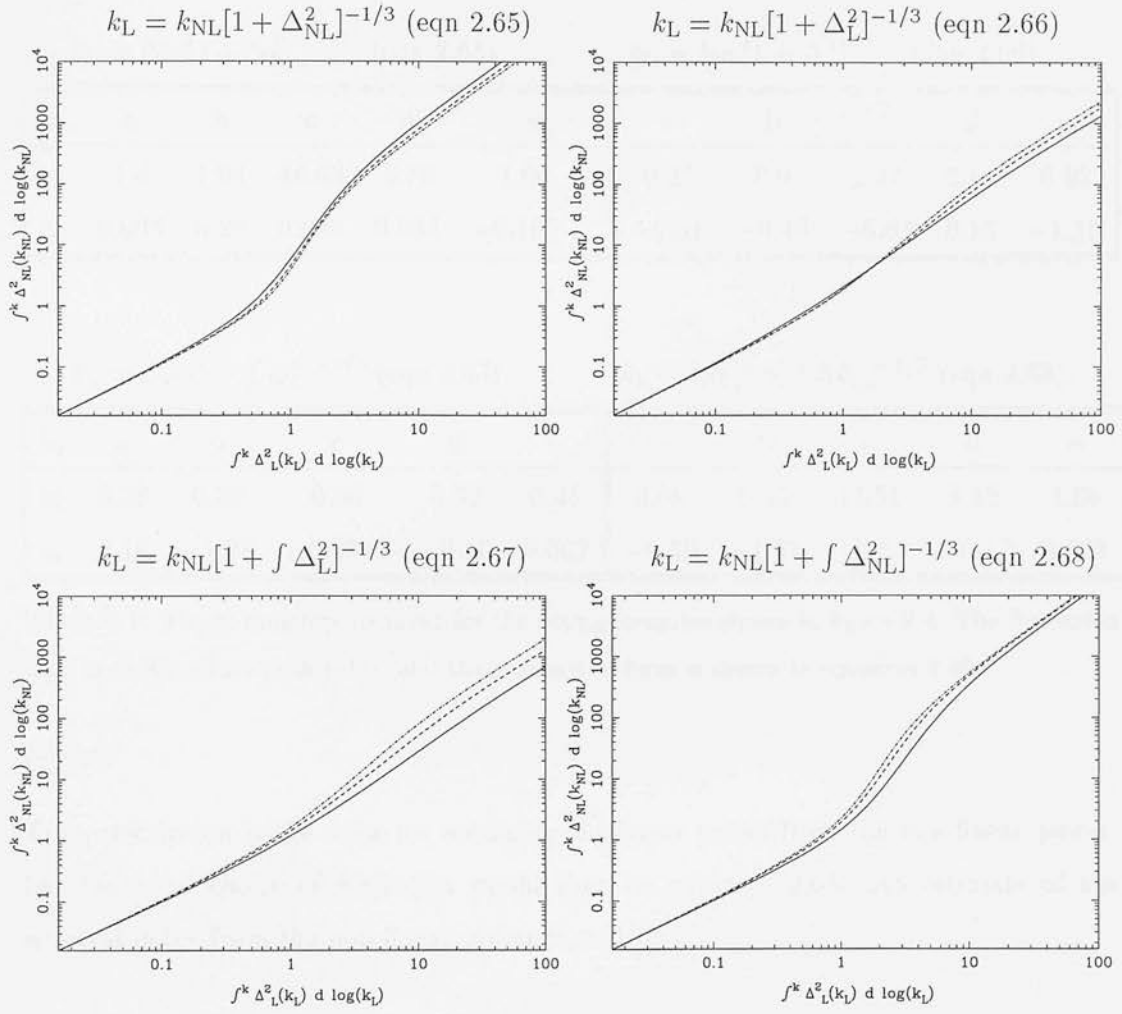


Figure 2.4: Loci for integrated power mappings. Each panel shows a different $k_{\rm L}$ to $k_{\rm NL}$ relationship. The top left uses equation 2.65; top right equation 2.66; bottom left equation 2.67; and bottom right equation 2.68.

(3) Determine $\int \Delta^2_{\rm NL}\,(k)\,{\rm d}k/k$ by applying the function, $f$ to the result from $\int \Delta^2_{\rm L}\,(k)\,{\rm d}k/k$. For the best accuracy, this requires a knowledge of the tangential spectral index, $n_j$ of $\Delta^2_{\rm L}$ at that $k_{\rm L}$-value. This can be approximated as:

$$n_j \simeq \left[\frac{\log\ \Delta^2_L\,(k_{j-1}) - \log\ \Delta^2_L\,(k_{j+1})}{\log\ k_{j-1} - \log\ k_{j+1}}\right] - 3. \qquad (2.72)$$

For relation 2.66, a crude determination is all that is needed.

(4) For each value of $\int \Delta^2_{\rm NL}$ assign a non-linear wavenumber $k_{\rm NL}$ using equation 2.66.

(5) Differentiate $\int \Delta^2_{\rm NL}$ with respect to $k_{\rm NL}$, to obtain the prediction for the non-linear

$k_{\rm L} = k_{\rm NL}[1+\Delta^2_{\rm NL}]^{-1/3}$ (eqn 2.65) $\quad$ $k_{\rm L} = k_{\rm NL}[1+\Delta^2_{\rm L}]^{-1/3}$ (eqn 2.66)

| $n_i$ | a | b | c | d | e | a | b | c | d | e |
|---|---|---|---|---|---|---|---|---|---|---|
| $x_i$ | 1.4 | 1.94 | 18.63 | 3.78 | 1.06 | 0.27 | 0.9 | 1.27 | 2.16 | 0.92 |
| $y_i$ | 0.008 | 0.22 | 0.049 | 0.033 | −0.155 | −1.81 | −0.49 | −0.87 | 0.18 | −1.55 |

$k_{\rm L} = k_{\rm NL}[1+\int \Delta^2_{\rm L}]^{-1/3}$ (eqn 2.67) $\quad$ $k_{\rm L} = k_{\rm NL}[1+\int \Delta^2_{\rm NL}]^{-1/3}$ (eqn 2.68).

| $n_i$ | a | b | c | d | e | a | b | c | d | e |
|---|---|---|---|---|---|---|---|---|---|---|
| $x_i$ | 0.28 | 0.25 | 0.66 | 5.52 | 0.25 | 0.69 | 0.23 | 11.31 | 2.12 | 1.66 |
| $y_i$ | 0.18 | −1.28 | −0.0013 | −0.10 | 0.062 | −0.39 | −1.91 | −0.25 | −0.17 | 0.021 |

Table 2.1: The parameters required for the fitting formulae shown in figure 2.4. The $k$-relation used is shown above each table, and the parametric form is shown in equation 2.69.

power.

The prescription is the same for obtaining the linear power from the non-linear power, but the ideal choice of $k$-relation would then be equation 2.65. An estimate of the spectral index from the non-linear power is sufficient.

### How well does it work?

The formula has been tested on the results of some Virgo Consortium[1] N-body simulations (Jenkins *et al.* 1998; J98) which uses a 17 million particle, parallel AP$^3$M code (Pearce *et al.* 1995, Pearce & Couchman 1997). The new fitting formula was used to obtain the linear power spectra from the output power spectra of the $\tau$CDM, $\Lambda$CDM, and open CDM simulations from J98, and the non-linear power spectra were predicted from the linear power spectrum inputs for the simulations. Figures 2.5, 2.6, and 2.7 show the power predictions for each of the simulations ($\tau$CDM, $\Lambda$CDM, and open CDM respectively), as deduced from the integrated fitting formula procedure described above.

[1]The Virgo Consortium is an international collaboration whose aim is to carry out large N-body and N-body/gas-dynamic simulations of large-scale structure and galaxy formation using parallel supercomputers.

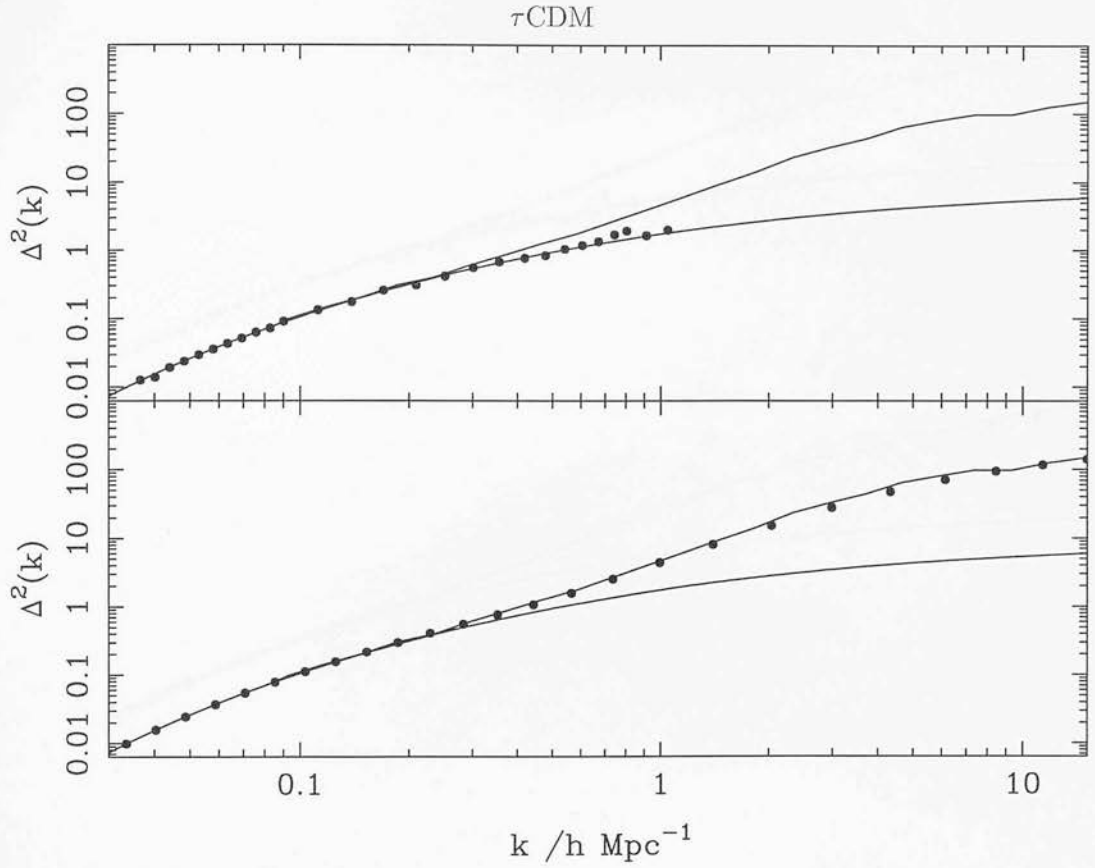


Figure 2.5: Comparison of the integrated fitting formula predictions for the evolution of power with the Virgo simulation results from J98. Solid lines are the linear and non-linear power spectra of a $\tau$CDM simulation from J98. The dots in the top panel show the fitting formula prediction for the linear power using J98's non-linear power spectrum as an input and equation 2.65 for the $k$-mapping. Dots in the lower panel are the fitting formula prediction for the non-linear power, starting from J98's linear input power spectrum, and using equation 2.68 for the $k$-mapping. $\Omega = 1$, and $\Gamma = \Omega_0 h = 0.21$.

There is clearly good agreement between the predictions and the simulation results.

### 2.4.2 Power spectra with features.

The fitting formula works well when applied to monotonic power spectra with smoothly varying spectral index, but how does it perform if the power spectrum contains kinks, or is not monotonic? An example of where this might be of interest is to model the non-linear power behaviour in a predominantly baryonic universe (see Chapter 1 section 1.5 on transfer functions) where the linear power oscillates, reflecting the essentially

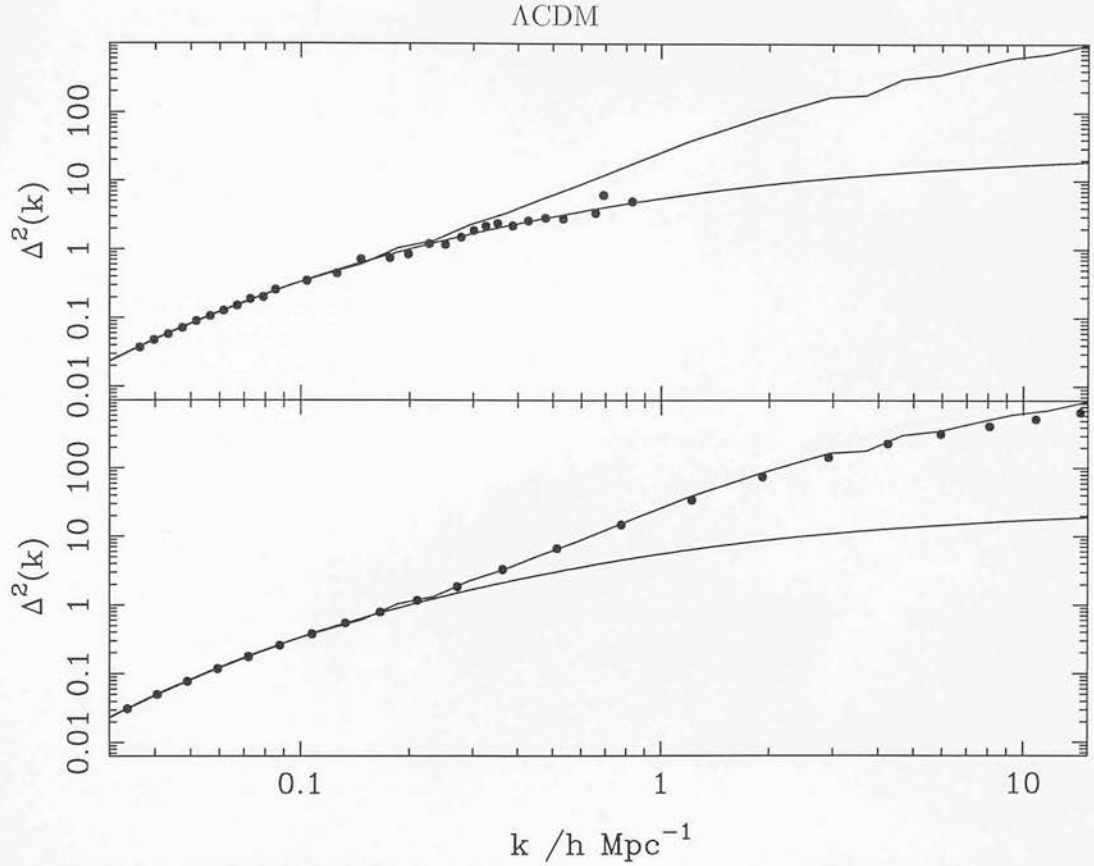


Figure 2.6: Solid lines are the linear and non-linear power spectra of a ΛCDM simulation from J98. The dots in the top panel show the fitting formula prediction for the linear power using J98's non-linear power spectrum as an input and equation 2.65 for the $k$-mapping. Dots in the lower panel are the fitting formula prediction for the non-linear power, starting from J98's linear input power spectrum, and using equation 2.68 for the $k$-mapping. $\Omega = 0.3$, $\Lambda = 0.7$, and $\Gamma = \Omega_0 h = 0.21$.

undamped oscillations of the initial matter distribution.

The spectra considered here are essentially modulated versions of smooth power laws, or CDM type spectra ($\Delta^2_{\rm smooth}(k)$). They have been created by taking the smooth function and multiplying it by a cosine based function so that the resultant power spectrum is given by:

$$\Delta^2_{\rm L}(k) = \Delta^2_{\rm smooth}(k)\left[1 + a\cos^2\left[\frac{\pi}{2}\frac{\log(k)}{o_{sc}}\right]\right], \tag{2.73}$$

where $a$ and $o_{sc}$ are adjustable parameters, and for power law models

$$\Delta^2_{\rm smooth}(k) \propto k^{n+3}. \tag{2.74}$$

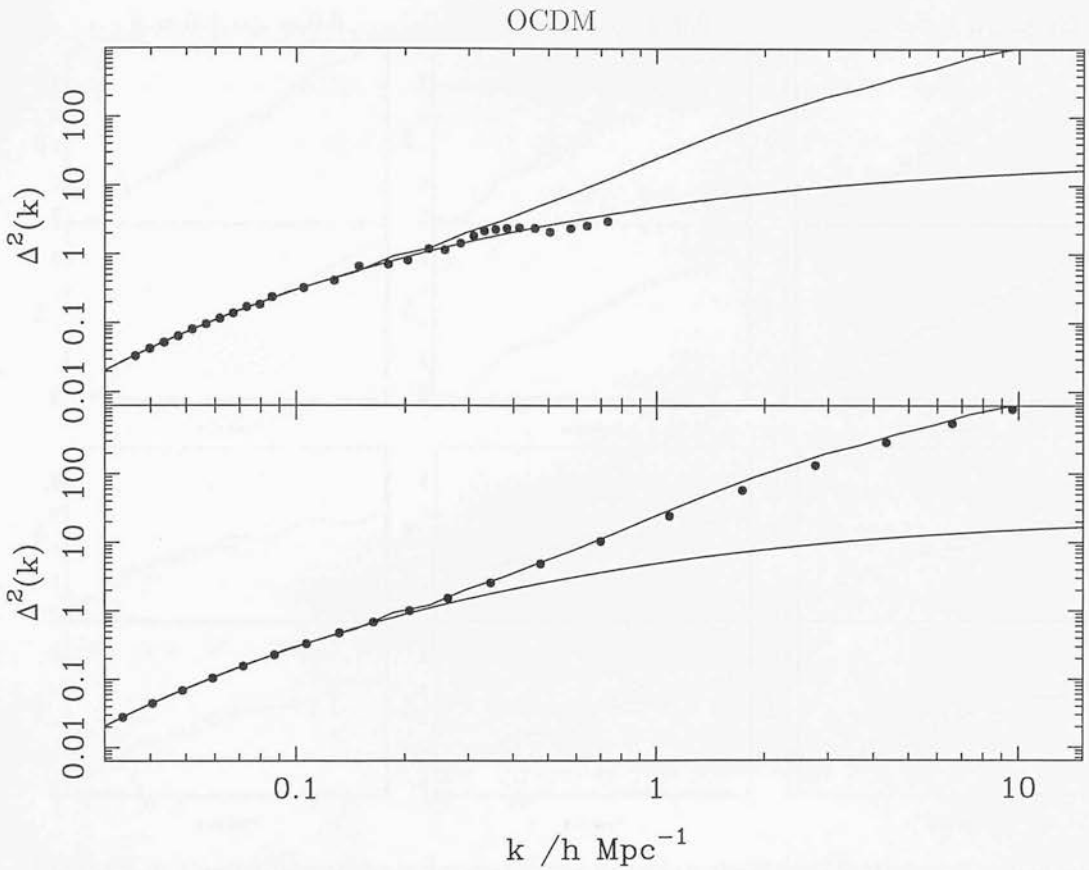


Figure 2.7: Solid lines are the linear and non-linear power spectra of an open CDM (OCDM) simulation from J98. The dots in the top panel show the fitting formula prediction for the linear power using J98's non-linear power spectrum as an input and equation 2.65 for the $k$-mapping. Dots in the lower panel are the fitting formula prediction for the non-linear power, starting from J98's linear input power spectrum, and using equation 2.68 for the $k$-mapping. $\Omega = 0.3$, $\Lambda = 0$, and $\Gamma = \Omega_0 h = 0.21$.

The $k$-relation used for these predictions was equation 2.67 for linear to non-linear predictions, and equation 2.65 for the non-linear to linear predictions. The graphs in figure 2.8 show the predictions for linear and non-linear power using $n = 0$ and a CDM model for the smooth power spectra, with $a$ taking values 0.4, and 0.7 and $o_{sc} = 0.3, 0.6$. For linear to non-linear predictions, this method works best for steeper smooth spectra, and for a higher frequency oscillatory function, but in general the prediction preserves the oscillatory nature of the function, whereas the simulation quickly loses this effect. The non-linear to linear predictions perform less well still, again probably because features in the non-linear power spectrum are wiped out below a certain scale, giving a non-unique

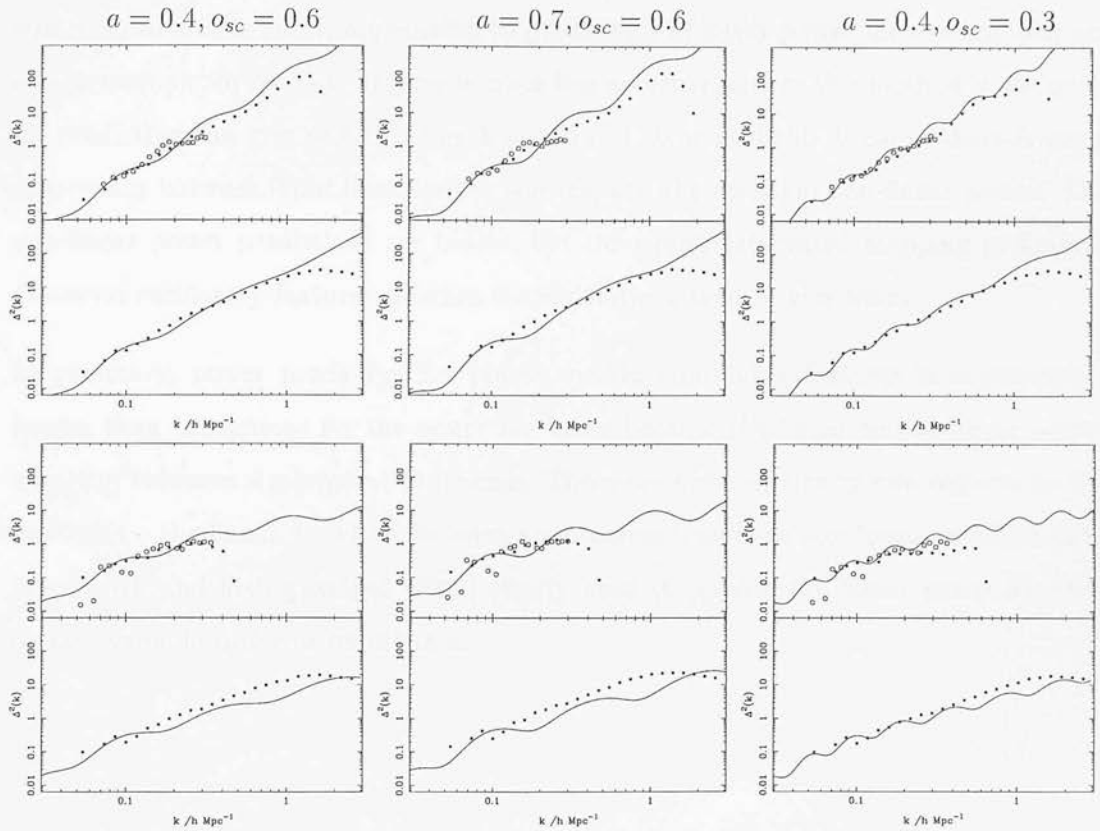


Figure 2.8: Comparison of the integrated fitting formula's predictions for the evolution of power with simulation results. Top panels are for non-linear to linear mapping, bottom are for linear to non-linear mapping. Each plot shows the actual power (filled dots), with its equivalent prediction (solid line for bottom panels, open circles for top panels). Left hand column uses parameters $a = 0.4, o_{sc} = 0.6$; middle column, $a = 0.7, o_{sc} = 0.6$; and right hand column $a = 0.4, o_{sc} = 0.3$. Top row uses a power law model with spectral index $n = 0$ for the underlying spectrum. Bottom row uses a CDM type initial smooth spectrum.

non-linear power spectrum for a given linear input.

### Concluding remarks

The integrated power mapping described above can be a useful tool for predicting the linear power spectrum for smoothly varying power spectra, since it is much less sensitive to the spectral index of the linear power spectrum than the PD96 formalism, and so no iteration is required to find a stable result. It also does not blow up for spectral indices of $n \simeq -3$, and so could be used to determine whether the linear power spectrum

was monotonic. However, application to predictions of linear power for spectra that are non-monotonic, or contain features is much less accurate, and so this method is not good for predicting the precise form of such spectra. This is probably because there is some degeneracy between input linear power spectra, and the resultant non-linear power. The non-linear power predictions are better, but the simple integrated mapping procedure preserves oscillatory features whereas the simulations tend to lose them.

In summary, power prediction for power spectra containing features is considerably harder than predictions for the power law cases because the linear to non-linear power mapping becomes a many-to-one process. There are however clearly two regimes to the evolution – the linear, in which features are preserved, and the non-linear in which they are erased, and fitting recipes would clearly need to smooth the linear power above a certain value in order to reflect this.

# Chapter 3

# EVOLUTION OF NON-GAUSSIAN FIELDS

## 3.1 Introduction

### 3.1.1 Aims

One of the first questions to ask when considering the feasibility of primordial non-Gaussian fields is whether non-Gaussian fluctuations in density can evolve under gravitational collapse to produce clustering statistically similar to that observed today. Clearly this is likely to depend on the type of non-Gaussian field considered – for instance skew-positive fields are likely to produce non-linear structures earlier than skew-negative ones simply because they start off with more high density peaks.

If certain non-Gaussian fields can give rise to sensible looking clustering then we can go on to ask whether they evolve in the same way as Gaussian fields. If the evolution differs then could some characteristic of their evolution be used as a discriminator between Gaussian and non-Gaussian fields? (for example by examining the change in the clustering pattern with redshift). The nature of the density field's evolution is also important to determine whether there are scales over which non-Gaussian fluctuations might still be detectable – for example on large scales does the field still evolve linearly even after

very non-linear structures have formed on smaller scales?

This chapter addresses how to create a set of non-Gaussian fields of specified power spectrum and statistics, and then asks whether the evolution of the power spectrum in these non-Gaussian cases can be described by the fitting formula provided in Peacock & Dodds (1996), which was originally derived for the evolution of Gaussian fields.

### 3.1.2 Previous work in the area

Work on the evolution of non-Gaussian fields has taken two distinct approaches. The first approach has been theoretical – where perturbation predictions for the second, third and fourth order moments of the density field have been applied to initially non-Gaussian fields. The second approach has been an empirical one in which toy non-Gaussian models have been evolved through N-body simulations, and the resulting statistics compared with their Gaussian counterparts. Much of the work for both approaches has concentrated on the evolution of the skewness and kurtosis, with the aim of trying to place constraints on non-Gaussian models using existing galaxy clustering data.

**Theoretical predictions from second order perturbation theory.**

The evolution of the variance, $\sigma^2$, for non-Gaussian models was studied by Fry & Scherrer (1994; FS94), who found that for non-Gaussian fields the lowest order correction to $\sigma^2 \equiv \xi(0)$ is of order $\mathcal{O}(\delta_0^3)$, whereas for Gaussian evolution the lowest order correction is $\mathcal{O}(\delta_0^4)$. This difference results in higher (/lower) values of $\sigma^2$ for a given evolution timescale for initially skew positive (/negative) fields than their Gaussian counterparts.

FS94 also investigated the evolution of skewness into the weakly non-linear regime, and concluded that non-Gaussian fields have an additional contribution to the evolved skewness ($\langle \delta^3 \rangle$). There are three contributions in all. These are: (1) the linearly evolved primordial value $\propto \delta_0^3$, (2) a contribution from non-linear evolution which is the same as the contribution in Gaussian fields, ($\propto \delta_0^4$), and (3) an additional term also $\propto \delta_0^4$ which is dependent on the initial skewness and kurtosis of the distribution. They conclude that the initial skewness need not necessarily dominate the final skewness, and that for small initial skewness and kurtosis the final skewness would be expected to be comparable

with the Gaussian skewness prediction.

Chodorowski & Bouchet (1996) complement the work of FS94 by applying perturbation theory to the prediction of kurtosis given non-Gaussian initial conditions. Again, they find that the lowest order contribution to the kurtosis ($\langle\delta^4\rangle$) is one order less than for the weakly evolved Gaussian case, *i.e.* the lowest order contribution in the non-Gaussian case is $\mathcal{O}(\delta_0^5)$, and in the Gaussian case it is $\mathcal{O}(\delta_0^6)$.

Unfortunately both of these papers' results are for the unsmoothed 'moments at a single point', and so their exact predictions may not be observationally relevant. Gaztañaga & Fosalba (1997, GF97), however have recently filled this gap, producing a spherical collapse analysis of density evolution, which they have been able to apply to smoothed initially non-Gaussian fields. Their unsmoothed results agree well with the perturbation theory predictions of FS94, also finding the evolved non-Gaussian variance to be higher for positively skewed models. Their smoothed results, however introduce an interesting spectral index dependence that was not predicted by FS94. They find that the evolution of $\overline{\xi}_2^{\text{smoothed}}$ departs least from the Gaussian prediction when $n = -1$, so that spectral indices on either side of $n = -1$ show greater departures from the Gaussian prediction for a given non-Gaussian field.

### Empirical Work

Most of the N-body work in this field was carried out before the perturbation theory predictions for the quasi-linear evolution of Gaussian and non-Gaussian moments, so it is interesting to compare their results in the light of the theorists' predictions. The nature of previous empirical work has been to use methods similar to those reviewed in Chapter 2 to set up non-Gaussian initial conditions, and to evolve these using an N-body code. The clustering properties (such as skewness and correlation functions) have then been compared with observation and Gaussian N-body simulations.

Most of the non-Gaussian models considered have been generated by performing a local non-linear operation on a Gaussian field *e.g.* Gaztañaga & Mähönen 1996, GM96; Coles *et al.* 1993, CMLMM; Messina *et al.* 1992, MLMM; Moscardini *et al.* 1991, who all operate on the potential field, and Weinberg & Cole (1992), who operate on the density

field itself. They look mainly at CDM power spectra, considering fields with positive and negative skewness (*e.g.* $\chi^2$ and lognormal fields), and fields with high kurtosis, such as the convolution of two Gaussians.

**Skewness conclusions.** The skewness, $\langle\delta^3\rangle$ was found to increase with time for all models considered in CMLMM; they and MLMM suggested that initial skewness was the dominant factor influencing the skewness-variance relationship at late times. The calculations of FS94, however suggest that this is only one of three contributory factors, and that the kurtosis as well as the Gaussian contribution to the non-linear evolution are equally important.

GM96 examined a non-Gaussian texture model with excess skewness and kurtosis, and found that the hierarchical moments, $S_J \equiv \overline{\xi}_J/\overline{\xi}_2^{\,J-1}$ tended towards the Gaussian evolved models as the simulation evolved. This has shown good agreement with GF97's recent theoretical predictions for the non-Gaussian evolution in the quasi-linear regime. If skewness does indeed increase (CMLMM), while $S_3$ tends to decrease, then the variance must be increasing faster in initially skew models than in Gaussian models, and this suggests that the power spectrum may evolve differently according to initial skewness. These results are in line with the predictions of FS94, and GF97.

**Evolution of power.** The evolution of power is mentioned in Messina *et al.* (1992), who looked at models with CDM type power spectra, and found that skew positive models gave little power on large scales compared with the Gaussian model, whereas skew negative models gave more power on large scales than the Gaussian model. The findings of MMLM are corroborated by Weinberg & Cole (1992) who carefully normalised all their simulations to a $\sigma_8^{NL}$ of unity. They looked at power law models, and found that skew-negative models generally resulted in shallower correlation functions, and thus give either more power on large scales, or less on small scales depending on choice of normalisation.

In the light of the work by FS94, and the above findings, the normalisation of CDM type power spectra clearly requires some care – if one normalises all results to a non-linear value for $\sigma_8$, evolving the simulations for varying amounts of time, then one is likely to find a dearth of power for skew positive fields on large scales. If however all fields are

normalised to a given linear value for $\sigma_8$, and evolved for the same amount of time, the skew positive fields are likely to show more power on large scales than the skew negative fields.

The work mentioned above has been qualitative in the comparisons of the different non-Gaussian fields, making direct comparisons between the different pieces of work difficult. The work in this chapter compares the non-linear evolution of power in non-Gaussian models with the Gaussian derived fitting formula of Peacock & Dodds (1994, 1996) for scale free power spectra. This has the advantage of eliminating questions of normalisation, and enables direct comparisons with Gaussian predictions in the highly non-linear regime.

## 3.2 Evolution of non-Gaussian models into the non-linear regime

### 3.2.1 Non-Gaussian models considered

In order to compare the evolution of non-Gaussian fields with Gaussian fields, it is important to be able to reproduce the same linear power spectrum for each of the models considered. For some types of fields, this is not necessarily an easy task, since to create a field which is non-Gaussian in density fluctuations with a specified power spectrum, one needs a knowledge of the distribution the Fourier modes, and these do not relate simply to the real space probability density function. For the Gaussian case however, it is simple. If the density is specified by a Gaussian random field in real space, then the amplitude squared of the Fourier modes will have an exponential distribution with random phases. A class of non-Gaussian models that render themselves easy to produce are those which are local, non-linear transformations of a Gaussian density field:

$$\delta^{\mathrm{NG}}(\mathbf{r}) = f\left[\delta^{G}(\mathbf{r})\right]. \tag{3.1}$$

In these models the problem is reduced to finding the required input power spectrum for the Gaussian model which will yield the desired power spectrum in the non-Gaussian model once the transformation $f$ has been applied.

In three of the models we consider, $f$ is just a product of a Gaussian field, $\delta_1^G$ either with itself or with another uncorrelated Gaussian field, $\delta_2^G$. The Fourier modes of the resultant field are given by:

$$\delta_{\mathrm{k}}^{\mathrm{NG}} = \mathcal{F}.\mathcal{T}.\left[\delta_1\left(\mathbf{r}\right)\delta_2\left(\mathbf{r}\right)\right] = \delta_1\left(\mathrm{k}\right) \star \delta_2\left(\mathrm{k}\right) \tag{3.2}$$

as a result of the convolution theorem (see *e.g.* Kendall & Stuart 1969, and Chapter 1). This gives a power spectrum

$$\begin{aligned}\left\langle \delta^{\mathrm{NG}}\left(\mathrm{k_a}\right)\delta^{\mathrm{NG}}\left(\mathrm{k_b}\right)^{\star}\right\rangle &= \frac{1}{\left(2\pi\right)^6}\left\langle\left\{\delta_1\left(\mathrm{k_a}\right)\star\delta_2\left(\mathrm{k_a}\right)\right\}\left\{\delta_1\left(\mathrm{k_b}\right)\star\delta_2\left(\mathrm{k_b}\right)\right\}^{\star}\right\rangle \\ &= \int\left\langle \delta_1\left(\mathrm{k_a}-\mathrm{k'}\right)\delta_2\left(\mathrm{k'}\right)\delta_1\left(\mathrm{k_b}-\mathrm{k''}\right)^{*}\delta_2\left(\mathrm{k''}\right)^{\star}\right\rangle \mathrm{dk''dk'}. \end{aligned} \tag{3.3}$$

If $\delta_1^G$ and $\delta_2^G$ are independent, then the ensemble average in equation 3.3 can be written as:

$$\left\langle \delta_1\left(\mathbf{k_1}\right)\delta_2\left(\mathbf{k_2}\right)\delta_1\left(\mathbf{k_3}\right)^{*}\delta_2\left(\mathbf{k_4}\right)^{*}\right\rangle = \left\langle \delta_1\left(\mathbf{k_1}\right)\delta_1\left(\mathbf{k_3}\right)^{*}\right\rangle\left\langle \delta_2\left(\mathbf{k_2}\right)\delta_2\left(\mathbf{k_4}\right)^{*}\right\rangle, \tag{3.4}$$

and this becomes:

$$\begin{aligned}\left\langle \delta^{\mathrm{NG}}(\mathrm{k_a})\,\delta^{\mathrm{NG}}(\mathrm{k_b})^{\star}\right\rangle &= \int P_1(\mathrm{k_a}-\mathrm{k'})\,P_2(\mathrm{k_b}-\mathrm{k''})\,\delta^{\mathrm{D}}(\mathrm{k'}-\mathrm{k''})\,\delta^{\mathrm{D}}(\mathrm{k'}-\mathrm{k''}+\mathrm{k_a}-\mathrm{k_b})\,\mathrm{dk''dk'} \\ &\equiv \left(2\pi\right)^3 P^{\mathrm{NG}}\left(k\right)\delta^{\mathrm{D}}\left(\mathrm{k_a}-\mathrm{k_b}\right)\end{aligned} \tag{3.5}$$

using the definition of the power spectrum from Chapter 1. So in terms of the power spectra of the Gaussian fields used to create the non-Gaussian field:

$$P^{\mathrm{NG}}\left(k\right) = P_1\left(k\right) \star P_2\left(k\right). \tag{3.6}$$

Since the aim is to give the resulting non-Gaussian field a specified power spectrum, we need to be able to calculate the power spectra required for the Gaussian fields that are used to generate the non-Gaussian field. Suppose we have already specified the correlation function of field (2), then the correlation function of field (1), $\xi_1$, is obtained by Fourier transforming equation 3.6:

$$\xi_1\left(\mathbf{r}\right) = \frac{\xi^{\mathrm{NG}}\left(\mathbf{r}\right)}{\xi_2\left(\mathbf{r}\right)}, \tag{3.7}$$

so $P_1\left(k\right)$ is:

$$P_1\left(k\right) = \frac{1}{\left(2\pi\right)^3}\int \exp\left(-i\mathrm{k}\cdot\mathbf{r}\right)\frac{\xi^{\mathrm{NG}}\left(\mathbf{r}\right)}{\xi_2\left(\mathbf{r}\right)}d^3\mathbf{r}. \tag{3.8}$$

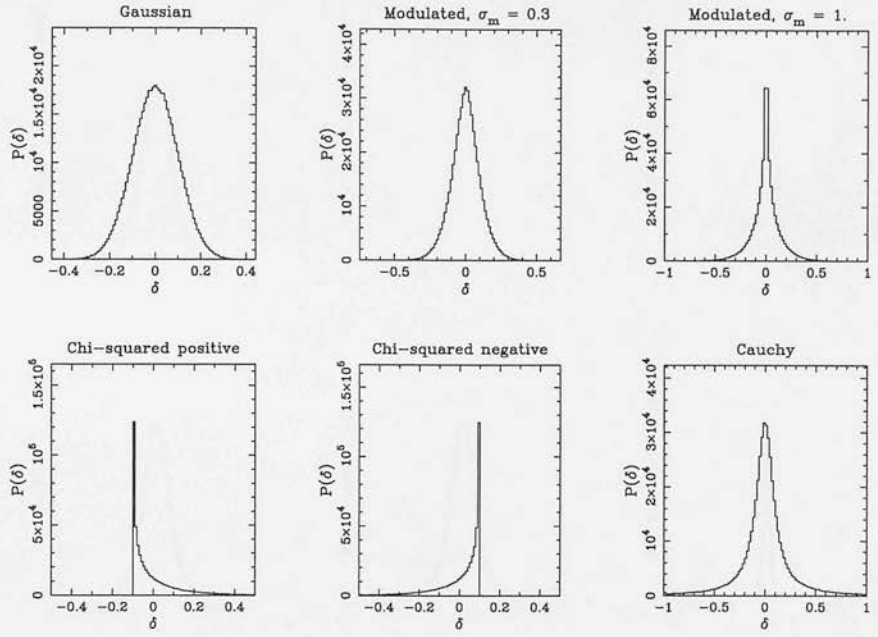


Figure 3.1: Probability density functions of density for the models described in section 3.2.1.

We can now go on to discuss the non-Gaussian fields that have been considered in this work. The three classes considered here are the modulated field, the $\chi^2$ field, and the Cauchy field, and their one point probability distributions are shown in figure 3.1. Their velocity distributions have also been plotted, and are shown in figure 3.2. We shall now consider how to generate these fields.

### Modulated field

The product of Gaussian model was suggested by Peebles (1983) as an attempt to reconcile the arguments about the idea that galaxies formed first, and subsequently grouped into clusters, rather than proto-clusters forming first, and then fragmenting. An argument in favour of the latter idea is that correlations in the density field are observed on vastly different scales. Peebles argues that this could in fact be due to the primaeval fluctuations existing over a large range of scales. One possibility for this distribution is a product of two Gaussian random fields model. A similar model has also been proposed by Yi & Vishniac (1993) as a multiple scalar field variant of inflation. Locally this field is Gaussian, but it has a varying amplitude on large scales, giving it a high kurtosis. It

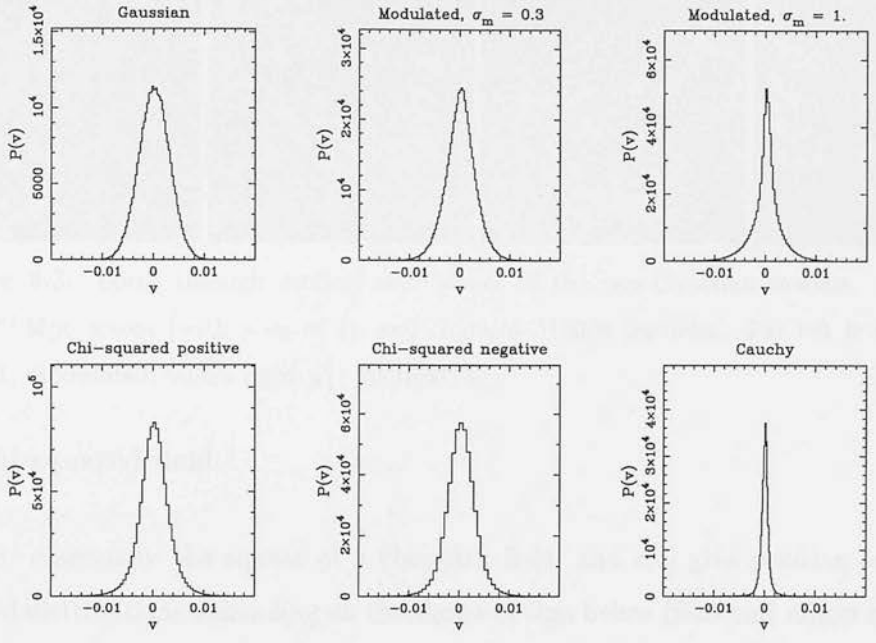


Figure 3.2: Probability density functions of velocity for the models described in section 3.2.1. The velocity considered is the component along the $x$-axis. Each model has been normalised to have a velocity standard deviation of 0.003 box units.

is generated by taking the product of two independent Gaussian fields:

$$\delta^{\mathrm{NG}}(\mathbf{r}) = {\delta_1}^G(\mathbf{r}) \left[1 + {\delta_2}^G(\mathbf{r})\right]. \tag{3.9}$$

This has a power spectrum:

$$P^{\mathrm{NG}}(\mathrm{k}) = {P_1}^G(k) + {P_1}^G(k) \star {P_2}^G(k). \tag{3.10}$$

For the modulating field, ${\delta_2}^G(\mathbf{r})$, we have chosen to use a white noise power spectrum with a Gaussian cut off:

$${P_2}^G(k) = \sigma_m^2 \exp\left[-(R_c\, k)^2\right], \tag{3.11}$$

where $R_c$ fixes the scale of the modulation and $\sigma_m$ can be chosen to give more or less deviation from a Gaussian field. The choice of power spectrum for the modulating field is to some extent arbitrary, although the Gaussian cut off has been chosen so that the modulating field introduces fluctuations only on large scales, resulting in a field that has large scale 'hot' and 'cold' patches, but which looks Gaussian on smaller scales. For the simulations shown, $\sigma_m = 1.0$, and $R_c = 30\,h^{-1}\,\mathrm{Mpc}$.

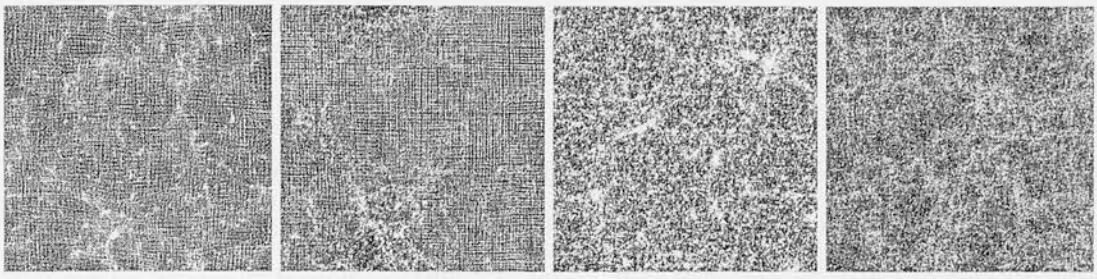

Figure 3.3: Slices through evolved simulations of the non-Gaussian models. Each box is $200\,h^{-1}$ Mpc across (with a $\sigma_8$ of 1), and contains 512000 particles. Far left is Cauchy; centre left, modulated; centre right $\chi^2_+$; far right, $\chi^2_-$.

### A Chi-squared field

This is essentially the square of a Gaussian field, and can give positive or negatively skewed distributions depending on the choice of sign below (plus and minus respectively)

$$\delta^{\mathrm{NG}}(\mathbf{r}) = \pm\left[{\delta_1}^{G}(\mathbf{r})^2 - \sigma^2\right]. \tag{3.12}$$

We shall refer to the positively skewed case as a '$\chi^2$ positive' distribution ($\chi^2_+$), and the negatively skewed case as a '$\chi^2$ negative' distribution ($\chi^2_-$). From equation 3.3, since this time $\delta_1 = \delta_2 \equiv \delta$, the ensemble average reduces to:

$$\begin{aligned}\langle \delta(\mathbf{k_a} - \mathbf{k'})\, \delta(\mathbf{k'})\, \delta(\mathbf{k_b} - \mathbf{k''})^{\star}\, \delta(\mathbf{k''})^{\star} \rangle \\ = \quad 2P(|\mathbf{k_a} - \mathbf{k'}|)\, P(k')\, \delta^{\mathrm{D}}(\mathbf{k'} - \mathbf{k''})\, \delta^{\mathrm{D}}(\mathbf{k_a} - \mathbf{k_b}),\end{aligned} \tag{3.13}$$

where the factor of two in the above equation comes from the fact that the four point ensemble average can be non-zero both when $\mathbf{k'} = \mathbf{k''}$, and when $\mathbf{k'} = \mathbf{k_b} - \mathbf{k''}$. This gives the following relation for the power spectrum of the $\chi^2$ field:

$$P^{\mathrm{NG}}(k) = 2P^{G}(k) \star P^{G}(k) \tag{3.14}$$

and so the chi-squared correlation function is given by:

$$\xi^{\mathrm{NG}}(r) = 2\,\xi^{\mathrm{G}}(r)^2. \tag{3.15}$$

The motivation for this model comes from Peebles (1997). In this paper, he proposes an isocurvature $\chi^2$-model to get structures forming earlier than in the standard CDM model. In this section we consider only power law models, and in section 3.3 we will examine Peebles' suggested model in greater detail.

### A Cauchy distributed field

This field was chosen because it has the property that the distribution of the average of many points in the field is also Cauchy distributed, (and is thus an exception to the Central Limit Theorem, see Chapter 1). The main motivation for this field comes from a paper by Taylor & Hamilton (1996), in which they deduce a prediction for the mildly non-linear power using the Zel'dovich approximation. In this paper, the mildly non-linear power is dependent on the probability density function of velocity differences in the field, which suggests that a field with a non-Gaussian velocity difference distribution should (under the Zel'dovich prediction) evolve differently from a Gaussian field. The Cauchy distribution was chosen to be sure of obtaining both a non-Gaussian velocity difference field, and the required input power spectrum. The densities have a Lorentzian one point distribution:

$$p(\delta) = \frac{1}{1+\beta^2\delta^2}. \tag{3.16}$$

The field has been generated by creating an incoherent velocity field with a Lorentzian distribution, which is then convolved with a smoothing function to produce the desired power spectrum for the density field. For this work, the power spectrum is chosen to be a power law, with spectral index $n = 0, -1$, or $-1.5$. Lorentzian distributed random variables, $V_i$ can be generated by:

$$V_i = \tan(\text{rand}) \, ; -\pi/2 < \text{rand} < \pi/2. \tag{3.17}$$

In order to obtain a power law power spectrum, the $k$-space velocities need to be multiplied by a smoothing function, $w(k)$, which is given by:

$$w(k) = k^{-n/2-1}. \tag{3.18}$$

So the $k$-space velocities become $V^{i\prime}_{\mathbf{k}} = V^i_{\mathbf{k}} w(\mathbf{k})$, and this yields a density power spectrum of spectral index $n$.

## 3.2.2 The simulations

An AP3M code was used to evolve the non-Gaussian models described above, and each model was given three different power law linear power spectra with spectral indices $n$,

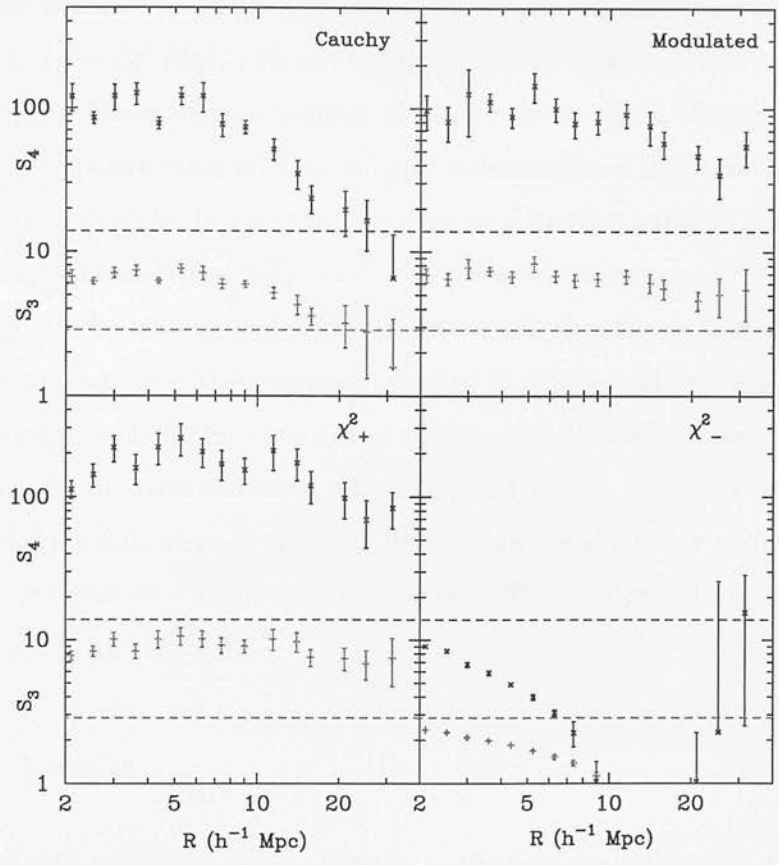


Figure 3.4: Hierarchical skewness (lower set of points on each panel) and kurtosis measurements (upper set) for the non-Gaussian fields used in the simulations. Top left is from a Cauchy field, top right from a modulated field, bottom left is from a $\chi^2_+$ field, and bottom right is $\chi^2_-$. All simulations here have spectral index $n = -1$. Dotted lines indicate second order perturbation theory predictions for a Gaussian simulation.

of 0, $-1$, and $-1.5$. The locus of the resulting non-linear power spectrum as it varied against the linear power spectrum was then plotted and compared with the Gaussian prediction from the Peacock & Dodds fitting formula described in section 2.4.

Most of the simulations were evolved using $80^3$ particles and integrated for 90 time-steps over an expansion factor of 10. Each particle was assigned to a grid point, and displaced from this using the Zel'dovich approximation (with no smoothing onto the grid). The Fourier mesh used to evolve the particles contained $128^3$ grid points, with the initial softening of the force set to one cell. This softening was allowed to decrease to a minimum of one tenth of the cell size, and the maximum force error permitted was 6%.

The time variable, $p$ used in the simulation is an adjustable function of the expansion factor, $a$, ($p = 3a^{\alpha}/2\alpha$), and $\alpha$ has been kept at a constant value of $\alpha = 3/2$ for all simulations. The maximum number of mesh refinements in clustered regions was also kept to a constant value of three subgrid refinements. A few simulations however did require more particles to keep the shot noise level low compared with the evolving power spectrum, and these were the $\chi^2$ models with spectral index $n = -1.5$. These simulations contained $100^3$ particles, and were evolved for 300 time steps. Comparisons were made between simulations with expansion factors of 10 and 15, and between simulations taking 90 time-steps, and 300 time-steps, and neither of these changes affected the results. The power in the fundamental mode ($2\pi/L_{\rm box}$) at the final epoch was required to be less than $\Delta^2(k) = 0.02$ so as to keep the low-$k$ modes in the linear regime, and largely the simulations were set up to have a box size of $\sim 200\,h^{-1}$ Mpc. All simulations shown here used $\Omega_m = 1$, and $\Omega_v = 0$.

### 3.2.3 Results

Figure 3.3 shows the simulation outputs at the final evolution time, for $n = -1$ simulations. The $\chi^2_+$ field displays the most highly clustered nature on small scales. Figure 3.4 shows the hierarchical skewness and kurtosis, $S_3$, $S_4$ for the four different non-Gaussian fields considered. On large scales, only the Cauchy field agrees with the Gaussian perturbation predictions, with the modulated and $\chi^2_+$ fields having hierarchical moments that are several times larger than the Gaussian predictions. The $\chi^2_-$ model has very low $S_3$, $S_4$, compared with the Gaussian perturbation prediction.

Figure 3.5 is a compilation of plots of non-linear power against linear input power for the different non-Gaussian fields discussed above. A notable feature of the graphs in figure 3.5 is how well the $n = -1$ models match the Gaussian locus compared with the $n = 0$, and $n = -1.5$ models. This appears to agree with the predictions of Gaztañaga & Fosalba (1997) that in the quasi-linear regime, $n = -1$ spectra deviate least from the Gaussian model. The non-Gaussian simulation that agrees best with the Gaussian prediction is the modulated field case. This is perhaps surprising given the Zel'dovich prediction that the evolution should depend on the velocity probability function, since

the modulated field has one of the most non-Gaussian velocity p.d.f.s. This field, however is locally Gaussian, so perhaps the dominant factor is the local probability distribution. By contrast, the other field with zero initial skewness and high kurtosis, the Cauchy field, appears not to have the scale invariant character of the modulated field for spectral indices $n = 0$, and $n = -1.5$, with different evolution epochs displaying a different locus on the $\Delta^2_{\rm NL}$ vs $\Delta^2_{\rm L}$ graphs. In these cases the non-linear power is significantly lower, although evolving towards the Gaussian prediction.

The skew positive $\chi^2$ models behave similarly to the Gaussian prediction, though the non-linear power amplitude evolves slightly faster than the Gaussian prediction for $n = -1$, and $n = -1.5$ spectra. This is what one might suspect, since there are a higher proportion of the more overdense regions at the start of the simulation than in the Gaussian case, and these will collapse faster than the 'less overdense regions'. At the same time, for the same power spectrum, there are fewer overdense regions than in the Gaussian case to compensate for the high density excursions, so the evolution is likely to be a trade off between the number of overdense regions, and just how overdense the overdensities are. The skew negative $\chi^2$ models evolve to give much lower non-linear power amplitudes for a given linear spectrum. Again this is likely to be a trade off argument: although there are lots of mildly overdense regions, the rate of collapse of these slightly overdense regions is too slow to compensate for their high number.

In general, the results here confirm the prediction of *e.g.* Weinberg & Cole of less power for skew-negative models than for skew-positive models for a given level of evolution, and provide confirmatory evidence, particularly in the Cauchy model case of $n = -1$ spectra showing closer to Gaussian evolution. It is interesting that both the Cauchy, and $\chi^2_-$ fields undershoot the non-linear power compared with the Gaussian prediction, and yet these have extremely different hierarchical moment properties. Similarly, although the hierarchical moments of the modulated and $\chi^2_+$ fields are at least a factor of three higher than the Gaussian moments, these fields evolve similarly to the Gaussian field.

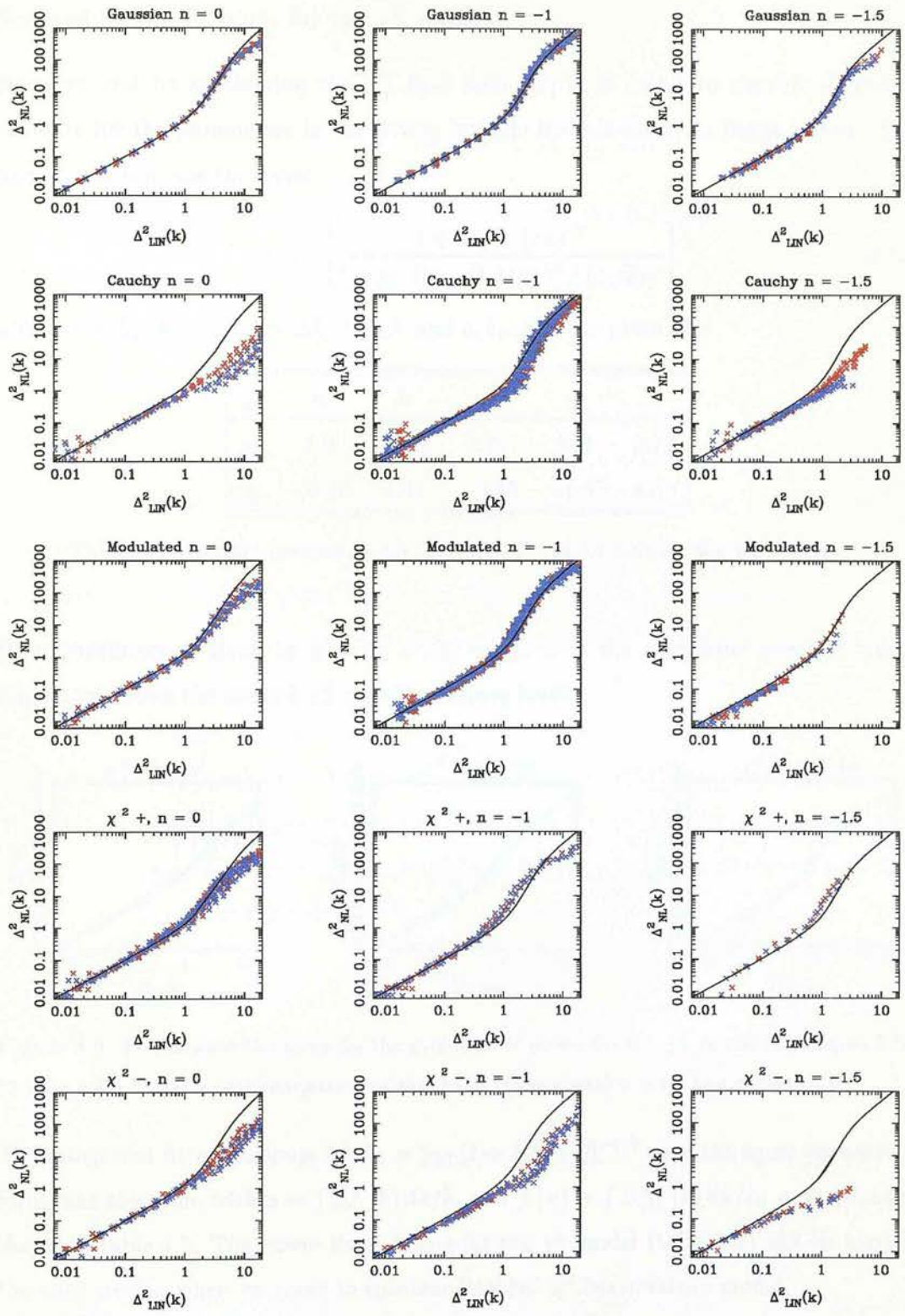


Figure 3.5: Evolution of power for non-Gaussian models. Blue points are for an expansion factor of 7.5, and red are for an expansion factor of 10. The solid line shows the Gaussian prediction taken from the PD96 fitting formula.

**Revised fitting formula for the $\chi^2_+$ model.**

Since we will be considering the $\chi^2_+$ field later on, it is useful to provide a revised estimate for the parameters in the fitting formula for non-linear to linear power. The parametrisation has the form:

$$f(x) = x\left[\frac{1 + bex + (ax)^{de}}{1 + \left[g^3(\Omega_m, \Omega_v)(ax)^d / (c\sqrt{x})\right]^e}\right]^{\frac{1}{e}} \tag{3.19}$$

where $x = \Delta^2_{\rm L}(k_{\rm L})$, $f(x) = \Delta^2_{\rm NL}(k_{\rm NL})$, and $a, b, c, d, e$ are given by:

| $y_i$ | a | b | c | d | e |
|---|---|---|---|---|---|
| $y_0$ | 1.9 | 12.03 | 2.77 | 0.9 | 8.77 |
| $y_1$ | −0.26 | 7.31 | −3.45 | −1.45 | 4.51 |

Table 3.1: Revised parameters for the PD96 fitting formula for the $\chi^2_+$ model.

Each parameter is given by $y = y_0 + ny_1$ where $n$ is the tangential spectral index. Figure 3.6 shows the revised $\chi^2_+$ power spectrum locus.

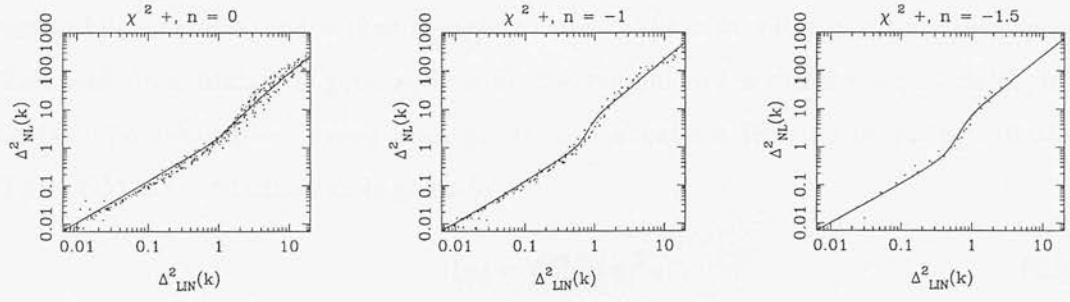


Figure 3.6: Points show the locus for the evolution of power for the $\chi^2_+$ model (*c.f.* figure 3.5), and the solid line is a parametrisation of this locus. (See equation 3.19, and table 3.1.)

The integrated fitting formula for $k_{\rm L} = k_{\rm NL}[1 + \Delta^2_{\rm NL}(k)]^{-1/3}$ uses the same parametric form, but this time with $x = \int \Delta^2_{\rm L}(k)\,{\rm d}k/k$, and $f(x) = \int \Delta^2_{\rm NL}(k)\,{\rm d}k/k$. $a, b, c, d, e$ are shown in table 3.2. The power locus fitting for the $\chi^2$ model (table 3.1) will be used in the next section when we come to consider Peebles' $\chi^2$ isocurvature model.

| $y_i$ | a | b | c | d | e |
|---|---|---|---|---|---|
| $y_0$ | 4.46 | 13.49 | 7.91 | 1.15 | 6.1 |
| $y_1$ | 0.88 | 7.99 | −9.29 | −1.3 | 2.72 |

Table 3.2: Revised parameters for the integrated fitting formula for the $\chi^2_+$ model.

## 3.3 The Peebles isocurvature model

### 3.3.1 Motivation for the model.

The evidence for assembly of some massive galaxies at redshifts as high as $z \sim 6$ (*e.g.* Dunlop *et al.* 1996) poses a problem for the adiabatic CDM model, which favours a later epoch for the collapse of objects. An alternative model for structure formation has been proposed by Peebles (1997; P97), who suggested that a non-Gaussian isocurvature model might be able to produce the required high redshift structures. In this model the initial fluctuations are isocurvature CDM, and their statistics are proportional to the square of a random Gaussian process. This gives a higher density contrast for the upward fluctuations, and is thus thought to allow objects to collapse at an earlier epoch. The cold dark matter is proposed to be the remnant of a massive scalar field, with initial inhomogeneities arising from quantum fluctuations freezing in during inflation. The CDM mass distribution is given by

$$\rho\left(\mathbf{x}\right) = M_0^2 \psi\left(\mathbf{x}\right)^2, \tag{3.20}$$

where $\psi\left(\mathbf{x}\right)$ is a random Gaussian process, and $M_0$ the field mass now or when it decayed to the present CDM.

We can write the non-Gaussian power spectrum in terms of the power spectrum of the Gaussian field, $\psi$:

$$P_\rho\left(k\right) = 2\ P_\psi\left(k\right) \star P_\psi\left(k\right) \tag{3.21}$$

(see section 3.2.1). In P97, the primordial power spectrum (before matter radiation equality) is chosen to be a power law:

$$P_\rho\left(k\right) = Ak^m, \tag{3.22}$$

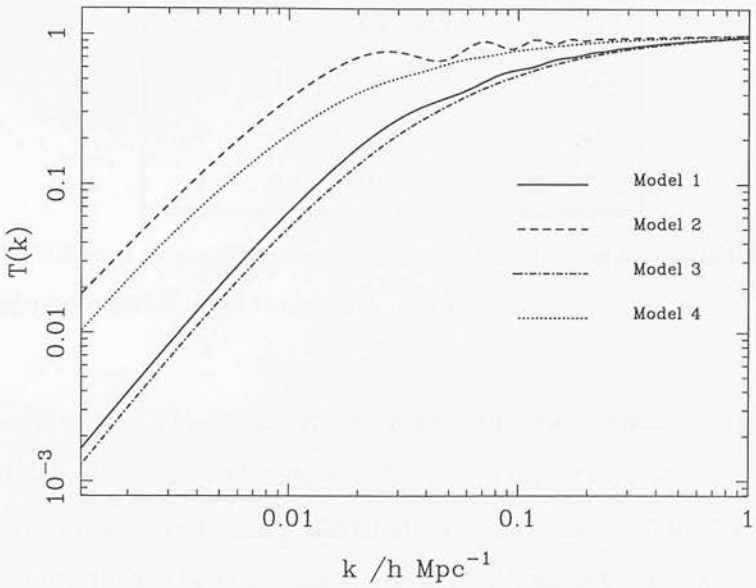


Figure 3.7: Transfer functions used in Peebles' models. Solid line, model 1; dashed, model 2; dot-dashed model 3; and dotted line model 4.

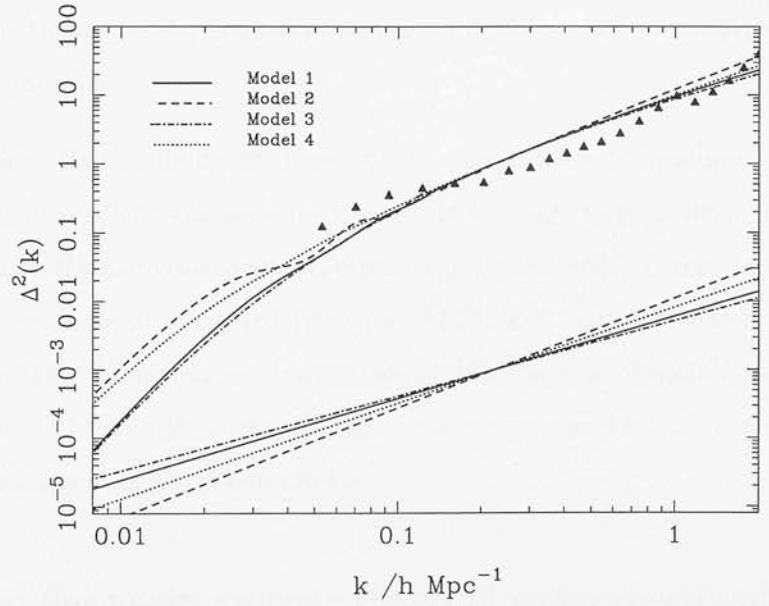


Figure 3.8: Graph showing the primordial scale free power spectra for Peebles' model (displaced downwards by three orders of magnitude), and above it the resulting power spectrum after recombination. Triangles show the linearised APM power spectrum using the fitting formula for $\chi^2_+$ initial conditions (equation 3.19), and parameters from table 3.1. This linearisation has assumed $\Omega_m = 0.3$, and $\Omega_v = 0$.

| Model | $\Omega$ | $\Omega_b$ | h | $m$ | $A$ |
|---|---|---|---|---|---|
| 1 | 0.3 | 0.05 | 0.7 | $-1.8$ | 174 |
| 2 | 0.1 | 0.05 | 0.7 | $-1.4$ | 108 |
| 3 | 0.3 | 0.01 | 0.7 | $-1.9$ | 210 |
| 4 | 0.1 | 0.01 | 0.7 | $-1.6$ | 87.1 |

Table 3.3: The different isocurvature models considered. The values quoted for $A$ are for the linearly evolved power spectrum at the current epoch.

in which $A$ and $m$ are chosen to fit the predicted linear r.m.s. amplitude of CBR fluctuations at $l \sim 10$, and to give $\sigma_8 = 1.0 \pm 0.1$. This gives a power spectrum with a slope similar to the observed galaxy distribution in the range $0.03h \leq k \leq 0.3\,h$ Mpc$^{-1}$ (Peacock & Dodds 1994; Lin *et al.* 1996), and is in agreement with the four year COBE data for $3 < \ell < 20$ (Górski *et al.* 1996). The model parameters are shown in table 3.3, and the isocurvature transfer functions required to obtain the matter dominated power spectrum for these model parameters are shown in figure 3.7, with the resulting power spectra in figure 3.8.

In this section, the feasibility of these isocurvature models is considered, starting with whether this type of non-Gaussian process could be made to reproduce the APM power spectrum, and then moving on to compare the higher order moments of the evolved distribution with those measured from the APM. The final subsection examines how such higher order moments are influenced by bias, and an estimate is given for the required level of biasing that would bring the skewness and kurtosis measurements into agreement with the APM measurements.

### 3.3.2 Can this model generate the APM power spectrum?

In assessing the viability of these isocurvature models, it is worth asking whether the model is capable of reproducing the observed power spectrum of our local universe. For $\chi^2$ fields, the correlation function of the non-Gaussian field can be specified in terms of the correlation function of the Gaussian precursors, as discussed in section 3.2.1, and

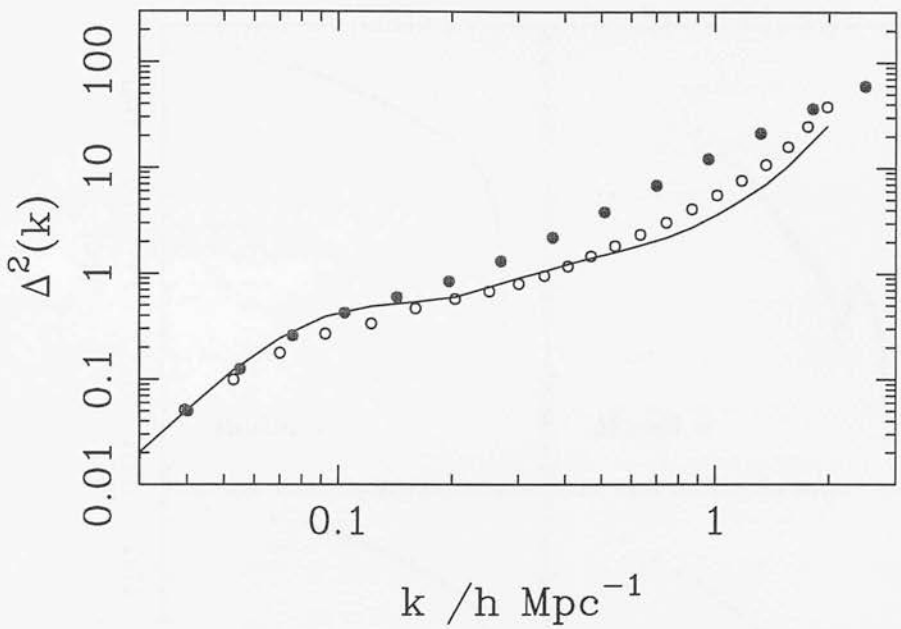


Figure 3.9: Unfilled circles show the predicted linear APM power spectrum for the $\chi^2$ model which has been obtained using the fitting formula in equation 3.19 with parameters from table 3.1. Filled circles show the observed APM power spectrum, and the solid line indicates the Gaussian prediction for linear power. This linearisation has assumed $\Omega_m = 0.3$, and $\Omega_v = 0$.

from equation 3.15, we have:

$$\xi_\rho(r) = 2\,\xi_\psi(r)^2\,, \tag{3.23}$$

where $\xi_\rho$ is the correlation function for the non-Gaussian field, and $\xi_\psi$ is the 'correlation function' for the Gaussian field, $\psi$. In order to generate the $\chi^2$ model from a real Gaussian field, the correlation function of the non-Gaussian field must be greater than zero for all separations.

In this section, the APM power spectrum has been linearised using the fitting formula for $\chi^2$ evolution (see equation 3.19, table 3.1, and figure 3.9) for the different cosmological models summarised in table 3.3. The linearised power, $P_{\rm lin}(k)$, was then divided by the square of the isocurvature transfer function to obtain the power spectrum before matter radiation equality, $P_{\rm prim}(k)$:

$$P_{\rm prim}(k) = P_{\rm lin}(k)/T_k^2. \tag{3.24}$$

$P_{\rm prim}$ has then been Fourier transformed to obtain the correlation function for the $\chi^2$ process, $\xi_{\rm prim} \equiv \xi_\rho$. If $\xi_{\rm prim}$ is not positive on all scales, then it is not possible to create

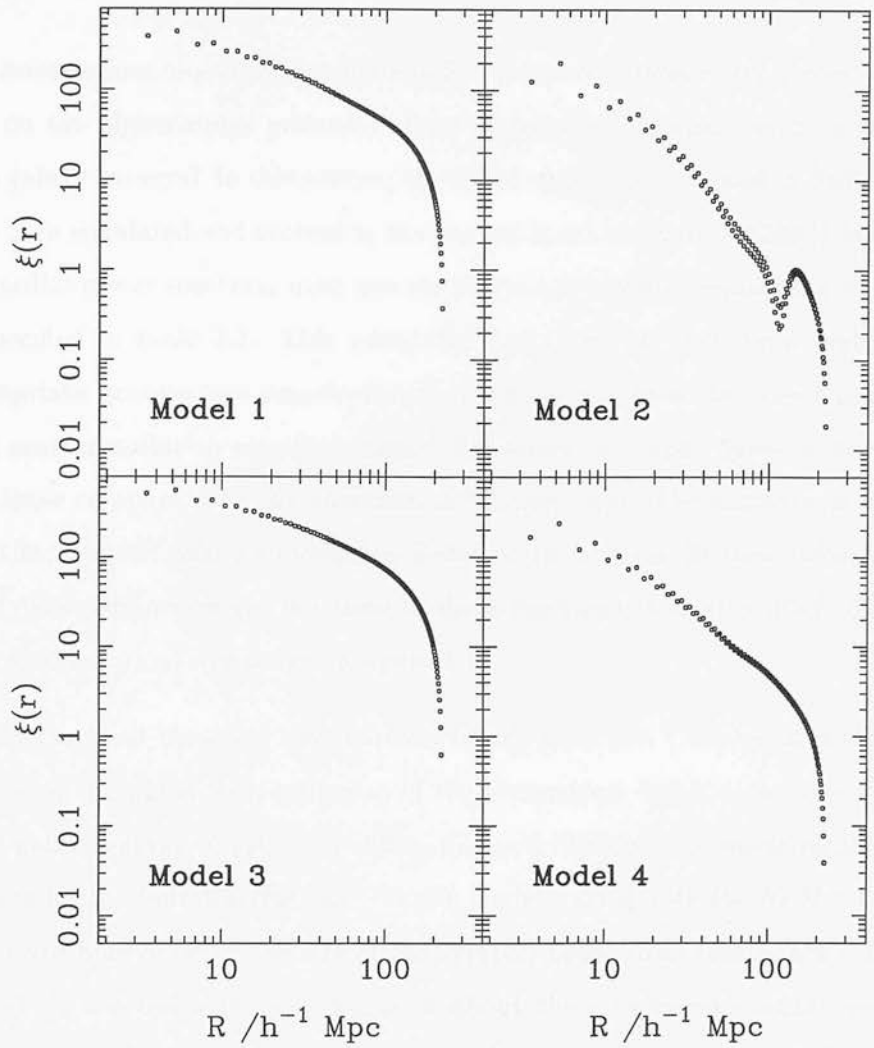


Figure 3.10: The predicted primordial correlation functions for the $\chi^2$ model. These were deduced by taking the linearised APM power spectrum from figure 3.9, dividing by the transfer function for the particular model, to give the primordial power spectrum, and then Fourier transforming to get the correlation function.

the field from the square of real Gaussian variables. Figure 3.9 shows the linearised APM power spectrum for a $\chi^2$ initial distribution, and figure 3.10 shows the primordial (before matter radiation equality) correlation functions required to yield the APM power spectrum before the universe has become matter dominated. 'Model 2' shows more oscillation than the others, but all of them remain above zero for the scales considered, indicating that they could all theoretically reproduce the observed APM power spectrum for an appropriate initial power spectrum.

### 3.3.3 Skewness and kurtosis of the Isocurvature models

The isocurvature model can be made to fit current estimates of the power spectrum, but how do the higher order moments of the distribution compare with current estimates from galaxy surveys? In this section, the initial conditions specified in P97 (see table 3.3) have been simulated and evolved to the present epoch using an AP3M N-body code. The primordial power spectrum used was the power law model in equation 3.22, with $A$, and $m$ specified in table 3.3. This primordial spectrum has then been multiplied by the appropriate isocurvature transfer function squared to obtain the linear power spectrum after matter radiation equality. Figure 3.8 shows the input linear power spectra and how these compare with the linearised APM spectrum. The simulations have used $80^3$ particles, evolved over an expansion factor of 10, and for 90 time-steps, and all other simulation parameters are the same as those described in section 3.2.2. Slices from the evolved simulations are shown in figure 3.11.

The hierarchical skewness and kurtosis of the field (see Chapter 2, section 2.2) have then been compared with estimates of the hierarchical higher order moments from the APM galaxy survey (Gaztañaga 1994). Figure 3.12 shows the hierarchical skewness and kurtosis for the four different isocurvature models, along with the APM estimates (these have error bars of order the size of the symbol) taken from Gaztañaga (1994). Clearly $S_3$ and $S_4$ are too high by a factor of about three to be compatible with the APM measurements for all the models considered here. The isocurvature models did not have exactly the same shape of power spectrum as the APM power spectrum (see figure 3.8), and there is likely to be a small discrepancy between the models' hierarchical moments

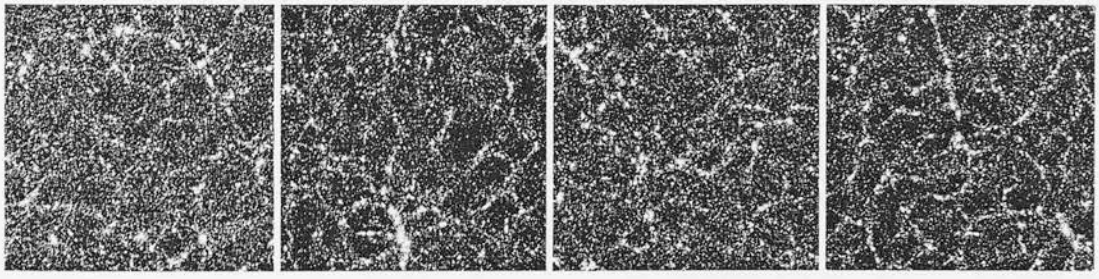

Figure 3.11: Slices through simulation boxes of the isocurvature models taken at the present epoch. Each box is $200\,h^{-1}$ Mpc across, and contains 512000 particles. Far left is model 1; centre left, model 2; centre right model 3; far right, model 4.

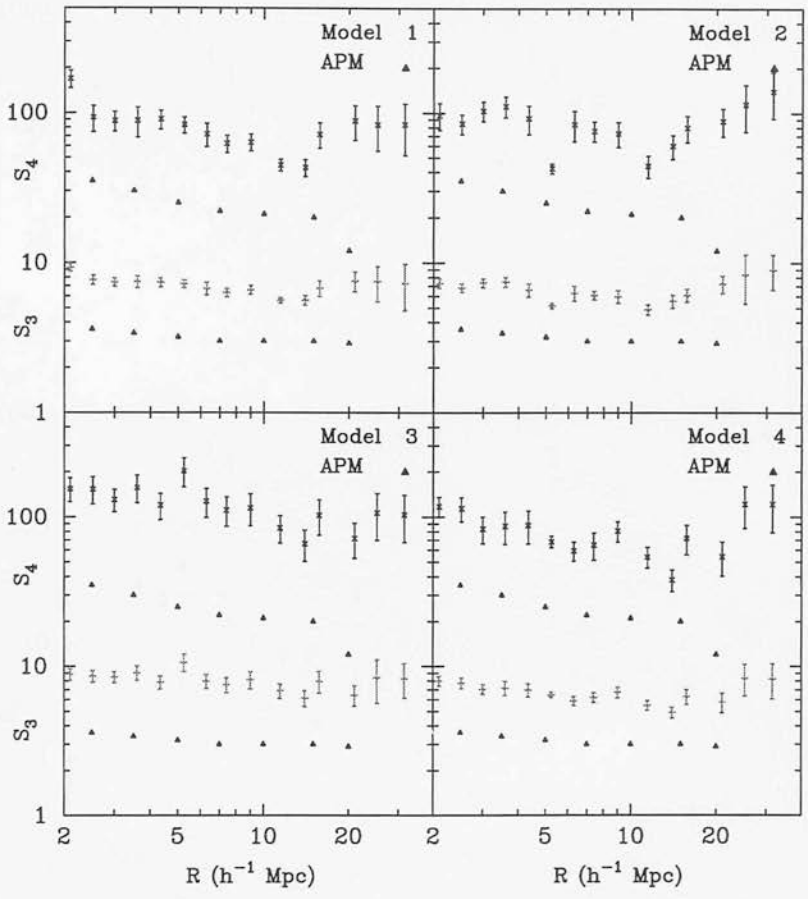


Figure 3.12: $S_3$ (lower points with error bars) and $S_4$ (upper points with error bars) for simulations of the isocurvature $\chi^2$ models in the absence of biasing. Triangles indicate APM estimates for $S_3$ and $S_4$.

and the APM moments as a result. However, the model power spectra are steeper than the APM spectrum (*i.e.* $n$ is more positive), and since the effect of using shallower power spectra is to raise the hierarchical moments (see figure 2.1), the observed discrepancy is expected to be greater still if the power spectra were identical.

### 3.3.4 The effect of bias on the model

If light does not trace mass, then the observed galaxy distribution will be biased relative to the underlying dark matter distribution, and this will affect the higher order moments of the measured distribution as well as the power spectrum. In this section different

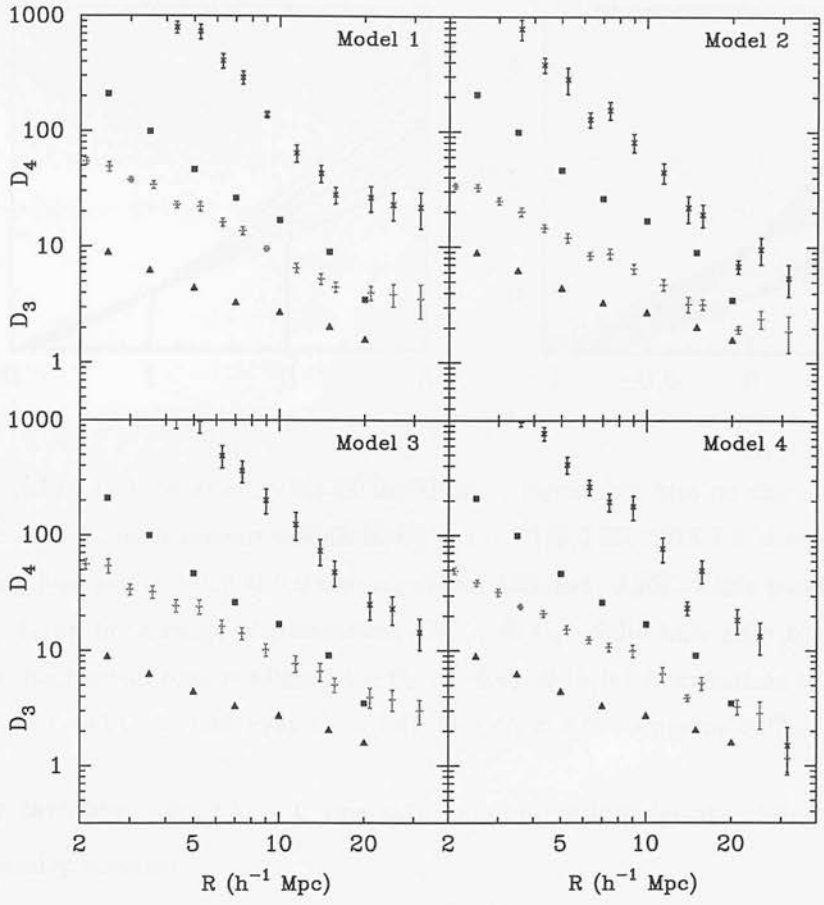


Figure 3.13: Dimensionless moments, $D_3$ (lower points with error bars) and $D_4$ (upper points with error bars) for simulations of the isocurvature $\chi^2$ models in the absence of biasing. Triangles show $D_3$ for the APM survey, and squares are for $D_4$. These have been calculated from the hierarchical moments, and the APM power spectrum.

biasing schemes are applied to the isocurvature model simulations to see if non-linear bias can bring the moments down in line with the APM measurements. The biasing schemes used here are the same as those considered in Mann *et al.* (1998), and the programs used to apply bias to the density field have kindly been provided by Bob Mann. While these schemes are not physically motivated, they aim to reflect feasible actions of bias, such as suppressing galaxy formation in low density regions, and augmenting it in high density regions. We consider three different empirical schemes. These are:

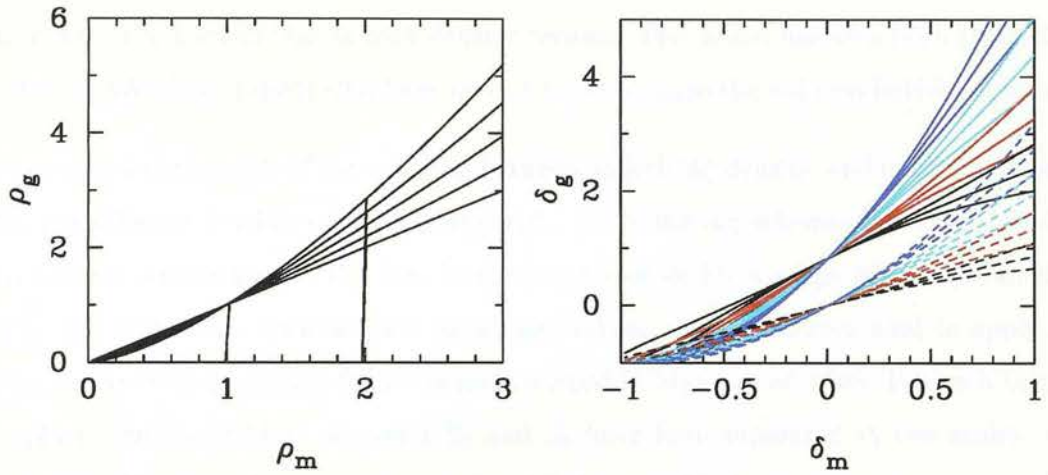


Figure 3.14: Left panel is a plot of the effect of power law bias on the mass density field. Lines from bottom to top correspond to $C_1 = 1.0, 1.125, 1.25, 1.375, 1.5$, with cut off points for censoring bias at $C_0 = 1.0$ & $2.0$ (see equations 3.25 and 3.26). Right panel is Cen-Ostriker biasing shown for a range of parameters, $C_0, C_1, \& \ C_2$. Solid lines have $C_0 = -0.4$, dashed $C_0 = 0$. Each set of coloured lines have $C_2 = -0.4, -0.15, 0.1$ from bottom to top. Black lines have $C_1 = 1$; red $C_1 = 1.33$; cyan $C_1 = 1.67$; blue $C_1 = 2$ (see equation 3.27).

**Power law bias.** For $C_1 > 1$, this acts to suppress low density regions, and augment high density regions:

$$\rho_g \propto \rho_m^{C_1}. \tag{3.25}$$

**Censoring bias.** This is a form of threshold biasing, in which galaxies are assumed to be unable to form if the density is lower than a certain value. It can be combined with the power law bias, so as to enhance galaxy formation in high density regions and suppress it for low density regions greater than the threshold. Below the threshold there is no luminous matter. This type of biasing is given by:

$$\rho_g \propto \begin{cases} \rho_m^{C_1} & \text{for } \rho_m \geq C_0 \\ 0 & \text{otherwise} \end{cases}. \tag{3.26}$$

**Cen-Ostriker bias.** As the name suggests, this formalism was developed by Cen & Ostriker (1992) who found that the galaxy density field could be expressed quite accurately in terms of the mass density field using the following relation:

$$\ln\left(\frac{\rho_g}{\overline{\rho}_g}\right) = C_0 + C_1 \ln\left(\frac{\rho_m}{\overline{\rho}_m}\right) + C_2 \left[\ln\left(\frac{\rho_m}{\overline{\rho}_m}\right)\right]^2. \tag{3.27}$$

This is essentially a more general form of the power law bias, and for $C_2 < 0$ can be used to reduce the level of bias in high density regions. The model has also been studied by Little & Weinberg (1994) who have used it to investigate the void probability function.

Figure 3.14 shows plots of the mapping between underlying density, and luminous density for the different biasing schemes considered. These biasing schemes have been applied to evolved simulations of the four isocurvature models for a range of bias parameters ($C_0$, $C_1$, $C_2$) which span sensible linear bias values. The techniques used to apply the bias to the N-body models follow those described in Mann *et al.* 1998. For each biasing applied, the hierarchical moments $S_3$ and $S_4$ have been measured at two scales – 10 and $20\,h^{-1}\,\mathrm{Mpc}$, and compared with the APM hierarchical moments at corresponding scales by measuring the $\chi^2$ deviation between the APM moments, and those found from the biased simulations. These $\chi^2$ values have been used to assess whether a particular biasing scheme can bring the hierarchical moments into statistical agreement with the APM moments.

**Results**

Firstly we look at how the hierarchical moments are affected by changing the biasing parameters for the power law bias model. Figure 3.15 shows how the hierarchical moments (averaged over scales between 7 and $20\,h^{-1}\,\mathrm{Mpc}$) change with different power law biasing. The moments decrease with increasing linear bias $b$, and are in agreement with the APM moments for values of $b$ greater than about $b \sim 2$. Figure 3.16 shows the hierarchical moments for an example of the Cen-Ostriker bias model ($C_0 = 0.35$, $C_1 = 3.4$, $C_2 = -0.36$, giving a linear bias value of $b \simeq 1.6$). While the hierarchical skewness for this particular model is in reasonable agreement with the APM moments, the hierarchical kurtosis is now too low. Notice also that there is little scale dependency on these biased moments.

The next stage is to consider what values of linear bias are required to bring all the different biasing mechanisms into agreement with the APM moments. Figure 3.17 is a contour plot in which shaded areas indicate biasing parameters that bring the moments of the distribution down to within one, two, and three sigma agreement with the APM third and fourth hierarchical moments (using a $\chi^2$ statistic, and quoting bias values that

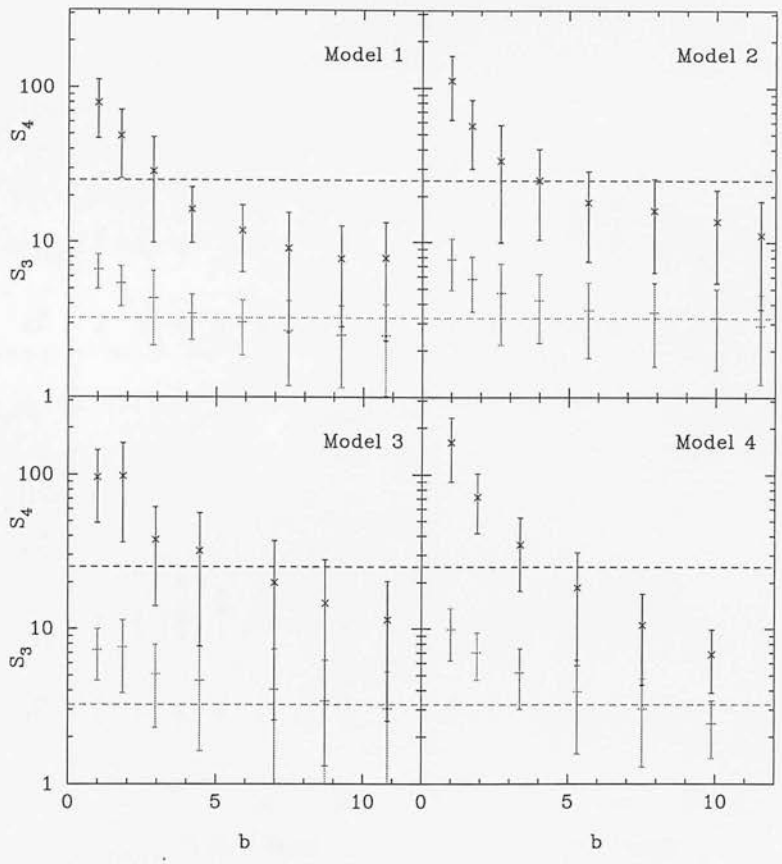


Figure 3.15: Graph showing how the hierarchical moments are affected by power law biasing. Upper points on each panel are $S_4$, and lower $S_3$. Moments have been averaged over scales between 7 and $20\,h^{-1}$ Mpc. $b$ is the linear bias parameter as defined in equation 1.57 from Chapter 1. The dotted lines indicate the equivalent averaged APM moments. Clearly a high level of bias (around $b = 3 - 5$) is required to match the measured APM results.

give $P_r\left(\chi^2 > \chi^2_{\text{measured}}\right) = 0.68,\ 0.95,\ 0.99$ respectively). Unshaded contours indicate lines of constant linear bias. The levels of biasing required to bring the hierarchical

| Model | b - Cen-Ostriker | b - Censor + power law |
|---|---|---|
| 1 | $5.6 - 6.2$ | $5.0 - 5.26$ |
| 2 | – | $3.3 - 9.4$ |
| 3 | $2.9 - 5.4$ | $4.0 - 6.0$ |
| 4 | – | $1.9 - 4.6$ |

Table 3.4: Linear bias values giving moments within one sigma of the APM moments

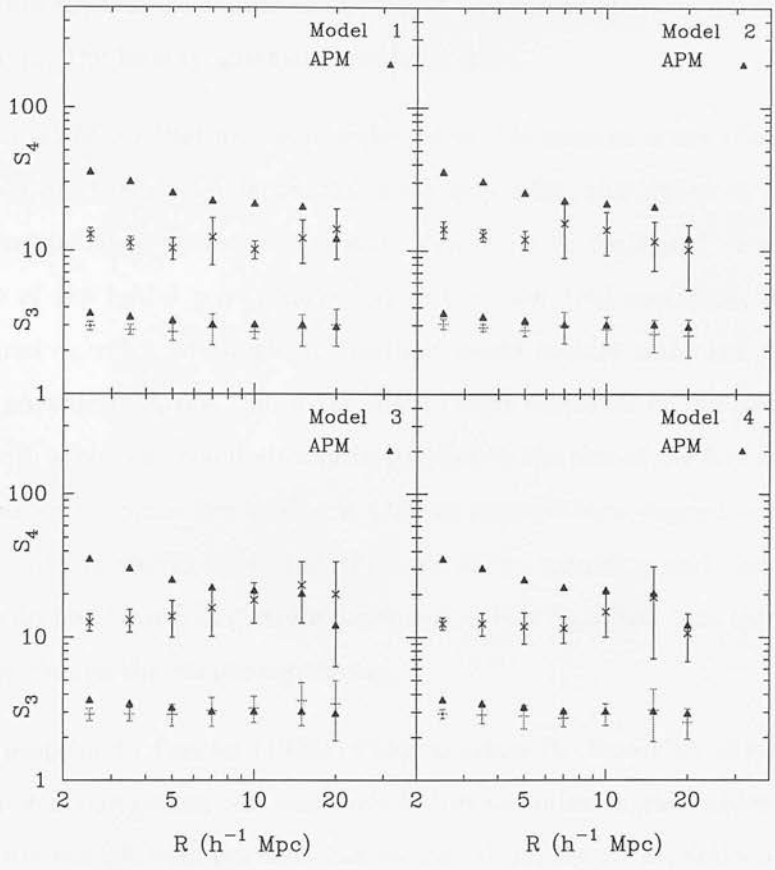


Figure 3.16: The hierarchical moments for a particular Cen-Ostriker bias model. Here, $C_0 = 0.35$, $C_1 = 3.4$, $C_2 = -0.36$, and the linear bias is $b \simeq 1.6$. While the hierarchical skewness has been brought down into agreement with the APM moments, the kurtosis has been brought down too far.

moments low enough to lie within one sigma of the APM moments are summarised in table 3.4. For the Cen-Ostriker model, which has three free parameters, $C_0$ has been fixed at a constant value of $C_0 = 0.35$. Variations of this parameter were found to have little effect on the results.

### Discussion

Current estimates of the redshift distortion parameter, $\beta$, favour a value of $\beta_{\rm optical} = 0.6 \pm 0.3$ (*e.g.* Peacock 1997). For the models used here, this corresponds to a linear bias in the range $0.54 \leq b \leq 1.62$ for $\Omega = 0.3$ models, and $0.28 \leq b \leq 0.84$ for $\Omega = 0.1$ models. The allowed ranges of bias from the Cen-Ostriker and Censor-power law models in table 3.4 are clearly too high to fall within these ranges. This suggests that the

isocurvature models are unable to fit current measurements from observations of galaxy clustering for the biasing schemes considered here.

An important factor that has been neglected in this analysis is the effect of these biasing schemes on $\sigma_8$. Clearly the larger the linear bias value, the higher $\sigma_8$ becomes, and this is an important observational constraint. This could be dealt with properly by changing the slope of the initial power spectrum so that the final spectrum, when biased gave the required $\sigma_8$ value, although this method would require many simulations to explore the bias parameter space. Since the hierarchical moments of the models do not vary greatly with scale, one could alternatively redefine the size of the box such that $\sigma_8$ when biased was unity. Since the biasing models considered here depend only on density, the only effect of this would be to shift the scale of the moments, and since even the biased moments do not have a large scale dependence, it is expected that compensating for $\sigma_8$ would not change the results significantly.

A recent preprint by Peebles (1998b; P98) examines the feasibility of a similar $\chi^2$ isocurvature model, comparing the non-evolved dimensionless higher order moments of the isocurvature models with current observations (from the APM, and Edinburgh-Durham Southern Galaxy Catalogues, EDSGC). In this paper, he finds $D_3 = 2.46$, and $D_4 = 9.87$ for his non-evolved isocurvature models, and finds these to be in agreement with observations from the APM and EDSGC surveys. A plot of the $D_3$ and $D_4$ values for the simulations used here (figure 3.13) also agrees with this estimate on large scales. However, this plot also shows the expected APM dimensionless moments (calculated from $S_3$ and $S_4$, and the APM power spectrum – see PD94 for the conversion formula to get between $\Delta^2(k)$, and $\overline{\xi}_2(r)$). On scales less than $30\,h^{-1}$ Mpc, there is clearly a discrepancy between the model and the APM results. It therefore seems that the reason these isocurvature models fail is due to their non-linear evolution, which was not tested in P98.

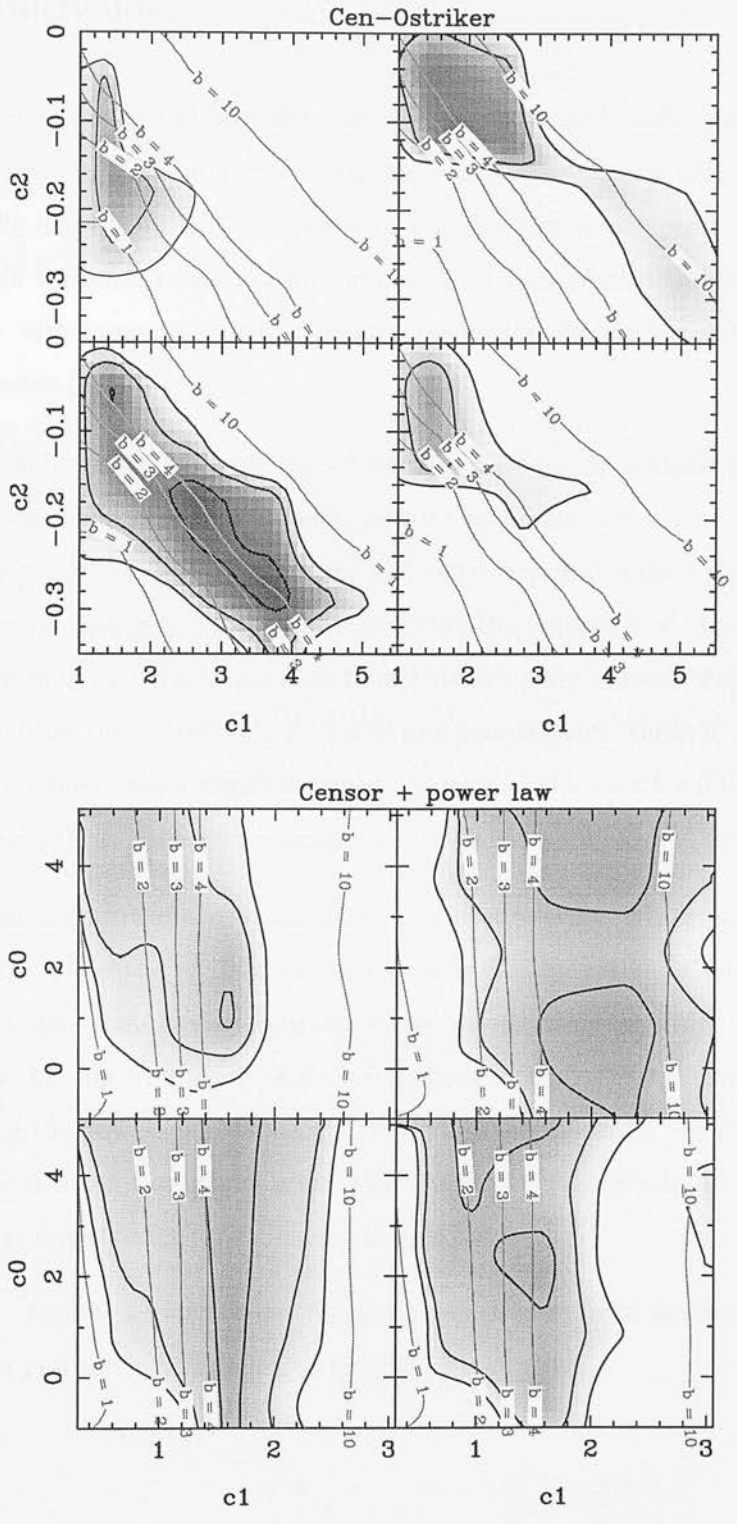


Figure 3.17: Shaded contours show areas of bias parameter space consistent with APM moments at the one, two & three $\sigma$ level. Lighter line contours indicate regions of constant linear bias. The top panel uses Cen-Ostriker biasing, with $C_0 = 0.35$ and the bottom panel uses Censor+power law biasing.

## 3.4 Conclusions

This chapter has looked at how the power spectra of non-Gaussian fields evolve into the non-linear regime. The findings are consistent with those in the literature – principally that initially skew positive fields result in a higher non-linear power for a given linear input. High initial kurtosis appears not to have a consistent influence on the power evolution – with some high kurtosis models displaying similar features to the low initial kurtosis models.

One of the aims of this chapter was to explore whether an analysis of the evolution of the power spectrum could be a useful test for non-Gaussian fields. This turns out to be a highly model dependent problem, and since in practice data yielding information about the early power spectrum has come from the detection of high redshift galaxies, and so from only one scale, distinguishing between non-Gaussian fields and the effects of low $\Omega$ or $\Lambda$ on the evolution is probably not possible until these parameters are more tightly constrained. Skew-negative models, however (which evolve more slowly than the Gaussian model) do not look promising whatever the cosmological model.

Higher order moment analyses are clearly required to constrain non-Gaussian models. For instance, while the $\chi^2$ isocurvature models can be made to reproduce the APM power spectrum, they cannot reproduce the observed higher order moments, $S_3$ and $S_4$. Various biasing prescriptions do bring these moments down (probably as a result of increasing the power spectrum amplitude), but the values for the linear bias required to bring them down enough to agree with the APM moments lie outside the range of currently favoured values for the linear bias parameter.

In the next chapter, a fourth order Fourier moment analysis of the density field is developed, which can easily be applied to redshift survey data.

# Chapter 4

# POWER CORRELATIONS

## 4.1 Introduction

In the previous chapter, the evolution of the power spectrum of initially non-Gaussian fields was studied with a view to finding an observable signature for non-Gaussian fields. The results of this chapter suggested that, while for some non-Gaussian fields, there is a marked difference in the evolution (*e.g.* negative $\chi^2$ models, and some Cauchy models), for other fields with equally high deviations from the Gaussian hierarchical moments, the evolution is very similar to the Gaussian case (*e.g.* the modulated fields).

It seems therefore a natural step to consider a higher order statistic to constrain non-Gaussian fields. We have already used higher order moment statistics such as $S_J$ and $D_J$ in Chapters 2 and 3, and these appear to discriminate well between different theoretical models. However, these statistics operate in real space, and lend themselves to a number of problems particularly when analysing real surveys. These arise mainly from the fact that in real space, correlations in the density field exist over a wide range of scales, and that in order to measure moments, the field must be smoothed. The correlations make analysis of errors a difficult task, and the smoothing is complicated in the presence of a selection function or mask. Since the effect of smoothing is essentially to average the density field, there is also the risk that sensitivity to non-Gaussian fields is reduced on account of the central limit theorem.

An alternative approach adopted by Feldman, Kaiser, and Peacock (1994; FKP) is to look at the density field in Fourier space, where modes are separated out on the basis of scale, making it easy to probe the linear regime. FKP proposed two possible tests for a Gaussian density field. Both make use of the property that at high resolution in $k$-space, independent Fourier modes have power values that fluctuate about the mean power for that particular scale. The first test was to look at the one-point distribution of these power fluctuations, which is predicted to be exponentially distributed in the Gaussian case. FKP found that for the QDOT 1-in-6 survey, the power distribution was in good agreement with the Gaussian prediction. However, Fan & Bardeen (1995) have subsequently argued that such one-point p.d.f. tests have little discriminatory power: for a large enough sample, most types of non-Gaussian field are also expected to have an exponential power distribution as a consequence of the central limit theorem. The second test suggested by FKP was to look at correlations between the power fluctuations which, for a Gaussian field, will be a function of the selection function only. This is effectively a four point test, and since it is expected to be sensitive to phase correlations between the modes, it is perhaps less susceptible to the swamping effects of the central limit theorem.

In this chapter, the power correlations test is developed and applied to the QDOT+1.2 Jy redshift survey, from which limits can be placed on a particular class of non-Gaussian models. An earlier version of this work is published in Monthly Notices of the Royal Astronomical Society (Stirling & Peacock, 1996).

## 4.2 Power Correlations

The general idea behind looking for correlations between power fluctuations is that for an infinite density field the Fourier modes are independent, *i.e.*

$$\langle \delta_{\mathbf{k}_1} \, \delta^*_{\mathbf{k}_2} \rangle = (2\pi)^3 P(k_1) \, \delta^{\mathrm{D}}(\mathbf{k}_1 - \mathbf{k}_2), \tag{4.1}$$

where $\delta^{\mathrm{D}}(\mathbf{k}_1 - \mathbf{k}_2)$ is the Dirac delta function and angle brackets denote the ensemble average. For a finite sample of the density field, however, this mode independence is lost. This is because the finite region is effectively a product of the true infinite field, $\delta^{\mathrm{infinite}}$, and a mask, $m$. In Fourier space the observed density modes $\delta^{\mathrm{observed}}_{\mathbf{k}}$ are then

a convolution of the 'true' density modes with the Fourier transform of the mask (see Chapter 1):

$$\delta_{\mathbf{k}}^{\text{observed}} = \delta_{\mathbf{k}}^{\text{infinite}} \star m_k, \tag{4.2}$$

where $\delta_{\mathbf{k}}$ is given by:

$$\delta_{\mathbf{k}} = \frac{1}{V} \int \delta(\mathbf{r})\, e^{i\mathbf{k}\cdot\mathbf{r}}\, d^3\mathbf{r}, \tag{4.3}$$

and $\delta(\mathbf{r}) \equiv [\rho(\mathbf{r}) - \overline{\rho}(\mathbf{r})]/\overline{\rho}(\mathbf{r})$ is the overdensity at position $\mathbf{r}$. This has the effect of mixing information between the modes over a $k$-scale comparable to the $k$-space width of the mask. Now, for a Gaussian field, the following relation applies (see section 4.3):

$$\begin{aligned} |\langle \delta_{\mathbf{k}_1}\, \delta^*_{\mathbf{k}_2} \rangle|^2 &= \langle |\delta_{\mathbf{k}_1}|^2 |\delta_{\mathbf{k}_2}|^2 \rangle - \langle |\delta_{\mathbf{k}_1}|^2 \rangle \langle |\delta_{\mathbf{k}_2}|^2 \rangle \\ &= \langle \hat{P}(\mathbf{k}_1)\, \hat{P}(\mathbf{k}_2)\, \rangle - P(\mathbf{k}_1)\, P(\mathbf{k}_2) \qquad (4.4) \\ &= \langle\, \delta P\,(\mathbf{k}_1)\; \delta P\,(\mathbf{k}_2)\, \rangle \qquad (4.5) \end{aligned}$$

where $P(k)$, the ensemble-average power, comes from equation 4.1; $\hat{P}(\mathbf{k})$ is the power in a single mode:

$$\hat{P}(\mathbf{k}) = |\delta_{\mathbf{k}}|^2; \tag{4.6}$$

and $\delta P\,(\mathbf{k}) = \hat{P}\,(\mathbf{k}) - P\,(k)$. Relation 4.5 is dependent on two properties of Gaussian fields – a normal distribution for the one-point p.d.f., and the independence of the Fourier modes (*i.e.* the modes should have uncorrelated phases). For a finite sample of a Gaussian field, there will therefore be correlations between the different power modes, with a two-point function for the power fluctuations which is the square of the two-point function for the Fourier amplitudes. For non-Gaussian fields in which intrinsic phase correlations exist, this result does not apply, and in section 4.6, specific non-Gaussian models in which the power correlations are broader than the Gaussian prediction are considered. This does not prove that all conceivable non-Gaussian fields could be detected in this way, but it does show that the correlations of the fluctuating power field give a necessary condition for the field to be considered Gaussian. Figure 4.1 shows how the measured field appears for the IRAS-galaxy data described in section 4.5.

## 4.3 Proof of $\langle|\delta_{k_1}|^2|\delta_{k_2}|^2\rangle$ relation

This relation is easily proved for Fourier modes which are independent. However, for a redshift survey with a selection function, we are left to deal with Fourier modes which are a convolution of the 'underlying' Fourier mode with the transform of the selection function, and in this case the proof becomes more tricky.

We shall start with the easy case. Clearly if $\mathbf{k}_1 \neq \mathbf{k}_2$, then $\langle|\delta_{\mathbf{k}_1}|^2|\delta_{\mathbf{k}_2}|^2\rangle = \langle|\delta_{\mathbf{k}_1}|^2\rangle\langle|\delta_{\mathbf{k}_2}|^2\rangle$. In the case $\mathbf{k}_1 = \pm\mathbf{k}_2$, then we have $\langle|\delta_{\mathbf{k}_1}|^4\rangle = 2\langle|\delta_{\mathbf{k}_1}|^2\rangle^2$ for a Gaussian distribution. So the whole answer can be written as:

$$\langle|\delta_{\mathbf{k}_1}|^2|\delta_{\mathbf{k}_2}|^2\rangle = \langle|\delta_{\mathbf{k}_1}|^2\rangle\langle|\delta_{\mathbf{k}_2}|^2\rangle + |\langle\delta_{\mathbf{k}_1}\delta^*_{\mathbf{k}_2}\rangle|^2 + |\langle\delta_{\mathbf{k}_1}\delta_{\mathbf{k}_2}\rangle|^2. \tag{4.7}$$

Now let us examine the convolved mode case. We can write the convolved modes ($\delta'_k$) in terms of convolutions with the underlying modes. For a single mode, this is just:

$$\delta'_{\mathbf{k}_1} = \frac{1}{(2\pi)^3}\int \delta_{\mathbf{k}'}\tilde{\psi}_{\mathbf{k}_1-\mathbf{k}'}\mathrm{d}\mathbf{k}'. \tag{4.8}$$

So for power correlations, we can write:

$$\langle|\delta'_{\mathbf{k}_1}|^2|\delta'_{\mathbf{k}_2}|^2\rangle = \frac{1}{(2\pi)^{12}}\int\langle\delta_{\mathbf{k}_a}\delta_{\mathbf{k}_b}\delta_{\mathbf{k}_c}\delta_{\mathbf{k}_d}\rangle\tilde{\psi}_{\mathbf{k}_1-\mathbf{k}_a}\tilde{\psi}^*_{\mathbf{k}_1+\mathbf{k}_b}\tilde{\psi}_{\mathbf{k}_2-\mathbf{k}_c}\tilde{\psi}^*_{\mathbf{k}_2+\mathbf{k}_d}\mathrm{d}\mathbf{k}_a\mathrm{d}\mathbf{k}_b\mathrm{d}\mathbf{k}_c\mathrm{d}\mathbf{k}_d. \tag{4.9}$$

Now the four point average under the integral sign is only non-zero under the following conditions:

$$\begin{aligned} \mathbf{k}_a &= -\mathbf{k}_b \quad , \quad \mathbf{k}_c = -\mathbf{k}_d \ ; \\ \mathbf{k}_a &= -\mathbf{k}_c \quad , \quad \mathbf{k}_b = -\mathbf{k}_d \ ; \\ \mathbf{k}_a &= -\mathbf{k}_d \quad , \quad \mathbf{k}_b = -\mathbf{k}_c \ ; \end{aligned} \tag{4.10}$$

so we can rewrite the four point average under the integral as:

$$\begin{aligned} \langle\delta_{\mathbf{k}_a}\delta_{\mathbf{k}_b}\delta_{\mathbf{k}_c}\delta_{\mathbf{k}_d}\rangle &= \langle|\delta_{\mathbf{k}_a}|^2|\delta_{\mathbf{k}_c}|^2\rangle\delta^D(\mathbf{k}_a+\mathbf{k}_b)\,\delta^D(\mathbf{k}_c+\mathbf{k}_d) \\ &+ \langle|\delta_{\mathbf{k}_a}|^2|\delta_{\mathbf{k}_d}|^2\rangle\delta^D(\mathbf{k}_a+\mathbf{k}_c)\,\delta^D(\mathbf{k}_b+\mathbf{k}_d) \\ &+ \langle|\delta_{\mathbf{k}_a}|^2|\delta_{\mathbf{k}_b}|^2\rangle\delta^D(\mathbf{k}_a+\mathbf{k}_d)\,\delta^D(\mathbf{k}_c+\mathbf{k}_b)\,. \end{aligned} \tag{4.11}$$

Now, substituting equation 4.7 into equation 4.11, and taking care not to double count instances where $|\mathrm{k}_a| = |\mathrm{k}_b| = |\mathrm{k}_c| = |\mathrm{k}_d|$ gives:

$$\langle \delta_{\mathrm{k}_a} \delta_{\mathrm{k}_b} \delta_{\mathrm{k}_c} \delta_{\mathrm{k}_d} \rangle = (2\pi)^6 P(k_a) P(k_c) \delta^D(\mathrm{k}_a + \mathrm{k}_b) \delta^D(\mathrm{k}_c + \mathrm{k}_d) \quad (4.12)$$

$$+ (2\pi)^6 P(k_a) P(k_b) \delta^D(\mathrm{k}_a + \mathrm{k}_c) \delta^D(\mathrm{k}_b + \mathrm{k}_d) \quad (4.13)$$

$$+ (2\pi)^6 P(k_a) P(k_c) \delta^D(\mathrm{k}_a + \mathrm{k}_d) \delta^D(\mathrm{k}_c + \mathrm{k}_b) . \quad (4.14)$$

We now need to consider how each of the terms 4.12, 4.13, and 4.14 contribute to the integral. Term 4.12 reduces to:

$$\frac{1}{(2\pi)^6} \int P(k_a) |\tilde{\psi}(\mathrm{k}_1 - \mathrm{k}_a)|^2 \mathrm{d}\mathrm{k}_a \int P(k_b) |\tilde{\psi}(\mathrm{k}_2 - \mathrm{k}_b)|^2 \mathrm{d}\mathrm{k}_b = P'(k_1) P'(k_2) , \quad (4.15)$$

and term 4.13 gives:

$$\frac{1}{(2\pi)^6} \int |\langle \delta_{\mathrm{k}_a} \delta_{\mathrm{k}_b} \rangle|^2 \tilde{\psi}(\mathrm{k}_1 - \mathrm{k}_a) \tilde{\psi}(\mathrm{k}_2 + \mathrm{k}_a) \tilde{\psi}^\star(\mathrm{k}_1 + \mathrm{k}_b) \tilde{\psi}^\star(\mathrm{k}_2 - \mathrm{k}_b) \mathrm{d}\mathrm{k}_a \mathrm{d}\mathrm{k}_b = |\langle \delta'_{\mathrm{k}_1} \delta'_{\mathrm{k}_2} \rangle|^2 . \quad (4.16)$$

Finally, term 4.14 gives:

$$\frac{1}{(2\pi)^6} \int |\langle \delta_{\mathrm{k}_a} \delta_{\mathrm{k}_b} \rangle|^2 \tilde{\psi}(\mathrm{k}_1 - \mathrm{k}_a) \tilde{\psi}^\star(\mathrm{k}_2 - \mathrm{k}_a) \tilde{\psi}^\star(\mathrm{k}_1 + \mathrm{k}_b) \tilde{\psi}(\mathrm{k}_2 + \mathrm{k}_b) \mathrm{d}\mathrm{k}_a \mathrm{d}\mathrm{k}_b = |\langle \delta'_{\mathrm{k}_1} \delta'^{\star}_{\mathrm{k}_2} \rangle|^2 . \quad (4.17)$$

So at last we get for the convolved four point ensemble average:

$$\langle |\delta'_{\mathrm{k}_1}|^2 |\delta'_{\mathrm{k}_2}|^2 \rangle = P'(k_1) P'(k_2) + |\langle \delta'_{\mathrm{k}_1} \delta'^{\star}_{\mathrm{k}_2} \rangle|^2 + |\langle \delta'_{\mathrm{k}_1} \delta'_{\mathrm{k}_2} \rangle|^2 , \quad (4.18)$$

which is the same relation as for the uncorrelated modes. We can generally neglect the last term in this relation, on the grounds that for a selection function narrower than $\simeq |k_1|^{-1}$, modes separated by $|\mathrm{k}_1 + \mathrm{k}_2|$ will be uncorrelated.

## 4.4 Definition of the power correlation function

Quantitatively, we can define a power correlation function, $\xi_P$ as follows:

$$\xi_P(\Delta\mathrm{k}) = \frac{\left\langle [\hat{P}(\mathrm{k}) - P(k)] [\hat{P}(\mathrm{k} - \Delta\mathrm{k}) - P(k - \Delta k)] \right\rangle}{\left\langle [\hat{P}(\mathrm{k}) - P(k)]^2 \right\rangle} \quad (4.19)$$

This is simply $|\langle \delta_{\mathrm{k}_1} \delta^*_{\mathrm{k}_2} \rangle|^2$ as in equation 4.5, but normalised so that $\xi_P(0) = 1$. We can now consider how to evaluate this function for practical datasets.

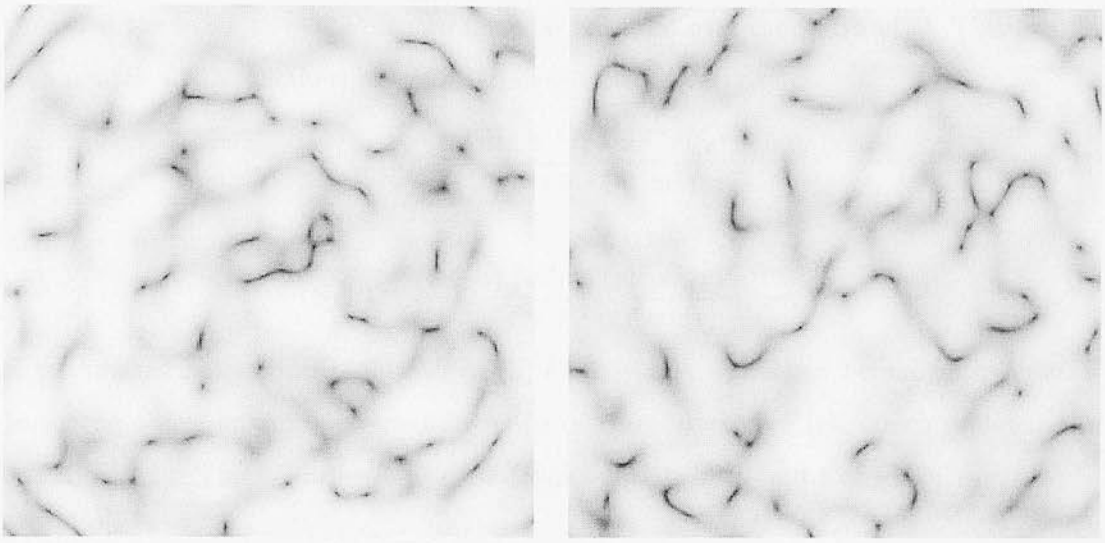

Figure 4.1: The fluctuating power field from the IRAS data described in Section 4.5. Equal area projections of power from shells of constant $|\mathbf{k}|$ are shown (Left panel at $k = 0.1\,h$ Mpc$^{-1}$, and right panel at $k = 0.15\,h$ Mpc$^{-1}$). Black corresponds to low, and white to high power. The panels have width $\Delta k = 0.25\,h$ Mpc$^{-1}$. While the power is not constant for a particular value of $|\mathbf{k}|$, there is a certain coherence scale over which there are significant correlations in power. As expected, this coherence scale does not appear to change with differing values of $|\mathbf{k}|$, and it forms the basis for a test for Gaussian fluctuations.

For a galaxy survey FKP defined the 'weighted galaxy fluctuation field', $F(\mathbf{r})$ as

$$F(\mathbf{r}) \equiv \frac{w(\mathbf{r})[n_g(\mathbf{r}) - \alpha n_s(\mathbf{r})]}{[\int d^3r\ \overline{n}^{\,2}(\mathbf{r})\ w^2(\mathbf{r})\ ]^{\,1/2}} \tag{4.20}$$

where $n_g(\mathbf{r}) = \Sigma_i\ \delta_{\rm D}(\mathbf{r} - \mathbf{r}_i)$ with $\mathbf{r}_i$ being the galaxy position vectors. The smooth background density is subtracted via the analogous number density $n_s$, which applies to a synthetic catalogue with number density $1/\alpha$ times that of the real catalogue. $\overline{n}(\mathbf{r})$ is the expected mean density of galaxies given the angular and luminosity selection criteria, and $w(\mathbf{r})$ is a weighting function designed to minimise the variance in power by favouring distant galaxies while the shot noise is not a dominant contributor to the power. We have used the weighting function from FKP, which is:

$$w(\mathbf{r}) = [1 + \overline{n}(\mathbf{r})P(k)\ ]^{-1}. \tag{4.21}$$

If this survey comes from an underlying Gaussian distribution, then FKP showed that the power correlation function would be of the form:

$$\xi_P\,(\Delta\mathbf{k}) = \frac{|\ P\,(k)\,Q\,(\Delta\mathbf{k}) + S\,(\Delta\mathbf{k})\ |^2}{[P\,(k) + S\,(0)]^{\,2}}, \tag{4.22}$$

provided the mean power, $P$ can be taken as constant over the width of Q. This expression contains two functions of the mean density:

$$Q(\mathbf{k}) \equiv \frac{\int d^3r\ \overline{n}^{\,2}(\mathbf{r})\ w^2(\mathbf{r})\ e^{i\mathbf{k}\cdot\mathbf{r}}}{\int d^3r\ \overline{n}^{\,2}(\mathbf{r})\ w^2(\mathbf{r})} \tag{4.23}$$

and

$$S(\mathbf{k}) \equiv \frac{(1+\alpha)\int d^3r\ \overline{n}(\mathbf{r})\ w^2(\mathbf{r})\ e^{i\mathbf{k}\cdot\mathbf{r}}}{\int d^3r\ \overline{n}^{\,2}(\mathbf{r})\ w^2(\mathbf{r})}. \tag{4.24}$$

$S$ is the shot noise contribution to $\langle \tilde{F}(\mathbf{k})\,\tilde{F}^{\star}(\mathbf{k}+\delta\mathbf{k})\rangle$. This can be shown by considering the above ensemble average in terms of transforms of $F(\mathbf{r})$, which is defined in equation 4.20. The following derivation follows that in section 2.1 of FKP:

$$\begin{aligned}\left\langle \tilde{F}(\mathbf{k})\,\tilde{F}^{\star}(\mathbf{k}+\delta\mathbf{k})\right\rangle &= A\int\langle w(\mathbf{r})[n_g(\mathbf{r})-\alpha n_s(\mathbf{r})]w(\mathbf{r}')[n_g(\mathbf{r}')-\alpha n_s(\mathbf{r}')]\rangle \\ &\qquad \times e^{-i(\mathbf{k}+\delta\mathbf{k})\cdot\mathbf{r}+i\mathbf{k}\cdot\mathbf{r}'}d^3rd^3r' \\ &= A\int w(\mathbf{r})w(\mathbf{r}')\overline{n}(\mathbf{r})\,\overline{n}(\mathbf{r}')\,\xi(\mathbf{r}-\mathbf{r}')\,e^{-i\delta\mathbf{k}\cdot\mathbf{r}}e^{i\mathbf{k}\cdot(\mathbf{r}'-\mathbf{r})}d^3rd^3r' \\ &\quad +A(1+\alpha)\int w(\mathbf{r})w(\mathbf{r}')\overline{n}(\mathbf{r})\,\delta_{\mathrm{D}}(\mathbf{r}-\mathbf{r}')\,e^{-i\delta\mathbf{k}\cdot\mathbf{r}}e^{i\mathbf{k}\cdot(\mathbf{r}'-\mathbf{r})}d^3rd^3r',\end{aligned} \tag{4.25}$$

where $1/A = \int d^3r\overline{n}^2(\mathbf{r})\,w^2(\mathbf{r})$ is the normalisation factor in equation 4.20, and we have used (from Chapter 1 and equation (2.1.5) in FKP) the following relations:

$$\begin{aligned}\langle n_g(\mathbf{r})\,n_g(\mathbf{r}')\rangle &= \overline{n}(\mathbf{r})\,\overline{n}(\mathbf{r}')\,[1+\xi(\mathbf{r}-\mathbf{r}')]+\overline{n}(\mathbf{r})\,\delta_{\mathrm{D}}(\mathbf{r}-\mathbf{r}'), \\ \langle n_g(\mathbf{r})\,n_s(\mathbf{r}')\rangle &= \alpha^{-2}\overline{n}(\mathbf{r})\,\overline{n}(\mathbf{r}')+\alpha^{-1}\overline{n}(\mathbf{r})\,\delta_{\mathrm{D}}(\mathbf{r}-\mathbf{r}'), \\ \langle n_s(\mathbf{r})\,n_s(\mathbf{r}')\rangle &= \alpha^{-1}\overline{n}(\mathbf{r})\,\overline{n}(\mathbf{r}').\end{aligned} \tag{4.26}$$

The term containing $\xi(\mathbf{r}-\mathbf{r}')$ in equation 4.25 can be written in terms of the power spectrum, and so becomes

$$A\int d^3rd^3r'\frac{d^3k''}{(2\pi)^3}w(\mathbf{r})w(\mathbf{r}')\overline{n}(\mathbf{r})\,\overline{n}(\mathbf{r}')\,P(k'')\,e^{-i\mathbf{r}'\cdot(\mathbf{k}''+\mathbf{k}-\delta\mathbf{k})}e^{i\mathbf{r}\cdot(\mathbf{k}''+\mathbf{k})}. \tag{4.27}$$

Since the selection function is narrow compared with the rate of change in the power spectrum, $P(k)$ can be pulled out of the integral, and term 4.27 reduces to

$$\begin{aligned}&AP(k)\int d^3rd^3r'\frac{d^3k''}{(2\pi)^3}w(\mathbf{r})w(\mathbf{r}')\overline{n}(\mathbf{r})\,\overline{n}(\mathbf{r}')\,e^{i(\mathbf{k}''+\mathbf{k})\cdot(\mathbf{r}-\mathbf{r}')}e^{i\mathbf{r}'\cdot\delta\mathbf{k}} \\ &\quad = AP(k)\int d^3rd^3r'w(\mathbf{r})w(\mathbf{r}')\overline{n}(\mathbf{r})\,\overline{n}(\mathbf{r}')\,\delta_{\mathrm{D}}(\mathbf{r}-\mathbf{r}')\,e^{-i\mathbf{r}'\cdot(\mathbf{k}-\delta\mathbf{k})+i\mathbf{r}\cdot\mathbf{k}} \\ &\quad = AP(k)\int d^3r\overline{n}^2(\mathbf{r})\,w^2(\mathbf{r})e^{i\delta\mathbf{k}\cdot\mathbf{r}}.\end{aligned} \tag{4.28}$$

This finally gives

$$\langle \tilde{F}(\mathbf{k})\,\tilde{F}^{\star}(\mathbf{k}+\delta\mathbf{k})\rangle = P(k)\,\frac{\int d^3r\;\overline{n}^{\,2}(\mathbf{r})\;w^2(\mathbf{r})\;e^{i\delta\mathbf{k}\cdot\mathbf{r}}}{\int d^3r\;\overline{n}^{\,2}(\mathbf{r})\,w^2(\mathbf{r})} + (1+\alpha)\,\frac{\int d^3r\;\overline{n}(\mathbf{r})\;w^2(\mathbf{r})\;e^{i\delta\mathbf{k}\cdot\mathbf{r}}}{\int d^3r\;\overline{n}^{\,2}(\mathbf{r})\,w^2(\mathbf{r})}. \tag{4.29}$$

Now from equations 4.18 and 4.19, $\xi_P(\Delta k)$ for a Gaussian field is given by:

$$\xi_P(\Delta k) = \frac{|\langle \tilde{F}(\mathbf{k})\,\tilde{F}^{\star}(\mathbf{k}+\Delta\mathbf{k})\rangle|^2}{\langle|\tilde{F}(\mathbf{k})|^2\rangle^2} \tag{4.30}$$

so the idea now is to estimate $\xi_P$ via equation 4.19 and to compare this with the Gaussian prediction in equations 4.30 and 4.29.

## 4.5 Application to IRAS Galaxies

### 4.5.1 Method

The power correlation function, $\xi_P$ was found for a combined dataset of $\sim 4500$ IRAS galaxies, consisting of the QDOT 1-in-6 0.6 Jy redshift survey (see Efstathiou *et al.* 1990; Lawrence *et al.* 1996) and the Berkeley 1.2 Jy redshift survey (Fisher *et al.* 1993, Fisher *et al.* 1995). The power in each Fourier mode, $(= |\delta_{\mathbf{k}}|^2)$ was found following the procedure described in FKP (see also Tadros & Efstathiou 1995), using a direct Fourier transform of the survey, and choosing $\sim 6000$ random orientations in the $k$-space shell over which to perform the integration. This was to sample power modes close enough together in $k$ space to determine the shape of the correlation function accurately. For an estimator of $P(k)$, $\hat{P}(\mathbf{k})$ has been averaged over these different orientations in the $k$-space shell:

$$P(k) \simeq \frac{1}{M\,N}\sum_{i=1}^{M}\sum_{j=1}^{N}\hat{P}(k,\theta_i,\phi_j). \tag{4.31}$$

$\xi_P$ was then evaluated using the assumption that the ensemble average can be replaced by an average over different orientations in $k$ space. This assumption holds for a Gaussian field, which is the hypothesis we will be testing against. There is a small amount of anisotropy introduced by the angular part of the mask, so in comparing $\xi_P(\Delta k)$ with its

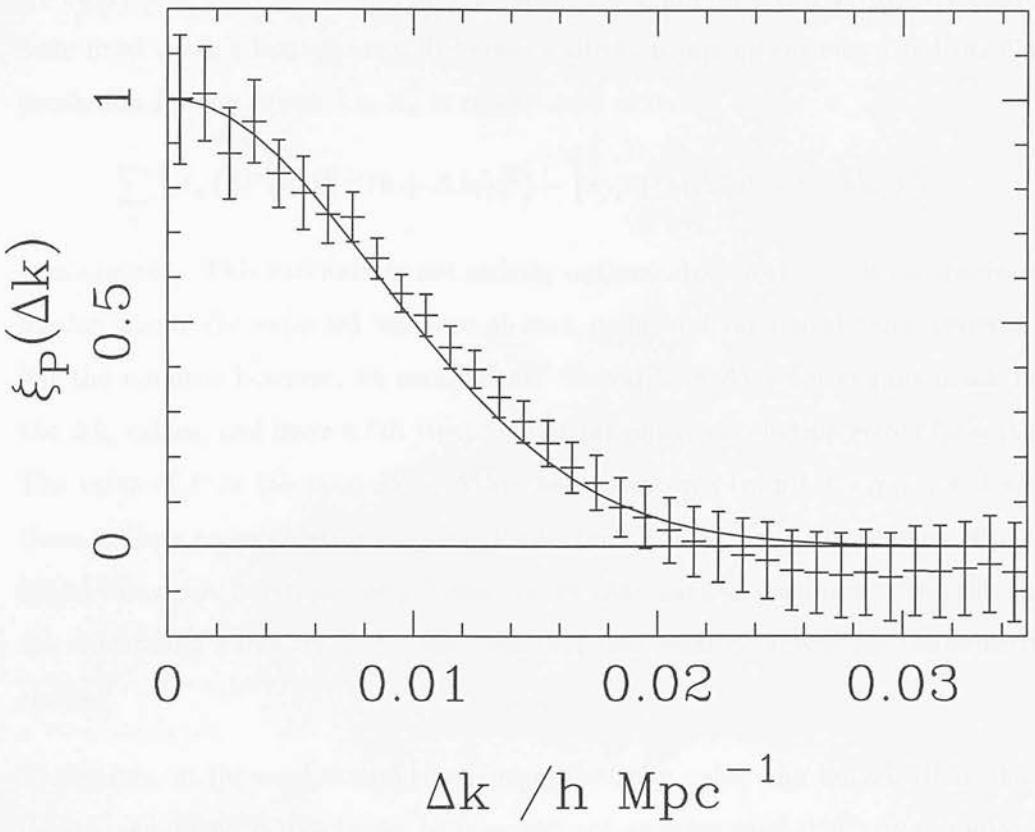


Figure 4.2: The power correlation function for the QDOT + 1.2 Jy survey. The solid line is the theoretical prediction for this survey if the underlying distribution is Gaussian. Error bars are based on Monte Carlo simulations of the deviations from the theoretical form for Gaussian surveys of the same size as the QDOT + 1.2 Jy. The correlations have been measured on a scale $|k| = 0.08\,h\,\mathrm{Mpc}^{-1}$.

theoretical prediction, $Q$, and $S$ have also been averaged over the different orientations in the $k$-space shell.

The normalisation of $\xi_P$ depends on the correct evaluation of the mean power, $P$, which can lead to problems if there are not enough independent patches in $k$ space to get an accurate estimate. This can be overcome by evaluating $\langle |F(\mathbf{k}_1)|^2 |F(\mathbf{k}_2)|^2 \rangle$ on a shell of fixed $|\mathbf{k}|$, for which the mean power is a constant. The normalisation is then left as a free parameter to fit for. The fitting can be done in a number of ways – for example one could use the fact that in the Gaussian case, at large $k$-separations $\langle |F(\mathbf{k}_1)|^2 |F(\mathbf{k}_2)|^2 \rangle \rightarrow \langle |F(\mathbf{k}_1)|^2 \rangle \langle |F(\mathbf{k}_2)|^2 \rangle$, and so use the tail of the curve as an estimate for $P(k) + P_{\mathrm{shot}}$. Similarly one could use the Gaussian relation for zero $k$-separation:

$\langle |F(\mathbf{k}_1)|^4 \rangle = 2\langle |F(\mathbf{k}_1)|^2 \rangle^2$. For this work, the amplitude of $\langle |F(\mathbf{k}_1)|^2 |F(\mathbf{k}_2)|^2 \rangle$ has been fixed using a least squares fit between all the points on the curve and the Gaussian prediction for the curve. *i.e.* $A_n$ is chosen such that:

$$\sum_i \left[ A_n \left\langle |F(\mathbf{k})|^2 |F(\mathbf{k}+\Delta\mathbf{k}_i)|^2 \right\rangle - \{P(k)\,Q(\Delta\mathbf{k}_i) + S(\Delta\mathbf{k}_i)\}^2 \right]^2 \tag{4.32}$$

is minimised. This estimate is not strictly optimal since it does not incorporate information about the expected variance at each point and the correlations between them. For the moment however, we assume that the variance does not change much between the $\Delta k_i$ values, and leave a full treatment of the power correlation errors for section 4.7. The value of $P$ in the term $PQ + S$ has been measured from the survey, and although there is likely to be an error associated with this, it is not too critical, since $S(\Delta k)$, and $Q(\Delta k)$ have similar functional forms. Since this method does not affect the shape of the correlation curve, it is the normalisation that least compromises the sensitivity of the test.

The values of $|\mathbf{k}|$ used were chosen experimentally using the criteria that the scales probed should be in the linear regime, but not so large that shot noise dominates the signal. The $k$-space shell also needed to have large enough radius for there to be enough independent coherent patches over which to find an average power correlation function.

The galaxy coordinates are in redshift space, and so peculiar velocities may affect the predicted shape of $\xi_P$. Empirically this is found to be a small effect, in the sense that $\xi_P$ appears to be similar in the radial and transverse directions, and it is examined in detail in the following chapter.

### 4.5.2 Results

Figure 4.2 is a plot of the power correlation function for the QDOT and 1.2 Jy survey with the prediction for an underlying Gaussian distribution. The error bars are based on expected deviations from the curve for a catalogue that has an underlying Gaussian distribution. These have been determined from a set of Monte Carlo simulations of the galaxy catalogue with Gaussian initial conditions, and finding the spread in the shape of the correlation functions. The simulations have been set up to have the same power

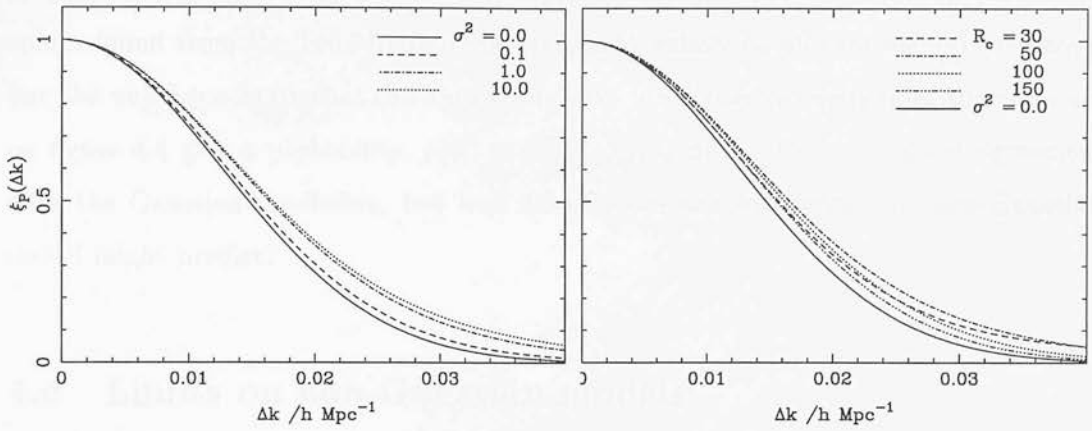


Figure 4.3: Predicted shapes of the correlation function for a product of Gaussian field: $\delta(\mathbf{r}) = \delta_G(\mathbf{r})[1 + \eta(\mathbf{r})]$ for varying forms of the power spectrum of $\eta$, $\langle|\eta_k|^2\rangle$. In the left panel, the modulating scale, $R_c$ is fixed at $50\,h^{-1}$ Mpc, and the different lines represent different values of $\sigma^2$: From the bottom up, the lines are for (1) zero amplitude of modulation (*i.e.* a Gaussian field); (2) $\sigma^2 = 0.1$; (3) $\sigma^2 = 1.0$; and (4) (the uppermost) $\sigma^2 = 10.0$. The right hand panel has a fixed amplitude, $\sigma^2$ of 3.0, with varying modulating scales. From the bottom up, line (1) is for the Gaussian prediction as in the graph above; (2) $R_c = 150\,h^{-1}$ Mpc; (3) the dashed line is for $R_c = 30\,h^{-1}$ Mpc; (4) $R_c = 100\,h^{-1}$ Mpc; and (5) (the uppermost line) for $R_c = 50\,h^{-1}$ Mpc.

spectrum as the initial catalogue, and have been generated by Poisson sampling from the parent simulations, giving all fake surveys the same angular mask and selection function as the real catalogue.

The figure shows that the QDOT+1.2 Jy survey appears to lie within the error bars predicted for an initial Gaussian distribution. Quantitatively, the goodness of fit can be characterised by performing a $\chi^2$-type test on the data:

$$\psi^2 = \sum_i \frac{(o_i - e_i)^2}{\sigma_i^2}, \tag{4.33}$$

where $o_i$ is the set of observed data points, $e_i$ is the equivalent set expected for a Gaussian distribution, and $\sigma_i$ is the standard deviation for the observed data points, which we have taken to be the same as that found for the Gaussian case from the Monte Carlo simulations. $\psi^2$ does not follow the conventional $\chi^2$ distribution, since the data points themselves are correlated, making the actual number of degrees of freedom fewer than the number of data points.

The probability distribution for $\psi^2$ has been determined from a frequency plot of $\psi^2$ values found from the 100 Monte Carlo simulated galaxy catalogues mentioned above. For the null hypothesis that the data set follows the Gaussian prediction, the contours on figure 4.4 give a probability, $p(\psi^2 > \psi^2_{\rm measured}) = 68\%$. This is in good agreement with the Gaussian prediction, but how does it compare with what any non-Gaussian model might predict?

## 4.6 Limits on non-Gaussian models

Since the power correlation function for the Gaussian case is a function of the selection function only, one particular class of non-Gaussian models can be analysed with relative ease. This class is the product of a Gaussian field with another stochastic field, uncorrelated with the former:

$$\delta(\mathbf{r}) = \delta_G(\mathbf{r})\,[1 + \eta(\mathbf{r})\,]. \tag{4.34}$$

This has been suggested as a possible alternative form for the density field, both on empirical grounds by Peebles (1983), and in some inflationary scenarios involving multiple scalar fields (*e.g.* Yi & Vishniac 1993). Locally, this field looks Gaussian, but on larger scales it is modulated so that the amplitude of fluctuations varies in different parts of space giving rise to quiet and noisy regions. This is equivalent to a field with zero skewness, but non-zero kurtosis. The one-point p.d.f. is a simple test for this form of non-Gaussian behaviour; however a simple transformation of the field would restore a Gaussian looking p.d.f., but it would still be modulated in a way which the power correlations analysis could detect.

We can predict the form of $\xi_P$ by treating the $(1 + \eta)$ part of the field as an extra part of the selection function, so that

$$\overline{n}w \rightarrow \overline{n}w(1 + \eta) \tag{4.35}$$

in equations 4.23, and 4.24. Q then becomes:

$$Q' = Q + 2\,Q \star \eta_{\mathbf{k}} + Q \star \eta_{\mathbf{k}} \star \eta_{\mathbf{k}}, \tag{4.36}$$

and S:

$$S' = S + S \star \eta_{\mathbf{k}}. \tag{4.37}$$

We can now use equation 4.22 to obtain the modified correlation function:

$$\xi'_P(\Delta\mathbf{k}) = \left\langle \frac{|\, P(k)Q'(\Delta\mathbf{k}) + S'(\Delta\mathbf{k})\,|^2}{[\,P(k)Q'(0) + S'(0)\,]^2} \right\rangle. \tag{4.38}$$

Substituting in the terms for $Q'$ and $S'$ from equations 4.36 and 4.37, and setting $PQ'(0) + S'(0) \equiv P'$ for ease of notation, this becomes:

$$\begin{aligned} P'^2 \xi'_P(\Delta\mathbf{k}) &= \left\langle |\, PQ + S\,|^2 \right\rangle + \left\langle |\, (2PQ + S) \star \eta_{\mathbf{k}} + PQ \star \eta_{\Delta\mathbf{k}} \star \eta_{\Delta\mathbf{k}}\,|^2 \right\rangle \\ &+ \langle\, (PQ + S)\,[\,(2PQ + S) \star \eta_{\Delta\mathbf{k}} + PQ \star \eta_{\Delta\mathbf{k}} \star \eta_{\Delta\mathbf{k}}]^\star \rangle \\ &+ \langle \text{conj.} \rangle\,. \end{aligned} \tag{4.39}$$

Now, by noting that odd powers in $\eta_{\mathbf{k}}$ average to zero, and that

$$\langle |\, f \star \eta_{\mathbf{k}}\,|^2 \rangle = \langle |\, f\,|^2 \rangle \star \langle |\, \eta_{\mathbf{k}}\,|^2 \rangle, \tag{4.40}$$

where $f$ is a function uncorrelated with $\eta$, we can rewrite equation 4.39 as:

$$\begin{aligned} P'^2 \xi'_P(\Delta\mathbf{k}) &= \xi^G_P + \langle\, |\, 2P(k)\,Q + S\,|^2 \rangle \star \langle\, |\, \eta_{\Delta\mathbf{k}}\,|^2 \rangle \\ &+ \langle\, |\, P(k)\,Q \star \eta_{\Delta\mathbf{k}} \star \eta_{\Delta\mathbf{k}}\,|^2 \rangle \\ &+ \langle\, (P(k)\,Q + S)[P(k)\,Q \star \eta_{\Delta\mathbf{k}} \star \eta_{\Delta\mathbf{k}}]^\star + \text{conj.}\,\rangle, \end{aligned} \tag{4.41}$$

and this can be written as:

$$\begin{aligned} P'^2 \xi'_P(\Delta\mathbf{k}) &= \xi^G_P(\Delta\mathbf{k}) + \langle\, |2P(k)Q(\Delta\mathbf{k}) + S(\Delta\mathbf{k})\,|^2 \,\rangle \star \langle |\eta_{\Delta\mathbf{k}}| \rangle^2 \\ &+ P(k)^2 \langle\, |Q(\Delta\mathbf{k}) \star \eta_{\Delta\mathbf{k}} \star \eta_{\Delta\mathbf{k}}|^2 \,\rangle \\ &+ 2\langle\, \mathrm{Re}\{P(k)Q(\Delta\mathbf{k})\;[P(k)Q(\Delta\mathbf{k}) + S(\Delta\mathbf{k})]^\star\}\rangle \int \langle |\eta_{\mathbf{k}}|^2 \rangle\, d\mathbf{k}, \end{aligned} \tag{4.42}$$

where $\xi^G_P$ is the Gaussian contribution to the power correlation function. The effect of $\eta$ is to broaden the correlation function by an amount dependent on the power spectrum of the modulating field, thus acting like an unaccounted for part of the selection function. Since this non-Gaussian field is a product of a Gaussian with a modulating field, and the modulating part can be treated as part of the selection function, we are still justified in our use of the approximation that the ensemble average power can be replaced by an average over $k$-space orientations (equation 4.31).

Figure 4.3 shows different shapes of the power correlation function for a range of power spectra for $\eta$. We have parametrised this power spectrum by supposing that the stochastic process, $\eta$, is white noise with an amplitude $\sigma^2$, and a Gaussian cut-off on scales $R_c$, so that

$$P_\eta = \langle\, |\eta_k|^{\,2}\,\rangle = (2\,\sqrt{\pi}\,R_c)^3\,\sigma^2 \exp\left[-k^2 {R_c}^2\right], \tag{4.43}$$

and

$$\frac{1}{(2\pi)^3}\int P_\eta\, d^3\mathrm{k} = \sigma^2. \tag{4.44}$$

In the absence of shot noise, equation 4.42 reduces to:

$$\begin{aligned}
\langle\, |Q'(\Delta k)|^2\,\rangle &= \langle |Q + 2Q\star\eta_k + Q\star\eta_k\star\eta_k|^2\rangle \\
&= Q^2\,(\Delta k)\left(1+\sigma^2\right)^2 + 4Q^2\star P_\eta + 2Q^2\star P_\eta\star P_\eta \\
&= \left(1+\sigma^2\right)^2 \exp[-\Delta k^2/2\gamma^2] \\
&\quad +4\sigma^2\left[\frac{2R_c^2\gamma^2}{1+2R_c^2\gamma^2}\right]^{3/2} \exp\left[-\Delta k^2 R_c^2/\left(1+2R_c^2\gamma^2\right)\right] \\
&\quad +2\sigma^4\left[\frac{R_c^2\gamma^2}{1+R_c^2\gamma^2}\right]^{3/2} \exp\left[-\Delta k^2 R_c^2/\left(2+2R_c^2\gamma^2\right)\right],
\end{aligned} \tag{4.45}$$

where $Q^2\,(\Delta k)$ has been parametrised as $\exp[-\Delta k/2\gamma^2]$. This expression is illustrated in figure 4.3.

We are now in a position to constrain the amplitude and scale of modulation that could possibly be present in the observed density field. The measured value of $\psi^2$ for the QDOT+1.2 Jy survey from the Gaussian prediction can be used to specify the largest allowed value of $\psi^2$ at a given level of confidence. For a given deviation, we can find a set of values of $\sigma$ and $R_c$ for the power spectrum of $\eta$ which would give this level of departure from the Gaussian prediction. These contours are shown in figure 4.4.

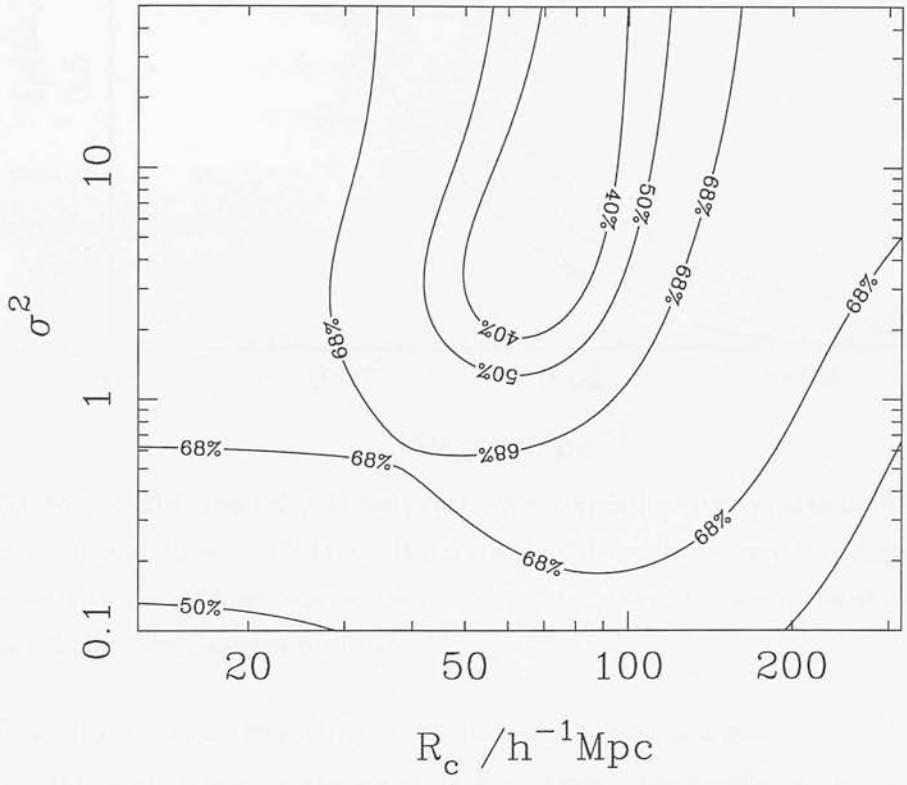


Figure 4.4: Contour plot of $\psi^2$ deviations in $R_c - \sigma^2$ parameter space for $|k| = 0.08\,h$ Mpc$^{-1}$. The contours represent different $\psi^2$ values for the deviation of $\xi_P$ from the Gaussian theoretical prediction. The 68% contour is the measured deviation, $\psi^2$ of $\xi_P$ for the QDOT+1.2 Jy survey from the Gaussian form. This corresponds to a probability that $\psi^2 > \psi^2_{\rm measured}$ of 68% if the survey is from a Gaussian distribution. The innermost contour indicates the region of parameter space for $\langle|\eta_k|^2\rangle$ that can be ruled out with 60% confidence as deduced from the form of $\xi_P$ for the QDOT+1.2 Jy, and the corresponding error bars. Clearly this is not a strong constraint on the parameters.

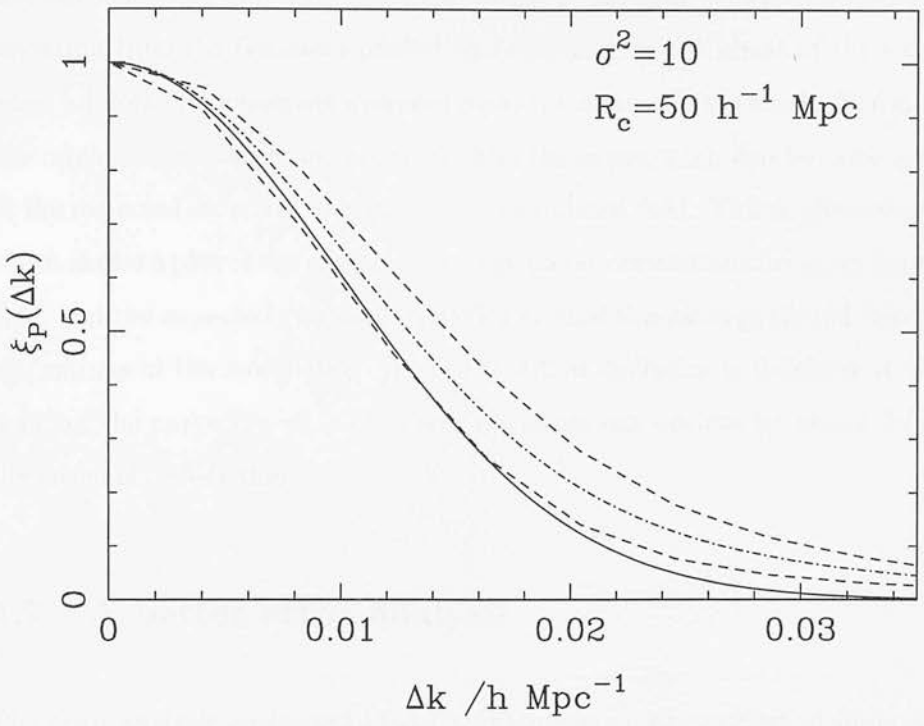


Figure 4.5: The expected variation in the power correlations for a modulated field of amplitude $\sigma^2 = 10$, and $R_c = 50\,h^{-1}\,\mathrm{Mpc}$. The dotted line shows the ensemble average prediction (c.f. figure 4.3), dashed lines indicate the one $\sigma$ deviation from this curve, and the solid line shows for reference the Gaussian prediction.

From figure 4.4, the sensitivity to modulations is peaked around scales of $\sim 80\,h^{-1}\,\mathrm{Mpc}$, and this scale is set by the depth of the survey. For smaller scale modulations, the effect on the power correlation function is to give extended wings at large $\Delta k$, and at small $\Delta k$, the dominant contribution to the shape is from the selection function. This effect, however is small at large $\Delta k$, and is comparable to or smaller than the expected deviations in the curve due to the finite number of coherence patches sampled. Sensitivity to such wings is also reduced because of the need to use the curve itself to normalise the power correlations (see equation 4.32). On large scales the sensitivity is lowered because there are fewer independent samples within the sample volume. Also, part of the effect of large scale modulations could be masked by the empirical determination of the selection function.

It is worth noting here that the ensemble prediction for large scale modulations is not necessarily meaningful when applied to a survey of comparable scale – this is because in

fact one is looking only at a single realisation of the field, which could show considerable deviation from the Gaussian prediction depending on the phase of the modulation, but when all possible phases are averaged over, the mean effect is small. The extent to which one might expect larger modulations than the expectation can be measured by looking at the expected standard deviation for a modulated field. This is illustrated in figure 4.5 which shows a plot of the ensemble average power correlations for a particular modulated field, and the expected standard deviation around this average (found from Monte Carlo realisations of the modulation $\eta$). The standard deviation is maximal at the half power point of the curve ($\xi_P = 1/2$), where the curve can deviate by about $\Delta\xi_P = 0.1$ from the ensemble prediction.

## 4.7 A better error analysis

The error analysis performed above is dependent on the number of shots and coherence patches for the shells. This section deals with a theoretical approach to analysing errors in the power correlation curve, making it possible to predict the errors without having to run Monte-Carlo simulations.

The first step is to compute the covariance function for the power correlations function. On the surface, this eight point function looks dauntingly tedious to calculate, but we apply the same principles as for the four point proof, and the terms drop out after a bit of combinatoric crunching. The main key to calculating this function is to remember that terms in the integrand such as

$$\psi\left(\mathbf{k}_1 - \mathbf{k}_a\right)\psi\left(\mathbf{k}_2 + \mathbf{k}_a\right) \tag{4.46}$$

oscillate to zero, so we only have to consider pairs of $\psi, \psi^\star$, and there are 24 of these, as opposed to 2520 pair combinations in total. It is then easiest to break these pairs into those that pair with themselves, yielding $|\psi\left(\mathbf{k}_1 - \mathbf{k}_a\right)|^2$ terms, and those that cross pair to give *e.g.* $\psi\left(\mathbf{k}_1 - \mathbf{k}_a\right)\psi^\star\left(\mathbf{k}_2 - \mathbf{k}_a\right)$. The problem then just becomes one of counting the number of different possible combinations of 'self' pairing, (s), and 'cross' pairing, (c). The account book is shown in table 4.1. Terms that 'self' pair give rise to $P_i'$, and 'cross' pair, $\langle\delta_i'\delta_j'^\star\rangle$, where the prime indicates that these are now functions convolved

| $\psi_1$ | $\psi_2$ | $\psi_3$ | $\psi_4$ | Number of combinations |
|---|---|---|---|---|
| s | s | s | s | 1 |
| c | c | c | c | 9 |
| s | c | c | c | 2 |
| c | s | c | c | 2 |
| c | c | s | c | 2 |
| c | c | c | s | 2 |
| s | s | c | c | 1 |
| c | s | s | c | 1 |
| c | c | s | s | 1 |
| c | s | c | s | 1 |
| s | c | s | c | 1 |
| s | c | c | s | 1 |

Table 4.1: Table showing the different combinations of 'cross' and 'self' pairing.

with the selection function, and subscripts $i$ and $j$ refer to $\mathbf{k}_i$ and $\mathbf{k}_j$. The end result is:

$$\begin{aligned}
\langle|\delta'_{k_1}|^2|\delta'_{k_2}|^2|\delta'_{k_3}|^2|\delta'_{k_4}|^2\rangle &= P'(k_1)\,P'(k_2)\,P'(k_3)\,P'(k_4) \\
&+ |\langle\delta'_1\delta'^{\star}_2\rangle|^2|\langle\delta'_3\delta'^{\star}_4\rangle|^2 + |\langle\delta'_1\delta'^{\star}_4\rangle|^2|\langle\delta'_2\delta'^{\star}_3\rangle|^2 + |\langle\delta'_1\delta'^{\star}_3\rangle|^2|\langle\delta'_2\delta'^{\star}_4\rangle|^2 \\
&+ \langle\delta'_1\delta'^{\star}_2\rangle\langle\delta'_2\delta'^{\star}_3\rangle\langle\delta'_3\delta'^{\star}_4\rangle\langle\delta'_4\delta'^{\star}_1\rangle + (5\text{ perms.}) \\
&+ 2P(k_1)\,\mathcal{R}e\left[\langle\delta'_2\delta'^{\star}_3\rangle\langle\delta'_3\delta'^{\star}_4\rangle\langle\delta'_4\delta'^{\star}_2\rangle\right] + (3\text{ perms.}) \\
&+ P(k_1)\,P(k_2)\,|\langle\delta'_3\delta'^{\star}_4\rangle|^2 + (5\text{ perms.}) \qquad (4.47)
\end{aligned}$$

From this, we can see that the points are likely to be correlated if $k_3$ and $k_4$ are within a coherence length of $k_1$ and $k_2$.

The covariance between the points on the four point correlation curve can be calculated from the above relation, and there are two possible approaches for doing this – the first is to evaluate all the spatial relationships between $k_1, k_2$ and $k_3, k_4$ that are used to evaluate the four point function, and average over all these combinations. Since the number of length pairs goes as $N^4$, and $N \sim 10^3$, this is not computationally realistic.

The second way is to take a more stochastic approach to the problem. In this approach,

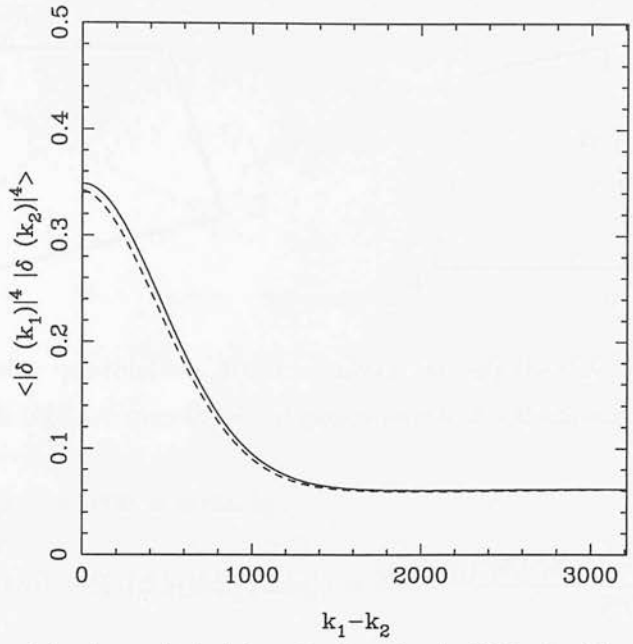


Figure 4.6: Plot of the theoretical eight point function (solid line) with a Monte Carlo simulation of the eight point function for comparison (dashed line).

the first step is to say that length pairs separated by more than some multiple of the coherence length are uncorrelated, so we only need to consider quadrilaterals formed within a coherence patch. The coherence patch is then approximated to be Euclidean rather than on the surface of a sphere, and a set of independent parameters are defined to specify the remaining four lengths of the quadrilateral given the lengths of two of the sides. These can be set up in a number of ways. One such set of parameters is given by the distance between the midpoints of lengths a and c, ($\equiv$ h), and the angles between a and h, ($\phi$), and c and h, ($\theta$) (see figure 4.7). These parameters can be set independently and their full range spans the full set of quadrilaterals given the sides $a$ and $c$.

Now since the estimate for $\xi_P$ is given by:

$$\xi_P(\Delta k) \simeq \frac{1}{N}\sum_{i=1}^{N}\left[\frac{|\delta'_{k_i}|^2|\delta'_{k_i+\Delta k}|^2}{P(k_i)\,P(k_i+\Delta k)} - 1\right] \equiv \frac{1}{N}\sum_{i=1}^{N}\hat{\xi}_i(\Delta k) \tag{4.48}$$

The covariance is given by:

$$\langle \xi_P(\Delta k_1)\,\xi_P(\Delta k_2)\rangle - \langle \xi_P(\Delta k_1)\rangle\langle \xi_P(\Delta k_2)\rangle = \tag{4.49}$$
$$\frac{1}{N_1 N_2}\sum_{i=1}^{N_1}\sum_{j=1}^{N_2}\left[\langle \hat{\xi}_i(\Delta k_1)\,\hat{\xi}_j(\Delta k_2)\rangle - \langle \hat{\xi}_i(\Delta k_1)\rangle\langle \hat{\xi}_j(\Delta k_2)\rangle\right],$$

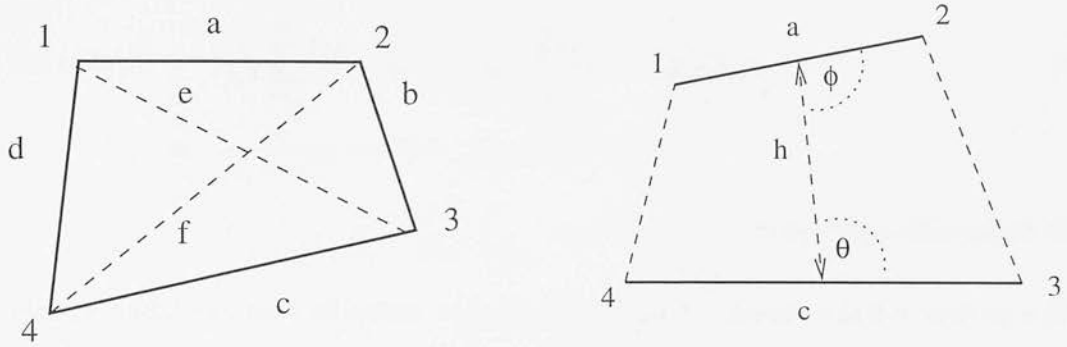


Figure 4.7: Left – quadrilateral. Right – diagram showing the three independent parameters, h, $\theta$ and $\phi$ which together span the set of quadrilaterals in a Euclidean plane.

where the bracketed term is given by:

$$\langle \hat{\xi}_i(\Delta k_1)\,\hat{\xi}_j(\Delta k_2)\rangle - \langle \hat{\xi}_i(\Delta k_1)\rangle\langle \hat{\xi}_j(\Delta k_2)\rangle = \frac{\langle |\delta'_a|^2|\delta'_b|^2|\delta'_c|^2|\delta'_d|^2\rangle - \langle |\delta'_a|^2|\delta'_b|^2\rangle\langle |\delta'_c|^2|\delta'_d|^2\rangle}{P(k)^4} \tag{4.50}$$

with $\Delta k_1 = \mathrm{k}_a - \mathrm{k}_b$, $\Delta k_2 = \mathrm{k}_c - \mathrm{k}_d$, for $\Delta k_1 \neq \Delta k_2$. Since the number of different combinations of quadrilaterals making up the term $\langle |\delta'_a|^2|\delta'_b|^2|\delta'_c|^2|\delta'_d|^2\rangle$ goes as the number of $k$-shots to the power of four, and the number of $k$-shots used is of order 1000, the sum in equation 4.49 can be replaced with an integral over all combinations of quadrilaterals, weighted by the probability of getting each combination. So the right hand side of equation 4.49 becomes:

$$\frac{1}{N_1 N_2}\sum_{i=1}^{N_1}\sum_{j=1}^{N_2}\left[\langle \hat{\xi}_i(\Delta k_1)\,\hat{\xi}_j(\Delta k_2)\rangle - \langle \hat{\xi}_i(\Delta k_1)\rangle\langle \hat{\xi}_j(\Delta k_2)\rangle\right] \simeq \tag{4.51}$$

$$\frac{1}{P(k)^4 N_c}\int \mathrm{cov}(\Delta k_1, \Delta k_2, h, \theta, \phi)\, p(h)\, p(\theta)\, p(\phi)\, \mathrm{d}h\, \mathrm{d}\theta\, \mathrm{d}\phi,$$

where $N_c$ is the number of coherence patches, given by the ratio of the area covered by the $k$-shots on the $k$-shell to the coherence area. 'cov' is given by:

$$\mathrm{cov}(a, c, h, \theta, \phi) \equiv \langle |\delta'_1|^2|\delta'_2|^2|\delta'_3|^2|\delta'_4|^2\rangle - \langle |\delta'_1|^2|\delta'_2|^2\rangle\langle |\delta'_3|^2|\delta'_4|^2\rangle, \tag{4.52}$$

and points $1, 2, 3, 4$ are related to $a, c, h, \theta, \phi$ as shown in figure 4.7. When $\Delta k_1 = \Delta k_2$, the covariance becomes the variance of $\xi$, $\Delta\xi^2$, and equation 4.51 needs to be modified slightly to allow for repeated instances of $\hat{\xi}_i$. We then get:

$$\begin{aligned}\Delta\xi\left(\Delta k_1\right)^2 &= \frac{1}{N_1^2}\sum_{i=1}^{N_1}\left[\hat{\xi}_i^2-\langle\hat{\xi}_i\rangle^2\right]+\frac{1}{N_1^2}\sum_{i\neq j}^{N_1}\left[\hat{\xi}_i\hat{\xi}_j-\langle\hat{\xi}_i\rangle\langle\hat{\xi}_j\rangle\right] \qquad (4.53)\\ &= \frac{1}{N_1 P\left(k\right)^4}\operatorname{cov}\left(\Delta k_1,\Delta k_1,0,\pi/2,\pi/2\right)\\ &\quad+\frac{1}{P\left(k\right)^4}\left[\frac{1}{N_c}-\frac{1}{N_1}\right]\int_{h,\theta,\phi}\operatorname{cov}\left(\Delta k_1,\Delta k_1,h,\theta,\phi\right)p\left(h\right)p\left(\theta\right)p\left(\phi\right)\mathrm{d}h\,\mathrm{d}\theta\,\mathrm{d}\phi.\end{aligned}$$

Now, $\theta$ and $\phi$ can take all values with equal frequency between 0 and $\pi$, and so $p\left(\theta\right)=p\left(\phi\right)=1/\pi$ and $h$ ranges from 0 to $2c_l$ where $c_l$ denotes the coherence patch radius. $p\left(h\right)$ is perhaps best determined empirically, and can be taken to be the same as the probability distribution of the length pairs, which is easily counted while computing $\xi_P$.

Figure 4.8 shows a comparison between the theoretical prediction derived above and the measured covariance matrix as derived from a set of 80 Monte-Carlo simulations of Gaussian distributed density fields. These independent estimates for the covariance agree within one sigma of the estimated Monte-Carlo covariances.

We are now in a position to use this statistic. Since many modes contribute to each estimate for $\xi_P$, this estimate can be taken to be Gaussian distributed about the ensemble mean prediction to a good approximation. So the probability that the data set in question has come from a Gaussian distribution can be expressed as a multivariate Gaussian:

$$p\left(\boldsymbol{\xi}_P\right)\propto\exp\left[-\frac{1}{2}\Delta\boldsymbol{\xi}_i C_{ij}^{-1}\Delta\boldsymbol{\xi}_j\right], \qquad (4.54)$$

where $\Delta\boldsymbol{\xi}_i=\xi_P\left(\Delta k_i\right)-\xi_P^{\mathrm{Gau}}\left(\Delta k_i\right)$ for values, $\Delta k_i$. $C_{ij}$ is the covariance matrix, 'cov', which we have derived above. The exponent:

$$\Delta\boldsymbol{\xi}_i C_{ij}^{-1}\Delta\boldsymbol{\xi}_j \qquad (4.55)$$

is then expected to have a $\chi^2$ distribution with as many degrees of freedom as there are points on the curve. This is because $C$ can be diagonalised and in this rotated frame, the elements of the new vector, $\boldsymbol{\xi}'$ are independent.

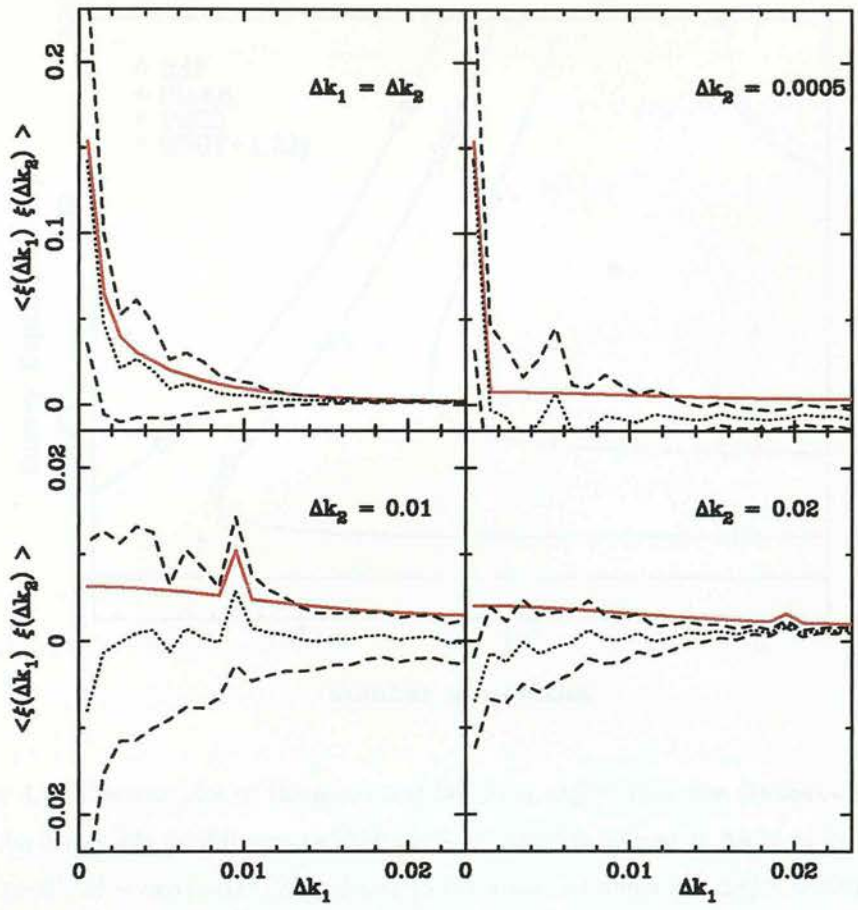


Figure 4.8: Comparison of the theoretical covariance curve with that determined empirically from 80 Monte-Carlo simulations. The red line indicates the theoretical prediction, dotted lines show the Monte-Carlo result, with one sigma error margins shown as dashed lines.

## 4.8 Improvements to sensitivity.

There are two principal factors affecting the sensitivity of the power correlations test. The first is the number of independent patches of $k$-space one can sample. Clearly for a given scale, the number of independent patches depends on the survey volume, $V$. The larger the volume of space sampled, the more information there is for a given scale, and so there are more independent modes contributing to a particular $k$-scale. We can write this as

$$N_c \simeq \frac{2\pi k^2}{\pi k_w^2}, \tag{4.56}$$

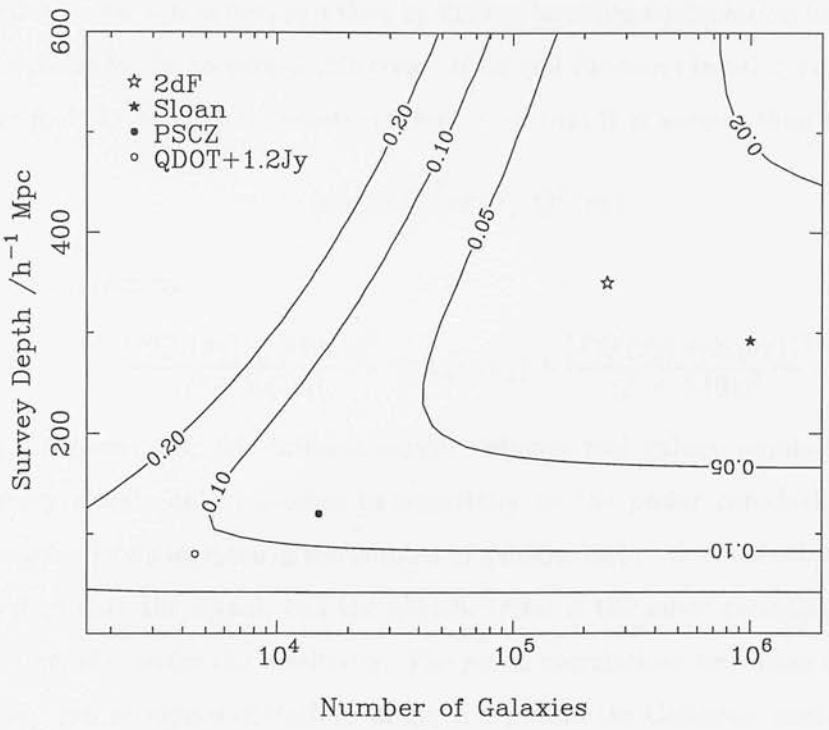


Figure 4.9: Contour plot of the minimum deviation, $\Delta\xi_P^{\min}$ from the Gaussian prediction that would be detectable for different redshift surveys. $\Delta\xi_P^{\min}$ is defined at $\Delta k = \sigma_k$ for a power correlation profile of $\sim \exp\left[-\Delta k^2/2\sigma_k^2\right]$. Inner to outermost contours are $\Delta\xi_P^{\min} = 0.02, 0.05, 0.1, 0.2$. The survey depth is taken to be roughly one third of the total extent of the survey.

where $N_c$ is the number of independent patches, and $k_w$ is the $k$-space width of the selection function ($k_w \propto V^{-1/3}$). Errors arising from taking a finite number of modes to sample $\xi$ therefore go down as the square root of $N_c$ (see equation 4.53).

The second factor affecting sensitivity is the shot noise, since $\xi_P(\delta k) = |PQ(\delta k) + S(\delta k)|^2/|P + S(0)|^2$. Now deviations from Gaussian clustering statistics result in changes to $Q$, so the larger the ratio $P : S(0)$, the less the information from $Q$ is swamped by that from $S$, which is not dependent on the galaxy distribution. We see from equation 4.24 that $S(0)$ is inversely proportional to the galaxy number density. Figure 4.9 shows a plot of how the sensitivity is dependent on redshift survey characteristic. The sensitivity is defined here as the minimum deviation from the Gaussian predicted curve that would be detectable given the errors. This has been found first by calculating $\Delta\xi_P(\sigma_k)$, (where $\sigma_k$ is the one sigma width of $\xi_P$) from equation 4.53 for the

given survey characteristics, and then by finding how large a deviation in $Q^2$ would have to be in order for $\xi_P$ to exceed this error. If we call the non-Gaussian curve $Q'$, then we want to find the minimum deviation, 'dev', such that it is greater than the error, $\Delta\xi_P$:

$$\text{dev} \equiv Q'^2(\sigma_k) - Q^2(\sigma_k) \tag{4.57}$$

where $Q'$ is given by:

$$\frac{|PQ'(\sigma_k) + S(\sigma_k)|^2}{|P + S(0)|^2} = \Delta\xi_P(\sigma_k) + \frac{|PQ(\sigma_k) + S(\sigma_k)|^2}{|P + S(0)|^2}. \tag{4.58}$$

Figure 4.9 plots 'dev' for different survey volumes and galaxy numbers. The size of the survey clearly only increases in sensitivity to the power correlations test if it is accompanied by an increase in the number of galaxies included, since otherwise shot noise effects dominate the signal, but the general trend is the more galaxies, and the larger the volume, the better the sensitivity. The power correlations test using the QDOT+1.2 Jy survey can recognise deviations of $\Delta\xi \simeq 0.2$ from the Gaussian prediction, and this looks set to improve by a factor of $4 - 10$ with the 2dF and Sloan redshift surveys, which are expected to contain $\sim 10^5$, and $\sim 10^6$ galaxies respectively (see *e.g.* Maddox *et al.* 1998 for the 2dF survey, Szalay 1998 for the Sloan survey). So for 2dF and Sloan type surveys, we can expect to be able to tighten limits on $\sigma^2$ by about one order of magnitude, and since the test is sensitive to modulations on scales of order the depth of the survey, we expect to be able to probe scales of around $300\,h^{-1}\,\text{Mpc}$.

## 4.9 Summary

This work suggests that power correlations can in principle be a useful tool in allowing quantitative limits to be placed on certain types of non-Gaussian fields. Present data sets unfortunately are not really sensitive to the effects of practical interest, but the sensitivity is expected to improve by about a factor of $4 - 10$ in the next generation of redshift surveys. The limits that have been placed on the modulated field apply to the ensemble average result, which is a conservative estimate given that for modulations of order the survey size, the power correlations might deviate much more than this, depending on the phase of the modulation. A natural extension to this work would

therefore be to include phase information about the modulated field as a parameter which can be constrained from the data.

The test is however expected to be affected by redshift distortions at a small level, and this needs to be allowed for to get maximum sensitivity from the test. This is examined in the following chapter.

# Chapter 5

# REDSHIFT DISTORTIONS

## 5.1 Introduction

A problem with mapping the density field using galaxies as tracers is the uncertainty about the line of sight distance to the galaxies. While Hubble's law, $\mathbf{v} = H_0\mathbf{r}$ (discussed in Chapter 1) relates a galaxy's Hubble flow velocity to its distance, it does not account for peculiar velocities induced by local fluctuations in the gravitational potential. A measure of a galaxy's recession velocity provides information about the sum of the Hubble flow velocity and the peculiar velocity along the line of sight, $\hat{\mathbf{r}}$:

$$v_{\text{recession}} = H_0 r + \hat{\mathbf{r}} \cdot \mathbf{v}_{\text{peculiar}}. \tag{5.1}$$

Redshift surveys use the galaxy recession velocity as a line of sight coordinate for the galaxy positions, and this clearly differs from a real space mapping because of the distorting effect of the peculiar velocities. On large scales, where the density field amplitude is relatively small, regions of higher overdensity are collapsing. Such overdensities (if they are distant) will appear to be squashed along the line of sight in redshift space because of the infall towards the centre of the clump. This will boost the apparent amplitude of fluctuations on large scales. On smaller scales where galaxies are in virialised clusters, the effect of the distortions is to spread out the galaxy redshift positions along the line of sight, giving rise to elongated structures which are commonly referred to as 'fingers of god'. These smear out the small scale power over a range of scales, and so act to

suppress power on smaller scales.

The anisotropic transfer of power to different scales results in the correlation function, $\xi(\mathbf{r})$, being a function of orientation, and this introduces correlations between the different Fourier modes. The loss of Fourier mode independence in redshift space affects the power correlations statistic discussed in Chapter 4. On large scales, for a Gaussian distribution, the redshift space densities are still Gaussian distributed because the transformation of the field is linear (as we shall see in equation 5.15), and so the relation (from Chapter 4):

$$\langle \delta P(k_1)\, \delta P(k_2) \rangle = |\langle \delta_{\mathbf{k}_1} \delta_{\mathbf{k}_2}{}^{*} \rangle|^2 \tag{5.2}$$

still holds. However, the correlation of the modes is now also affected by redshift induced correlations and these need to be accounted for.

The rest of this chapter deals with applying the redshift distortion formalism to density mode correlations with a view to accounting for redshift correlations in the power correlation statistic, and then to using the mode correlations as a method for measuring $\beta$. A standard formalism for the effect of redshift distortions on the measured density field is set up in section 5.2, and this is followed with a brief discussion of previous work in the field of redshift distortions in section 5.3. The effect of redshift distortions on the correlation between density Fourier modes is investigated in section 5.4, and the distortions' effect on the sensitivity of the power correlations test is discussed section 5.5. In sections 5.6, and 5.7 a statistic is developed to measure $\beta$, which is applied to simulations and IRAS galaxy catalogues. Finally, an improvement to the method for measuring $\beta$ is outlined in section 5.8.

## 5.2 Redshift distortion formalism

In this section we aim to derive the redshift space density in terms of the real space density to linear order. The formalism outlined here follows for the most part that of Kaiser (1987), with extensions from Zaroubi & Hoffman (1996) outlined in section 5.4.

If we denote the peculiar velocity along the line of sight, $\hat{\mathbf{r}} \cdot \mathbf{v}_{\text{peculiar}}$ as $U(\mathbf{r})$, then the

coordinates, $\mathbf{s}$ used in redshift space are:

$$\mathbf{s} = \frac{\mathbf{v}_{\text{recession}}}{H_0} \tag{5.3}$$

$$= \mathbf{r}\left[1 + \frac{U(\mathbf{r}) - U(\mathbf{0})}{r}\right], \tag{5.4}$$

where the units of $U$ have been chosen such that $H_0$ is 1, and $U(\mathbf{0})$ is a reference velocity for the measurements (for instance our velocity relative to the microwave background). In linear theory, the redshift space field can be treated as a transformation of the real space field, in which volume elements can reasonably be considered because the distortions are assumed to act continuously with a unique mapping from real to redshift space. Clearly, on cluster scales, where galaxies become virialised, while the transformation in equation 5.4 still holds, treatment of the galaxy distribution in terms of 'fluid' volume elements becomes difficult. This is because the mapping does not necessarily behave continuously, and 'one to many' mappings become likely if the element contains more than one galaxy. On linear scales, the radial distortion affects volume elements in redshift space in two ways – first there is some compression or extension along the line of sight, and second, the apparent size of the volume element is altered by the difference in perceived distance to the object. These distortions are given by the Jacobian, which is best derived by considering a volume element in spherical polar coordinates – $s^2 \mathrm{d}s\ \mathrm{d}\cos\theta\ \mathrm{d}\phi$ in redshift space, and $r^2 \mathrm{d}r\ \mathrm{d}\cos\theta\ \mathrm{d}\phi$ in real space. Following Kaiser's analysis (1987):

$$\begin{aligned}
\mathrm{d}^3\mathbf{s} &= s^2\ \mathrm{d}\cos\theta\ \mathrm{d}\phi\ \mathrm{d}s \\
&= r^2\left[1 + \frac{U(\mathbf{r}) - U(\mathbf{0})}{r}\right]^2 \mathrm{d}\cos\theta\ \mathrm{d}\phi\ \mathrm{d}r \frac{\mathrm{d}s}{\mathrm{d}r} \\
&= r^2\left[1 + \frac{U(\mathbf{r}) - U(\mathbf{0})}{r}\right]^2 \mathrm{d}\cos\theta\ \mathrm{d}\phi\ \mathrm{d}r\left[1 + \frac{\mathrm{d}U(\mathbf{r})}{\mathrm{d}r}\right] \\
&= \mathrm{d}^3\mathbf{r}\left[1 + \frac{U(\mathbf{r}) - U(\mathbf{0})}{r}\right]^2\left[1 + \frac{\mathrm{d}U(\mathbf{r})}{\mathrm{d}r}\right].
\end{aligned} \tag{5.5}$$

We can now use equation 5.5 to derive a relationship between real and redshift densities in terms of the redshift distortion parameter, $\beta = \Omega^{0.6}/b$. Since the number of galaxies is preserved, we have:

$$\rho^S(s)\,\mathrm{d}^3\mathbf{s} = \rho^R(r)\,\mathrm{d}^3\mathbf{r}, \tag{5.6}$$

so (ignoring for the moment the effect of selection functions)

$$\rho^S(s) = \rho^R(r)\left[1 + \frac{U(\mathbf{r}) - U(\mathbf{0})}{r}\right]^{-2}\left[1 + \frac{\mathrm{d}U(\mathbf{r})}{\mathrm{d}r}\right]^{-1}. \tag{5.7}$$

Now, expressing equation 5.7 in terms of the overdensity, $\delta = \rho/\overline{\rho} - 1$ and expanding to first order in $U$ gives:

$$\begin{aligned}\left[1+\delta^S(s)\right]\overline{\rho} &= \overline{\rho}\left[1+\delta^R(r)\right]\left[1-\frac{\mathrm{d}U(\mathbf{r})}{\mathrm{d}r}\right]\left[1-2\frac{U(\mathbf{r})-U(\mathbf{0})}{r}\right] \\ &= \overline{\rho}\left[1+\delta^R(r)\right]\left[1-\frac{\mathrm{d}U(\mathbf{r})}{\mathrm{d}r}-2\frac{U(\mathbf{r})-U(\mathbf{0})}{r}\right]. \qquad (5.8)\end{aligned}$$

In the distant observer approximation, the term $[U(\mathbf{r}) - U(\mathbf{0})]/r$ can be ignored on the grounds that $r$ is much larger than typical radial peculiar velocities. This is clearly a fair assumption if the redshift survey includes only 'distant' galaxies, but debatable for flux limited surveys. For the time being, however, we shall make the assumption, and assess its implications later on. So ignoring terms in $U/r$, we get:

$$\delta^S(s) = \delta^R(r)\left[1-\frac{\mathrm{d}U(\mathbf{r})}{\mathrm{d}r}\right]-\frac{\mathrm{d}U(\mathbf{r})}{\mathrm{d}r}. \qquad (5.9)$$

From linear theory (Peebles 1980, & Chapter 1), $U$ is related to the overdensity via the continuity equation, $\nabla \cdot \mathbf{v} \propto \delta$:

$$\mathbf{v}_\mathbf{k} = -i\beta\frac{\mathbf{k}}{k^2}\delta_\mathbf{k}, \qquad (5.10)$$

where $\beta$ is a function of the density parameter at the present epoch, and the linear bias parameter, $b$, and is well approximated by: $\beta = \Omega^{0.6}/b$. $U$ is therefore given by:

$$\begin{aligned}U &= \mathbf{v}\cdot\hat{\mathbf{r}} \qquad (5.11)\\ &= -\frac{\beta}{(2\pi)^3}\int \exp(-i\mathbf{k}\cdot\mathbf{r})\,\frac{(i\mathbf{k}\cdot\hat{\mathbf{r}})}{k^2}\delta^R(\mathbf{k})\,\mathrm{d}^3k. \qquad (5.12)\end{aligned}$$

Differentiating with respect to $r$ gives:

$$\frac{\mathrm{d}U}{\mathrm{d}r} = -\frac{\beta}{(2\pi)^3}\int \exp(-i\mathbf{k}\cdot\mathbf{r})\left(\frac{\mathbf{k}\cdot\mathbf{r}}{kr}\right)^2\delta^R(\mathbf{k})\,\mathrm{d}^3k. \qquad (5.13)$$

Substituting equation 5.13 into equation 5.9 then gives:

$$\delta^S(s) = \frac{\beta}{(2\pi)^3}\left[1+\delta^R(\mathbf{r})\right]\int \exp(-i\mathbf{k}\cdot\mathbf{r})\left(\frac{\mathbf{k}\cdot\mathbf{r}}{kr}\right)^2\delta^R(\mathbf{k})\,\mathrm{d}^3k+\delta^R(\mathbf{r}), \qquad (5.14)$$

which to first order in $\delta^R$ can be rewritten as:

$$\delta^S(\mathbf{s}) = \frac{1}{(2\pi)^3}\int \exp(-i\mathbf{k}\cdot\mathbf{r})\left[1+\beta\left(\frac{\mathbf{k}\cdot\mathbf{r}}{k\,r}\right)^2\right]\delta^R(\mathbf{k})\,\mathrm{d}^3k. \qquad (5.15)$$

For some survey geometries, this expression can be simplified somewhat. For instance in the distant observer approximation, $\mathbf{r}$ on the right hand side of equation 5.15 can

be replaced with $\mathbf{s}$ using equation 5.4. If the survey subtends a small solid angle, with centre $\mathbf{R}$, then $(\mathbf{k}\cdot\mathbf{r})\,/\,(k\,r)^2$ in equation 5.15 can be written as:

$$\left(\frac{\mathbf{k}\cdot\mathbf{r}}{k\,r}\right) = \frac{\mathbf{k}\cdot(\mathbf{r}'+\mathbf{R})}{k\sqrt{r'^2+R^2}}, \tag{5.16}$$

which for large $\mathbf{R}$ can be reduced to:

$$\frac{\mathbf{k}\cdot(\mathbf{r}'+\mathbf{R})}{k\sqrt{r'^2+R^2}} = \frac{\mathbf{k}\cdot\mathbf{R}}{k\,R} \equiv \mu. \tag{5.17}$$

In this limit, the Fourier modes are:

$$\delta^S(\mathbf{k}) = \delta^R(\mathbf{k})\,[1+\beta\mu^2]. \tag{5.18}$$

## 5.3 Previous work

The beautiful simplicity of the linear redshift space transformation, which was originally derived by Kaiser (1987), has led to many attempts to measure the redshift distortion parameter, $\beta$. These have followed a variety of methods, working both with correlation functions, and power spectra. The main results and methods used to date are described briefly in this section, but for a thorough review of the field of linear redshift distortions, consult Hamilton (1997). There have been three principal approaches to the measurement of $\beta$. The first has been to measure the angle averaged amplitude boost to the power spectrum, or correlation function; the second uses the ratio of quadrupole to monopole moments of the redshift space power spectrum; and the third is a maximum likelihood approach in which both the power spectrum and $\beta$ are parametrised, and chosen in such a way as to fit the data optimally.

### 5.3.1 Angle averaged redshift boost

Equation 5.18 in the previous section shows that in redshift space, Fourier modes have an increased amplitude by a factor $(1+\beta\mu^2)$. Applied to the power spectrum this gives a boost of:

$$P^s(k) = \left[1+2\mu^2\beta+\mu^4\beta^2\right]P(k)\,. \tag{5.19}$$

If this is averaged over all directions, this gives:

$$P^s(k) = \left[1 + \frac{2}{3}\beta + \frac{1}{5}\beta^2\right] P(k). \tag{5.20}$$

A similar relation is expected for the redshift space correlation function. This can be derived by working out the expectation $\langle \delta^s(\mathbf{s})\, \delta^s(\mathbf{s} + \Delta\mathbf{s}) \rangle$ using equation 5.15, invoking the distant observer approximation to bring $\mu$ out of the integral, and performing an angle average to calculate $\langle \mu^2 \rangle \equiv \langle \cos^2\theta \rangle_\theta$ and $\langle \mu^4 \rangle \equiv \langle \cos^4\theta \rangle_\theta$. The prediction of an amplitude increase has been tested using N-body simulations by *e.g.* Gramman *et al.* (1993). In these simulations, they assess over what scales the linear approximation in equation 5.20 would be expected to apply, and find that for $\Omega = 0.2$ the linear regime starts upwards of $60\,h^{-1}$ Mpc, and for $\Omega = 1.0$ it starts upwards of $200\,h^{-1}$ Mpc.

Clearly to measure the redshift boost of the power spectrum, one also needs the real space power spectrum. This can be deduced using a deprojection method if one has a large enough number of galaxies' angular positions. The real space power spectrum is related to the angular correlation function using Limber's equation (1954)(*e.g.* Peebles 1980, Coles & Lucchin 1995):

$$w(\theta) = \int_0^\infty y^4 \phi^2 \mathrm{d}y \int_{-\infty}^\infty \xi\left(\sqrt{x^2 + y^2\theta^2}\right) \mathrm{d}x, \tag{5.21}$$

where the selection function has been normalised so that $\int y^2 \phi(y)\, \mathrm{d}y = 1$, and the above relation applies for small angles $\theta$. This equation is obtained by considering the probability of finding two galaxies in a pair of volume cells within magnitude intervals $\delta M_1, \delta M_2$, and then integrating over the magnitude range (multiplied by the selection function), and over distance in the radial direction to get the number counts per angular separation assuming that the absolute magnitude of each galaxy is independent of its position with respect to other galaxies. In Fourier space, this can be recast in terms of spatial and angular power spectra (*e.g.* Peacock 1991):

$$\Delta_\theta{}^2(K) = \frac{\pi}{K} \int \Delta^2(Ky)\, y^5 \phi^2(y)\, \mathrm{d}y. \tag{5.22}$$

With both the real and redshift power spectra (or correlation functions), $\beta$ can be found from equation 5.20. The method works best if the redshift catalogue is drawn from the angular catalogue, since it samples the same structures, and reduces errors due to the variance in the power modes.

This method has been applied to a number of surveys – analysis of IRAS galaxies includes Fry & Gaztañaga (1994; FG94), who use a 2 Jy IRAS redshift survey (Strauss *et al.* 1992), and compare the volume averaged correlation function for conical and spherical shaped volume cells; and Saunders *et al.* (1991) who use the QDOT 0.6 Jy survey (Saunders *et al.* 1992) and compare its correlation function with the parent Point Source Catalog's angular correlation function.

For optical galaxies, FG94 have used the CfA1 (Huchra *et al.* 1983) and SSRS (da Costa *et al.* 1991) surveys; and Ratcliffe *et al.* (1997) have used the Durham/ UKST redshift survey and the Edinburgh/Durham Southern Galaxy Catalogue (Collins *et al.* 1988, Collins *et al.* 1992). Baugh (1996), Loveday *et al.* (1996a), and Tadros & Efstathiou (1996) have made use of the APM-Stromlo survey (Loveday 1996b) and compared it with the APM angular survey (Maddox *et al.* 1990, 1996). Peacock & Dodds 1994, Peacock 1997 used the APM angular survey and compared it with the APM-Stromlo & CfA2 (Vogeley *et al.* 1992) surveys.

Values found for $\beta$ using this method range between $0.20 \lesssim \beta_{\rm optical} \lesssim 1.10$ for optically selected galaxies, and $0.39 \lesssim \beta_{\rm IRAS} \lesssim 1.29$ for IRAS selected galaxies. This method is potentially sensitive to systematic errors, since it relies on measuring the power spectrum accurately from two different surveys using different techniques. This problem has motivated looking at the redshift anisotropy in more detail. Two techniques which can extract $\beta$ from a single redshift survey are described below. The rest of the chapter concentrates on developing a third method which can also be used to obtain $\beta$ from a single redshift survey.

### 5.3.2 Quadrupole to monopole ratio of the power spectrum

In this technique, the redshift space power spectrum from equation 5.19 is expanded in terms of Legendre polynomials, $\mathcal{P}_\ell(\mu)$:

$$P^s(k,\mu) = \sum_{\ell=0}^{\infty} P_\ell^s(k)\,\mathcal{P}_\ell(\mu)\,. \tag{5.23}$$

The moments, $P_\ell^s$ can be determined from the inversion formula:

$$P_\ell^s(k) \equiv \frac{2\ell+1}{2}\int_{-1}^{+1} \mathrm{d}\mu P^s(k,\mu)\,\mathcal{P}_\ell(\mu)\,, \tag{5.24}$$

and for equation 5.19 the power spectrum can be made up from the zeroth, second and fourth moments, where

$$P_0^s(k) = \left(1+\frac{2}{3}\beta+\frac{1}{5}\beta^2\right)P^R(k) \quad (5.25)$$

$$P_2^s(k) = \left(\frac{4}{3}\beta+\frac{4}{7}\beta^2\right)P^R(k) \quad (5.26)$$

$$P_4^s(k) = \left(\frac{8}{35}\beta^2\right)P^R(k) \quad (5.27)$$

for which the Legendre polynomials are $\mathcal{P}_0(\mu) = 1, \mathcal{P}_2(\mu) = (3\mu^2-1)/2, \mathcal{P}_4(\mu) = (35\mu^4-30\mu^2+3)/8$. Now, since the redshift distortions contribute differently to each of the moments of the power spectrum, a comparison of the different modes in the expansion can yield $\beta$. The main work on this has been carried out by Cole, Fisher & Weinberg (1994, 1995) who use the quadrupole ($P_2^s$) to monopole ($P_0^s$) ratio of the power spectrum to determine $\beta$ from the IRAS 1.2 and 0.6 Jy QDOT surveys. To keep the distant observer approximation and avoid the effects of the mask, they divide the survey into several subsurveys – each subtending an angle less than 50°. Using this method, they find $\beta$ to be $0.52 \pm 0.13$ for the 1.2 Jy survey, and $0.54 \pm 0.3$ for the QDOT survey.

A similar simpler method is to make use of the difference in redshift space correlations between separations that are parallel and perpendicular to the line of sight. This has been applied to the 1.2 Jy survey by Fisher *et al.* (1994), who find $\beta = 0.45^{+0.27}_{-0.18}$.

### 5.3.3 Spherical Harmonics – maximum likelihood

The spherical harmonic approach is also to determine the different modes of the power spectrum, breaking up the contributions into a radial part, and an angular part. The relative boost of the radial part compared with the angular part can be used to obtain $\beta$. This approach provides enough information to be able to fit independently for $\beta$ and a parametrised form for the power spectrum, and has been analysed using maximum likelihood approaches. The work in this area has been carried out on the 1.2 Jy survey by *e.g.* Fisher *et al.* (1994), who get $\beta \sim 1$; Heavens & Taylor (1995), who find $\beta = 1.1 \pm 0.3$, and Ballinger *et al.* (1995), who get $\beta = 1.04 \pm 0.3$. The spherical harmonic approach has also been tackled by Hamilton & Culhane (1996) who develop an operator formalism for analysing correlation functions in terms of spherical Eigen functions.

### 5.3.4 Higher order moments

Some work has also been carried out on the effect of redshift distortions on higher order moments. Fry & Gaztañaga (1994) conclude that the three and four point functions are quite insensitive to redshift distortions. Hivon *et al.* (1995) have used a Lagrangian approach to come up with theoretical predictions for the effect of redshift distortions on skewness and the bispectrum.

### 5.3.5 Translinear regime

The 'finger of god' effect, in which the velocities of galaxies in virialised clusters act to spread out the cluster along the line of sight in redshift space, becomes important on scales where the power spectrum amplitude reaches unity. In the mildly non-linear regime, this has been modelled by Peacock & Dodds (1994) as a convolution of the velocity distribution, $f(v)$ of galaxies in virialised clusters with the correlation function. The power spectrum is therefore simply reduced by a factor given by the Fourier transform of the velocity distribution, which for the distant observer approximation gives:

$$P^S(\mathbf{k}) = \tilde{f}(k\mu_{\mathbf{k}}) \left(1 + \beta\mu_{\mathbf{k}}^2\right)^2 P(k) . \tag{5.28}$$

$f(v)$ in the literature has been modelled both as a Gaussian velocity distribution, (*e.g.* Peacock & Dodds 1994; Heavens & Taylor 1995; Tadros & Efstathiou 1996) with

$$f(v) \propto \exp\left[-\frac{v^2}{2\sigma^2}\right] , \tag{5.29}$$

and as an exponential pairwise velocity distribution (*e.g.* Fisher *et al.* 1994):

$$f(v) \propto \exp\left[-\frac{\sqrt{2}\,|v|}{\sigma}\right] . \tag{5.30}$$

$\sigma$ in both these models (and in the rest of the chapter) is given by the pairwise radial velocity dispersion. The redshift space power spectrum is currently thought to be best fit by the exponential distribution (Park et al, 1994; Bromley, Warren & Zurek 1997).

### 5.3.6 Summary

Hamilton (1997), in his review, collates all the measurements of $\beta$ in the literature, and assigning equal weight to each author's value, finds the mean and standard deviation of $\beta$. For optically selected galaxies, he finds $\overline{\beta}_{\rm optical} = 0.52 \pm 0.26$, and for IRAS galaxies, $\overline{\beta}_{\rm IRAS} = 0.77 \pm 0.22$.

## 5.4 Correlation of Fourier modes.

The effect of redshift distortions is to mix scales anisotropically so that Fourier density modes become correlated. This section goes through the theory for analysing the correlations introduced as a result of redshift distortions. In outline it follows the unpublished work of Kaiser (private communication, 1993), and the published work of Zaroubi and Hoffman (1996), but this work is extended here to account for mildly non-linear scales. The formalism is then applied to a spherical survey geometry.

The level of correlation between redshift space Fourier modes is dependent on the angle between the Fourier wave-vectors, $\mathbf{k}_1$ and $\mathbf{k}_2$. Since this chapter involves much discussion about the angles between these two $k$-vectors, it is worth introducing some nomenclature here. The two main situations considered are (1) when $\mathbf{k}_1$ and $\mathbf{k}_2$ are parallel to each other (see figure 5.1, centre panel), and (2) when $\Delta\mathbf{k} \equiv \mathbf{k}_1 - \mathbf{k}_2$ is perpendicular to $\mathbf{k}_1$ (figure 5.1, right hand panel). For a given $|\Delta k|$, the latter case gives the maximum

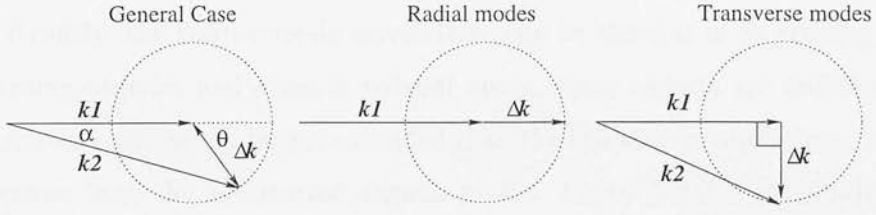


Figure 5.1: Diagram showing the angles between two $k$-vectors, $\mathbf{k}_1$, and $\mathbf{k}_2$. Circles indicate the locus of $\mathbf{k}_2$ for a given $\Delta k$. Radial modes have $\mathbf{k}_1$ parallel to $\mathbf{k}_2$ (*i.e.* $\theta = 0$, centre panel), and transverse Fourier modes have $\Delta\mathbf{k}$ perpendicular to $\mathbf{k}_1$ ($\theta = \pi/2$, right panel). The latter case gives the maximum possible angular separation, $\alpha$, of $\mathbf{k}_1$ and $\mathbf{k}_2$.

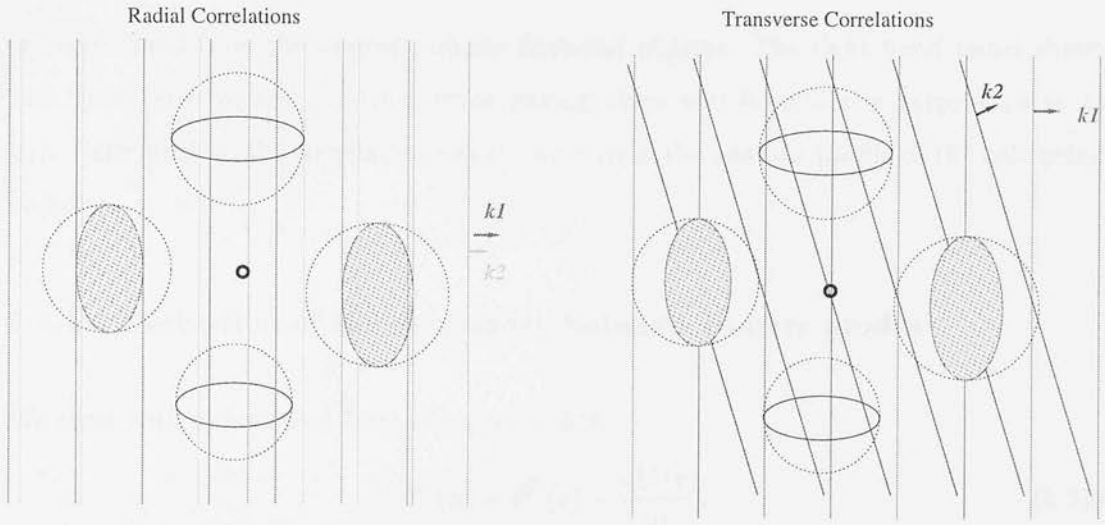


Figure 5.2: Diagram showing real and redshifted structures from an observer's point of view at 'o', in each panel. Circles indicate real space overdensities, and ellipses the same structure in redshift space. Parallel sets of lines represent the crests of Fourier waves. Shaded ellipses indicate the main contribution to the amplitude enhancement of the Fourier waves shown. The left panel shows two parallel wave-vectors, which derive most of their enhancement from the radially flattened shaded objects (hence the name radial correlations), and the right panel shows two Fourier waves whose vector separation is perpendicular to $\mathbf{k}_1$. These waves probe information about the objects' angular profiles, and correlations involving this set of wave-vectors are referred to as transverse correlations.

possible angle between $\mathbf{k}_1$ and $\mathbf{k}_2$ (for $|\Delta k| < |\mathbf{k}_1|$)[1]. Since most of the contribution to the parallel correlations comes from radially squashed structures, correlations arising between parallel $k$-modes will also be referred to as 'radial correlations'. Conversely, modes for which $\Delta\mathbf{k}$ is perpendicular to $\mathbf{k}_1$ will be referred to as 'transverse correlations'. Crudely, the Fourier mode correlations can be thought of as probing the profile of collapsing objects, and since in redshift space, these objects are radially flattened, radial correlations tend to be less extended than the transverse correlations, whose main signal comes from the undistorted angular profile. Figure 5.2 is a schematic picture of Fourier waves going through redshifted structure for an observer placed at the centre, 'o', of each diagram. The left panel shows two parallel waves, which derive a large part

[1]Note that the distant observer approximation is not used in this analysis, and 'parallel' and 'perpendicular' refer to the angle between one of the $k$-vectors, $\mathbf{k}_1$, and the separation $k$-vector, $\Delta\mathbf{k}$. It contains no 'line of sight' information.

of their signal from the shaded radially flattened objects. The right hand panel shows two 'transverse waves' (*i.e.* the vector joining these two $k$-vectors is perpendicular to $\mathbf{k}_1$). Here much of the correlation signal comes from the angular profile of the collapsing objects.

### 5.4.1 Derivation of the covariance between Fourier modes

We start with a linearised form of equation 5.9:

$$\delta^S(s) = \delta^R(\mathbf{r}) - \frac{\mathrm{d}U(\mathbf{r})}{\mathrm{d}r}. \tag{5.31}$$

In the presence of a selection function, $\Psi(\mathbf{r})$, the real space density is multiplied by the selection function, so the observed density field becomes:

$$\delta^S(s)' = \Psi(\mathbf{r})\left[\delta^R(r) - \frac{\mathrm{d}U(\mathbf{r})}{\mathrm{d}r}\right]. \tag{5.32}$$

Fourier transforming this gives:

$$\delta^S(\mathbf{k}) = \int \exp(i\mathbf{k}\cdot\mathbf{r})\,\Psi(\mathbf{r})\left[\delta^R(\mathbf{r}) - \frac{\mathrm{d}U(\mathbf{r})}{\mathrm{d}r}\right]\mathrm{d}^3r. \tag{5.33}$$

Now, substituting equation 5.13 for $\mathrm{d}U/\mathrm{d}r$ into equation 5.33 gives:

$$\delta^S(\mathbf{k}) = \frac{1}{(2\pi)^3}\int\int \exp(i\mathbf{k}\cdot\mathbf{r})\,\Psi(\mathbf{r})\exp(-i\mathbf{k}'\cdot\mathbf{r})\,\delta^R(\mathbf{k}')\left[1+\beta\left(\frac{\mathbf{k}'\cdot\mathbf{r}}{k'r}\right)^2\right]\mathrm{d}^3k'\mathrm{d}^3r. \tag{5.34}$$

The covariance of the observed Fourier modes, $\delta^S(\mathbf{k})$ is:

$$\begin{aligned}\langle\delta^S(\mathbf{k}_1)\,\delta^S(\mathbf{k}_2)^\star\rangle &= \frac{1}{(2\pi)^3}\int P(k'')\,\tilde{\Psi}(\mathbf{k}_1-\mathbf{k}'')\,\tilde{\Psi}^\star(\mathbf{k}_2-\mathbf{k}'')\;\mathrm{d}^3k'' \\ &+ \frac{\beta}{(2\pi)^3}\int P(k'')\left[\tilde{\Psi}(\mathbf{k}_1-\mathbf{k}'')\,\tilde{\Psi}^\star_{ij}(\mathbf{k}_2-\mathbf{k}'') + \tilde{\Psi}^\star(\mathbf{k}_1-\mathbf{k}'')\,\tilde{\Psi}_{ij}(\mathbf{k}_2-\mathbf{k}'')\right]\hat{k}''_i\hat{k}''_j\;\mathrm{d}^3k'' \\ &+ \frac{\beta^2}{(2\pi)^3}\int P(k'')\,\tilde{\Psi}_{ij}(\mathbf{k}_1-\mathbf{k}'')\,\tilde{\Psi}^\star_{lm}(\mathbf{k}_2-\mathbf{k}'')\,\hat{k}''_i\hat{k}''_j\hat{k}''_l\hat{k}''_m\;\mathrm{d}^3k'',\end{aligned} \tag{5.35}$$

where $\hat{k}_i$ is the unit vector component of $\mathbf{k}$ in the $\mathbf{r}$ direction. If the power spectrum can be taken to be constant over the width of the Fourier transformed selection function, then this simplifies to:

$$\begin{aligned}\langle\delta^S(\mathbf{k}_1)\,\delta^S(\mathbf{k}_1+\delta\mathbf{k})^\star\rangle &\simeq \\ P(k_1)&\left[\widetilde{\Psi^2}(\delta\mathbf{k}) + 2\beta\hat{k}_i\hat{k}_j\widetilde{\Psi^2}_{ij}(\delta\mathbf{k}) + \beta^2\hat{k}_i\hat{k}_j\hat{k}_l\hat{k}_m\widetilde{\Psi^2}_{ijlm}(\delta\mathbf{k})\right],\end{aligned} \tag{5.36}$$

where

$$\widetilde{\Psi^2}(\mathbf{k}) = \frac{1}{(2\pi)^3}\int \mathrm{d}^3k'\tilde{\Psi}(\mathbf{k}')\,\tilde{\Psi}^{\star}(\mathbf{k}'+\mathbf{k}) = \int \mathrm{d}^3r\Psi^2(\mathbf{r})\,e^{i\mathbf{k}\cdot\mathbf{r}} \tag{5.37}$$

$$\widetilde{\Psi^2}_{ij}(\mathbf{k}) = \frac{1}{2(2\pi)^3}\int \mathrm{d}^3k'\left(\tilde{\Psi}(\mathbf{k}')\,\tilde{\Psi}^{\star}_{ij}(\mathbf{k}'+\mathbf{k}) + \tilde{\Psi}_{ij}(\mathbf{k}')\,\tilde{\Psi}^{\star}(\mathbf{k}'+\mathbf{k})\right)$$

$$= \int \mathrm{d}^3r\Psi^2(\mathbf{r})\,\hat{r}_i\hat{r}_j e^{i\mathbf{k}\cdot\mathbf{r}}$$

$$\widetilde{\Psi^2}_{ijlm}(\mathbf{k}) = \frac{1}{(2\pi)^3}\int \mathrm{d}^3k'\tilde{\Psi}_{ij}(\mathbf{k}')\,\tilde{\Psi}^{\star}_{lm}(\mathbf{k}'+\mathbf{k}) = \int \mathrm{d}^3r\Psi^2(\mathbf{r})\,\hat{r}_i\hat{r}_j\hat{r}_l\hat{r}_m e^{i\mathbf{k}\cdot\mathbf{r}}.$$

### 5.4.2 Extension into the mildly non-linear regime

An extension to take into account the effects of the mildly non-linear regime can be made using the velocity dispersion factor mentioned in subsection 5.3.5. In Fourier space the Gaussian velocity distribution (equation 5.29) becomes:

$$\tilde{f}(k\mu_{\mathbf{k}}) = \exp\left[-\frac{(\sigma k\mu_{\mathbf{k}})^2}{2}\right], \tag{5.38}$$

and the exponential distribution (equation 5.30) becomes:

$$\tilde{f}(k\mu_{\mathbf{k}}) = \frac{1}{1+\frac{1}{2}(\sigma k\mu_{\mathbf{k}})^2}. \tag{5.39}$$

For the work used here, we use the first two terms of the Taylor expansion of the Fourier space velocity distribution on the assumption that $(\sigma k)^2 \lesssim 1$, which corresponds to scales of $k \simeq 0.3\,h\,\mathrm{Mpc}^{-1}$ for velocity dispersions $\sigma \simeq 350\ \mathrm{km\,s}^{-1}$, so the precise nature of the distribution of the pairwise velocities is of little consequence.

We start by assuming that individual Fourier modes are also reduced by a factor $[\tilde{f}(k\mu_{\mathbf{k}})]^{1/2}$, so the Fourier modes become:

$$\delta^S_{\mathbf{k}} \to \delta_{\mathbf{k}}\left[1+\beta\mu^2\right]\left[1-k^2\mu^2\sigma^2/4\right] \star \tilde{\Psi}(\mathbf{k}), \tag{5.40}$$

where $\mu \equiv \mu_{\mathbf{k}} \equiv \mathbf{k}\cdot\mathbf{r}/(kr)$ is now taken to be defined under the integral over all $\mathbf{r}$ as in equation 5.34:

$$\delta^S(\mathbf{k}) = \frac{1}{(2\pi)^3}\int\int\{\exp(-i\mathbf{k}\cdot\mathbf{r}+i\mathbf{k}'\cdot\mathbf{r})\ \mathrm{x}$$

$$\Psi(\mathbf{r})\,\delta^R(\mathbf{k}')\left[1+\beta\left(\frac{\mathbf{k}'\cdot\mathbf{r}}{k'r}\right)^2\right]\left[1-\frac{k^2\sigma^2}{4}\left(\frac{\mathbf{k}'\cdot\mathbf{r}}{k'r}\right)^2\right]\}\mathrm{d}^3k'\mathrm{d}^3r. \tag{5.41}$$

If we neglect terms to fourth order in $k\sigma$, (which is consistent with the approximation used for the Fourier transformed velocity distribution) then the covariance of the modes becomes:

$$\begin{aligned}\left\langle \delta^S\left(\mathbf{k_1}\right)\delta^S\left(\mathbf{k_1}+\delta\mathbf{k}\right)^*\right\rangle \simeq\ & P\left(k_1\right)\Big[\,\widetilde{\Psi^2}\left(\delta\mathbf{k}\right)+2\beta\hat{k}_i\hat{k}_j\widetilde{\Psi^2}_{ij}\left(\delta\mathbf{k}\right) \\ & \qquad +\beta^2\hat{k}_i\hat{k}_j\hat{k}_l\hat{k}_m\widetilde{\Psi^2}_{ijlm}\left(\delta\mathbf{k}\right)\Big] \\ & -P\left(k_1\right)\frac{\sigma^2k^2}{4}\Big[\,\hat{k}_i\hat{k}_j\widetilde{\Psi^2}_{ij}\left(\delta\mathbf{k}\right)+2\beta\hat{k}_i\hat{k}_j\hat{k}_l\hat{k}_m\widetilde{\Psi^2}_{ijlm}\left(\delta\mathbf{k}\right) \\ & \qquad +\beta^2\hat{k}_i\hat{k}_j\hat{k}_l\hat{k}_m\hat{k}_n\hat{k}_p\widetilde{\Psi^2}_{ijlmnp}\left(\delta\mathbf{k}\right)\Big]. \qquad (5.42)\end{aligned}$$

While this looks somewhat intractable, it is simplified a great deal for a spherical survey.

### 5.4.3 Spherical surveys

The results from the previous two sections can be applied quite easily to a spherical survey. Since this simplifies the integrals considerably, it is a good model to use to show how the mode correlations are affected by redshift distortions. In order to solve equation 5.42, we need to be able to evaluate integrals of the form used in equations 5.37:

$$\int \mathrm{d}^3r\ f\left(r\right)\left[\hat{r}_i\cdots\hat{r}_j\right]_n\ e^{i\mathbf{k}\cdot\mathbf{r}}. \qquad (5.43)$$

These can be rewritten as a differential under the integral:

$$\begin{aligned}\int \mathrm{d}^3r\ f\left(r\right)\left[\hat{r}_i\cdots\hat{r}_j\right]_n\ e^{i\mathbf{k}\cdot\mathbf{r}} &= \int\frac{f\left(r\right)}{r^n}\left\{\frac{\partial}{i\partial k_i}\cdots\frac{\partial}{i\partial k_j}\right\}_n e^{i\mathbf{k}\cdot\mathbf{r}}\mathrm{d}^3r \\ &= \left\{\frac{\partial}{i\partial k_i}\cdots\frac{\partial}{i\partial k_j}\right\}_n\int\frac{f\left(r\right)}{r^n}e^{i\mathbf{k}\cdot\mathbf{r}}\mathrm{d}^3r \\ &= \left\{\frac{\partial}{i\partial k_i}\cdots\frac{\partial}{i\partial k_j}\right\}_n 4\pi\int\frac{f\left(r\right)}{r^{n-2}}j_0\left(kr\right)\mathrm{d}r, \qquad (5.44)\end{aligned}$$

where $j_0\left(x\right)=\sin x/x$. We can now use the recursion relation for spherical Bessel functions:

$$\frac{\mathrm{d}}{\mathrm{d}x}\left[x^{-n}j_n\left(x\right)\right]=-x^{-n}j_{n+1}\left(x\right). \qquad (5.45)$$

Applying the above mechanism to equation 5.36 and defining $\nu\equiv\mathbf{k}\cdot\delta\mathbf{k}/\left(|\mathbf{k}||\delta\mathbf{k}|\right)$ gives for the integrals of functions of $\Psi^2\left(\mathbf{r}\right)$:

$$\hat{k}_i\hat{k}_j\widetilde{\Psi}^2_{ij} = 4\pi\int\mathrm{d}r\ r^2\Psi^2\left(r\right)\left\{\frac{j_1\left(kr\right)}{kr}-\nu^2j_2\left(kr\right)\right\} \qquad (5.46)$$

$$\hat{k}_i\hat{k}_j\hat{k}_l\hat{k}_m\widetilde{\Psi}^2_{ijlm} = 4\pi\int \mathrm{d}r\; r^2\Psi^2(r)\left\{3\frac{j_2(kr)}{(kr)^2} - 6\nu^2\frac{j_3(kr)}{kr} + \nu^4 j_4(kr)\right\}, \quad (5.47)$$

where $j_n$ are spherical Bessel functions of order $n$. Finally, for the quasi-linear regime, $\widetilde{\Psi}^2_{ijlmnp}$ in equation 5.42 is given by:

$$\hat{k}_i\hat{k}_j\hat{k}_l\hat{k}_m\hat{k}_n\hat{k}_p\widetilde{\Psi}^2_{ijlmnp} = \quad (5.48)$$
$$4\pi\int \mathrm{d}r\; r^2\Psi^2(r)\left\{15\frac{j_3(kr)}{(kr)^3} - 45\nu^2\frac{j_4(kr)}{(kr)^2} + 15\nu^4\frac{j_5(kr)}{(kr)} - \nu^6 j_6(kr)\right\}.$$

These integrals can be evaluated numerically to predict the mode correlations for different values of $\beta$, and how these change in the quasi-linear regime. We can now write the correlations in terms of coefficients of $\nu$, where $\nu$ is cosine of the angle between the k-vector for one of the Fourier modes, and the separation vector, $\mathbf{\Delta k}$ between the two Fourier modes. This will prove to be useful later on in this chapter. In the linear regime, we have:

$$\langle\delta^S(\mathbf{k_1})\,\delta^S(\mathbf{k_1}+\delta\mathbf{k})^*\rangle = P(k_1)\times \quad (5.49)$$
$$\left\{\mathcal{J}_0(\delta k) + 2\beta\mathcal{J}_2(\delta k) + 3\beta^2\mathcal{J}_3(\delta k) + \nu^2[2\beta\mathcal{J}_1(\delta k) + 6\beta^2\mathcal{J}_4(\delta k)] + \nu^4\beta^2\mathcal{J}_5(\delta k)\right\},$$

where $\mathcal{J}_n$ are the integrals of the Bessel functions above with coefficients of $\beta$ and $\nu$. For example $\mathcal{J}_2$ is given by:

$$\mathcal{J}_2(\delta k) = 4\pi\int \mathrm{d}r\; r^2\Psi^2(r)\left\{\frac{j_1(kr)}{kr}\right\}. \quad (5.50)$$

### 5.4.4 The effect of $\beta$ on density mode correlations

In this section equations 5.36 and 5.42 are integrated up for a Gaussian spherically symmetric selection function to show the effect of redshift distortions on the mode correlations. Figure 5.3 shows the theoretical prediction for mode correlations in the linear regime (*i.e.* neglecting the damping effect of randomised cluster velocities) for radial and transverse modes for $\beta = 0.5$ (top) and $\beta = 1.0$ (bottom). The characteristic scale over which parallel (radial) modes are correlated is smaller than the real space correlation because objects are squashed relative to their real space counterparts and parallel modes pick up this radial squashing. Transverse modes probe information about an object's unsquashed state, and so the correlations are broader than radial correlations.

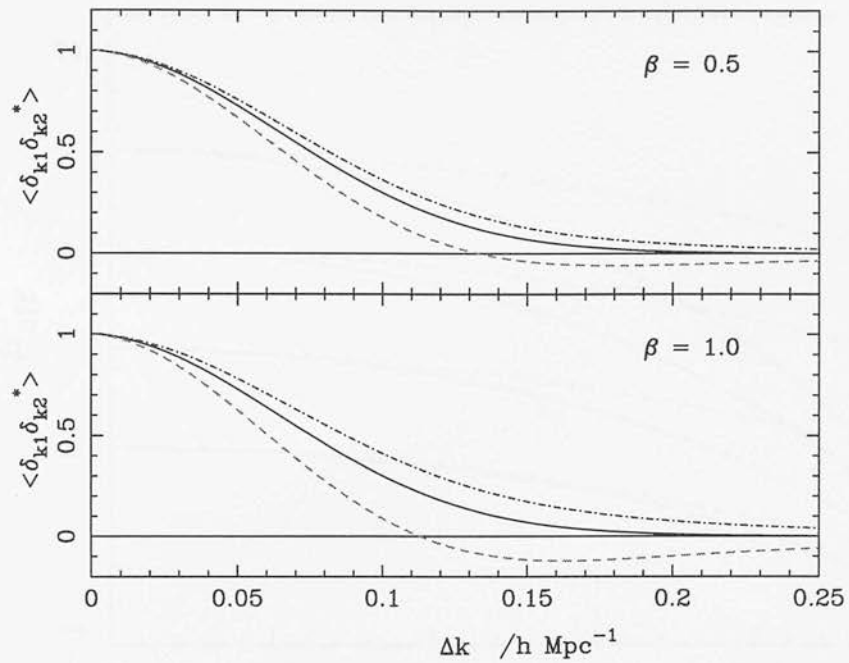


Figure 5.3: The expected effect of redshift distortions on the radial and transverse correlation curves. These curves probe the linear regime (small $k$), where the effect of damping from virialised clusters has been neglected. The top panel has $\beta = 0.5$, and the bottom panel $\beta = 1.0$. Dashed lines indicate the radial correlations and dot-dashed the transverse correlations. The solid line shows the correlation in the absence of redshift distortions.

On smaller scales where the finger of god effect becomes important, the radial modes become correlated over larger $\Delta k$ separations, and the initial effect is to decrease the separation between the radial and transverse curves. A measurement of $\beta$ on these scales without taking into account the velocity dispersion would give a lower estimate of $\beta$ than its 'true' value. We shall define the 'effective $\beta$' to be the value that one would measure for $\beta$ from the difference in correlations between radial and transverse modes *neglecting* the damping effect of virialised clusters, *i.e.* the best fit parameter $\beta$ that would be obtained if the correlation curves were modelled only from equation 5.49. Figure 5.4 shows how the estimated value of $\beta$ ('effective $\beta$') would be expected to change with scale.

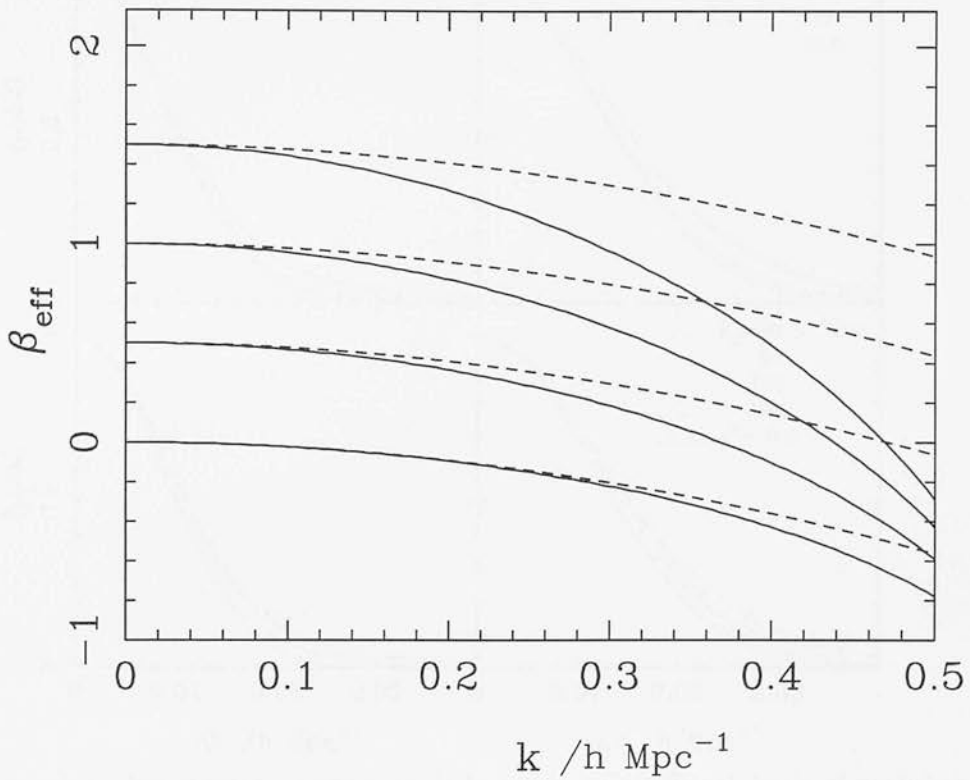


Figure 5.4: Solid lines show the effective $\beta$ for the mode correlation statistic at different scales. The velocity dispersion used here is 300 kms$^{-1}$, and the dashed line indicates how the effective $\beta$ inferred from the amplitude boost of the redshift space power spectrum relative to the real space power spectrum is expected to change with scale (also neglecting the damping effects of virialised clusters). At $k = 0$, $\beta_{\rm eff} = \beta_{\rm true}$, but on smaller scales, the effect of incoherent velocities becomes noticeable. This damping effect appears to be more marked for the mode correlation method of determining $\beta$.

## 5.5 The effect of redshift distortions on the power correlations test for modulated fields.

For a Gaussian distributed field, the power correlation statistic is simply the square of the Fourier mode correlation function, so in redshift space $\beta$ will also affect the correlations of the power modes. In the absence of knowledge of $\beta$, the Gaussian prediction for the power correlation curve is not precisely known, and so the sensitivity of the test for non-Gaussian fields is reduced.

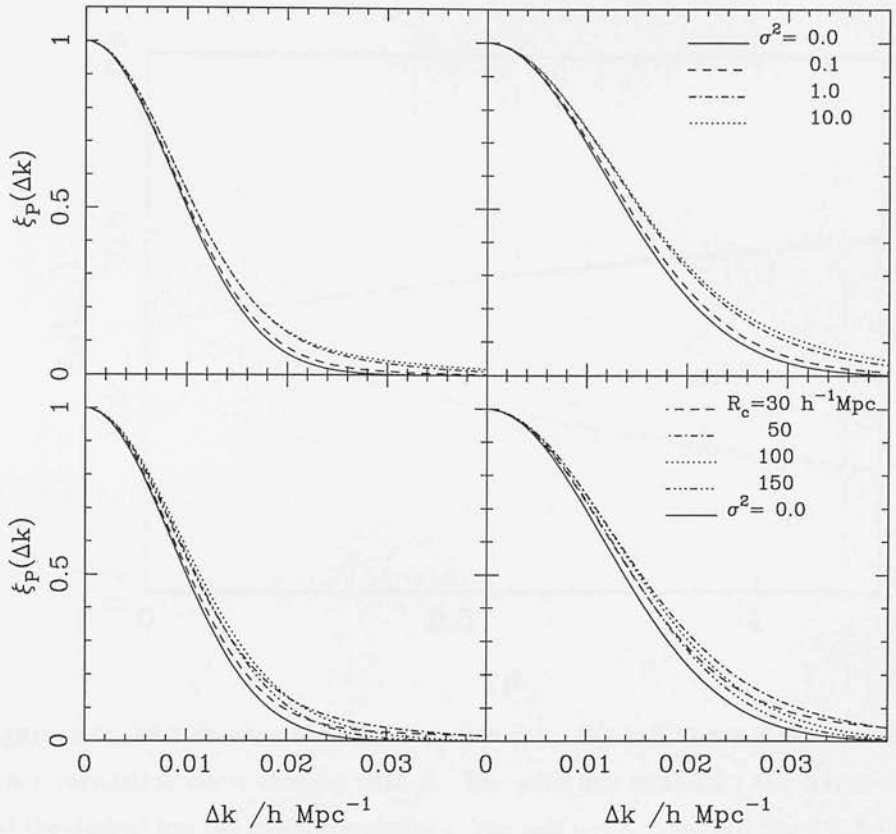


Figure 5.5: The expected power correlation statistic for different levels of modulation. Top panels have $R_c = 50\,h^{-1}\,\mathrm{Mpc}$, for amplitudes of modulation (from bottom to top) $\sigma^2 = 0$, 0.1, 1.0, 10. Bottom panels have $\sigma^2 = 3$, and modulation scales $R_c = 30\,h^{-1}\,\mathrm{Mpc}$ (dashed), $R_c = 50\,h^{-1}\,\mathrm{Mpc}$ (dot-dashed), $R_c = 100\,h^{-1}\,\mathrm{Mpc}$ (dotted), and $R_c = 150$ (dot-dot-dashed). The solid line is the Gaussian prediction (*i.e.* $\sigma^2 = 0$). In the left panels, $\beta = 0$, in the right $\beta = 5$. Clearly the size of $\beta$ has only a marginal effect on the shapes of the correlation curves.

$\beta$ is taken into account by replacing $Q\left(\delta\mathrm{k}\right) = \widetilde{\Psi^2}\left(\delta\mathrm{k}\right)$ with:

$$Q' = \left[\, \widetilde{\Psi^2}\left(\delta\mathrm{k}\right) + 2\beta\nu^2\widetilde{\Psi^2}_{ij}\left(\delta\mathrm{k}\right) + \beta^2\nu^4\widetilde{\Psi^2}_{ijlm}\left(\delta\mathrm{k}\right) \,\right] \tag{5.51}$$

as in equation 5.36. $\Psi\left(\mathbf{r}\right)$ is the weighted selection function, given by $\Psi\left(\mathbf{r}\right) = \overline{n}\left(\mathbf{r}\right) w\left(\mathbf{r}\right)$ using the same notation as Chapter 4.

Figure 5.5 shows the power correlations statistic (using transverse correlations only) for a range of modulations. The left panels use $\beta = 0$, and the right $\beta = 5$. This high value for $\beta$ has been chosen so that there is at least some noticeable difference between the curves, and serves to demonstrate how weakly the transverse correlations are affected by $\beta$.

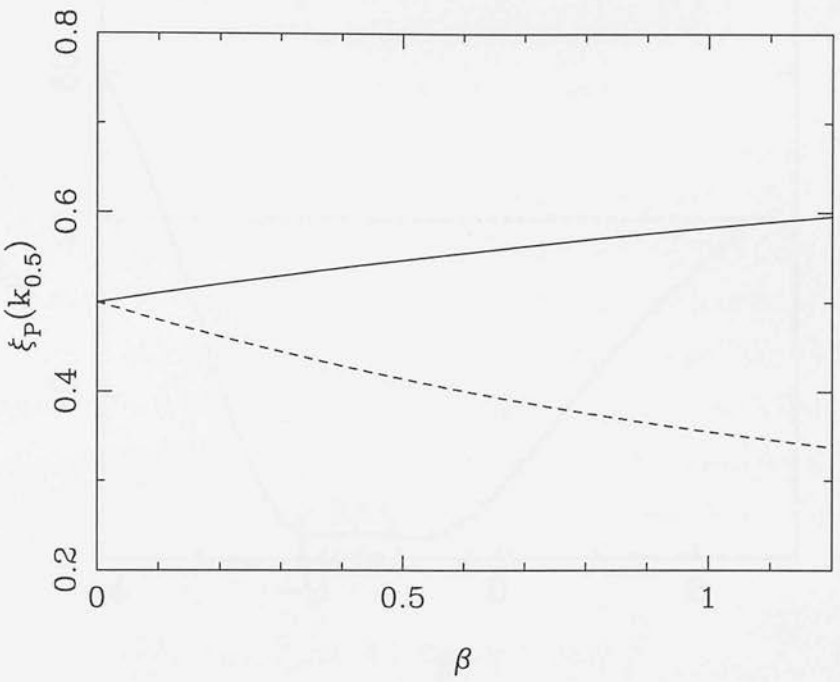


Figure 5.6: Plot showing how the deviation from the half power point for the unmodulated power correlation curve changes with $\beta$. The solid line represents the transverse correlations, and the dashed line the radial correlations. The half power point is defined to be the value of the power correlation function at $\Delta k_{0.5}$, where $\Delta k_{0.5}$ is the $k$-separation at which the *unredshifted, Gaussian* power correlation function has the value 0.5. Clearly, when $\beta = 0$, $\xi_P = 0.5$, but as $\beta$ increases, the effect of the redshift distortions is to separate the radial from the transverse correlations. The radial correlations become less extended (so the value of $\xi_P$ at $k_{0.5}$ drops), and the transverse correlations become more extended, making $\xi_P\,(k_{0.5})$ increase with $\beta$. In the absence of knowledge of $\beta$, this effect decreases the sensitivity of $\xi_P$ to non-Gaussian fields.

Figure 5.6 shows how the deviation in $\xi_P$ from the undistorted prediction at a fixed $k$-separation, '$\Delta k_{1/2}$' changes with $\beta$ (where $\Delta k_{1/2}$ is the $k$-separation for which the undistorted $\xi_P = 0.5$). For an uncertainty in $\beta$ of $\sim 0.3$, this corresponds to an uncertainty in $\xi_P$ of $\Delta\xi_P^{\rm Trans} \simeq 0.025$ for the transverse correlations, and $\Delta\xi_P^{\rm Rad} \simeq 0.041$ for the radial correlations. This increases the minimum deviation in the power correlations that might be detectable by 0.025 (see figure 4.9 in Chapter 4 – this plot considers only transverse correlations). Of course, one would expect the error in $\beta$ to decrease with the next generation of redshift surveys, which would also reduce this estimate of the reduction in sensitivity.

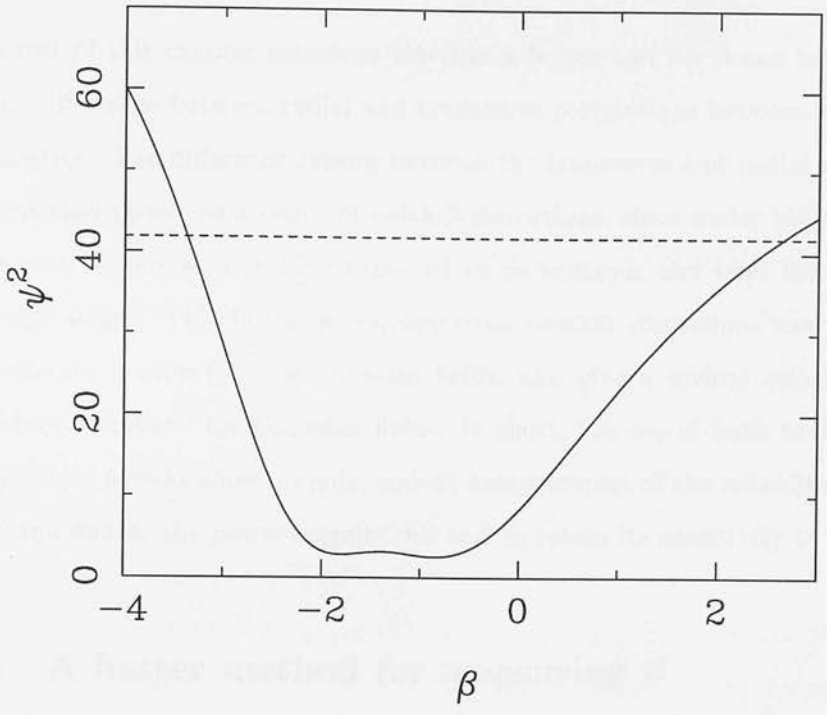


Figure 5.7: Graph showing the deviation $\psi^2$ from the Gaussian prediction for a range of values of $\beta$. The dotted line indicates the value of $\psi^2$ for which $p\left(\psi^{2\prime} > \psi^2\right) = 0.33$. These correspond to one sigma errors on the estimate of $\beta$. Again the accuracy to which $\beta$ is determined is poor because of the small effect of $\beta$ on the transverse power correlation function.

### 5.5.1 Inferring $\beta$ from power correlations

While the transverse power correlations statistic is clearly only very mildly sensitive to $\beta$, it should still be possible infer a value for $\beta$ (with large errors) under the assumption of Gaussian density fields. This has been done by measuring the $\psi^2$ statistic, where $\psi^2$ is given by:

$$\psi^2 = \sum_i \frac{\left[d_i\left(\delta\mathrm{k}\right) - t\left(\beta, \delta\mathrm{k}\right)\right]^2}{\left[e_i\left(\delta\mathrm{k}\right)\right]^2}, \tag{5.52}$$

where $d_i$ are the measured power correlation data points, $e_i$ their associated errors, and $t\left(\beta, \delta\mathrm{k}\right)$ the theoretical prediction for the power correlation function at a separation $\delta\mathrm{k}$ as a function of $\beta$. Using the probability distribution for $\psi^2$ obtained from the Monte-Carlo simulations described in Chapter 4, the most likely value of $\beta$ can be determined with its associated error bar. This is shown in figure 5.7, with the dotted line indicating a one sigma error bar. $\beta$ is found to be between -3.3 and 2.6. This is clearly not an accurate method for finding $\beta$!

The rest of this chapter examines whether a better test for $\beta$ can be found by looking at the difference between radial and transverse correlations between the Fourier modes themselves. The difference arising between the transverse and radial correlations would be expected purely as a result of redshift distortions, since under the cosmological principle, any cosmological field is expected to be isotropic and tend towards homogeneity on large scales. This break in isotropy from redshift distortions can therefore be used to estimate $\beta$ even for non-Gaussian fields, and give a revised estimate of the power correlation statistic for Gaussian fields. In short, the use of both radial and transverse correlations should allow an independent measurement of the redshift distortion parameter, and enable the power correlations test to retain its sensitivity to modulated fields.

## 5.6 A better method for measuring $\beta$

### 5.6.1 Aims

In this section the formalism for the correlation between Fourier modes is used to measure $\beta$, and is tested by applying it to a number of N-body simulations with different values for $\Omega_0$. This serves a number of purposes – primarily to determine whether the method can be made to work, and to what accuracy one might expect to be able to measure $\beta$ from a typical survey. Since a number of approximations are used to come up with a final formula for the mode correlations (*e.g.* treating the velocity difference term in equation 5.7 as negligible, and extending the translinear virialised cluster approximation to apply to mode correlations), it is also of interest to determine whether the method is biased in its determination of $\beta$.

Since the calculations presented here apply only to spherically symmetric surveys, and we have the misfortune of living in a galaxy, any application to real redshift surveys requires an extension of the analysis to include the effects of a mask. Here we deal with a very simple extension of the analysis to see whether it can be applied to masked data sets.

### 5.6.2 FFTs vs Direct Fourier transforms

Measuring the Fourier mode correlations can be quite tricky. For a start there is the question of whether to use direct Fourier transforms to obtain the Fourier information, which are time consuming, with c.p.u. time increasing as $M \times N$ (where M is the number of modes one wishes to determine, and N is the number of particles in the redshift survey or simulation), or to use the much faster 'Fast Fourier Transform', for which the time goes as $M \ln M$. While the FFT is faster, it has the disadvantage of being less accurate because the data are binned, and the mode separation is determined by the size of the box into which the data is put. In order to probe modes which are very close together, this can end up being very time consuming with an FFT, as the data need to be put in a box far larger than the volume the galaxies occupy. In order to retain the resolution of the transform, the number of bins in the mesh has to be very large, which in turn slows down the transform. This problem can however be side stepped by performing several FFTs of the data, but each time changing the box size slightly, so that slightly different k-vectors are obtained. This is a good method for increasing the number of radial modes which have small separations. In order to increase the number of modes with small transverse separations the data set needs to be rotated slightly. In practice, however, this method appears to give rise to systematic effects in the Fourier correlation function, arising perhaps from the binning of the data.

The results presented below have used the direct Fourier transform, for which one has more control over the choice of Fourier modes, and which for realistic simulations of redshift surveys is not much slower than the FFT method.

### 5.6.3 Determination of $\delta_k$

In FKP and in Chapter 4 the Fourier modes were determined by treating each galaxy as a delta function, and Fourier transforming the galaxy field. The mean Fourier density, $\overline{\rho}_k$ was found by Fourier transforming a set of points with the same selection function, but otherwise randomly positioned. In practice this leads to an increase in the shot noise of the mode determination, so the more points in the random sample the better. Here

$5 \times 10^5$ random points have been used in the fake data set. To save time, these have been Fast Fourier transformed. The box size used, however, was not large or fine enough to obtain exactly the same modes as those used in the direct transform of the data, and so the exact modes have been deduced by interpolating between the mesh modes. Since the selection function varies smoothly, the Fourier transform of the selection function is also expected to be smooth, making interpolation a reasonable approximation to the true Fourier modes.

In order to calculate the mean correlation function between the modes, one needs as large a $k$-range as possible, and since the power spectrum is not generally flat, it is necessary to weight each pair of Fourier modes by dividing by the power spectrum for that wavenumber, so as not to weight unfairly modes of smaller wavenumbers (in the case of a negative spectral index for the power spectrum). So if the Fourier transform of the density contrast is given by $f_k$ (using the same notation as in Chapter 4), then we look at correlations between $g_k$, which are given by:

$$g_k \equiv \frac{f_k}{\langle |f_k|^2 \rangle^{1/2}} \tag{5.53}$$

In the following analysis, the effects of shot noise are taken into account in the theory, rather than subtracting their effects from the data.

### 5.6.4 Determination of $\beta$

The Fourier mode correlation function is found by going through all the pairs of modes in a particular $k$-range, measuring their $k$-space separation, $\Delta\mathrm{k}$ and the angle the separating vector $\Delta\mathrm{k}$ makes with one of the mode $k$-vectors, $\theta_k$. The product, $g\,(\mathrm{k})\,g^{\star}\,(\mathrm{k}+\Delta\mathrm{k})$ is then binned in both $k$-separation, and angle $\theta_k$. The number of modes in each bin is then counted, and the mean for each bin found.

The range of scales has been chosen so that the smallest $k$-mode probed contains at least five independent coherence patches, and the largest $k$-mode is chosen so that $\Delta^2\,(k_{\mathrm{max}}) \lesssim 1$. Since the effective $\beta$ is expected to decrease with increasing $|k|$ owing to fingers of god, this $k$-range has been split up into separate regions of order three times the $k$-space width of the selection function. The correlation function is then determined for this

range of $k$-values, and the effect of virialised clusters fitted for using a single parameter $\sigma$ to fit for the change in shape of the correlation functions with $|k|$.

There are several methods one could use to determine $\beta$ from a set of correlation curves as a function of $|k|$ and $\theta_k$. The first possibility is to use only the radial correlation function. $\beta$ and the pairwise velocity dispersion parameter $\sigma^2$ are free parameters in the theory, and these are adjusted to minimise a difference statistic between the theoretical curves and the actual curves. The difference statistic ($\psi^2$) used here is a $\chi^2$-like statistic, in which the sum of the square of the differences divided by an estimate for the error is minimised. As in Chapter 4, this statistic would not be expected to follow a $\chi^2$ distribution, owing to the correlation of the points. A contour plot can then be plotted of lines of constant $\psi^2$, and this related to probabilities by running an ensemble of Monte Carlo simulations. An alternative, but very similar method is to use the difference between the radial and transverse curves. This has three advantages: (1) the effect of different $\beta$ values is more pronounced, (2) the need for evaluating an accurate value for the mean Fourier density, $\overline{\rho}_k$, is eliminated, since terms involving $\overline{\rho}_{k_1}\overline{\rho}_{k_2}$ in $< g_{k_1} g^*_{k_2} >$ cancel, and (3) although the errors in this statistic might be slightly larger than those from a single correlation curve, the correlation between errors at different $\Delta k$'s is significantly reduced, and so the $\chi^2$ treatment of the data is a better approximation.

### 5.6.5 Determination of errors

While the errors could be determined theoretically, this is no mean task, and requires previous knowledge of $\beta$ for this evaluation. Here, errors in the correlation curves have been found empirically by breaking up the $k$-shell into octants, and measuring the standard deviation between each octant. Provided the octants are not significantly correlated themselves, this should provide a reasonable estimate for the errors. This is checked in the discussion section.

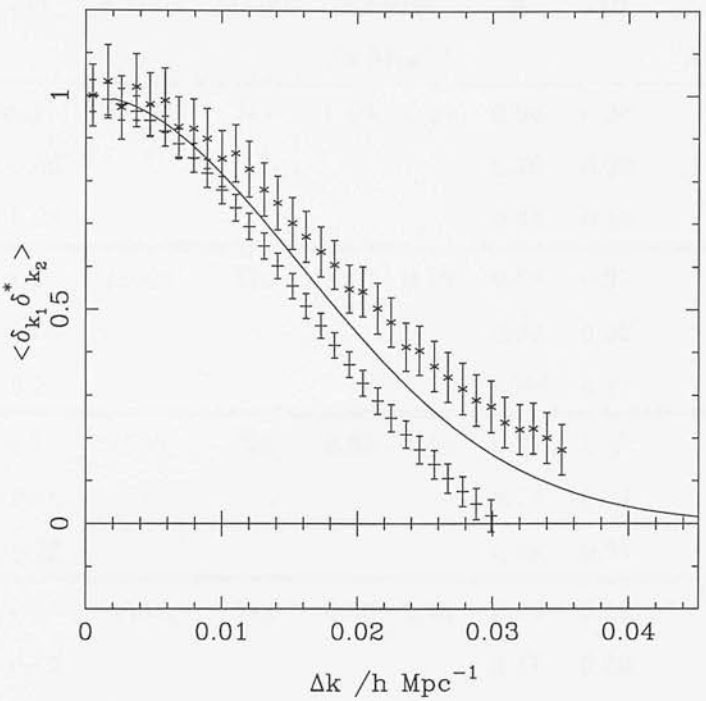


Figure 5.8: Mode correlations from an $\Omega = 1$ simulation, with box size of $600\,h^{-1}$ Mpc, 28000 'galaxies', and taken at a scale $|k| = 0.08\,h$ Mpc$^{-1}$. Upper points (x) indicate transverse correlations, and lower points (+) radial. Error bars here are determined from the spread in results in different octants of the $k$-space shell. The solid line indicates the mode correlation prediction in the absence of redshift distortions.

### 5.6.6 Choice of simulations

In order to test the program with simulations, the simulation box needs to be large enough to contain enough linear modes to be able to calculate the correlation function in the linear regime. The simulations used here have a power law power spectrum with spectral index $n = -1$, and $\Delta^2(k) \simeq 1$ on scales $\sim 23$ times smaller than the box size. So physically the box size corresponds to about a $(600\,h^{-1}\,\mathrm{Mpc})^3$ volume. The selection function has been chosen to be a spherically symmetric Gaussian, with width, $\sigma \simeq 90\,h^{-1}$ Mpc. This allows maximal use of the simulation box while retaining the Gaussian shape of the selection function.

| Model | # Gals | Mask? | $k$-range / $h$ Mpc$^{-1}$ | $\overline{\beta}$ | $\Delta\beta$ | $\overline{\sigma^2}$ /$10^4$ km$^2$s$^{-2}$ | $\Delta\sigma^2$ |
|---|---|---|---|---|---|---|---|
| $\beta = 1$ | 28000 | No | 0.03 - 0.19 | 0.96 | 0.28 | 57.7 | 13.1 |
| $\beta = 0.66$ | | | | 0.70 | 0.29 | 37.0 | 21.7 |
| $\beta = 0.25$ | | | | 0.34 | 0.19 | 21.7 | 18.2 |
| $\beta = 1$ | 28000 | Yes | 0.03 - 0.19 | 0.58 | 0.27 | 48.0 | 15.2 |
| $\beta = 0.66$ | | | | 0.27 | 0.22 | 18.7 | 17.3 |
| $\beta = 0.25$ | | | | 0.084 | 0.12 | 9.5 | 12.0 |
| $\beta = 1$ | 4505 | No | 0.03 - 0.19 | 0.88 | 0.27 | 47.8 | 11.4 |
| $\beta = 0.66$ | | | | 0.78 | 0.24 | 39.1 | 13.8 |
| $\beta = 0.25$ | | | | 0.46 | 0.24 | 26.9 | 16.1 |
| $\beta = 1$ | 4505 | Yes | 0.03 - 0.19 | 0.62 | 0.29 | 41.8 | 17.0 |
| $\beta = 0.66$ | | | | 0.47 | 0.30 | 26.7 | 14.8 |
| $\beta = 0.25$ | | | | 0.22 | 0.19 | 15.1 | 18.3 |

Table 5.1: Mean best fit $\beta$ from 25 simulations, with standard deviation between the different simulations.

### 5.6.7 Extension to masked surveys

The above analysis has also been applied to N-body simulations for which a QDOT survey-type mask has been applied. For these simulations, the masked area has been filled in with fake galaxies that have a Poisson distribution, while following the number counts of the selection function in the radial direction. The effect this treatment has on the estimate of $\beta$ is shown in the following section.

### 5.6.8 Results

**(1) Spherically symmetric, 28000 galaxies.** Figure 5.8 shows a typical pair of radial and transverse correlation curves for a simulation which has $\Omega = 1$, 28000 galaxies, and no mask. As expected, the radial correlation curve is narrower than the transverse curve (see figure 5.3).

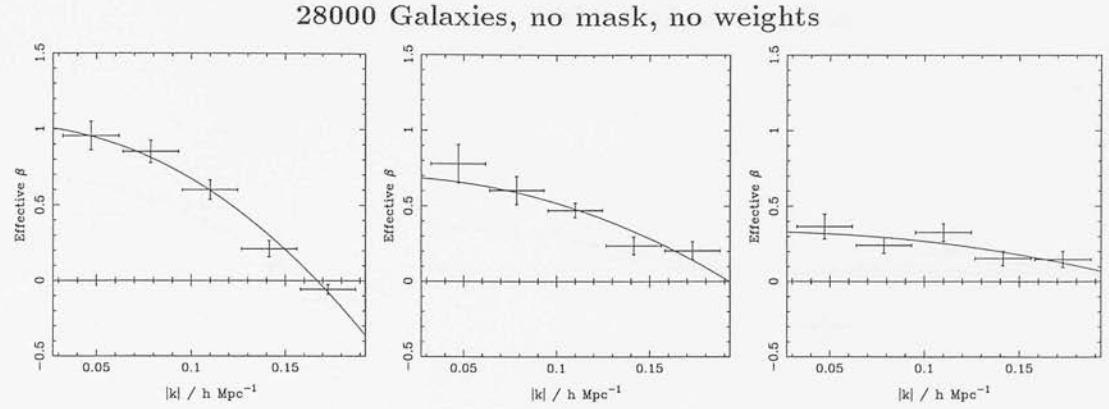


Figure 5.9: Graphs showing how effective $\beta$ changes with scale. Each graph is the average from 25 simulations. The solid lines indicate the prediction for the change in effective $\beta$ with scale once the velocity dispersion has been fitted for using a minimum $\chi^2$ fit. Left panel: $\beta = 1$, $\sigma = 809\,\mathrm{kms}^{-1}$; centre : $\beta = 0.66$, $\sigma = 660\,\mathrm{kms}^{-1}$; right: $\beta = 0.25$, $\sigma = 316\,\mathrm{kms}^{-1}$

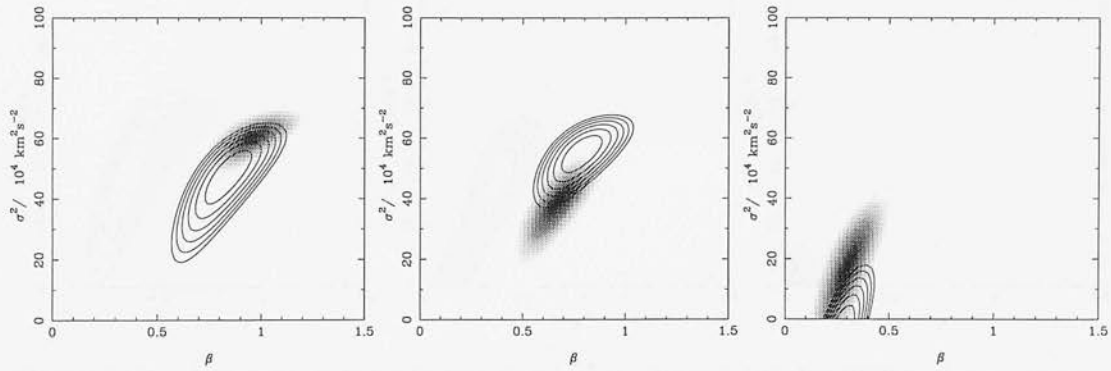


Figure 5.10: $\chi^2$ contour plots for finding $\beta$ and $\sigma^2$. Contours are for an individual simulation chosen at random, and represent 0.5 steps in $\log\mathcal{L}$, so the second, fourth and sixth contours correspond to one, two and three $\sigma$ error margins respectively. The shaded area indicates the average area enclosed by the 3 $\sigma$ contour, found from the average of 25 simulations. Left panel is for $\beta = 1$; centre, $\beta = 0.66$; and right $\beta = 0.25$. This is for a spherically symmetric survey geometry.

The effect of virialised clusters on the measurement of $\beta$ is shown in figure 5.9 – this shows nicely that the effective value decreases with $|k|$. The solid line shows the theoretical prediction for how $\beta$ is expected to fall off, using a best fit value for the velocity dispersion parameter, $\sigma^2$. These graphs are the averaged results for a set of 25 simulations for each $\beta$ value. Horizontal error bars indicate the range of $|k|$ used to determine each point, and vertical error bars are the error on the mean $\beta_{\mathrm{eff}}$.

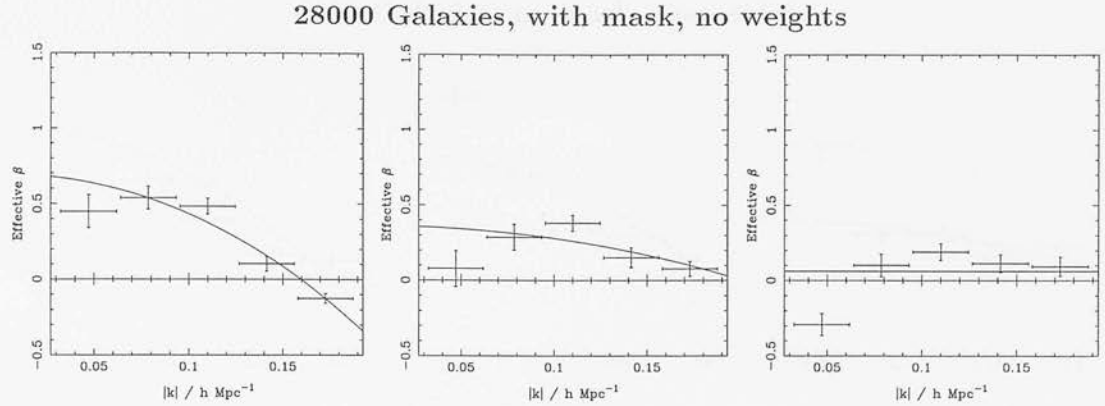


Figure 5.11: Effective $\beta$ as it changes with scale (as figure 5.9), for masked simulations and 28000 galaxies. Left panel: $\beta = 1$, $\sigma = 735\,\mathrm{kms}^{-1}$; centre: $\beta = 0.66$, $\sigma = 469\,\mathrm{kms}^{-1}$; right: $\beta = 0.25$, $\sigma = 346\,\mathrm{kms}^{-1}$.

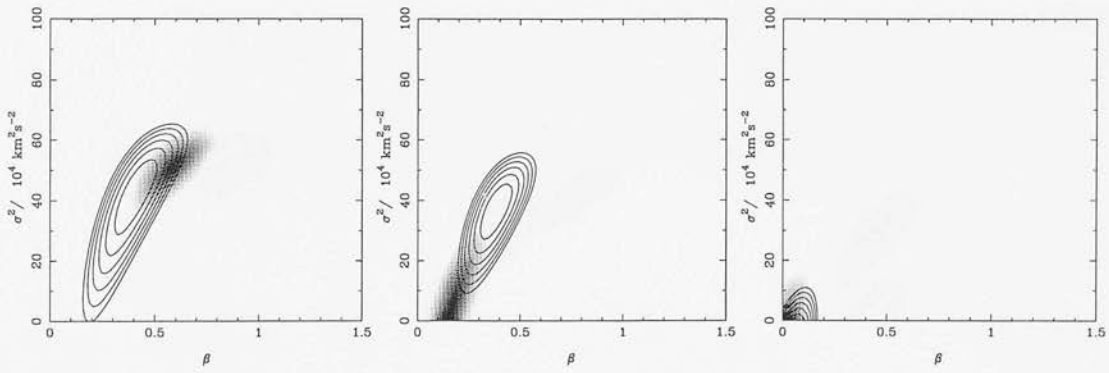


Figure 5.12: $\chi^2$ contour plots for finding $\beta$ and $\sigma^2$ (as figure 5.10). For 28000 galaxies, and a mask applied. The left panel is for $\beta = 1$; centre panel $\beta = 0.66$; and right $\beta = 0.25$.

Figure 5.10 shows a contour plot of the best fit values for $\beta$ and $\sigma^2$ – the shaded area indicates the 95 % confidence limit on the average of the 25 simulations. The contours are for a single simulation, and show increments of 0.5 in $\log \mathcal{L}$. The outermost contours show the 95% confidence region.

The rest of the results have the same format as above:

**(2) Masked simulation, 28000 galaxies.** For simulations with 28000 galaxies, and a mask applied, the effective $\beta$ plots are shown in figure 5.11, and the contour plots in figure 5.12.

**(3) Spherically symmetric, 4500 galaxies.** For spherically symmetric surveys containing 4500 galaxies, the results are displayed in figure 5.13 for the effective $\beta$ plots and

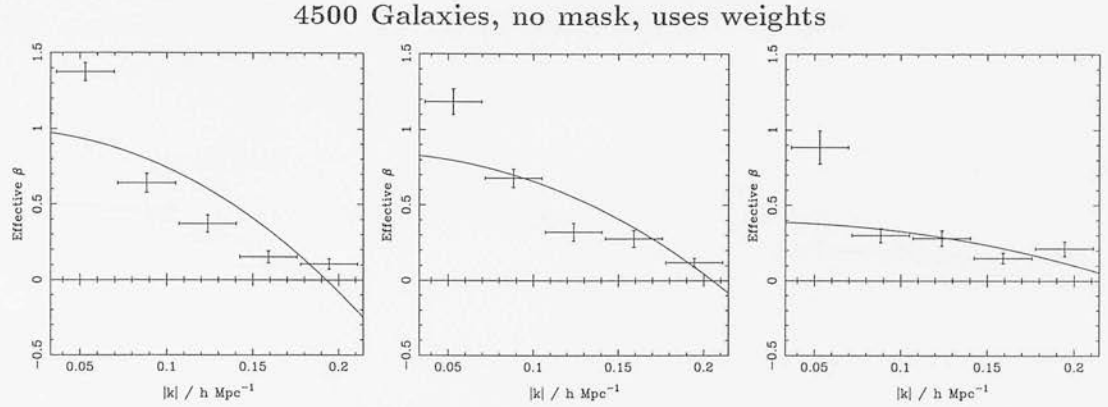


Figure 5.13: Effective $\beta$ for a survey containing 4500 weighted galaxies, and spherically symmetric survey geometry (see figure 5.9). Left panel: $\beta = 1$, $\sigma = 728\,\mathrm{kms}^{-1}$; centre: $\beta = 0.66$, $\sigma = 640\,\mathrm{kms}^{-1}$; right: $\beta = 0.25$, $\sigma = 566\,\mathrm{kms}^{-1}$.

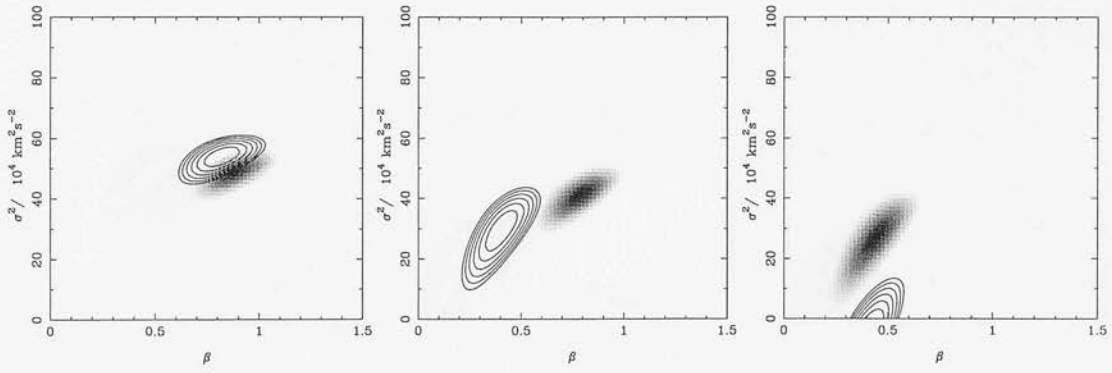


Figure 5.14: $\chi^2$ contour plots for $\beta$ and $\sigma^2$ (as figure 5.10). For 4500 weighted galaxies, and no mask. The left panel is for $\beta = 1$; centre panel $\beta = 0.66$; and right $\beta = 0.25$.

figure 5.14 for the contour plots.

**(4) Masked simulation, 4500 galaxies.** For masked simulations, containing 4500 (and thus resembling the QDOT+1.2 Jy survey), the results are shown in figures 5.15, and 5.16.

Table 5.1 is a summary of the mean and standard deviation of the $\beta$ and $\sigma^2$ values found.

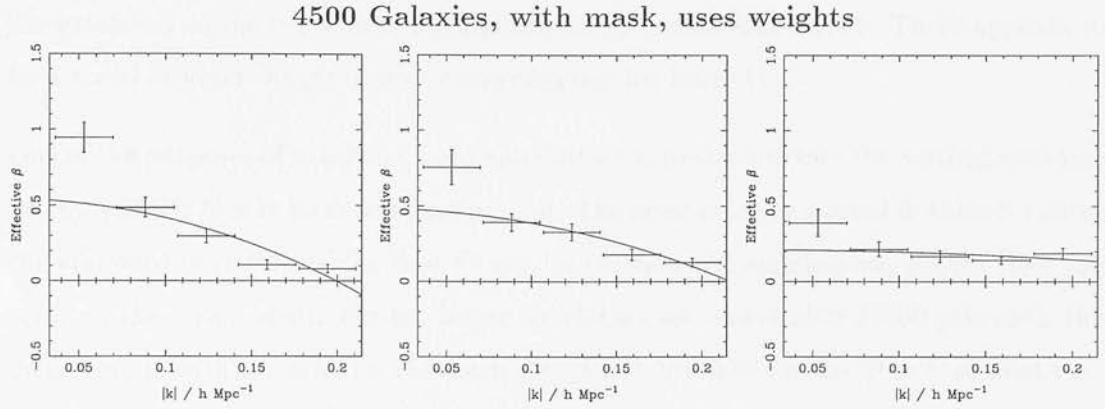


Figure 5.15: Effective $\beta$ for a survey containing 4500 weighted galaxies, and a mask applied (see figure 5.9). Left panel: $\beta = 1$, $\sigma = 755\,\mathrm{kms}^{-1}$; centre: $\beta = 0.66$, $\sigma = 624\,\mathrm{kms}^{-1}$; right: $\beta = 0.25$, $\sigma = 520\,\mathrm{kms}^{-1}$.

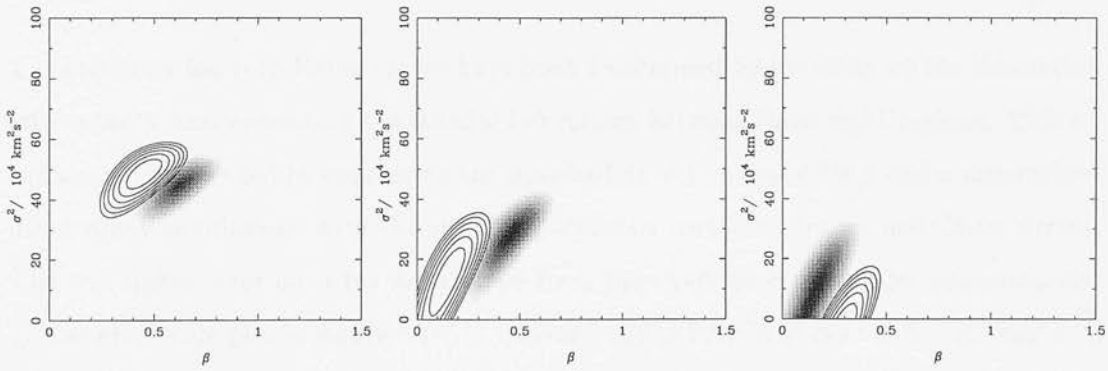


Figure 5.16: $\chi^2$ contour plots for $\beta$ and $\sigma^2$ (as figure 5.10). For 4500 weighted galaxies, and a mask applied. The left panel is for $\beta = 1$; centre panel $\beta = 0.66$; and right $\beta = 0.25$.

### 5.6.9 Discussion

#### Spherically symmetric surveys

The shaded area of the contour plot in figure 5.10 represents the average best fit parameter space for 25 different simulations, with the limits of the shading representing a probability 5% of the maximum probability value. Clearly these contours encompass the input value of $\beta$, and this suggests that the correlations between Fourier modes can be used to obtain an estimate of $\beta$.

Figure 5.9 shows clearly the effect of virialised clusters bringing down the level of distortion caused by collapsing objects, and this appears to be able to be fitted well using

the extension to the translinear regime mentioned in subsection 5.4.2. There appears to be a trend of lower 'finger of god' contamination for lower $\Omega$.

One of the purposes of analysing many simulations is to test whether the method contains any systematic bias in its determination of $\beta$. The error margins quoted in table 5.1 show the standard deviation of the best fit results between the simulations, rather than the error on the mean result. For the larger simulation set (containing 28000 galaxies), the mean results with the error on the mean are: $\overline{\beta} = 0.96 \pm 0.06$ for the '$\beta = 1$' simulations; $\overline{\beta} = 0.70 \pm 0.06$, for '$\beta = 0.66$'; and $\overline{\beta} = 0.34 \pm 0.04$ for '$\beta = 0.25$'. The first two results enclose the true value for $\beta$ within these error bars. The third result, however is just over $2\sigma$ higher, suggesting that perhaps for low $\Omega$ models, there is a slight bias in favour of higher $\beta$ values.

The errors on the correlation curves have been determined by breaking up the simulation into octants, and measuring the standard deviation between these eight regions. This estimate can be checked by comparing the standard deviation found for $\beta$ and $\sigma$ determined using many simulations with the standard deviation predicted for an individual survey. The one sigma error on $\beta$ (as determined from the example contour plot superimposed on the grey scale plot in figure 5.10) is typically $\Delta\beta \simeq 0.12$, and $\Delta\sigma^2 \simeq 8 \times 10^4\,\mathrm{km^2\,s^{-2}}$, whereas the dispersion of mean results is (taking results from the top part of table 5.1) $\Delta\beta = 0.29$, and $\Delta\sigma^2 = 19$, so the shaded areas probably more accurately represent one sigma regions, rather than two sigma, as estimated from the internal error calculation. The second question to ask is whether the approximation that each point (on the difference curve $< g_{k_1} g^{\star}_{k_2} >^{\mathrm{Radial}} - < g_{k_1} g^{\star}_{k_2} >^{\mathrm{Transverse}}$) is independent and so the number of degrees of freedom is given by the total number of points used. This is likely to manifest itself as a minimum reduced $\chi^2$ value which is less than 1. The mean minimum reduced $\chi^2$ value for the set of simulations contributing to figure 5.10 is $\chi^2_{\mathrm{min}} = 0.45 \pm 0.13$, also suggesting that this approximation is underestimating $\chi^2$ by a factor of about two. Error bars quoted on estimates of $\beta$ in the next sections will therefore be quoted from the simulation-to-simulation standard deviation, rather than from the contour plots.

The effect of reducing the survey volume by a factor of about two, and this time weighting the data to give the same level of correlations between the modes, is to shift high values

down, and low values up towards $\beta = 0.5$. The true value is however still contained within the 95% shaded contour in figure 5.14.

### Masked surveys

Simulations with a mask superimposed are shown in figures 5.12, and 5.16. The masked regions were replaced with points that were randomly placed apart from being required to fulfill the selection criteria in the radial direction. The masked areas covered $\sim 17\%$ of the sky. The effect of this operation is to reduce the measurement of $\beta$ by $\Delta\beta \simeq 0.35$ for the 28000 galaxy set of simulations, and $\Delta\beta \simeq 0.3$ for the 4505 galaxy simulation set, and this is unsurprising given that a randomly placed set of points should display no correlation differences between the radial and transverse directions.

## 5.7 Application to IRAS galaxies

Since the aim is to measure $\beta$ from redshift surveys of the local universe, in this section limits are placed on $\beta$ for the QDOT+1.2 Jy survey. The ideal data set for this analysis is the PSCZ redshift survey, which is the one-in-one version of the QDOT survey. (Politics in the world of cosmology, have however so far kept access to this survey limited to the privileged few.) Here, we make do with the next best thing, and also apply the analysis to simulations of the PSCZ redshift survey, which have generously been made available by Cole *et al.* (1998) at the web site http://star-www.dur.ac.uk/~cole/mocks/main.html. These simulations have enabled two studies to be made – first, the machinery described above has been applied to a few mock QDOT+1.2 Jy survey catalogues, which have been generated by Poisson sampling from Cole's mock PSCZ simulations. Second, the analysis has been applied to the PSCZ simulations, with a view to estimating how well one might be able to measure $\beta$ using this method.

### 5.7.1 Simulations used

The simulated models also incorporate galaxy biasing, which was not used in the simulations of the previous section. There are three models, and these are called in Cole *et al.* 'E3S$_a$', 'E3S$_b$', and 'O4S'. The E3S models are both realisations of $\tau$CDM models, with $\Omega_0 = 1$, $\Lambda = 0$, and $b = 1.8$, where $b$ is the linear bias parameter. The O4S model has $\Omega = 0.4$, $\Lambda = 0$ and $b = 1.1$.

### 5.7.2 Analysis of the QDOT+1.2 Jy data set

The shot noise for the QDOT+1.2 Jy survey is quite large, and since the shot noise affects the extent to which the radial and transverse curves differ, it is important to get the right ratio of shot noise to real power contribution. With a real data set, this is harder, since one does not have a very accurate estimate for the power spectrum over the $k$-range considered. The analysis of the correlation curves for the QDOT+1.2 Jy data set have therefore been performed assuming that the power is 4000, 5000, & 6000 $(h^{-1}\,\mathrm{Mpc})^3$. These values cover the reasonable range for the power spectrum on these scales, and have been taken from Feldman, Kaiser & Peacock (1994), which estimates the power from the QDOT and the 1.2 Jy surveys.

Figure 5.17 shows the results for the PSCZ data set with and without a mask applied, and figure 5.18 shows the equivalent results for the QDOT+1.2 Jy simulated data set. The mean values for $\beta$ found are tabulated in table 5.2. The results for the QDOT+1.2 Jy dataset are shown in figures 5.19, and table 5.3.

| Model | $\Omega_0$ | $b$ | $\beta^{\rm True}$ | # Gals | Mask? | $k$-range / $h$ Mpc$^{-1}$ | $\overline{\beta}$ | $\Delta\beta$ | $\overline{\sigma^2}/10^4$ km$^2$s$^{-2}$ | $\Delta\sigma^2$ |
|---|---|---|---|---|---|---|---|---|---|---|
| E3S$_a$ | 1.0 | 1.8 | 0.55 | 13156 | No | 0.06 – 0.2 | 0.49 | 0.16 | 31.1 | 11.42 |
| | | | | | Yes | | 0.24 | 0.20 | 15.2 | 20.3 |
| E3S$_b$ | 1.0 | 1.8 | 0.55 | 12679 | No | 0.06 – 0.2 | 0.25 | 0.16 | 8.61 | 12.8 |
| | | | | | Yes | | 0.065 | 0.06 | 2.78 | 3.95 |
| O4S | 0.4 | 1.1 | 0.52 | 14063 | No | 0.06 – 0.2 | 0.63 | 0.13 | 42.0 | 7.4 |
| | | | | | Yes | | 0.44 | 0.31 | 41.3 | 22.8 |
| E3S$_a$ | 1.0 | 1.8 | 0.55 | 5218 | No | 0.06 – 0.2 | 0.49 | 0.29 | 28.9 | 21.1 |
| | | | | | Yes | | 0.17 | 0.20 | 35.7 | 22.7 |
| E3S$_b$ | 1.0 | 1.8 | 0.55 | 5030 | No | 0.06 – 0.2 | 0.46 | 0.17 | 11.9 | 18.1 |
| | | | | | Yes | | 0.0 | 0.0 | 12.4 | 11.44 |
| O4S | 0.4 | 1.1 | 0.52 | 5591 | No | 0.06 – 0.2 | 0.90 | 0.33 | 42.8 | 8.75 |
| | | | | | Yes | | 0.23 | 0.24 | 24.6 | 22.2 |

Table 5.2: $\beta$ and $\sigma^2$ measured for the different simulation models. Top half is for PSCZ-type simulations, bottom half for QDOT+1.2 Jy-type simulations. $\Delta\beta$ is taken from the contour plots, and represents the maximum width in $\beta$ for which the $\chi^2$ values are incremented by one from the minimum $\chi^2$ value.

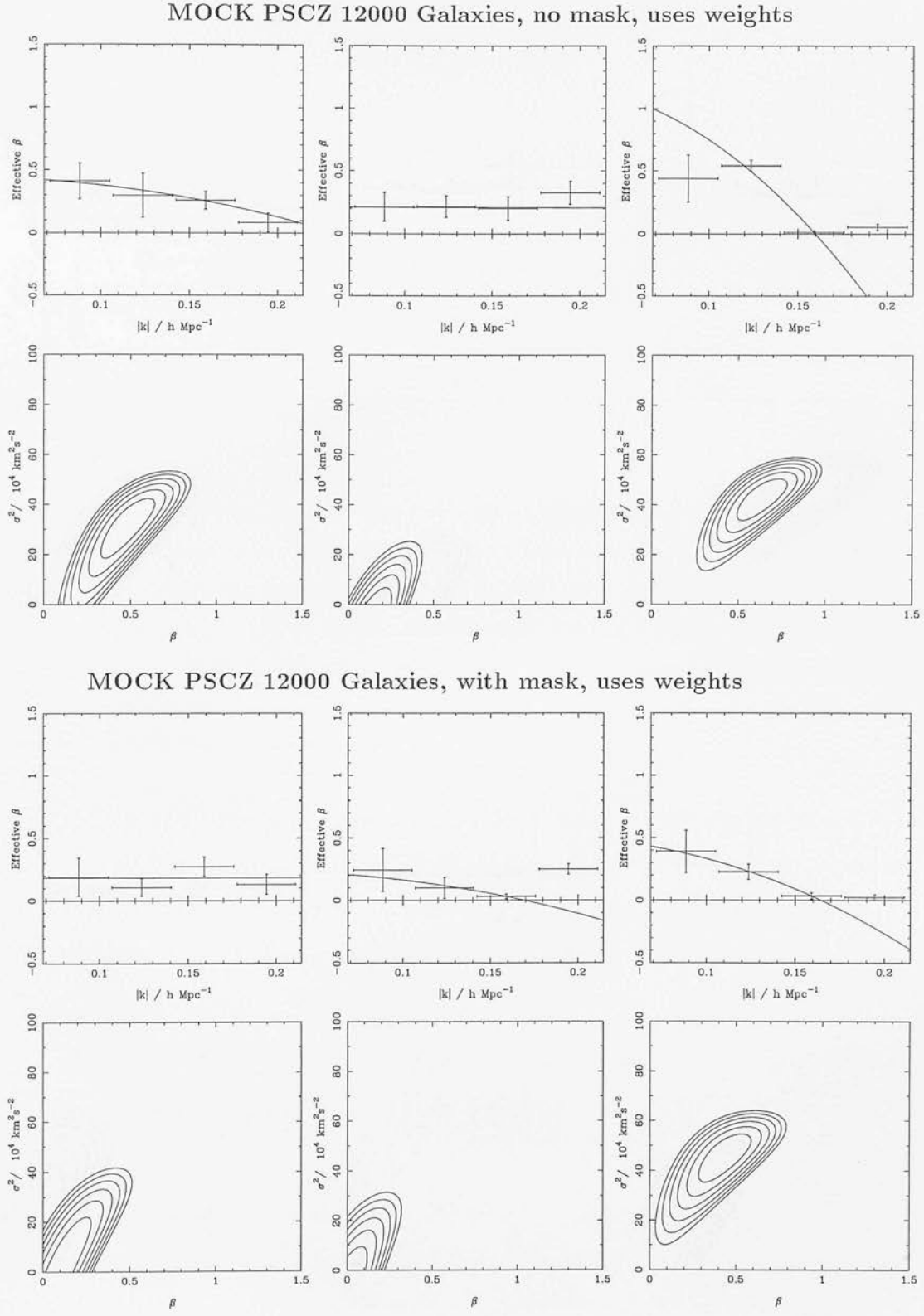


Figure 5.17: Left panels are 'E3S$_a$', $\beta = 0.55$; centre '$E3S_b$', $\beta = 0.55$; and right 'O4S', $\beta = 0.52$. All plots are for a PSCZ type simulation, top two rows for no mask, bottom two rows with a mask applied.

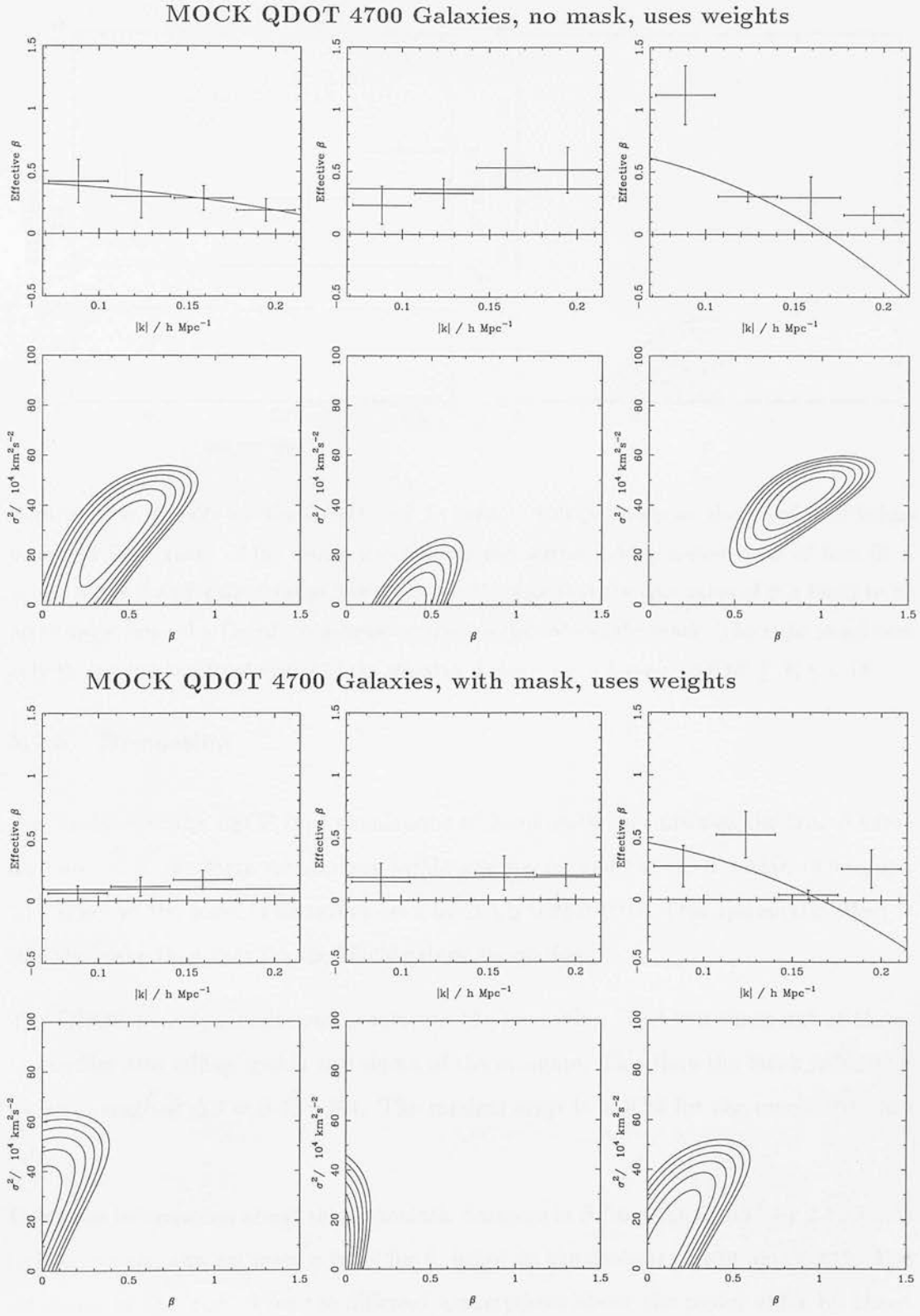


Figure 5.18: Left panels are 'E3S$_a$', $\beta = 0.55$; centre 'E3S$_b$', $\beta = 0.55$; right 'O4S', $\beta = 0.52$. Poisson sampled from the PSCZ simulations. Top two rows have no mask, bottom two rows are with a mask applied.

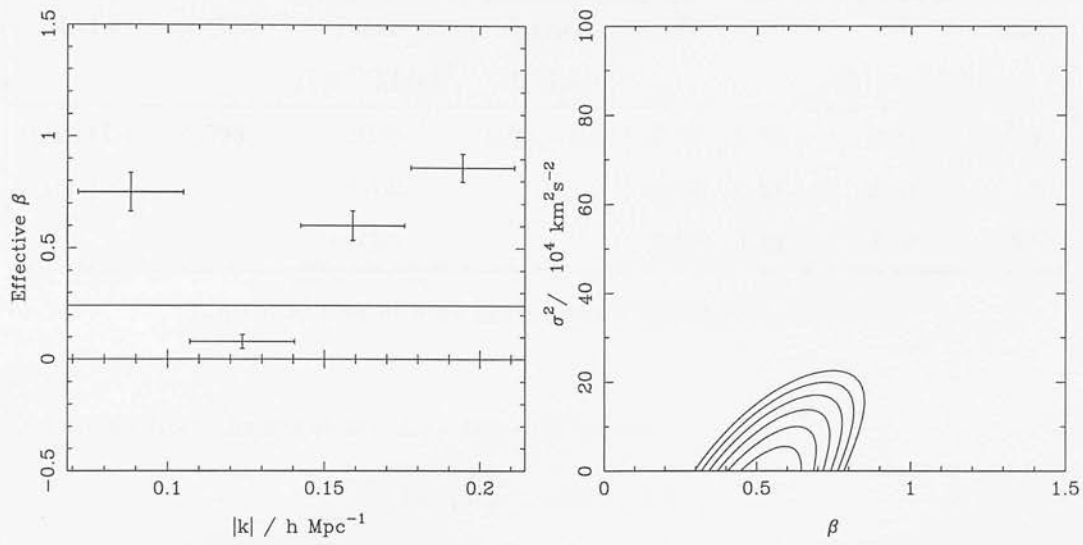


Figure 5.19: Results for the QDOT+1.2 Jy survey. Left panel shows the effective $\beta$ values measured for a range of $|k|$, centre panel shows the corresponding contour plot of best fit $\beta$ values to the data for the $k$-range $0.08 \leq |k| \leq 0.21$. Note that the true value of $\beta$ is likely to be up to twice this value found, on account of the missing data in the mask. The right panel uses only the second and third points of the effective $\beta$ plot – *i.e.* a $k$-range of $0.08 \leq |k| \leq 0.14$.

### 5.7.3 Discussion

The analysis of the PSCZ type simulations with no mask encompasses the true $\beta$ value for two out of the three simulations within one sigma, and the third within two sigma. The effect of the mask is to reduce beta by $\Delta\beta \simeq 0.21 \pm 0.02$. This systematic effect is slightly lower than that for the 28000 galaxy simulation.

The QDOT+1.2 Jy simulations encompass the true value for $\beta$ two times out of three, the outlier also falling within two sigma of the estimate. This time the mask reduced $\beta$ by an average of $\Delta\beta = 0.48 \pm 0.1$. The random error is $\simeq 0.26$ for the unmasked data sets.

Using the information about the systematic decrease in $\beta$ from the QDOT+1.2 Jy simulations, we can now estimate a value for $\beta$, based on the contour plot in figure 5.19. The estimates of the 'raw' $\beta$ for the different assumptions about the power differ by about 0.06 - a relatively small effect. The $P = 5000\,(h^{-1}\,\mathrm{Mpc})^3$ value for $\beta$ is $\beta = 0.57 \pm 0.12$. A crude estimate of the true $\beta$ value can then be obtained by adding on the systematic

| Model | # Gals | Power $/(h^{-1}\,\mathrm{Mpc})^3$ | $k$-range $/\,h\,\mathrm{Mpc}^{-1}$ | $\overline{\beta}$ | $\Delta\beta$ | $\overline{\sigma^2}$ $/10^4\,\mathrm{km^2 s^{-2}}$ | $\Delta\sigma^2$ |
|---|---|---|---|---|---|---|---|
| 'QDOT+ | 4505 | 5000 | 0.06 – 0.21 | 0.57 | 0.12 | 2.53 | 5.31 |
| 1.2 Jy' | | 6000 | | 0.51 | 0.11 | 2.34 | 4.9 |
| | | 4000 | | 0.66 | 0.13 | 2.78 | 5.9 |

Table 5.3: Best fit $\beta$ for the combined QDOT+1.2 Jy survey.

effect found from the simulated data sets. This gives

$$\beta = 1.05 \pm_r 0.26 \pm_s 0.1, \tag{5.54}$$

the first error bar being the random error ($\pm_r$) on the unmasked QDOT+1.2 Jy simulations, and the second the error on the systematic correction ($\pm_s$).

While this is based on judging systematic corrections from a very small amount of information, we can also use the weighted simulations of the previous section to perform the same analysis. Again, the random error on the unmasked data sets are $\Delta\beta \simeq 0.25$. The systematic correction is $\Delta\beta = 0.27 \pm 0.22$, so this would give

$$\beta = 0.84 \pm_r 0.25 \pm_s 0.22\ , \tag{5.55}$$

which also covers the range calculated above. The PSCZ simulation results suggest that this analysis could measure $\beta$ within an error of $\Delta\beta = \pm_r 0.15 \pm_s 0.1$ – a reduction of the random error by about $\Delta\beta \sim 0.1$.

Of course, ideally one would account for the mask theoretically. While an expression for this can be written (see equation 5.42), the full three dimensional integral would have to be performed. This could be reduced to a two dimensional integral if the mask was assumed to be rotationally symmetric – again an approximation, but far closer to the actual survey geometry.

### 5.7.4 Conclusions

In this section, $\beta$ has been measured from a set of PSCZ and QDOT+1.2 Jy type simulations. This has shown that without a mask, the method can be used to measure

$\beta$ to within 0.15 for the PSCZ surveys, and within 0.26 for the QDOT+1.2 Jy survey.

With a mask, systematic effects become important, and these have been estimated empirically here. For the real QDOT+1.2 Jy survey, taking into account systematic errors gives an estimate for $\beta$ of $\beta = 1.05 \pm_r 0.26 \pm_s 0.1$. This is consistent with previous estimates using these catalogues (*e.g.* Heavens & Taylor 1995; Ballinger, Heavens & Taylor 1995).

## 5.8 What about the neglected term, $[\mathbf{u}(\mathbf{r}) - \mathbf{u}(\mathbf{0})]/r$?

In order to calculate the radial and transverse correlation functions we have assumed in equation 5.9 that the term in $[U(\mathbf{r}) - U(\mathbf{0})]/r$ is negligible compared with terms in $\mathrm{d}U/\mathrm{d}r$ on the grounds that it scales as the inverse depth of the survey unlike the other terms (Kaiser 1987). Zaroubi & Hoffman (1996) point out that that in our local universe we measure velocities of a few times $10^3$ km s$^{-1}$, so on scales of $10^4$ km s$^{-1}$ the effect is not necessarily negligible. What they missed however is that the $[U(\mathbf{r}) - U(\mathbf{0})]/r$ term affects only the coefficients of $\nu^0$, and $\nu^2$ in equation 5.49. We can therefore use a multipole expansion of the correlation function to find a prediction for $\beta$ that does not depend on the velocity difference term, and so is exact to linear order.

To linear order and keeping the term in $U/r$, we can approximate equation 5.8 as:

$$\delta^S(\mathbf{s}) = \delta^R(\mathbf{r}) - \frac{\mathrm{d}U}{\mathrm{d}r} - 2\frac{U(\mathbf{r}) - U(\mathbf{0})}{r}. \tag{5.56}$$

Equation 5.12 gives the linear theory prediction for $U$, so $U(\mathbf{r})/r$ can be expressed as:

$$U(\mathbf{r}) = \beta \int \exp(i\mathbf{k}\cdot\mathbf{r}) \frac{\mathbf{k}\cdot\mathbf{r}}{k^2 r^2} \delta_r(\mathbf{k})\, \mathrm{d}^3k. \tag{5.57}$$

Now the crucial part here is to note that this integrand contains a term which is linear in $\hat{\mathbf{k}}\cdot\hat{\mathbf{r}} = \hat{k}_i\hat{r}_i$, so when looking at Fourier mode correlations, there will be a term in $\hat{k}_i\hat{k}_j\hat{r}_i\hat{r}_j$. Referring back to equations 5.47, 5.47, and 5.48 one can see that $n^{th}$ order terms in $\hat{k}_i$ give rise to integrals whose maximum order coefficient is $\nu^n$. So we can expect terms relating to the velocity difference to have a maximum order of $\nu^2$. This turns out to be very convenient, as there is a $\nu^4$th term (see equation 5.49) for which no information comes from the velocity difference term.

The term in $\nu^4$ can be extracted using Legendre polynomials as outlined in section 5.3 under 'Quadrupole to monopole ratio of the power spectrum', but this time applied to mode correlations rather than the power spectrum. From equation 5.24 and 5.49 we have for the hexadecapole moment:

$$\frac{9}{2}\int_{-1}^{1} \mathrm{d}\nu \mathcal{P}_4(\nu) \left\langle \delta^S(\mathbf{k_1})\, \delta^S(\mathbf{k_1}+\delta\mathbf{k})^\star \right\rangle = P(k_1)\left\{\beta^2 \mathcal{J}_5(\delta k)\right\}, \tag{5.58}$$

where $\hat{k}_1 \cdot \hat{\delta k} = \nu$. The quadrupole moment is given by:

$$\frac{5}{2}\int_{-1}^{1} \mathrm{d}\nu \mathcal{P}_2(\nu) \left\langle \delta^S(\mathbf{k_1})\, \delta^S(\mathbf{k_1}+\delta\mathbf{k})^\star \right\rangle = P(k_1)\left\{2\beta \mathcal{J}_1(\delta k) + 6\beta^2 \mathcal{J}_4(\delta k)\right\}, \tag{5.59}$$

and the monopole by:

$$\frac{1}{2}\int_{-1}^{1} \mathrm{d}\nu \mathcal{P}_0(\nu) \left\langle \delta^S(\mathbf{k_1})\, \delta^S(\mathbf{k_1}+\delta\mathbf{k})^\star \right\rangle = P(k_1)\left\{\mathcal{J}_0(\delta k) + 2\beta \mathcal{J}_2(\delta k) + 3\beta^2 \mathcal{J}_3(\delta k)\right\}. \tag{5.60}$$

Figure 5.20 shows the theoretical curves for the monopole, quadrupole and hexadecapole of the mode correlation function. The curves have been normalised so that $P^z(k) = 1$. Clearly the hexadecapole mode correlation contributes a tiny effect relative to the monopole and quadrupole moments, so it is of limited use in determining $\beta$. The quadrupole moment, however looks to contribute the greatest difference in effect to the correlation curves, which is unsurprising given that redshift distortions are expected to induce squashing along the line of sight. While there would potentially be a benefit from taking the ratio of quadrupole to monopole, and hexadecapole to monopole since the real space power spectrum would then factor out, this advantage is probably outweighed by the fact that the correlation curves go to zero at large $k$-separation, and so could introduce huge errors in the resultant curve (see figure 5.21). If the main interest is to test the validity of the approximation that the velocity difference term is negligible, then since both the quadrupole and monopole terms are affected by this assumption, it is better to normalise the curves by dividing by the redshift space power spectrum, $P^z(k)$. This then only affects the scaling of the curve, and not its shape. In general, the use of these Legendre polynomial moment curves would give a more complete analysis of the redshift induced correlations – both because of being able to constrain the velocity difference term, and because it makes use of all angular information, rather than the specific instance of the radial and transverse curves.

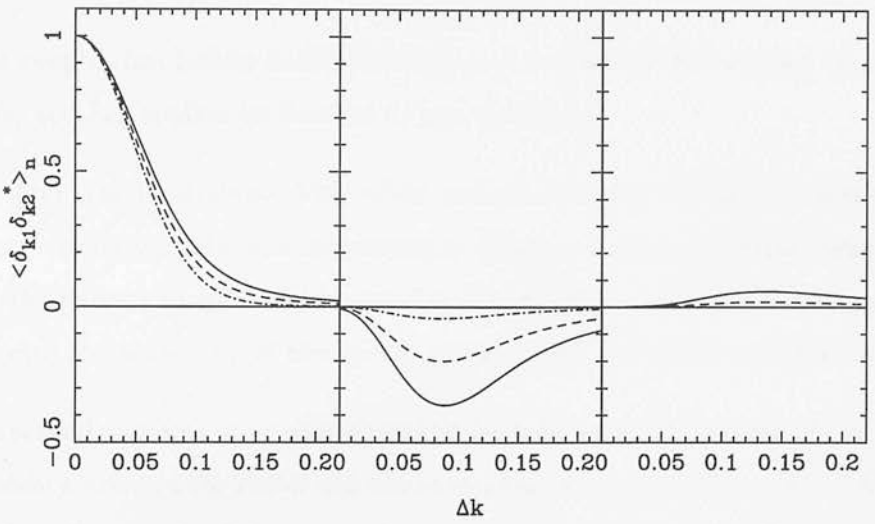


Figure 5.20: Mode correlation curves for different coefficients of $\nu$ and different values of $\beta$. The left panel shows the monopole correlation, the middle panel the quadrupole moment, and right panel the hexadecapole moment. For each one $\beta$ takes values 0.1 (dot dashed), 0.5 (dashed), and 1.0 (solid).

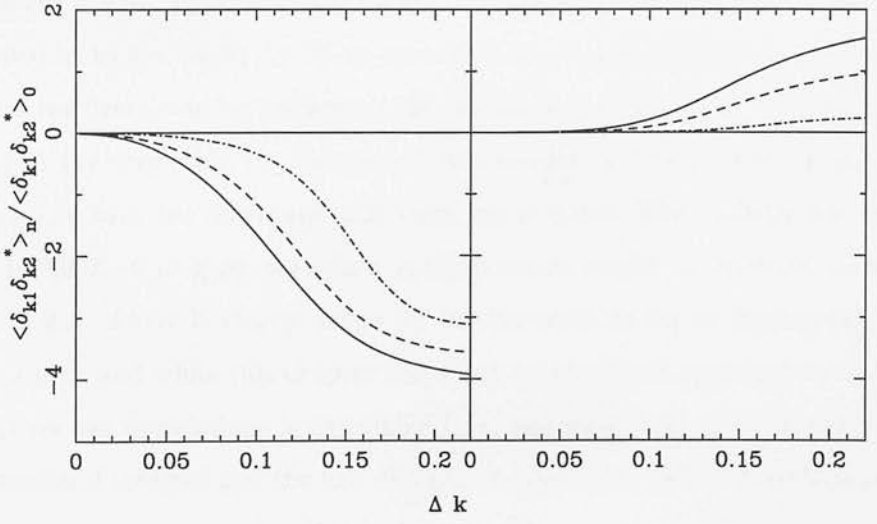


Figure 5.21: Mode correlation curves for the quadrupole to monopole ratio (left), and hexadecapole to monopole ratio (right) for different values of $\beta$. The left panel shows the monopole correlation, the middle panel the quadrupole moment, and right panel the hexadecapole moment. For each one $\beta$ takes values 0.1 (dot dashed), 0.5 (dashed), and 1.0 (solid).

## 5.9 Summary

This chapter has looked at the correlation of Fourier modes induced by redshift distortions, and has applied its findings to two problems.

The first was to establish what effect redshift induced correlations would have on the power correlations statistic introduced in Chapter 4. For transverse power correlations, and the current range of values for $\beta$ in the literature, redshift distortions are likely to decrease the sensitivity of the test by at most 10% for QDOT and PSCZ-type surveys.

The second part was to develop a method for measuring $\beta$ from redshift surveys using the difference between the radial and transverse Fourier mode correlations. This involved extending the analysis of Zaroubi & Hoffman (1996) and Kaiser to the quasi-linear regime, where the effect of virialised velocities in clusters becomes important. For spherically symmetric surveys, the analysis worked well, with no evidence for this statistic giving biased estimates for $\beta$. The method was then applied to surveys that contained a mask. These surveys were dealt with by filling in masked areas with randomly positioned points (but which obeyed the radial selection criteria of the survey). This time, the measured value for $\beta$ was found to be systematically smaller by $\Delta\beta = 0.27 \pm 0.22$. Applying this correction to the QDOT+1.2 Jy survey, $\beta$ was found to be $\beta = 1.05 \pm_r 0.26 \pm_s 0.1$, where the first error bar represents the random error, and the second error bar is for the error in the correction for the systematic decrease in $\beta$ as a result of the mask. This is consistent with the literature, and rules out $\beta \lesssim 0.5$. The analysis was also applied to mock PSCZ catalogues, for which random errors would be expected to be reduced by $\Delta\beta = 0.1$. There is clearly scope for further work as far as dealing with the mask is concerned, and while this chapter has taken an empirical approach to the problem, the effect on the correlations is calculable from equation 5.36. This would involve a three dimensional integral and the loss of angular degeneracy of the correlations.

Finally, a Legendre polynomial method was suggested as a more complete analysis of the redshift distortions in Fourier space. The hexadecapole moment has the advantage of being exact to linear order, and this could enable an analysis of the importance of the velocity difference term, which has been neglected in the rest of this chapter. The

results presented here, however, suggest that this term is not a significant contributor to $\beta$, since for an ensemble of large spherically symmetric simulations, the mean value of $\beta$ was found to be consistent with the true value.

# Chapter 6

# CONCLUSIONS

This chapter gives a summary of the main results of the preceding chapters, and explores the prospects for future work on placing limits on non-Gaussian primordial fluctuations.

### Non-linear evolution of the power spectrum

Peacock & Dodds (1996) have produced a fitting formula which maps initially power law power spectra onto their evolved, non-linear counterparts. In Chapter 2, an alternative method was explored to allow initially non-power law power spectra to be mapped. This involved plotting the integrated linear power against the integrated non-linear power. The integrated power locus was found to be less dependent on spectral index, and enabled good fitting for monotonic, smoothly varying power spectra without the need for iteration, and with only a rough guess for the tangential spectral index. The formula was also applied to cases where the initial power spectrum contained oscillatory features, and here it was found to break down. This seems to be due to a qualitatively different behaviour that occurs in the evolution of oscillatory power spectra – while the oscillations are preserved in the linear regime, they are completely erased in the non-linear regime, and this process requires a many to one mapping, which is beyond the scope of the fitting formula considered here. It is possible that these power spectra could be mapped in two stages – with the first stage involving some form of smoothing of the power spectrum above a certain linear amplitude, and the second stage a mapping to

the non-linear power. While this would make retrieving the linear power spectrum difficult, the degeneracy arising in the evolved power spectrum starting from different initial linear power spectra is itself an issue that merits further work.

The first part of Chapter 3 addressed the evolution of the power spectrum of initially non-Gaussian fields, comparing the evolution of different power law linear power spectra with that predicted for power spectra with Gaussian initial conditions. A number of different non-Gaussian models were considered, with high and low skewness and kurtosis, as well as fields that were locally Gaussian with a modulation of the amplitude of clustering on large scales. Broadly, the evolution on scales where the linear power amplitude was less than one followed the Gaussian locus for linear evolution, and the main differences came in the quasi-linear regime, with the slope of the turn off from linear behaviour being the discriminator between Gaussian and non-Gaussian evolution. The evolution of the modulated, locally Gaussian fields was found to be very similar to the Gaussian evolution, while the $\chi^2_+$ models, with high skewness appeared to evolve faster, producing a higher non-linear power amplitude for a given linear input. Conversely, low skewness models evolved much less than the Gaussian prediction for a given linear amplitude. It seems however that skewness and kurtosis amplitudes cannot give the full indication for the evolution of the power spectrum, since some fields with similar higher order hierarchical moments displayed very different evolutionary behaviour (*e.g.* the Cauchy field compared with the $\chi^2_+$ field).

The evolution was also found to be spectral index dependent, with all $n = -1$ models evolving closest to the Gaussian locus. Qualitatively, this agrees with the predictions of Gaztañaga & Fosalba (1998) who have investigated the mildly non-linear evolution of non-Gaussian models.

The faster evolution of the $\chi^2_+$ model has made it a possible alternative to Gaussian fluctuations in the standard CDM scenario, which has trouble reproducing the high redshift structures that are now being observed. The second part of Chapter 3 considered the viability of four isocurvature models with $\chi^2_+$ initial conditions, asking whether such models could be made to produce the observed APM power spectrum, and whether the higher order moments of the evolved fields agreed with existing APM measurements. The

models were found to be able to produce the APM power spectrum, but their hierarchical moments were a factor of three too high to be compatible with the APM hierarchical moments. A number of different biasing schemes were then applied to evolved simulations of the models to see if this could bring the biased moments into agreement with the APM moments. It was found that biasing levels of order $2 \lesssim b \lesssim 6$ would be required to get agreement with the APM data, and these levels seem to be too high to be consistent with current estimates for $\beta_{\rm optical}$ and $\Omega_0$, which favour bias values of $b \lesssim 2$.

### Power correlations

Higher order moments are clearly a better discriminator between non-Gaussian and Gaussian fields, and in Chapter 4, a four point Fourier based test for Gaussian fields was developed. Working in Fourier space has several advantages – firstly, Fourier modes separate information on the basis of scale, and since large scale modes evolve independently of smaller, non-linear modes, it is a useful means for probing the linear regime. Secondly, the effects of masks and selection functions can be dealt with easily, and given that the underlying Fourier modes are statistically independent, (if the Universe is homogeneous and isotropic), a full error analysis is possible.

The power correlations test involves measuring correlations between the amplitude squared of the Fourier modes (power modes), and comparing these with correlations between the Fourier modes themselves, which, for a Gaussian field are function only of the mask and selection function. This statistic is sensitive to phase correlations of the Fourier modes and the kurtosis of the density fluctuations. It was applied to the QDOT+1.2 Jy survey, and on scales of $k = 0.08\,h$ Mpc$^{-1}$, the galaxy density fluctuations were found to be consistent with a Gaussian distribution. The test was then extended to place quantitative limits on a certain class of non-Gaussian models – the modulated field, in which the density field is the product of two independent Gaussian fields. For the QDOT+1.2 Jy survey, however, no strong limits could be placed on these fields, and these await the next generation of redshift surveys, for which the sensitivity is projected to improve by about a factor of four to ten for the 2dF and Sloan redshift surveys. While the results of this chapter relied on empirical determination of the errors, a description of a fuller

error analysis was outlined, which would allow a likelihood analysis to be performed for future tests.

### Redshift Distortions

The power correlations test is to some degree affected by redshift distortions, and in Chapter 5, these were considered in some detail. The sensitivity of the test was found to be reduced by about 10% for a rough estimate of $\beta$ with an error range of $\sim 0.6$. It was, however possible to develop the power correlations method to account for $\beta$, by looking at the mode correlations.

The existing analyses of Kaiser (1993), and Zaroubi & Hoffman (1996) were extended to include the effects of the quasi-linear regime, in which galaxy velocities in clusters act to damp the measurement of the linear infall. This fuller analysis of mode correlations in redshift space was then used to develop a method for measuring $\beta$, which involved looking at the difference in correlations between modes with parallel $k$-vectors, and those whose $k$-vector separation was perpendicular to one of the $k$-vectors. These two angular configurations for the $k$-vectors give the extrema of the effect on the mode correlations – with parallel correlations being the least extended, and the perpendicular correlations, the most extended.

The method was tested on simulations of spherical redshift surveys, and found to work well, with little sign of biasing in the determination of $\beta$. It was then adapted to take into account masked areas in realistic surveys by filling in the mask with random points. Determination of $\beta$ from these masked surveys gave a systematic underestimate of $\beta$, as expected. The amplitude of this underestimate was determined empirically for a number of QDOT+1.2 Jy-type simulations, and the test with empirical corrections was applied to find an estimate for $\beta$ from the real QDOT+1.2 Jy redshift survey. This gave an estimate for the redshift distortion parameter of $\beta_{\rm IRAS} = 1.05 \pm_r 0.26 \pm_s 0.1$, where subscripts $r$ indicate the random error, and $s$ the error in the systematic correction. This result is consistent with values measured for this survey in the literature. The systematic error could be eliminated if the mask was taken into account in the theory, and this would be a simple extension to the present analysis. A more complete analysis was suggested in which all pairs of $k$-vector configurations were analysed in terms of Legendre polynomials

for the different orientations of the $k$-vectors. This has an advantage that the velocity difference term, $\Delta U/r$, which was neglected for the above analysis, does not feature in the hexadecapole moment, making this moment exact to linear order. A Legendre polynomial method would therefore enable an analysis of the extent to which the velocity difference term contributes to mode correlations.

**Prospects for constraining primordial non-Gaussian density fields**

A number of theories set out to explain the initiation of density perturbations in the early Universe, and since most of these theories require new physics, it is of great interest to try to constrain them. The prediction of Gaussian or non-Gaussian distributed initial perturbations is a key discriminator between theories of inflation and topological defects, and this provides a vital, testable prediction with which to investigate theories of perturbation initiation.

Over the past decade, many cosmologists have studied the density field with a view to constraining the statistics. So far, the density field as measured from redshift surveys and super-horizon scale microwave background experiments, has been found to be consistent with a Gaussian distribution. There are two complementary approaches to placing limits on the distribution – the first being to place limits on specifically motivated non-Gaussian distributions, and the second to measure moments of the distribution to increasing orders, and check their consistency with a Gaussian field. The higher the order of the moment investigated, the larger the volume that needs to be sampled to retain the same accuracy of the estimate. At present, redshift data has limited tests to measuring moments to fourth or fifth order, and to scales less than $\sim 60\,h^{-1}\,\mathrm{Mpc}$. Cosmology is on the verge of an explosion of observational data, and in the next decade, we can expect to improve current limits by orders of magnitude. The developments come from a number of fields.

A number of new instruments have recently opened up the field of high redshift cosmology, for example 'SCUBA' (the Sub-millimetre Common User Bolometric Array), which has enabled studies of very high redshift galaxies, and the Keck ten metre optical telescopes, which have facilitated accurate redshift determination of distant galaxies. As our knowledge of the distribution of high redshift galaxies increases, this should tighten

limits on the rate of evolution of structure.

Redshift surveys are an extremely important tool in analysing the three dimensional distribution of large scale structure. This thesis has used the QDOT+1.2 Jy combined redshift survey, and in the past couple of years, its one-in-one parent, the PSCz survey has been completed, containing around 15000 galaxies, and covering 83% of the sky. In the next five years, these surveys will be superceded by two redshift surveys that will outdo existing surveys by orders of magnitude in both the number of galaxies, and the volumes probed. The 2dF (two degree field), and Sloan digital sky surveys plan to use multi-fibre spectrographs to measure the redshifts of between $10^5$, and $10^6$ galaxies, probing scales out to $\sim 500\,h^{-1}\,\mathrm{Mpc}$. This should allow extremely accurate determinations of higher order moments of the galaxy density field on scales greater than $30\,h^{-1}\,\mathrm{Mpc}$, which is the onset of the linear regime.

There are, however, some intrinsic limitations to the use of redshift surveys for inferring information about the primordial density field. The first of these is redshift distortions, which affect our precise knowledge of the radial spatial component of each galaxy. Statistically, on linear and quasi-linear scales, however, this distortion can be accounted for, as we have seen in Chapter 5. On scales less than $30\,h^{-1}\,\mathrm{Mpc}$, non-linear evolution of the density field limits what we can infer about the linear density field, and we currently rely on perturbation theory and simulation approaches to analyse these scales. Most problematic though, is our lack of understanding of how the positions of galaxies relate to the underlying matter distribution. Until we understand how galaxies form, inferences from redshift surveys are subject to assumptions about the nature of bias. Work in the fields of galaxy formation and gravitational lensing are therefore extremely important complementary fields to measuring large scale structure from redshift surveys.

Finally, technological developments in the field of microwave receivers, (namely the use of actively cooled HEMT receivers and arrays of detectors) have initiated two new satellite projects to measure the fluctuations in the microwave background temperature – 'Planck', a European based mission, and 'MAP' (Microwave Anisotropy Probe), a US funded mission. These projects, set to fly in 2004, and 2001 respectively, aim to measure CMB fluctuations down to angular scales of less than one degree, and in the case

of Planck down to $7'$ with a sensitivity of a few $\mu K$. The importance of measuring fluctuations on sub-degree scales is that it probes matter fluctuations on sub-horizon scales, which are of great interest for structure formation. In the absence of an era of reionisation, these projects are potentially of revolutionary value to cosmology, allowing the accurate measurement of many cosmological parameters, and because the microwave background directly probes linear mass fluctuations, it is here that we can expect the tightest limits on non-Gaussian fields to be placed.

The standard CDM picture of the Universe is now struggling to account for current observations. It seems therefore timely that observational cosmology is set to make great advances, allowing existing models to be properly constrained, perhaps challenging our current picture of structure formation, and most importantly encouraging the birth of new ideas.

## REFERENCES


Adler R., 1981, 'The Geometry of Random Fields', Wiley

Allen T.J., Grinstein B., Wise M.B., 1987, Phys Lett B, **197**, no 1,2, 66

Alpher R.A., Herman R.C., 1949, Phys. Rev., **75**, 1089

Arfken G., 1985, 'Mathematical Methods for Physicists', Academic Press Ltd

Avelino P.P., Shellard E.P.S., Wu J.H.P., Allen B., 1998, astro-ph/98903120

Bagla J.S., Padmanabhan T., 1997, MNRAS, **286**, 1023

Ballinger W.E., Heavens A.F., Taylor A.N.T., 1995, MNRAS, **276**, 59

Banday A.J., Górski K.M., Bennett C.L., Hinshaw G., Kogut A., Lineweaver C., Smoot G.F., Tenorio L., 1997, **475**, 393

Bardeen J.M., Bond J.R., Kaiser N., Szalay A.S., 1986, ApJ, **304**, 15

Bardeen J.M., Steinhardt P.J., Turner M., 1983, Phys. Rev. D **28**, 679

Barnes J., Hut P., 1986, Nature, **324**, 446

Barrow J.D., Liddle A.R., 1997, GReGr, **29**, 1501

Baugh C.M., 1996, MNRAS, **280**, 267

Baugh C.M., Efstathiou G., 1994, MNRAS, **270**, 183

Baugh C.M., Gaztañaga E., Efstathiou G., 1995, MNRAS, **274**, 1049

Bernardeau F., 1994, ApJ, **433**, 1

Bernardeau F., Juskiewicz R., Dekel A., Bouchet F., 1995, MNRAS, **274**, 20

Bondi H., 1947, MNRAS, **107**, 410

Bromley B.C., Warren M.S., Zurek W.H., 1997, ApJ, **475**, 414

Canavezes A. *et al.* , 1998, MNRAS, **297**, 777

Carr B, 1994, ARA& A, **32**, 531

Carroll S.M., Press W.H., Turner E.L., 1992, ARA&A, **30**, 499

Cen R.Y, Ostriker J.P., Spergel D.N., Turok N., 1991, ApJ, **383**,1

Cen R.Y., Ostriker J.P., 1992, ApJ, **399**, L13

Chodorowski M.J., Bouchet F.R., 1996, MNRAS **279**, 557

Cole S., Fisher K.B., Weinberg D.H., 1994, MNRAS, **267**, 785 (Paper I)

Cole S., Fisher K.B., Weinberg D.H., 1995, MNRAS, **275**, 515 (Paper II)

Cole S., Hatton S., Weinberg D.H., Frenk C.S., 1998, MNRAS submitted

Coles P., Jones B., 1991, MNRAS, **238**, 1

Coles P., Lucchin F., 1995 'Cosmology - The Origin and Evolution of Cosmic Structure', Wiley

Coles P., 1993, MNRAS, **262**, 1065

Coles P., Barrow J.D., 1987, MNRAS, **228**, 407

Coles P., Moscardini L., Lucchin F., Matarrese S., Messina A., 1993, MNRAS, **264**, 749

Collins C.A., Heydon-Dumbleton N.H., MacGillivray H.T., 1988, MNRAS, **236**, 7P

Collins C.A., Nichol R.C., Lumsden S.L., 1992, MNRAS, **254**, 295

Colombi S., Bernardeau F., Bouchet F.R., Hernquist L., 1997, MNRAS, **287**, 241

Cooley J.W., Tukey J.W., 1965, Math. Computation, **19**, 297

Couchman H.M.P., 1991, ApJ, **368**, L23

Da Costa L.N., *et al.* , 1994 ApJ **424**L, 1

Dekel A., Rees M.J., 1987, Nature, **326**, 455

Dunlop J.S., Peacock J.A., Spinrad H., Dey A., Jimenez R., Stern D., Windhorst R.A., 1996, Nature, **381**, 581

Eastwood J.W., Hockney R.W., 1974, J. Comput. Phys., **16**, 342

Efstathiou G., Davis M., White S.D.M., Frenk C.S., 1985, ApJS **57**, 241

Efstathiou G., Kaiser N., Saunders W., Lawrence A., Rowan-Robinson M., Ellis R. S., Frenk C. S., 1990, MNRAS, **247**, 10P

Fan Z. H., Bardeen J. M., 1995, Phys. Rev. D, **51**, 6714

Feldman H.A., Kaiser N., Peacock J.A., 1994, ApJ, **426**, 23

Feller W., 1966, 'An Introduction to Probability Theory and its applications', Volume II

Fisher K.B., Davis M., Strauss M. A., Yahil A., Huchra J. P., 1993, ApJ, **402**, 42

Fisher K.B., Huchra J.P., Strauss M.A., Davis M., Yahil A., Schlegel D., 1995, ApJS, **100**, 69

Fisher K.B., Scharf C.A., Lahav O., 1994, MNRAS, **266**, 219

Fisher K.B., Davis M., Strauss M.A., Yahil A., Huchra J.P., 1994b, MNRAS, **267**,927

Fisher K.B., Davis M., Strauss M.A., Yahil A., Huchra J.P., 1994a, MNRAS, **266**, 50

Freedman W.L., Mould J.R., Kennicutt R.C., Madore B.F., 1997, IAUS 183E, 14 'Cosmological Parameters and the Evolution of the Universe'

Frenk C., White S., 1985, Nature, **317**, 670

Fry J.N., Gaztañaga E., 1994, ApJ, **425**, 1

Fry J.N., Scherrer R.J., 1994, ApJ, **429**, 36

Gamow G., 1948, Phys. Rev., **74**, 505

Gaztañaga E., 1992, ApJ, **398**, L17

Gaztañaga E., Baugh C.M., 1998, MNRAS, **294**, 229

Gaztañaga E., Mähönen, P., 1996, ApJL, **462**,1

Gaztañaga E., 1994, MNRAS, **268**, 913

Gaztañaga E., Fosalba, P., 1998, MNRAS, **301**, 524

Górski K.M., Banday A.J., Bennet C.L., Hinshaw G., Kogut A., Smoot G.F., Wright E.L., 1996, ApJ, **464**L, 11

Gott J. R., III, Weinberg D. H., Melott A. L., 1987, ApJ, **319**, 1

Governato F., Baugh C.M., Frenk C.S., Cole S., Lacey C.G., Quinn T., Stadel J., 1998, Nature, **392**, 359

Gramann M., Cen R., Bahcall N.A., 1993, ApJ, **419**, 440

Guth A.H., 1981, Phys Rev D, **23**, 347

Guth A.H., Pi S.Y., 1982, Phys Rev Lett, **49**, 1110

Hamilton A.J.S., 1997, astro-ph/9708102

Hamilton A.J.S., Culhane M., 1996, MNRAS, **278**, 73

Hamilton A.J.S., Kumar P., Lu, E., Matthews A., 1991, ApJ, **374**, L1

Harrison E.R., 1970, Phys Rev, D., **1**, 2726

Heavens A.F., Taylor A.N.T., 1995, MNRAS, **275**, 483

Hivon E., Bouchet F.R., Colombi S., Juskiewicz R., 1995, A&A, **298**, 643

Hockney R.W., Eastwood J.W., 1988, IOP 'Computer simulation using particles'

Hubble E., 1929, Proc. Nat. Acad., **15**, 168

Huchra J., Davis M., Latham D., Tonry J., 1983, ApJS, **52**, 89

Irvine W.M., 1961, Ph.D. Thesis, Harvard University

Jain B., Mo H.J., White S.D.M., 1995, MNRAS, **276**L, 25

Jenkins A., Frenk C.S., Thomas P.A., Colberg J.M., White S.D.M., Couchman H.M.P., Peacock J.A., Efstathiou G., Nelson A.H., 1998, ApJ, **499**, 20

Juskiewicz R., Bouchet F., Columbi S., 1993, ApJ, **419**, L9

Kaiser N., 1987, MNRAS, **227**, 1

Kendall M. G., Stuart, A., 1969, 'The Advanced Theory of Statistics', Volume II, Griffin, London

Kim A.G. *et al.* , 1997, ApJ, **476**, 63

Knop, R.A.*et al.* , 1997, AAS, **191**, 9501

Layzer D., 1963, ApJ. **138**, 174

Lawrence A., Rowan-Robinson M., Saunders W., Parry I.R., Xia X, Ellis R.S., Frenk C.S., Efstathiou G., Kaiser N., Crawford J., 1996, MNRAS in press

Limber D.N., 1954, ApJ, **119**, 655

Lin H., Kirshner R.P., Schectman S.A., Landy S.D., Oemler A., Tucker D.L., Schechter P. L., 1996, ApJ, **471**, 617

Little B., Weinberg D.H., 1994, MNRAS, **267**, 605

Longair M.S., 1984, 'Theoretical Concepts in Physics', Cambridge University Press

Loveday J., Efstathiou G., Maddox S.J., Peterson B.A., 1996a, ApJ, **442**, 457

Loveday J., Peterson B.A., Maddox S.J., Efstathiou G., 1996b, ApJS **107**, 201

Loveday J., Efstathiou G., Maddox S.J, Peterson B.A., 1996, ApJ, **468**, 1

Maddox S.J., Efstathiou G., Sutherland W.J., 1996, MNRAS, **283**, 1227

Maddox S.J., Sutherland W., Efstathiou G., Loveday J., 1990, MNRAS, **243**, 692

Maddox S.J. *et al.* ,1998, 'Proceedings of the 12th Potsdam Cosmology Workshop', Eds. V. Mueller, S. Gottloeber, J.P. Muecket, J. Wambsganss, World Scientific, p. 91-96

Mann R.G., Peacock J.A., Heavens A.F., 1998, MNRAS, **293**, 209

Mather J.C. *et al.* , 1994, ApJ, **420** no.2, 439

Messina A., Lucchin F., Matarrese S., Moscardini L., 1992, Astroparticle physics, **1**, 99

Moore B., Frenk C. S., Weinberg D. H., Saunders W., Lawrence A., Ellis R. S., Kaiser N., Efstathiou G., Rowan-Robinson M., 1992, MNRAS, **256**, 477

Moscardini L., Matarrese S., Lucchin F., Messina A., 1991, MNRAS, **248**, 424

Møller C., 1972, 'The Theory of Relativity', Oxford University Press

Mészáros P., 1974, A & A **37**, 225

Nusser A., Dekel A., Yahil A., 1995, ApJ, **449**, 439

Padmanabhan T., 1996, MNRAS, **278**, L29

Park C., Gott J. R., III, Da Costa L. N., 1992, ApJ, **392**L, 51

Park C., Vogeley M.S., Geller M.J., Huchra J.P., 1994, ApJ, **431**, 569

Peacock J.A., 1997, MNRAS, **284**, 885

Peacock J.A., Heavens A.F,. 1985, MNRAS, **217**, 805

Peacock J.A., Dodds S.J., 1996, MNRAS, **280**, L19

Peacock J.A., Dodds S.J., 1994, MNRAS **267**, 1020

Peacock J.A., 1991, 'The Statistics of cosmological density fields', in 'New Insights into the Universe', Springer, eds Martinez V., Portilla M., Saez D., Valencia

Peacock J.A., Nicholson, D., 1991, MNRAS, **253**, 307

Peacock J.A., 1998, 'Cosmological physics', Cambridge University Press

Peacock J.A., Jimenez R., Dunlop J.S., Waddington I., Spinrad H., Stern D., Dey A., Windhorst R.A., 1998, MNRAS, **298**, 1089

Pearce F.R., Couchman, H.M.P., 1997, NewA, **2** 411

Pearce F.R., Couchman H.M.P., Jenkins A. R., Thomas P.A., 1995, 'Hydra – Resolving a parallel nightmare', Dynamic Load Balancing on MPP systems.

Peebles P.J.E., 1980, 'The large scale structure of the universe', Princeton University Press

Peebles P.J.E., 1983, ApJ, **274**, 1

Peebles P.J.E., 1997, ApJ, **483**L, 1

Peebles P.J.E., 1998(a) astro-ph/9805194

Peebles P.J.E., 1998(b), astro-ph/9805212

Penzias A.A., Wilson R.W., 1965, ApJ, **142**, 419

Perlmutter S. *et al.* , 1998, Nature, **391**, 51

Ratcliffe A., Shanks T., Fong R., Parker Q.A., 1998, MNRAS, **296**, 191

Reeves H., Audouze J., Fowler W.A., Schramm D.N., 1973, ApJ, **179**, 909

Riess A.G., et al, 1998, to appear in ApJ, astro-ph/9805201

Rowan-Robinson M, 1988, SSRv **48**, 1

Saunders W., Frenk C., Rowan-Robinson M., Lawrence A., Efstathiou G., 1991, Nature, **349**, 32

Saunders W., Rowan-Robinson M, Lawrence A., 1992, MNRAS, **258**, 134

Saunders W., *et al.* , 1998, in Extragalactic Astronomy in the Infrared, eds Mamon G.A., Trinh Xuan Thuan & Tran Thanh Van (Gif-sur-Yvette: Editions Frontieres)

Shectman S.A., Landy S.D., Oemler A., Tucker D.L., Lin H., Kirshner R.P., Schecter P.L., 1996, ApJ, **470**, 172

Silk J., 1967, Nature, **215**, 1155

Silk J., 1986, 'Inner Space / Outer Space', p 143, eds Kolb E.W., Turner M.S., Lindley D., Olive K., Seckel D., Univ. Chicago Press, Chicago

Steidel C.C., Adelberger K.L., Dickinson M., Giavalisco M., Pettini M., Kellogg M., 1998, ApJ, **492**, 428

Stirling A.J., Peacock J.A., 1996, MNRAS, **283**, L99

Strauss M.A., Huchra J.P., Davis M., Yahil A., Fisher K., Tonry J., 1992, ApJS **83**, 29

Szalay A., 1998, AAS, **192**, 6405

Tadros H., Efstathiou G., 1995, MNRAS, **276**, L45

Tadros H., Ballinger W.E., Heavens A.F., Taylor A.N., Efstathiou G., Frenk C.S., Keeble O., MacMahon R., Maddox S.J., Oliver S., Rowan-Robinson M., Saunders W., Sutherland W.J., White S.D.M., 1998, in preparation for submission to MNRAS

Tadros H., Efstathiou G., 1996, MNRAS, **282**, 1381

Taylor A.N., Hamilton A.J.S., 1996, MNRAS, **282**, 767

Taylor A.N., Rowan-Robinson M., 1992, Nature, **359**, 396

Trimble V., 1987, ARA& A, **25**, 425

Tripp R., 1997, A & A, **325**, 871

Turok N., 1989, Phys Rev Lett **63**, 2625

Vogeley M. S., Park C., Geller M. J., Huchra J. P., Gott J. R., III, 1994, ApJ, **420**, 525

Vogeley M.S., Park C., Geller M.J., Huchra J.P., 1992, ApJ, **391**, L5

Walker T.P., Steigman G., Schramm D.N., Olive K.A., Kang H., 1991, ApJ, **376**, 51

Weinberg D.H., Cole S., 1992, MNRAS, **259**, 652

White S.D.M., Frenk C.S., Davis M., 1983, ApJ, **273**, L1

Yi I., Vishniac E.T., 1993, APJS, **86**, 333

Zaroubi S., Hoffman Y., 1996, ApJ, **462**, 25

Zel'dovich Ya.B., 1970, A&A, **5**, 84

Zel'dovich Ya.B., 1972, MNRAS, **160**, 1P

Zwicky F., 1933, Helv. Phys. Acta, **6**, 110